

Dissertation

submitted to the

Combined Faculties of the Natural Sciences and Mathematics
of the Ruperto-Carola-University of Heidelberg, Germany

for the degree of

Doctor of Natural Sciences

Put forward by

Constanze Hasterok

born in Dresden

Oral examination on 25th October 2017

**Gas Purity Analytics,
Calibration Studies,
and Background Predictions
towards
the First Results of XENON1T**

1st Referee: Prof. Dr. Manfred Lindner

2nd Referee: Jun. Prof. Dr. Loredana Gastaldo

Abstract

The XENON1T experiment aims at the direct detection of the well motivated dark matter candidate of weakly interacting massive particles (WIMPs) scattering off xenon nuclei. The first science run of 34.2 live days has already achieved the most stringent upper limit on spin-independent WIMP-nucleon cross-sections above masses of 10 GeV with a minimum of $7.7 \cdot 10^{-47} \text{ cm}^2$ at a mass of 35 GeV. Crucial for this unprecedented sensitivity are a high xenon gas purity and a good understanding of the background.

In this work, a procedure is described that was developed to measure the purity of the experiment's xenon inventory of more than three tons during its initial transfer to the detector gas system. The technique of gas chromatography has been employed to analyze the noble gas for impurities with the focus on oxygen and krypton contaminations. Furthermore, studies on the calibration of the experiment's dominating background induced by natural gamma and beta radiation were performed. Hereby, the novel sources of radioactive isotopes that can be dissolved in the xenon were employed, namely ^{220}Rn and tritium. The sources were analyzed in terms of a potential impact on the outcome of a dark matter search. As a result of the promising findings for ^{220}Rn , the source was successfully deployed in the first science run of XENON1T. The first WIMP search of XENON1T is outlined in this thesis, in which a background component from interactions taking place in close proximity to the detector wall is identified, investigated and modeled. A background prediction was derived that was incorporated into the background model of the WIMP search which was found to be in good agreement with the observation.

Kurzdarstellung

Das XENON1T Experiment hat sich zum Ziel gesetzt, den gut motivierten dunkle Materie Kandidaten der schwach wechselwirkenden Teilchen (WIMPs) durch Streuung an Xenonatomkernen nachzuweisen. Schon nach der ersten Datennahme konnte die führende Ausschlusskurve auf spinunabhängige Wechselwirkungen von WIMPs mit Nukleonen oberhalb Massen von 10 GeV gesetzt werden, mit einem Minimum von $7.7 \cdot 10^{-47} \text{ cm}^2$ bei einer Masse von 35 GeV. Von zentraler Bedeutung für diese noch nie da gewesene Sensitivität sind eine hohe Reinheit des Xenongases, sowie ein gutes Verständnis für den Untergrund.

In der vorliegenden Arbeit wurde eine Prozedur entwickelt, die die Reinheit des Xenon Inventars des Experiments, bestehend aus über drei Tonnen Gas, während des ersten Transfers in das Gassystem des Detektors misst. Die Analysemethode der Gaschromatographie wurde angewandt, um das Edelgas auf Verunreinigungen zu untersuchen, mit Fokus auf Sauerstoff- und Kryptonkontaminationen. Des Weiteren wurden Studien zur Kalibrierung des dominierenden Untergrunds, verursacht durch natürliche Gamma- und Betastrahlung, durchgeführt. Dabei wurden neuartige Quellen radioaktiver Isotope, die im Xenon gelöst werden können, eingesetzt: ^{220}Rn und Tritium. Die Quellen wurden hinsichtlich ihres möglichen Einflusses auf die Suche nach dunkler Materie verglichen. Als Resultat kam die ^{220}Rn -Quelle erfolgreich in der ersten Datenperiode von XENON1T zum Einsatz. Die erste WIMP-Suche von XENON1T, in welcher eine Untergrundkomponente von Interaktionen nahe der Detektorwand identifiziert, untersucht und modelliert wurde, wird in dieser Arbeit beschrieben. Eine Untergrundvorhersage, welche gut mit der Beobachtung übereinstimmt, wurde abgeleitet und in der WIMP-Analyse angewandt.

Contents

1	The Dark Matter Mystery	3
1.1	Astrophysical and Cosmological Indications	3
1.2	Explaining the Dark Matter Nature	6
1.3	The WIMP Candidate	7
1.4	WIMP Detection Techniques	9
1.5	WIMP Direct Detection in Xenon	10
1.5.1	WIMP Recoil Rates	10
1.5.2	Current Status of Direct Detection	13
2	The XENON Experiments	17
2.1	The Two-Phase TPC Principle	18
2.2	Xenon as Detection Medium	19
2.3	Generation of Light and Charge Signals	21
2.3.1	Primary Scintillation Light (S1)	22
2.3.2	Secondary Scintillation Light (S2)	23
2.3.3	Energy Scale	24
2.3.4	Position Dependent Signal Corrections	25
2.4	Event Waveforms	26
2.5	Electronic Recoil Background	28
2.5.1	Radioactivity from Detector Materials	29
2.5.2	Intrinsic ^{222}Rn	30
2.5.3	Intrinsic ^{85}Kr	30
2.5.4	^{136}Xe Double-Beta Decay and Solar Neutrinos	31
2.6	The XENON100 Experiment	31
2.7	The XENON1T Experiment	34
3	Xenon Gas Purity Analytics	39
3.1	Motivation	39
3.2	Basics of Gas Chromatography	41
3.3	Experimental Setup	42
3.3.1	XENON1T Bottle Rack	43
3.3.2	The Gas Chromatograph	44
3.4	Measurement Procedure	46
3.5	Evaluation of Impurity Concentrations	49
3.5.1	Calibration Method and Background Subtraction	50

3.5.2	Re-Calibration of O ₂	52
3.5.3	Uncertainties	53
3.5.4	Decision Threshold	54
3.5.5	Verification of Calibration Method	55
3.6	Results	57
3.6.1	Total Impurities in the Xenon Inventory	60
3.6.2	Validation of Gas Handling Procedures	62
3.7	Summary and Outlook	63
4	Calibration of the Background Region	67
4.1	Calibration Source Characteristics	68
4.2	Event Selection	70
4.2.1	Alpha Spectroscopy	70
4.2.2	Low Energetic Electronic Recoils	72
4.3	Injection of Radio-Isotopes into the TPC	74
4.3.1	Injection Mechanism	74
4.3.2	Activity Evolution and Electronic Recoil Calibration Rate	75
4.3.3	Distinction of Datasets	79
4.4	Distribution of Electronic Recoils	80
4.5	The Electronic Recoil Band	83
4.5.1	The Band Shape	84
4.5.2	Variations of the Band Shape	86
4.6	Impact of the Calibration on the Dark Matter Results	92
4.6.1	Electronic Recoil Background Model	93
4.6.2	Results	94
4.7	Discrimination Power in XENON100 and XENON1T	96
4.8	Summary and Discussion	99
5	First Dark Matter Result of XENON1T	101
5.1	Data Quality and Event Selection	101
5.2	Nuclear Recoil Calibration	103
5.3	Studies on Electronic Recoil Calibration Data	104
5.3.1	The Electronic Recoil Band	105
5.3.2	Blinding Criterion	106
5.3.3	Compatibility of Calibration and Background Data	108
5.4	Investigation of Wall Events	111
5.4.1	Considerations on the Fiducial Volume Choice	112
5.4.2	²¹⁰ Po Alpha Decays at the Wall	113
5.4.3	Position Resolution and Charge Loss of Wall Events	119
5.4.4	Comparison of Wall Events from ²¹⁰ Po and Low Energy Background	122
5.5	The XENON1T Background Model	125
5.5.1	The Background Components	125
5.5.2	Wall Leakage Background	128
5.6	Results on WIMP-Nucleon Interactions	131
5.7	Summary and Conclusions	133

Appendices	141
A Virial Theorem	143
B Gas Compositions	145
C Electronic Recoil Calibration Studies	147
C.1 Spatial Distribution of ER Data in XENON1T	147
C.2 ^{220}Rn and Thorium Data	147
D Wall Event Studies	151

Introduction

For many decades the mystery of the absence of mass inferred by gravitational interactions within the Universe remains unresolved. This phenomenon, known as dark matter, has been observed on cosmological and astrophysical scales and is an active field in modern research. Multiple models have been developed to explain the dark matter nature and encouraged scientists to develop new detection techniques that are able to probe these hypotheses. A popular dark matter candidate is the weakly interacting massive particle (WIMP) on whose direct detection the XENON collaboration has specialized. A small but finite probability of WIMPs scattering off Standard Model particles is expected, resulting in low rates of the order of 0.01 interactions per year and target mass. Hence, the suppression of interactions induced by natural radioactivity or cosmic rays is a major common challenge of all dark matter search experiments despite their different detection technologies. A good understanding of the sources and features of background radiation is crucial in order to be able to detect a rate excess that might be induced by a new particle.

After the detector technology of time projection chambers (TPC) containing liquid xenon has been successfully proven with target masses up to a few hundred kg, XENON1T is the first experiment that passes the ton scale frontier. This poses new challenges like the assurance of the target purity as well as on the understanding of the detector's background. Both subjects are addressed within this work.

The present thesis is outlined as follows: After an introduction to the foundations of dark matter searches and an overview on the current status of WIMP direct detection in Chapter 1, the detector technology of the XENON experiments is explained in Chapter 2.

The following Chapter 3 deals with the gas purity analytics performed to monitor impurities in the xenon inventory of XENON1T. The measurement technique is presented and the results are discussed with the focus on their impact on the experiment's performance. Chapter 4 is devoted to the calibration of the dominating background component induced by natural gamma and beta radiation. Novel sources of radio-isotopes such as tritium and ^{220}Rn , that are dissolved in the xenon target, are investigated and compared in terms of their suitability for a usage within the XENON1T experiment.

In the final Chapter 5 the first WIMP search analysis of XENON1T is outlined. The calibration data acquired with the ^{220}Rn source is studied and a background component from interactions that take place close to the borders of the detector is identified. By studying the event properties in this outer region, an understanding is developed which is finally used to model the expected background contribution. The chapter concludes with the presentation of the XENON1T first results.

Chapter 1

The Dark Matter Mystery

The mystery of the new form of non-luminous matter is that its presence can only be inferred from gravitational effects on baryonic matter. It is one of the most outstanding questions that drives modern research in various fields of physics. Revealing its nature would mean tremendous progress in explaining the composition and history of the Universe.

Only 4% of the Universe's total energy content is made up of baryonic matter as we see it all around us: on our planet, in stars, galaxies, hydrogen clouds, etc. Among other measurements, its content is well-known from element abundances in primordial nucleosynthesis about 100 seconds after the Big Bang. The remaining 96% are the so-called dark ingredients, namely *dark energy* (69%) and *dark matter* (27%). Their contributions are derived from the Standard Model of cosmology, called Λ CDM. Its name indicates the main ingredients: the cosmological constant Λ and cold (i.e. non-relativistic) dark matter (CDM). Originally introduced by Einstein as a parameter of general relativity to ensure a static Universe, Λ nowadays is attributed to dark energy, which is hypothesized to cause the accelerated expansion of the Universe. The investigation of the second main ingredient, dark matter, provides the motivation for this work.

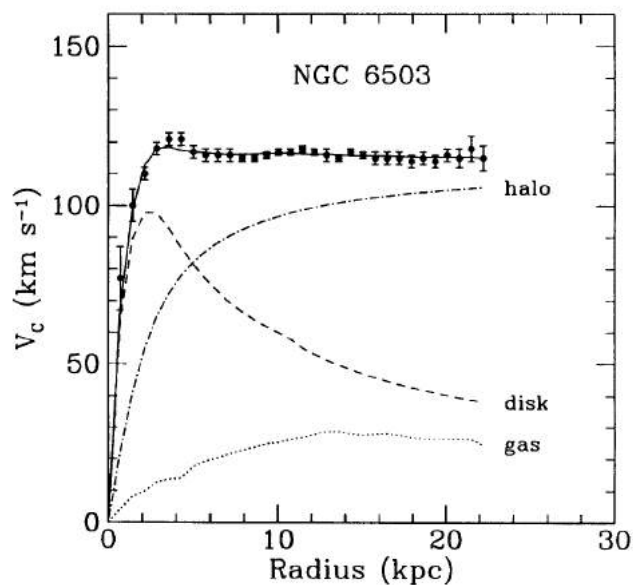
In this chapter, some of the indications for the existence of dark matter on astronomical and cosmological scales are outlined in Section 1.1 and possible dark matter candidates are briefly discussed in Section 1.2. One of the most popular models, the WIMP candidate is introduced in Section 1.3. In Section 1.4, the various approaches that are followed to prove the existence of WIMPs, are outlined. The direct detection approach is the one employed in this thesis. The WIMP detection method, the expected signal rate and the current status of the dark matter search in the field of direct detection of WIMPs, are described in Section 1.5. For a more detailed review of the dark matter mystery, the reader is referred to [1] and [2].

1.1 Astrophysical and Cosmological Indications

The overwhelming evidence of dark matter comprises a wide variety of measurements on different scales. The existence of a new form of non-luminous matter was inferred by Fritz Zwicky in 1933 [3]. Using the virial theorem¹ he found a contradiction between the velocity

¹The complete notation of the virial theorem can be found in the Appendix A

Figure 1.1: Circular velocity of the stars in the galaxy NGC 6503 as a function of radial distance to the center. The labeled lines show the contributions from the the galactic gas (dotted), the disc (dashed), and a halo of a non-luminous matter type (dot-dashed). Adding up all three components, the model (solid line) is in good agreement with the data. Figure from [9]



dispersion of individual nebulae and their luminous mass². Since then, various other observations resulted in the same conclusion.

In the 1970s, Ford and Rubin investigated the rotational velocities v of stars within galaxies as a function of their radial distance r to the galactic center [4]. In contrast to their expectation, they observed that these so-called *rotation curves* are flat. This is in contradiction to Newtonian dynamics, assuming that they are only driven by the visible galaxy mass: $v \propto 1/\sqrt{r}$. Nowadays, similar curves are found for all galaxies [5, 6, 7], including our Milky Way [8]. Figure 1.1 shows the rotation curve of the galaxy NGC 6503. The simplest explanation to describe the data is adding a hypothetical component, the *dark matter halo*. It generates the force that is responsible for speeding up the outer orbits.

Another hint on such dark matter halos comes from gravitational lensing. According to Einstein's theory of general relativity, light follows the time-space curvature caused by massive objects like galaxies which thus can act like a lens. The image of a distant object behind the lens will be distorted, sheared, composed of multiple images, or will be simply brighter in case the composed image cannot be resolved. Provided that the distance to the object is known from redshift measurements, its mass can be calculated from the deflection seen in the image [10, 11]. Comparisons to the mass determined by summing up all the luminous components show a large discrepancy and suggest that a non-luminous matter component has to be present. This technique provides the means to see dark matter up to much larger distances from the galactic center than possible with rotation curves. For comparison: data from rotation curves is available for radii of tens of kpc, whereas gravitational lensing can probe the space up to 200kpc. On even larger Mpc scales, measurements find evidence for dark matter in filaments of the cosmic web [12, 13].

The Bullet Cluster gives another impressive hint of the existence of dark matter. It was formed by the collision of two smaller clusters. Figure 1.2 shows an x-ray measurement in

²“[...] würde sich also das überraschende Resultat ergeben, dass dunkle Materie in sehr viel grösserer Dichte vorhanden ist als leuchtende Materie.” [3]



Figure 1.2: Overlaid images of the Bullet Cluster (1E 0657-558): optical image (NASA/STScI; Magellan/U.Arizona/D.Clowe et al.), x-ray map (NASA/CX- C/CfA/M.Markevitch et al.) and mass distribution from gravitational lensing (NASA/STScI; ESO WFI; Magellan/U.Arizona/D.Clowe et al.). The dominant mass constituents (marked in blue) have been separated from the colliding luminous mass of the intergalactic medium (marked in red). See text for more explanations.

pink, performed by the Chandra x-ray observatory that illustrates the two intergalactic gas clouds. While friction processes during collision are clearly visible in their shapes, the dark matter components deduced from gravitational lensing (blue clouds) seem to have traversed unaffectedly. The result is the separation of the baryonic matter from the dark matter. This effect can be seen in 72 further galaxy cluster collisions resulting in a constraint on the self-interaction cross section that disfavors some proposed extensions of the Standard Model of particles [14].

All these observations suggest the presence of more gravitational interacting matter than calculated from the luminous constituents. However, a quantification of dark matter in terms of its contribution to the total energy content of the Universe was due for decades. In 1965, Penzias and Wilson prepared the ground by discovering the Cosmic Microwave Background (CMB) radiation. Its black body spectrum with a temperature of 2.725 K promoted the consensus of being a remnant from the Big Bang and not the result of scattered starlight from distant galaxies. It was found that small anisotropies of the order 10^{-3} K in the CMB temperature encode the dynamics present in the baryon-photon plasma at the time of photon-decoupling 380000 years after the Big Bang (see Figure 1.3). They correspond to regions of slightly different densities and represent the seeds of the Universe's structure as observed today. The sky map can be transformed into a so-called *power spectrum*, essentially showing the correlation strength between every possible combination of two points in the sky as a function of the angular distance. A characteristic pattern becomes visible as can be seen in Figure 1.4. The peaks result from acoustic oscillations in the baryon-photon plasma of the early universe. Their angular scale and height are powerful probes of the Λ CDM model by providing access to the current baryonic ($\Omega_b h^2$), dark matter ($\Omega_c h^2$), and dark energy (Ω_Λ) densities whereas the former two are usually normalized to the Hubble constant via $H_0 = 100h \text{ km s}^{-1} \text{ Mpc}^{-1}$. The most recent and precise measurement was performed by the *Planck* experiment resulting in the following energy densities [15]:

$$\Omega_b h^2 = 0.02226 \pm 0.00023, \quad \Omega_c h^2 = 0.1186 \pm 0.0020, \quad \Omega_\Lambda = 0.692 \pm 0.012.$$

This translates into the abundances of $\sim 69\%$ dark energy, $\sim 27\%$ dark matter, and $\sim 4\%$ ordinary matter.

The very precise result of the CMB is confirmed by Big Bang nucleosynthesis (BBN). A few

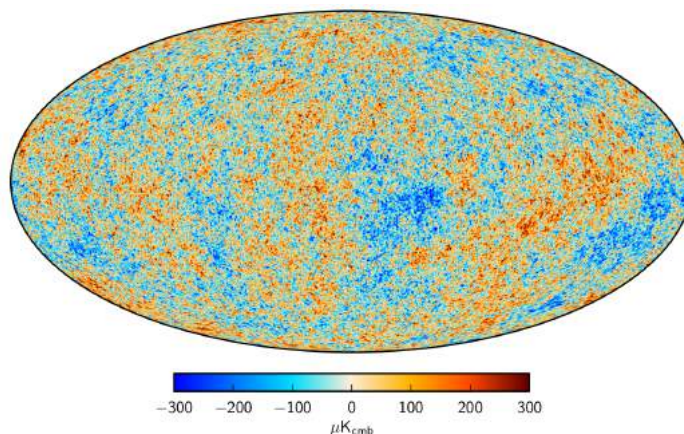


Figure 1.3: Sky map of temperature fluctuations in the cosmic microwave background as measured by Planck. Figure from [17].

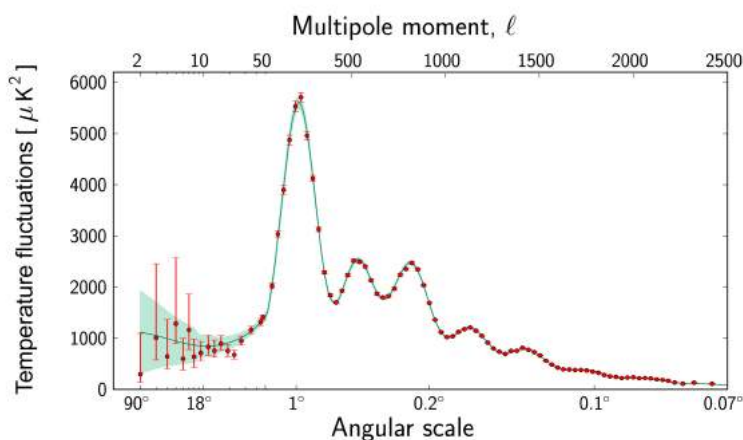


Figure 1.4: Power spectrum of CMB temperature fluctuations. The green line shows the fit of the Λ CDM model to the data together with its uncertainty indicated by the light green band. Figure from [18].

hundred seconds after the Big Bang when the temperature of the Universe was decreased to about ten billion degrees, deuterium became stable: $p + n \rightarrow D + \gamma$. This was the foundation for the formation of helium and lithium. Since heavier elements like carbon, nitrogen and oxygen can only be formed in stars a billion years later, fractional abundances in relation to hydrogen of about 25% for helium, 10^{-5} for deuterium, and 10^{-10} for lithium are expected from the BBN [16]. Under the assumption that baryonic matter makes up only 4% of the total constituents of the Universe, the BBN predictions exactly match the observations.

Although the existence of dark matter is secured by these and many other observations, the knowledge of its true nature is relatively small, as will be discussed in the next section. There are many ideas about possible explanations and particle candidates. However, so far none of them has been proven to be right with high level of confidence.

1.2 Explaining the Dark Matter Nature

As outlined in the previous section, the term dark matter refers to a gravitational potential that cannot be accounted for by ordinary luminous matter. A possible solution to describe some of the mentioned astronomical measurements is the modification of gravitational laws. The galactic rotation curves can, for example, be described by modified Newtonian dynamic

models like MOND [19] or the relativistic extension TeVeS [20]. However, on larger scales such as the CMB structure, MOND cannot be confirmed [21] and TeVeS shows problems in simultaneously fitting observations from gravitational lensing and rotation curves [22].

Also the large observed mass to light ratios cannot be explained by assuming the existence of massive objects like neutron stars, black holes, brown dwarfs or unassociated planets that emit almost no radiation. It was shown that such massive compact halo objects (MACHOs) can only make up about 20% of the dark matter in our galaxy [23].

Regarding dark matter as being a particle is the most common assumption that shows no disagreement with any of the astrophysical observations. Its baryonic nature can be ruled out by the CMB and BBN models. The electromagnetic interaction is excluded by the absence of light absorption or electromagnetic interactions with the interstellar medium. Only neutrinos could therefore be a candidate for dark matter within the Standard Model of particles. However, these light particles cannot explain the observed structure on galactic and intergalactic scales. Due to their relativistic velocities in the early Universe, these structures would be washed out, as can be shown in N-body simulations [24].

Hence, going beyond the Standard Model seems necessary to find a viable dark matter particle candidate. A very popular and widely tested candidate is the weakly interacting particle (WIMP) which is in the focus of this thesis.

1.3 The WIMP Candidate

An important aspect of any dark matter particle candidate is its stability over the age of the Universe and its correct abundance. This can be realized by the freeze-out model.

The concept of freeze-out successfully explained the photon decoupling (observed as the CMB) and the Big Bang nucleosynthesis (validated by the abundance of light elements). It is hence natural to apply it to dark matter as well. In the early Universe, WIMPs are assumed to be in a production-annihilation equilibrium with the thermal plasma [25]. This implies that dark matter particles can be transformed into pairs of Standard Model particles by colliding with their anti-partners, and vice versa. The annihilation rate Γ_{ann} is given by:

$$\Gamma_{\text{ann}} = \langle \sigma_{\text{ann}} v \rangle n, \quad (1.1)$$

where σ_{ann} is the WIMP annihilation cross section, v is the relative velocity of the annihilating particles, and n is their number density. The brackets indicate the average over the WIMP thermal distribution that is assumed to be a Boltzmann distribution.

The annihilation process releases energy, equivalent to two particle masses. For the production reaction, this amount of energy has to be delivered in the form of the kinetic energy of the colliding particles. Due to the Universe's expansion, the temperature drops below the WIMP mass and causes its decoupling from the plasma. The dark matter density starts to decrease as only particles in the high velocity tail of the Boltzmann distribution can still contribute to the production. In parallel, the expansion causes a decrease of n and therefore of the annihilation rate. As soon as the expansion rate H becomes larger than Γ_{ann} , the WIMP abundance stabilizes and stays approximately constant in a co-moving volume. This freeze-out mechanism is depicted in Figure 1.5 where the number density n normalized by the entropy density s is plotted versus m/T with m being the dark matter mass and T the

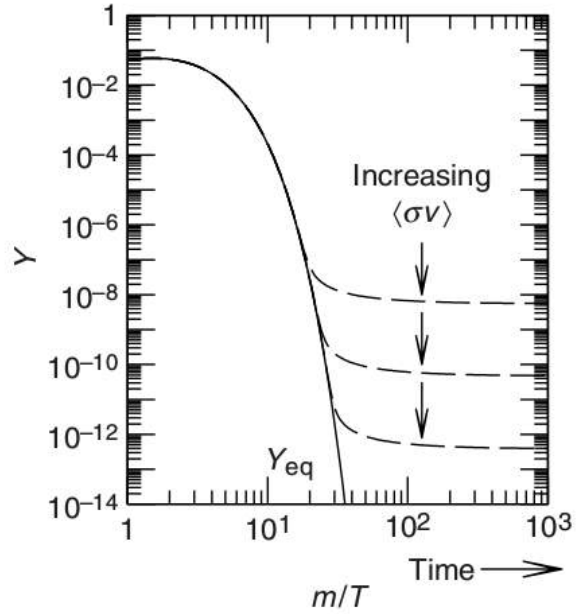


Figure 1.5: Evolution of the normalized WIMP density $Y = n/s$, where s is the entropy density during the epoch of the decoupling from the thermal plasma. m/T denotes the ratio between WIMP mass m and universal temperature T and is a measure for the time before the start of the decoupling process. Figure from [25]

temperature that is proportional to the time. As illustrated, the observed dark matter density as of today is sensitive to the term $\langle\sigma_{\text{ann}}v\rangle$. With increasing self-interaction cross sections, the abundance decreases. The relic dark matter density can be approximated by [25]:

$$\Omega_c h^2 \approx \frac{3 \cdot 10^{-27} \text{ cm}^3 \text{ s}^{-1}}{\langle\sigma_{\text{ann}}v\rangle}. \quad (1.2)$$

If the annihilation cross section $\langle\sigma_{\text{ann}}v\rangle$ is of the order of the weak interaction strength, the equation results in the correct abundance. This coincidence is also known as *WIMP miracle* and is the reason why this model has been extensively probed in experiments.

Since WIMP is a general term for a particle beyond the Standard Model that interacts gravitationally and weakly, a variety of models can provide particles with the required properties. A well motivated WIMP candidate is the neutralino, the lightest supersymmetric particle (LSP) as theorized by the Minimal Supersymmetric Standard Model. This model predicts a supersymmetric partner for each Standard Model particle which allows to stabilize the mass scale of the electroweak symmetry breaking. The neutralino masses range from a few GeV to several TeV. Other WIMP candidates can be found in extra-dimensional models like Kaluza-Klein [26][27].

It should be noted that WIMPs are only one of many dark matter candidates. Another potential candidate are, for example, sterile neutrinos that do not interact with ordinary matter but can mix into the active sector by oscillations. They feature possible masses between 1 keV and tens of keV [28] [29]. Other models that try to explain the conservation of the P and CP symmetries in QCD or the origin of ultra-high energetic cosmic rays provide viable candidates as well, such as axions and WIMPzillas [30, 31] [32]. However, these dark matter candidates are beyond the scope of this thesis. Therefore, only the WIMP detection techniques will be outlined in the following.

1.4 WIMP Detection Techniques

There are three general WIMP search approaches: the production by colliding two standard model particles, the search for interactions between a WIMP and a standard model particle denoted as *direct detection*, and the search for the products of WIMP annihilation denoted as *indirect detection*. Figure 1.6 illustrates these three channels. χ refers to a WIMP and P to a Standard Model particle.

The production of dark matter is possible at colliders like the LHC, where the WIMP would escape detection and the detected energy of the products would not sum up to the energy present before collision. Hence, *missing energy* is searched for in data [33]. So far no evidence has been found but limits on the WIMP-fermion cross section have been set. They are most stringent below ~ 4 GeV and ~ 700 GeV for spin-independent and spin-dependent interactions³, respectively [34, 35, 36]. However, even if a signature is observed, collider experiments cannot prove the lifetime of the escaping particle to be of the order of the age of the Universe as required for its observation nowadays.

The indirect detection channel investigates particle fluxes from astrophysical objects like stars, galaxies, galactic centers or our own Sun. Dark matter particles accumulate in such objects due to gravitation and an enhanced self-annihilation rate is expected [37]. Examples of possible annihilation channels are:

$$\chi\bar{\chi} \rightarrow \gamma\gamma, \gamma Z, \gamma H, q\bar{q}, W^-W^+, ZZ. \quad (1.3)$$

The unstable particles decay further into e^-e^+ , $p\bar{p}$, γ -rays and neutrinos. These detection channels can additionally include contributions from WIMP decays to charged particles, photons and neutrinos. So far, no conclusive indirect dark matter signal has been observed [38].

The direct detection method searches for WIMPs scattering off a nucleus in the detector target material. This technique has been first proposed in the 1980s [39, 40]. Due to their non-relativistic velocities, WIMPs are expected to produce nuclear recoils between a few to tens of keV. In order to be able to claim a potential discovery, precise knowledge of the expected signal as well as on the background sources and rates are crucial. However, the strength of the indirect detection technique is its high sensitivity to WIMP candidates regardless of the interaction operator. An interpretation of data from particle colliders is only possible in the context of a specific operator with which the transition from Standard Model particles to dark matter particles can be modeled.

One detection technique alone cannot provide a full proof of the WIMP hypothesis. Thus, a discovery in one channel always needs a verification by at least one other channel. Furthermore, exploiting their complementarity also means getting a more complete picture of the WIMP properties.

This thesis follows the direct detection approach using a liquid xenon target. We will outline the expected interaction rate in such an experiment and motivate the usage of xenon in the next section.

³See Section 1.5 for the definition of spin-dependent and spin-independent interactions.

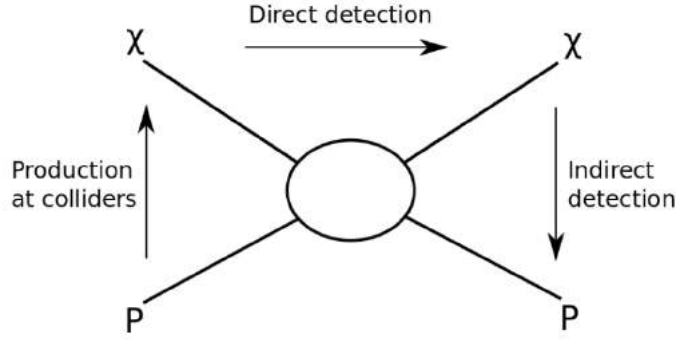


Figure 1.6: Illustration of the possible WIMP detection channels. χ indicates the WIMP and P a Standard Model particle. See text for more explanations. Figure from [1].

1.5 WIMP Direct Detection in Xenon

Direct detection experiments aim to measure the energy transferred to the nucleus in order to gain access to the WIMP particle's kinetic energy and hence its mass. The signature of a potential discovery would be the increased nuclear recoil rate over the background. Consequently, the main challenge is the precise knowledge of the background sources and their control. In order to make statements about the WIMP cross section, the expected WIMP rate has to be provided by theoretical models.

1.5.1 WIMP Recoil Rates

In general, the number of interactions dN per unit time dt between two particles is given by

$$\frac{dN}{dt} = \sigma \cdot L \quad (1.4)$$

where σ denotes the cross section which holds information on the particle physics such as interaction strength, form factors, etc. The luminosity L is a measure of the chance that two particles become close enough to each other in order to scatter⁴. In the context of WIMP direct detection it is calculated as the product of the number of target atoms N_T and the dark matter flux F_χ through the detector that is determined by the dark matter halo properties.

As the transferred nuclear recoil energy E_{nr} is dependent on the WIMP mass, one is usually interested how the rate behaves as a function of E_{nr} . Furthermore, it is common to normalize by the target mass $M_T = N_T \cdot m_N$, with m_N the mass of a single target nucleus. Hence, the following equation is found:

$$\frac{dR}{dE_{nr}} \equiv \frac{1}{M_T} \frac{d^2N}{dE_{nr}dt} \approx \frac{d\sigma}{dE_{nr}} \cdot \frac{1}{N_T m_N} \underbrace{\frac{N_T \rho_0}{m}}_L \langle v \rangle. \quad (1.5)$$

⁴The luminosity is widely used in collider physics where it provides a measure for collider performance. It is influenced by the beam focus, the number of accelerated particles, and the number of bunches that are brought to collision.

The last term represents the luminosity with ρ_0 the local dark matter density at our position in the Milky Way, m the WIMP mass and $\langle v \rangle$ the mean WIMP velocity. ρ_0 can be evaluated from the dynamics of the stars in our galaxy and takes a value of about 0.3 GeV/cm^3 [41]. The WIMP cross section is not only a function of E_{nr} but also of the WIMP velocity. Hence, we have to take into account its velocity distribution that is commonly assumed to be an isotropic Maxwell-Boltzmann distribution:

$$f(\mathbf{v}) = \frac{1}{\sqrt{2\pi}\sigma_v} \cdot \exp\left(-\frac{|\mathbf{v}|^2}{2\sigma_v^2}\right) \quad (1.6)$$

The velocity dispersion σ_v is determined by the circular velocity of our Sun via $\sigma_v = \sqrt{3/2} v_c$. The standard value used in most data interpretations is the average of results from several analyses and amounts to $v_c = (220 \pm 20) \text{ km/s}$ [42]. The second important input parameter is the escape velocity that marks the cut-off of the velocity distribution at which the gravitational bonding to our galaxy can be overcome. Its value is calculated using data from the RAVE survey that allows velocities between 498 km/s and 608 km/s in a 90% confidence interval [43]. Commonly, the escape velocity is set to $v_{\text{esc}} = 544 \text{ km/s}$.

Taking the previous considerations into account, Equation 1.6 transforms to [44]:

$$\frac{dR}{dE_{\text{nr}}} = \frac{\rho_0}{m_N m} \cdot \int_{v_{\text{min}}(E_{\text{nr}})}^{v_{\text{esc}}} v f(\mathbf{v}) \cdot \frac{d\sigma(E_{\text{nr}}, v)}{dE_{\text{nr}}} d^3 v, \quad (1.7)$$

where v_{min} is the minimal WIMP velocity necessary to cause a recoil of energy E_{nr} in the detector. Since WIMPs are assumed to be non-relativistic, v_{min} can be calculated from the elastic back-scattering at 180° by:

$$v_{\text{min}}(E_{\text{nr}}) = \sqrt{\frac{m_N E_{\text{nr}}}{2\mu^2}}, \quad \text{where} \quad \mu = \frac{m_N m}{m_N + m}. \quad (1.8)$$

The dark matter halo, determined by the parameters ρ_0 , v_c , and v_{esc} , is denoted as standard halo model. It is used for comparing the results of direct detection experiments amongst each other. However, as indicated, v_{esc} has a wide confidence interval and v_c is the average of several measurements that vary beyond their uncertainties. The choice of these parameters has an impact on the interpreted results of direct detection experiments, namely their sensitivity and limits [45].

Having discussed the astrophysical influences on the WIMP recoil rate, we now want to briefly explain the particle physics component. The WIMP-nucleon cross section splits up into a spin-dependent (SD) part where only unpaired nucleons take part in the scattering process, and a spin-independent (SI) part where neutrons and protons contribute equally:

$$\frac{d\sigma}{dE_{\text{nr}}} \propto \sigma_0^{\text{SI}} F_{\text{SI}}^2(E_{\text{nr}}) + \sigma_0^{\text{SD}} F_{\text{SD}}^2(E_{\text{nr}}). \quad (1.9)$$

The index 0 indicates that σ_0 is considered at zero momentum transfer. The parameter $F(E_{\text{nr}})$ is the form factor that takes into account the nuclear structure. For spin-independent interactions the Helm parameterization [46] is commonly used for the form factors whereas for the

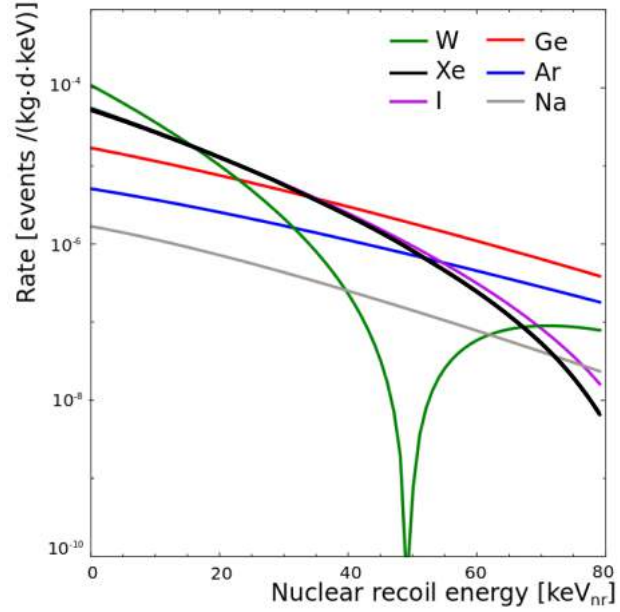


Figure 1.7: Comparison of the differential event rates for a spin-independent WIMP-nucleon interaction between different target materials. The WIMP mass is set to $100\text{GeV}/c^2$ and its cross section to 10^{-45}cm^2 . Figure from [1].

the spin-dependent case they are derived from nuclear shell model calculations [47, 48]. The SI cross section at zero momentum is related to the atomic number Z and the mass number A of the target nucleus by

$$\sigma_0^{\text{SI}} \propto (Z \cdot f^{\text{p}} + (A - Z) \cdot f^{\text{n}})^2, \quad (1.10)$$

where f^{p} and f^{n} are the SI WIMP-proton and WIMP-neutron coupling strengths, respectively. Usually, the assumption $f^{\text{p}} = f^{\text{n}}$ is used which results in an A^2 dependence of σ_0^{SI} . Figure 1.7 shows the number of events per keV, day and kg over the nuclear recoil energy for a spin-independent WIMP-nucleon interaction depending on the target material. The WIMP mass is assumed to be $100\text{GeV}/c^2$ and its cross section 10^{-45}cm^2 . Both, the A^2 dependence of the cross section and the form factor have an impact on the shape of the rate spectrum. Heavier elements like tungsten, xenon and iodine have high rates at low recoil energies due to the A^2 enhancement. However, at higher energies the form factor decreases the rate as a consequence of coherence loss⁵. Due to the high expected rates at low deposited energies, xenon is a good choice for a detector target. Further advantages of xenon as detection medium that influenced the XENON collaboration to choose this noble-gas, will be discussed in Chapter 2.

In the case of a spin-dependent interaction, the cross section at zero momentum transfer is given by

$$\sigma_0^{\text{SD}} \propto \frac{(J+1)}{J} \cdot [a_{\text{p}} \langle S_{\text{p}} \rangle + a_{\text{n}} \langle S_{\text{n}} \rangle] \quad (1.11)$$

where J is the total spin of the nucleus, $\langle S_{\text{p,n}} \rangle$ is the expectation value of the spin state of the protons and neutrons, and $a_{\text{p,n}}$ is the WIMP-proton and WIMP-neutron coupling parameter.

⁵The coherence loss comes from the transition from the point-like nucleus to a nucleus with structure. The wavelength associated to the momentum transfer becomes smaller than the nuclear radius. This is more prominent for large nuclei since the radius is proportional to $A^{1/3}$

The condition for an experiment that is sensitive to SD interactions is hence the presence of target nuclei with odd mass numbers.

Using all relations from above, the expected number of events in an experiment can be calculated from the differential rate. Typically, an energy region of interest $[E_{\min}, E_{\max}]$ is defined over which the rate is integrated:

$$N(m, \sigma_0^{\text{SI,SD}}) = T \cdot M_T \int_{E_{\min}}^{E_{\max}} \frac{dR}{dE_{\text{nr}}} dE_{\text{nr}}, \quad (1.12)$$

where T is the measurement time. By comparing the expected number of events with the number observed in an experiment, the spin-dependent and spin-independent models can be probed in dependence on the WIMP mass m .

Assuming the standard halo model to be true, the WIMP flux on Earth is of the order of $10^5 \text{ cm}^{-2} \text{ s}^{-1}$ for a WIMP mass of 100 GeV. At the present experimental limits this implies an expected signal rate of the order of 0.01 events per year and kg target mass in a LXe detector [49]. This low rate emphasizes the need for a good background discrimination and reduction in dark matter experiments.

Another detection strategy is the search for an annual modulation in the overall measured rate. It exploits the expected variation of the WIMP event rate due to the revolution of the Earth around the Sun. The relative WIMP velocity changes by $\pm 30 \text{ km/s}$ with a maximum in June and the minimum in December. This increases or decreases the number of events exceeding the detector threshold.

In the following section, the results of the best performing direct detection experiments are presented.

1.5.2 Current Status of Direct Detection

As indicated in Figure 1.7, the WIMP rate is largest at low recoil energies. Hence, the challenge for each experiment is to measure energies down to a few keV and at the same time being sensitive to low event rates in the range from 10^{-6} to 10^{-4} events/(kg·day·keV).

There are three main readout channels for energy depositions within the target: heat, ionization, and scintillation. Cryogenic bolometers, for example, operated at mK temperatures are able to transform small changes of temperature into an electrical signal. Photosensors are able to count single photons. Charges from ionization can be detected by the application of electric fields in order to extract them from the interaction site.

Figure 1.8 shows these observables together with the most common detector technologies. There are detectors that use only one or a combination of two channels (placed between the corresponding observables in Figure 1.8). Even though measuring all three signals is in principle possible, such an experiment presently does not exist. The read-out of two of the channels provides the means to discriminate signal-like events (e.g. neutrons, WIMPs) against background events from photon interactions, beta decays etc.

For a detailed review of different detector technologies the reader is referred to [1] and [50].

Figure 1.9 gives an overview on the current status of direct dark matter searches by reflect-

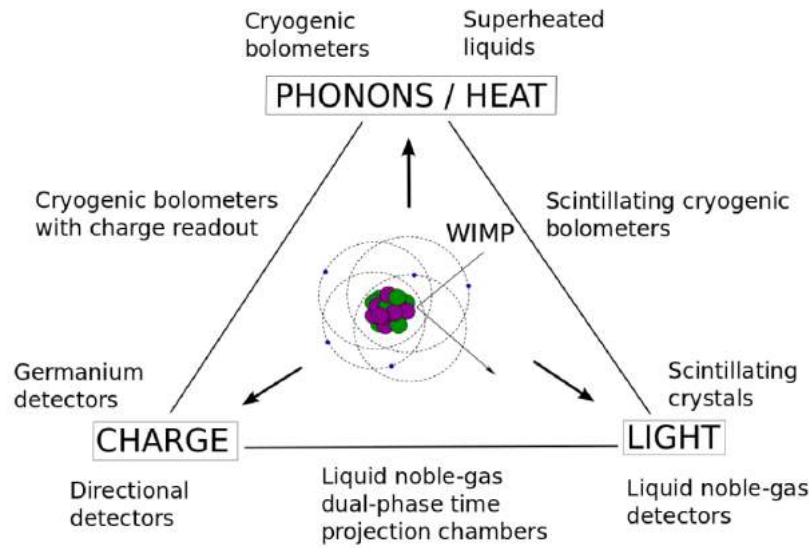


Figure 1.8: Scheme of common energy readout channels in direct detection experiments. Figure from [1].

ing the results of the best performing experiments in the spin-independent WIMP-nucleon cross section vs. WIMP mass parameter space. In the left panel the low mass regime and in the right panel the high mass regime are shown. The parabolic lines mark the upper exclusion limits set by various experiments. The most constraining result at low WIMP masses is published by the CRESST-II collaboration [51] which reads out the phonon channel by operating a CaWO_4 single crystal at mK temperatures. The CDMS Low Ionization Threshold Experiment (CDMSlite) reports the leading results for WIMP masses between 1.6 to $5.5 \text{ GeV}/c^2$ [52]. They use cryogenic germanium detectors and read out the phonon as well as the ionization signal.

In the high WIMP mass regime, the dual phase time projection chamber technique using a xenon target has the highest sensitivity. Currently, the XENON1T experiment quotes the most stringent exclusion limit [53] followed by LUX [54], PandaX [55], and XENON100 [56]. At the time of writing, only one experiment claims the observation of a signal. It is marked by the two red circles that enclose the parameter space that consistent with the observation (see Figure 1.9 right), and has a significance of 9.3σ [57]. The DAMA collaboration operates NaI(Tl) crystal scintillators and searches for an annually modulating signal on top of a background that is expected to be constant. Depending on the considered target nucleus the signal can be translated into two signal regions in the spin-independent WIMP-nucleon cross section vs. WIMP mass parameter space. The interpretation of the DAMA signal as a spin-independent WIMP-nucleon interaction is in tension with the results of other direct detection experiments such as XENON1T, LUX, XENON100, DarkSide [58], EDELWEISS [59], and PICO-60 [60]. Furthermore, a dedicated search of four years of XENON100 data for an annual modulation signal excludes the DAMA signal with a significance of 5.7σ [61]. The analysis of the XENON1T data resulting in the most stringent limit on SI WIMP-nucleon interactions in the high WIMP mass regime, at the time of writing, will be presented in Chapter 5.

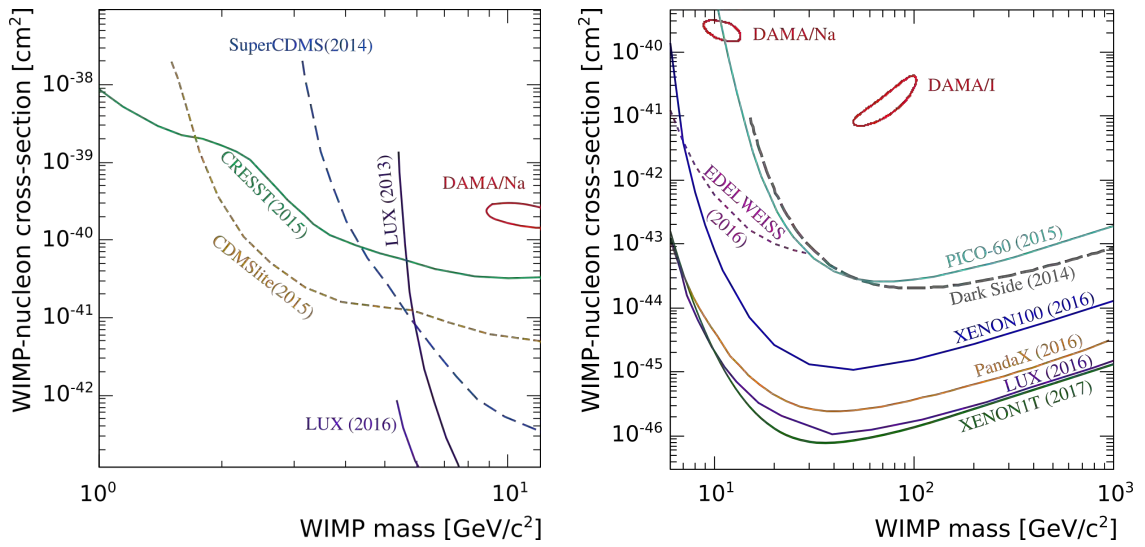


Figure 1.9: Overview on current results of direct detection experiments in the parameter space of spin-independent WIMP-nucleon cross sections σ_0^{SI} vs. WIMP mass m . The left plot shows the low energy and the right one the high energy regime. The two red circles indicate the signal claims of the DAMA collaboration interpreted for their two target nuclei sodium and iodine.

Chapter 2

The XENON Experiments

Among the different WIMP detection techniques, briefly outlined at the end of Chapter 1, the XENON collaboration is specialized on the construction of dual-phase (liquid-gas) time projection chambers (TPC) filled with xenon.

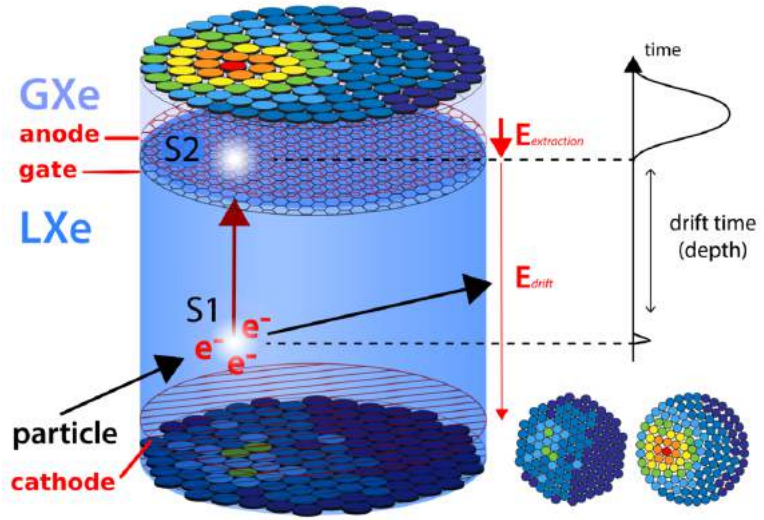
Like all direct detection searches, the XENON experiments are challenged by the steeply falling recoil energy spectrum of WIMP interactions in the low energy region and the small predicted interaction cross sections. This raises the need for low energy thresholds and a low background radiation. Amongst others, the former is achieved by operating the detector in the underground laboratory INFN Laboratori Nazionali del Gran Sasso (LNGS) in Italy [62]. The shielding by $\sim 1300\text{m}$ of rock ($\sim 3800\text{m w.e.}$) reduces the muon flux by six orders of magnitude with respect to the surface, from about $100\text{m}^{-2}\text{s}^{-1}$ to $(3.41 \pm 0.01) \cdot 10^{-4}\text{m}^{-2}\text{s}^{-1}$ [63] and therefore decreases the muon-induced background level. Additionally, the dual-phase TPC technology allows using two of the three energy readout channels, which were introduced in the previous chapter, namely charge and light. By exploiting the difference in energy loss per unit track length, gamma and beta radiation can be discriminated from WIMP candidate events. Furthermore, the three dimensional position of each event can be reconstructed, which provides the ability to use only the innermost target volume for the dark matter search in order to exploit the self-shielding of the liquid xenon (LXe) for the suppression of radiation from surrounding materials.

The XENON100 experiment was operated between 2009 and 2016 and collected a total of 477 days of dark matter search data between 2010 and 2014. The final results in the context of spin-dependent and spin-independent WIMP-nucleon interactions are reported in [56]. During the last two years, the detector was mainly used for R&D in preparation of the successor experiment XENON1T. Besides the trial of radon removal by means of cryogenic distillation [64], the performance of new calibration sources was tested. Some results of these calibration tests are presented in Chapter 4.

The XENON1T experiment started its commissioning beginning of 2016 and took the first dark matter search data between November 2016 and January 2017. The first WIMP analysis of this data is outlined in Chapter 5.

This chapter shall give an overview of the functional principle of the two XENON detectors, sensitize the reader for the challenges in background reduction, describe the detector setups and introduce the auxiliary detector systems that are of importance for the work presented in the following chapters.

Figure 2.1: Sketch of the working principle of the XENON two-phase liquid-gas time projection chamber (TPC). Particle radiation induces prompt scintillation light (S1) as well as ionization. The electrons are extracted into the gas phase where proportional scintillation takes place (S2). From the time between the two signals the depth (Z coordinate) can be inferred, and from the light pattern in the top PMT array, the coordinates in the X-Y plane can be evaluated. See text for more details. Figure from [65].



2.1 The Two-Phase TPC Principle

Figure 2.1 shows the scheme of the two-phase time projection chamber (TPC) used in the XENON experiments. It is equipped by two arrays of photomultiplier tubes (PMTs) that are optimized for responses in the vacuum ultraviolet (VUV) regime. One is immersed into the liquid xenon at the bottom and one is located in the gaseous xenon phase at the top, each of them facing the inner volume.

Through the interaction of a particle in the liquid xenon (LXe), scintillation photons and electrons from ionization are produced. Furthermore, a small amount of energy is lost to heat that is not detected (quenching). The division into the light, ionization and heat channels depends on the type of interacting particle, its energy and the electric field [66]. While the light signal (also direct scintillation signal), denoted as S1 signal, is instantaneously detected by the PMTs, the detection of the ionization electrons is delayed. The charges are extracted from the interaction site and drifted toward the liquid-gas interface by a drift field E_{drift} applied between two conductive meshes: The cathode is installed above the bottom PMT array and the grounded gate is located a few mm beneath the liquid-gas interface. Having reached the gate, the electrons are extracted from the liquid into the gas phase by the stronger extraction field $E_{\text{extraction}}$ applied between the gate and the anode. The anode is located a few mm above the liquid-gas interface. Under the influence of the extraction field, the process of proportional scintillation is induced [67, 68, 69]. This second signal is denoted as S2 or charge signal and is detected by the PMTs as well. If a field larger than 10kV/cm is present in the gas phase, close to 100% of the electrons reaching the liquid surface are extracted [70, 71].

The light and charge signal are separated in time due to the finite electron drift velocity in LXe [72, 73]. The time difference Δt is dependent on the distance of the interaction site from the liquid-gas interface and on the applied drift field. It is associated with the Z-coordinate by:

$$Z = -v_d \Delta t, \quad (2.1)$$

where v_d is the electron drift velocity. Note that the origin of the Z axis is at the gate and points into the upwards direction. Hence, Z takes on only negative values. v_d is approximately proportional to the electric field strength for values of hundreds of V/cm [72] as applied in the XENON100 and XENON1T detectors and is known from dedicated measurements [73].

The X - and Y -coordinates can be inferred from the distribution of the proportional scintillation light on the PMTs in the top array (PMT hit pattern). An example for such a hit pattern is depicted in Figure 2.1 at the bottom right. Since the S2 signal generation happens very close to the top array, only some PMTs are illuminated. In contrast, the S2 is spread widely over the bottom array, providing a better scale for the S2 size due to the reduced sensitivity to potential performance issues of individual PMTs.

Different algorithms for the X - Y position reconstruction have been tested. Common to all algorithms is the idea to compare the observed PMT hit pattern to the one generated by a Monte Carlo simulation. In XENON100, the standard algorithm uses a neural network [74] that was trained on simulated samples and takes into account non-functioning PMTs. A radial resolution of < 3 mm was confirmed by calibration measurements with a collimated external ^{57}Co source [75]. The so-called *top pattern fit* algorithm is used for XENON1T. It searches for the X - Y position for which the corresponding simulated hit pattern provides the highest likelihood to be compatible with the observed hit pattern.

As shown, the TPC technology allows for a three dimensional position reconstruction of each event. This is crucial for defining a fiducial volume¹ in the detector in order to reduce the number of events induced by radioactive radiation from surrounding materials.

The ratio between the S2 and S1 provides the means for a distinction between particle interactions with the xenon nucleus (nuclear recoil) or the electron shell (electronic recoil). A better understanding for this feature will be given when the production mechanism of light and charge signals in LXe will be explained in Section 2.3.

2.2 Xenon as Detection Medium

The usage of liquid noble-gases as detector target offers the advantage of large and homogeneous detection media as well as high scintillation and ionization yields.

Major advantages of xenon are its large atomic number that ensures high expected WIMP scattering rates (see Figure 1.7), as well as its low intrinsic radioactivity. The only radioactive isotope ^{136}Xe is produced by cosmogenic activation and decays via a double beta decay. It features a relatively long lifetime of $2.2 \cdot 10^{21}$ years [76], and therefore, does not contribute to the background of detectors with target masses up to a few tons. In contrast, argon that is extracted from air contains the radioactive isotope ^{39}Ar that is produced by cosmogenic activation as well. It decays by emitting a beta particle with an endpoint of 565 keV and a half-life of 270y. Natural argon exhibits a radioactive rate of 1 Bq/kg from ^{39}Ar . This rate is reduced for argon from underground sources. However, its production is more challenging and expensive.

For the functioning of the TPC, as explained above, it is crucial that both, scintillation light

¹In low-background experiments the term fiducial volume refers to an inner volume of the detector in which background is suppressed.

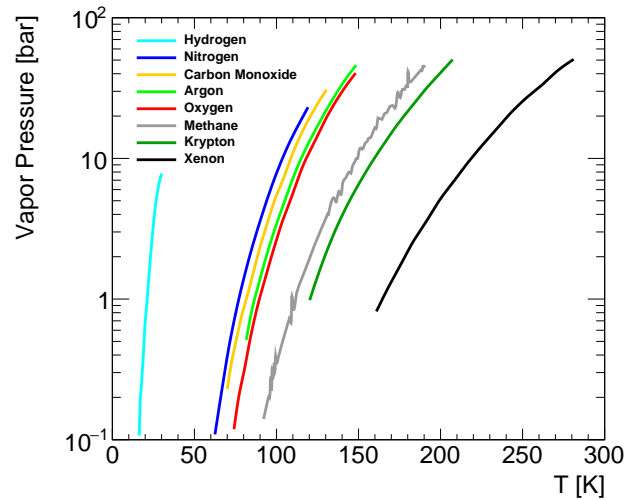


Figure 2.2: Vapor pressures curves for some gas components of air. Data extracted from [77] and for methane from [78]

and ionization electrons, are created by particle interactions with the target. This is a unique feature of LXe that is only shared by liquid argon (LAr) among liquid rare gases [72]. However, in contrast to LAr, the wavelength of 178 nm of the produced photons in xenon can be detected directly by PMTs featuring windows made out of quartz. In LAr it is common to use wavelength shifters in order to transfer the lower scintillation wavelength of 128 nm in into the visible range (~ 400 nm). LXe has the highest scintillation light yield compared to all liquid rare gases [72].

As pointed out in Chapter 1, the high atomic weight of xenon, which has an average of 131.30, yields in high expected WIMP interaction rates. Furthermore, it has a high stopping power for penetrating background radiation due to its density of ~ 3 g/cm³ in the liquid phase. This makes the method of background reduction by selecting a fiducial volume very efficient.

These arguments provide the motivation for the usage of xenon as a target for the direct search for dark matter.

Xenon is naturally occurring as a trace gas in the Earth's atmosphere with a fraction of 87 ppb² [79]. It is obtained commercially as a by-product of nitrogen and oxygen production from air. Figure 2.2 shows the vapor pressure curves as a function of temperature for some of the gases contained in air. In the process of air liquefaction, cryogenic distillation is used in order to separate the individual components from each other. The more different the boiling temperatures at a given pressure are, the more efficient is the separation. After the first separation step of nitrogen and oxygen, the oxygen product will contain small quantities of krypton and xenon. The krypton abundance in the atmosphere yields 1140 ppb [79]. By further distillation, krypton and xenon are separated from the oxygen. Pure xenon is then gained by processing the xenon/krypton mixture again with the distillation column.

Depending on the number of distillation cycles and the performance of the utilized column, the xenon product contains a small amount of krypton as intrinsic impurity, given that the krypton concentration is ten times higher than xenon in air. This is relevant for the experi-

²parts per billion

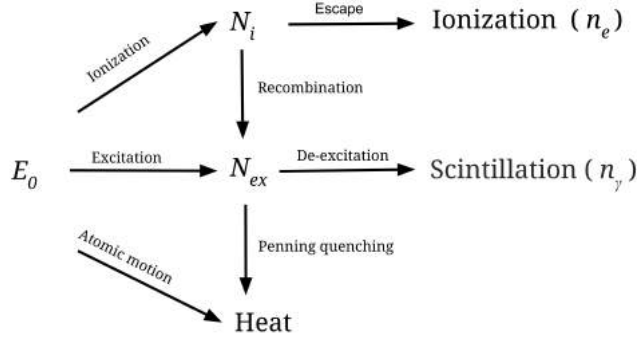


Figure 2.3: Schematic of the transformation of deposited energy E_0 in xenon into a measurable number of electrons n_e and photons n_γ . Figure from [83]

ment since natural krypton contains traces of the radioactive isotope ^{85}Kr , mainly produced by nuclear fission and released by nuclear fuel reprocessing plants and nuclear weapon tests. In Europe, the ^{85}Kr abundance in natural krypton has been determined to 0.02 ppb [80].

Further intrinsic impurities in the xenon product may result from air contamination during gas handling processes or from insufficient cleaning of storage cylinders. If those contaminations feature high electronegativities³, they can attach free electrons in the xenon and hence cause a reduction of the S2 signal.

Part of this thesis was dedicated to the control of the xenon gas purity with special focus on krypton contaminations and electronegative impurities like oxygen (see Chapter 3).

2.3 Generation of Light and Charge Signals

The electronic shell of liquid rare gases like krypton, argon and xenon features a band structure [81, 82] which is crucial for the generation of light and charge signals induced by particles interacting with the liquid.

As depicted in Figure 2.3, the energy E_0 deposited by incoming radiation in xenon can be transformed into a number of electron-ion pairs N_i , excited atoms N_{ex} and heat dissipation (quenching). The energy that is deposited in xenon is only transferred to the heat channel for nuclear recoils owing to secondary recoils. Additionally, free electrons are generated along the track, referred to as sub-excitation electrons, due to their kinetic energy below the first excitation level [84]. While electron-ion pairs have the possibility to recombine, sub-excitation electrons contribute directly to the number of charges n_e that can be read-out.

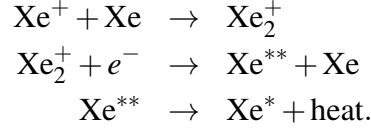
By colliding with surrounding xenon atoms, the excitons Xe^* can combine to excited dimers Xe_2^* , also referred to as excimers. When they decay to their ground level, scintillation light is emitted [85, 86, 87]:



The electron-ion pairs can either recombine or the electrons may escape from the interaction site. The probability of these two cases depends on the presence and strength of an externally

³Electronegativity is a chemical property that describes the potential of atoms and molecules to attract electrons.

applied electric field, as well as on the type of the ionizing particle [72]. The process of electron-ion recombination contributes to the emission of scintillation light by the production of excitons via:



The created excitons undergo the same processes as formulated in Equations (2.3) and (2.3). Independent of its production mechanism, the exciton decays on a time scale of a few to tens of nanoseconds [88], resulting in signals from primary scintillation that are narrow in time. This scintillation light is detected as the S1 signal within a two-phase TPC.

The recombination process increases the number of immediately created excited atoms $N_{\text{ex}'}$ by

$$N_{\text{ex}} = N_{\text{ex}'} + rN_i, \quad (2.4)$$

where N_{ex} is the final number of excitons, N_i is the number of electron-ion pairs, and r is the recombination probability for which applies $r \in [0, 1]$. It is assumed that the efficiency of photon emission by an excited state is close to 100% [89]. Hence, the number of scintillation photons can be directly inferred from:

$$N_{\text{ex}} = n_\gamma \quad (2.5)$$

Consequently, the number of electrons, which are extracted from the interaction site by an external electric field, is given by the fraction that escapes from recombination:

$$N_q = (1 - r)N_i \quad (2.6)$$

The fraction of extracted electrons $(1 - r)$ is dependent on the deposited energy and the structure of the ionization track. Due to their high electronic stopping power, which is roughly equivalent to the ionization density, alpha particles feature an almost point-like interaction resulting in high recombination rates even at strong external fields [90]. In contrast, gamma radiation interacting via Compton scattering in several steps at multiple interaction sites features a small recombination fraction.

The strength of the anti-correlation between light and charge is determined by the ratio between the number of the initially formed excitons and the electron-ion pairs. The larger N_i , the stronger the anti-correlation. For ionizing radiation, $N_{\text{ex}'}/N_i$ yields ~ 0.06 [91] while for interactions with the xenon nucleus only ~ 1.09 is found [92]. Thus, a strong anti-correlation of the charge and light signals is observed for electronic recoils while the scintillation induced by direct excitation or recombination is equally strong for nuclear recoils.

2.3.1 Primary Scintillation Light (S1)

The emitted scintillation photons n_γ do not all contribute to the observed S1 signal. The detector geometry has a significant influence on the collection efficiency of the photons by PMTs. The periphery of the TPC is equipped with PTFE surfaces that feature a reflectivity

of around 50% for VUV light [93]. Depending on the position of the interactions, photons travel large distances and are reflected multiple times before they hit the photocathode of one of the PMTs or are absorbed, due to the finite attenuation length in LXe. The attenuation length is restricted by the presence of impurities in the liquid which have absorption energies that overlap with the VUV spectrum, e.g. oxygen and water vapor [72]. Those two mentioned effects contribute to the position dependent light collection efficiency (LCE) that is defined as the fraction of emitted photons that reach a PMT photocathode.

A further efficiency is introduced since not all photons are converted to photoelectrons in a PMT. The quantum efficiency (QE) states the probability for this process and is specific to each PMT exemplar. The average QE value is 30% for XENON100 PMTs and 34.5% for XENON1T [75, 94]. Furthermore, the photoelectron has to be accelerated onto the PMT dynodes in order to generate a measurable signal. The photoelectron collection efficiency is about 70% and about 90% for the XENON100 and XENON1T PMTs, respectively.

The combination of the mentioned efficiencies results in detection probabilities of only a few percent for an individual photon. Consequently, the resolution of the S1 signal is not dominated by the statistics of the initially produced photons but is expected to follow a binomial distribution $B(N_{\text{PE}}, n_{\gamma}, p)$ where p is the probability of a generated photon to induce a number of measurable photoelectrons N_{PE} [95]. N_{PE} is summed over all PMTs that have seen a fraction of the signal. Furthermore, the resolution is influenced by the PMT response itself. The photoelectrons are amplified by inducing secondary avalanche electrons. This process is well described by a Gaussian function of the form $G(S1_{\text{obs}}, N_{\text{PE}}, \sigma_{S1})$ where $S1_{\text{obs}}$ is the observed signal and σ_{S1} is the width that is related to the single photoelectron PMT resolution Δ_{PMT} by $\sigma_{S1} = \Delta_{\text{PMT}} \cdot \sqrt{N_{\text{PE}}}$. This description assumes the acceleration of photoelectrons by the PMTs to be uncorrelated processes. The PMT resolution is measured by biasing the PMTs with LED light on a regular basis during the experiment's runtime [96].

The short excitation decay time and the fast PMT response result in pulses of the prompt scintillation signal that are narrow in time, in the order of tens of nanoseconds. Figure 2.4 shows an example of the typical pulse shape of an S1 signal in the bottom left.

2.3.2 Secondary Scintillation Light (S2)

The charge signal S2 results from the produced electrons that escape from recombination due to the applied drift field. They are extracted into the gas phase by the extraction field where proportional scintillation takes place [67, 68, 69]. A 100% extraction efficiency is achieved for field strengths of 10keV/cm or larger [70, 71]. The accelerated electrons induce multiple scintillation photon emission along their tracks. The resulting signal depends on the track length, the strength of the extraction field and the vapor pressure. Like the S1, the secondary scintillation signal S2 is the sum of photoelectrons collected by all PMTs.

The gain factor g_{S2} is defined as the number of photoelectrons produced by proportional scintillation of one electron. It directly relates the number of extracted electrons n_e to the number of measured photoelectrons: $S2 = g_{S2} \cdot n_e$

In contrast to the S1, the S2 signal resolution is not limited by efficiencies or the PMT resolution itself. Due to the amplification, S2 takes high enough values such that its distribution can be well described by a Gaussian of the form $G(S2, g_{S2} \cdot n_e, \sigma_{S2})$. This assumes that the signals generated by the individual electrons are independent. Hence, the Gaussian width is

determined by the width of the single electron S2 distribution Δg_{S2} and the square root of the number of electrons: $\sigma_{S2} = \Delta g_{S2} \cdot \sqrt{n_e}$. The detector response to single electron signals is determined by the experiment [97].

As a result of longitudinal diffusion of the electron cloud and the amplification process, the S2 is spread over a much longer time (1-2 μ s) than the S1. A typical pulse shape of an S2 signal is shown in Figure 2.4 bottom right.

2.3.3 Energy Scale

As explained above, the energy deposited by particles interacting with LXe transforms into the three channels scintillation light, ionization electrons, and atomic motion, i.e., heat. The correlation of the scintillation and ionization yields depends on the recombination probability, i.e., the particle track geometry. For ionizing radiation like beta and gamma particles, the geometry is such that the full number of the produced quanta, i.e., electrons and photons, can be transformed into S1 or S2 signals. Hereby, the electric field and the energy dependent particle stopping power regulate the recombination probability. Hence, the electronic recoil energy E_{ER} can be inferred by⁴ [98]:

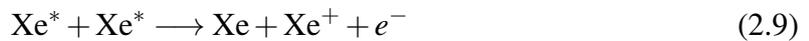
$$E_{ER} = W(n_\gamma + n_e), \quad (2.7)$$

$$= W \left(\frac{S1}{g_1} + \frac{S2}{g_2} \right), \quad (2.8)$$

where W is the average energy needed to produce a quantum. It has been determined by experiment to amount to 13.7 ± 0.2 eV/quantum [89]. n_γ and n_e are related to the S1 and S2 signals by the electron and photon gains g_1 and g_2 indicating how many photo-electrons are produced from the respective quantum. The gain values are specific for each detector since they depend on the secondary scintillation gain and efficiencies relating the number of generated photons to the number of detected ones. The gains are determined by measuring the signals of mono-energetic lines with different energies and fitting a linear function to the data in the $S2/E_{ER}$ vs. $S1/E_{ER}$ space.

Equation (2.8) does not hold for alpha particles due to their cylindrical track shape. Most of the energy is lost in a dense core featuring a high recombination rate, surrounded by delta rays. This particular geometry does not allow a complete charge collection and hence the sum of produced quanta is highly dependent on the electric field strength. Even at an electric field of 20 kV/cm, less than 10% of the total number of produced electrons can be extracted from the interaction site [72].

For nuclear recoils, the scintillation yield (number of free photons per unit energy) is significantly reduced compared to electronic recoils. This is a result of nuclear quenching [99] and a higher excitation density in the particle tracks where collisions between excitons can induce the emission of an electron by [100, 101]:



⁴Equations (2.8), (2.10), and (2.11) are commonly applied with the S1 and S2 signals that are corrected for detector related signal variations for an improved energy resolution (see Section 2.3.4).

The number of excitons is reduced by this process and hence the number of scintillation photons. To account for these two effects in the estimation of the nuclear recoil energy scale, an effective scintillation yield function L_{eff} is used. It is defined as the ratio between the measured number of photo-electrons per unit energy and the S1 measured from the full-absorption peak of the 122 keV gamma line from ^{57}Co . The S1 signal can be translated to the nuclear recoil energy N_{NR} by⁴ [102]:

$$E_{\text{NR}} = \frac{S1}{L_{\text{eff}}(E_{\text{NR}}) \cdot L_y} \cdot \frac{S_{\text{ER}}}{S_{\text{NR}}}, \quad (2.10)$$

where L_y is the light yield of the 122 keV gamma line and S_{ER} and S_{NR} are the factors accounting for the field dependence of electronic and nuclear recoil signals, respectively. L_{eff} depends on the nuclear recoil energy and is determined experimentally [102, 103].

In contrast to the S1 signal, the S2 signal can be related to the nuclear recoil energy without using any reference point by⁴ [104]:

$$E_{\text{nr}} = \frac{S2}{Y} \frac{1}{Q_y(E_{\text{nr}})}, \quad (2.11)$$

where Y is the gain of the secondary scintillation from single electrons [97] and Q_y is the charge yield of nuclear recoils, i.e., the number of electrons extracted from the interaction site per unit of deposited energy. Q_y could be determined by multiple external measurements as well as by matching simulated data to $^{241}\text{AmBe}$ calibration data of XENON100 [104].

2.3.4 Position Dependent Signal Corrections

As explained in Section 2.1, the TPC technology holds the major advantage of a three dimensional position reconstruction of particle interaction vertices. This feature is crucial for the reduction of background radiation from the detector materials by selecting an inner fiducial volume. Furthermore, it allows correcting the measured signals for spatial dependencies. The data taken with the XENON100 and XENON1T detectors exhibits small inhomogeneities in the electric drift field at the TPC edges due to its geometry or charges that may accumulate on PTFE surfaces. The bending of the field lines, and therefore also the electron drift lines, increases the drift time. The result is a larger reconstructed Z value for the event position. Additionally, the reconstructed X - Y position is shifted with respect to the true event position. This effect is corrected by the computation of the electric field shape using finite element methods. After the correction, events can be placed outside of the TPC due to the poorer position resolution at the detector edges. In principle, this should not be a problem in a dark matter analysis, since here only an inner volume is selected in which the position resolution is smallest. However, in Chapter 5 it is shown that a very poor resolution at the TPC walls can result in an additional background component that has to be taken into account.

As mentioned above, the S1 signal suffers from photon losses due to absorption on their way to the PMTs. Depending on the path length and on the number of times the photons are reflected at the PTFE walls, more or less light can be collected. To compensate, light collection maps are constructed from mono-energetic decays that occur homogeneously within

the TPC. In XENON100, the 40 keV and 164 keV gamma lines from ^{129}Xe and ^{131m}Xe were used, which result from excitation in neutron calibration runs. In XENON1T, ^{83m}Kr , which is emitting conversion electrons with energies of 9.4 keV and 32 keV, has been distributed homogeneously in the detector. In the following, the S1 signal that is corrected for its spatial dependency will be denoted as cS1.

A similar correction is applied to the S2 signal. Depending on the horizontal position of the point at which the electrons are extracted from the liquid into the gas phase, the light of the proportional scintillation is detected with varying efficiency. This is caused by the reduced PMT coverage of secondary scintillation light that is emitted in the outer regions of the gas gap. The corresponding correction map is obtained from the same samples of mono-energetic decays as used for the S1 correction map. In contrast to the correction of the S1 signal, the X - Y -correction of the S2 has to be done before the electric field position correction is applied since the S2 light collection efficiency is only sensitive to the point where the electrons are extracted from the liquid into the gas phase.

The dominant spatial dependency of the charge signal, however, is coming from the electrons that are lost by the attachment to electronegative impurities such as O_2 , SF_6 , and N_2O in the LXe. The effect is dependent on the drift-time Δt and the impurity concentrations. The number of surviving electrons can be calculated by [72]:

$$n_e(\Delta t) = n_e(0) e^{-\Delta t/\tau}, \quad (2.12)$$

where τ is the *electron lifetime* that is a function of the impurity concentration and the compound specific attachment rate. Consequently, $e^{\Delta t/\tau}$ gives the correction factor that is related to the Z -position of the event by Equation (2.1). During normal detector operation, the electron lifetime increases over time due to the continuous removal of impurities from the xenon by hot metal getters. τ is therefore evaluated on a regular basis by fitting an exponential to the size of the S2 signal as a function of the drift time in calibration data. In XENON100, the full absorption peak of ^{137}Cs gamma rays and for XENON1T ^{83m}Kr decays, homogeneously distributed within the TPC, were used for this purpose. The S2 signal corrected for the charge loss due to electron attachment, as well as for the X - Y -dependent light collection efficiency in the gas gap, will be denoted as cS2 in the following.

It should be noted that Equations (2.8), (2.10), and (2.11) are used with corrected signal values in order to improve the energy resolution by suppressing detector related signal variations. Hence, the S1 and S2 should be substituted by cS1 and cS2, respectively.

Further details on the signal corrections in the two XENON detectors can be found in [75, 105].

2.4 Event Waveforms

The light and charge signals induced in the liquid xenon, are recorded by the PMTs and transformed to waveforms.

The term *waveform* refers to the sum of all PMT signals over time. In XENON100, an event is a recorded waveform of typically $400\ \mu\text{s}$, where the trigger threshold is exceeded by the sum of the PMT signals of 68 inner PMTs in the top array and 16 PMTs in the center of the bottom array. In XENON1T, the waveform length is variable and defined by a software

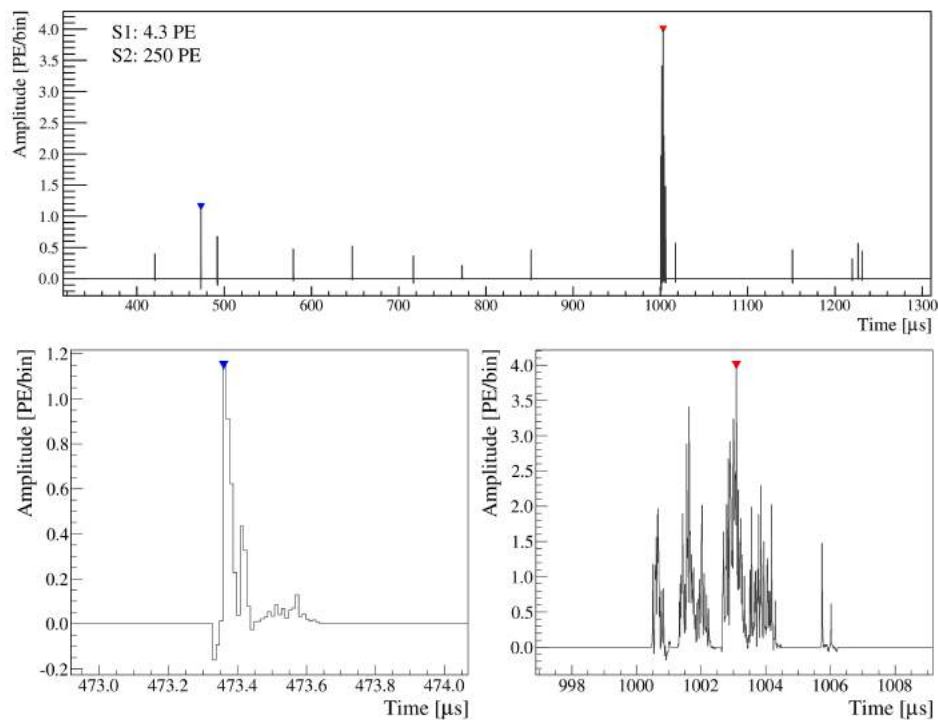


Figure 2.4: Example of an event waveform from a low energy single scatter nuclear recoil recorded by XENON1T during a $^{241}\text{AmBe}$ calibration run. The sum of all PMT signals is shown as a function of time for the whole event in the upper panel where the S1 and S2 signals are marked with a blue and a red marker, respectively. The smaller additional peaks are uncorrelated pulses from PMT dark counts which are only detected by individual channels. The lower panels present a zoom into the S1 (left) and the S2 (right) pulses that feature uncorrected areas of 4.3 PE and 250 PE, respectively. The time between the two signals of $529.7\ \mu\text{s}$ corresponds to $Z = -75.9\ \text{cm}$. Figure from [105].

event builder that scans the signals from all PMTs individually and groups them into causally connected events.

Figure 2.4 top shows an example of a raw waveform from a low energy single scatter NR (as expected to be induced by WIMPs) recorded in XENON1T. As mentioned above, S1 and S2 signals can be well distinguished due to their different pulse shapes. This is done by the data processor that additionally derives physical quantities of the event.

In XENON100, a ROOT [106] based C++ program is used for the event processing. After the application of a low-pass filter that removes high frequency noise from the waveform, the program searches for S2 peak candidates that exceed a threshold of 10 mV for at least 600 ns and feature a $\text{FWHM} > 350\ \text{ns}$. The corresponding S1 signal is searched in the time window before the S2 signal by identifying peaks in the unfiltered sum waveform that exceed a threshold of 3 mV ($\sim 0.33\ \text{PE}$). The detection efficiency for a single photoelectron collected by one PMT is $> 80\%$, $> 95\%$ for double photoelectrons and $> 99\%$ for three photoelectrons. The properties of all peak candidates are evaluated, such as the position in the waveform, the peak area and width, and the PMT coincidence level. The application of further quality criteria to the peaks, such as a PMT coincidence level and the pairing of S1 and S2 pulses to physical interactions, is done at a later stage in the offline analysis.

In XENON1T, physical quantities of the events are determined by the custom-developed PAX data processor. It first identifies so-called *hits*, i.e., photon signals in each individual PMT above a certain threshold. Those hits are grouped into clusters separated by $2\mu\text{s}$ or more and split at local minima in the PMT gain corrected sum waveform. The properties of each summed cluster signal from all contributing PMTs are calculated, such as the total area, amplitude, and pulse width. Using these quantities, a classification into S1, S2, or unknown peaks is performed. For a valid S1 candidate, three PMT hits recorded within 50ns have to contribute to the corresponding cluster.

In a later stage of XENON100 and XENON1T data processing and analysis, S1 and S2 pairs are created for which the event position and related signal corrections are calculated. Using the gain values measured for each individual PMT on a regular basis by biasing them with LED photons, the peak areas are converted into the unit of photoelectrons (PE).

More details on the generation of event waveforms from raw PMT signals and the data processors of XENON100 and XENON1T can be found in [75, 105].

2.5 Electronic Recoil Background

All experiments that search for rare particle interactions with very low cross sections share the major challenge of background discrimination and reduction. As explained in Section 2.1, energy depositions from ionizing particles can be distinguished from neutral particle interactions using the S2/S1 ratio. However, due to the overlap of the two populations in S2/S1, a 100% distinction cannot be achieved. Statistical leakage of electronic recoil (ER) events into the nuclear recoil (NR) region can mimic a dark matter signal. Therefore, besides the obvious necessity of neutron background reduction, the control of the ER background is crucial for the success of the experiment.

NR background events are induced by radiogenic neutrons from surrounding materials, cosmogenic neutrons from cosmic radiation and their secondary processes, and by coherent scattering of solar neutrinos. Since this work was dedicated to the reduction of ER background by gas purity analytics and to the calibration of the ER background, this section will focus on the origin of the ER events only. Details on the NR background in XENON100 and XENON1T can be found in [107, 108].

Two categories of ER background sources can be distinguished: intrinsic and extrinsic. Extrinsic sources comprise radioactive contaminations of the detector materials and its surroundings. Intrinsic sources consist of radioactive nuclei such as ^{222}Rn and its progenies, ^{85}Kr , and ^{136}Xe distributed in the LXe. In contrast to intrinsic sources, extrinsic ones can be reduced by exploiting the good self-shielding properties of xenon and by considering only an inner volume for the dark matter analysis. While in XENON100 the main ER background was coming from the detector materials, XENON1T is large enough such that its background is intrinsically dominated by decays of ^{222}Rn daughters [108]. An additional background component is given by solar neutrinos scattering off electrons. This source does not fit into any of the two categories since it neither can be reduced by fiducialization nor by the purification of the xenon gas and the detector materials.

Figure 2.5 shows the low energetic ER background rate measured with XENON100 in

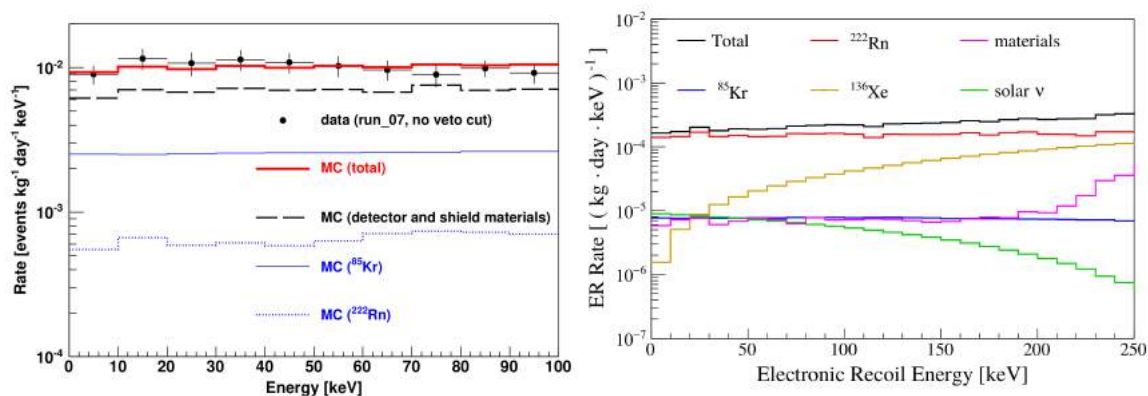


Figure 2.5: Left: ER background rate in XENON100 in a 30kg super-ellipsoidal fiducial volume and within the low energy region. The expected rate from Monte Carlo (MC) simulations is shown by the red line for the sum of all contributions and divided into the individual background sources as indicated in the legend. The double beta decay of ^{136}Xe was found to have a negligible contribution to the background below 100 keV. Figure from [109]. **Right:** ER background rate in XENON1T predicted by Monte Carlo simulations for a one ton cylindrical fiducial volume. The total rate is given by the black line and its individual contributions by the colored lines as indicated in the legend. Figure from [108].

a 30kg fiducial volume [109] on the left. The lines indicate the prediction from Monte Carlo (MC) simulations for the sum of all components (red), detector materials alone (black dashed), ^{85}Kr alone (blue solid), and ^{222}Rn alone (blue dashed). On the right in Figure 2.5, the total ER background rate in the low energy region predicted by MC is shown for XENON1T (black line) [108]. The rates from the individual contributions are plotted as well and are indicated in the legend. The integrated total rate, which was measured within the first science run, is in good agreement with the prediction [53]. Contributions from solar neutrinos and ^{136}Xe double-beta decays that play a role in XENON1T have been found to be negligible in XENON100.

The following paragraphs explain the individual background sources in more detail.

2.5.1 Radioactivity from Detector Materials

The background component from the detector materials comprises events generated by gammas from the ^{238}U and ^{232}Th decay chains that reach the internal TPC volume, produce a low energy Compton scatter, and exit the detector without any further interactions.

Prior to detector construction, almost all materials have been screened for radioactivity [110, 111] by germanium detectors using the screening facilities Gator [112], GeMPI [113], and GIOVE [114]. Exploiting their high sensitivities to gamma rays, the gamma activity of the individual isotopes within the decay chains was determined. For XENON1T, mass spectrometry measurements were additionally conducted for complementarity, where the amount of ^{238}U and ^{232}Th was directly counted.

For deposited energies below 200keV, the spectrum from this background component is almost flat and features photo-absorption peaks only at energies above the WIMP search region. In XENON100 the dominating contribution to the background from detector com-

ponents results to $\sim 65\%$ from the PMTs, followed by $\sim 25\%$ of stainless steel from the cryostat, pipes, and bell structure⁵ [109]. In cooperation with the company Hamamatsu, the light sensors have been improved for the XENON1T experiment where special attention was given to the reduction of their internal radioactive contaminations. Therefore, the highest contribution to the ER background from materials in XENON1T originates from the cryostat with $\sim 61\%$, followed by the PMTs with $\sim 23\%$ [108].

2.5.2 Intrinsic ^{222}Rn

^{222}Rn is the first gaseous element within the ^{238}U decay chain. Once produced from contaminations in the detector materials, it can emanate from the detector components and its gas system, and distribute itself in the xenon. Having a relatively long half-life of 3.8 days, it has the chance to distribute homogeneously inside the LXe. The ER background, however, is not coming from ^{222}Rn itself which decays via an alpha, but from beta decays of its daughters. Hereby, the most dangerous contribution is represented by ^{214}Pb decaying to ^{214}Bi . For the dark matter search analysis only single particle interactions are of interest since WIMPs are not expected to scatter twice within the detector volume due to their low cross sections. Therefore, the direct decay to ground-state with an end-point energy of 1019 keV is the most relevant one because no further gammas are emitted that can induce a second interaction with the LXe. However, close to the borders of the TPC, decays to other energy levels become important as well. In those outer regions, accompanying gammas can escape without detection with higher probability. Hence, the ^{222}Rn background component shows a slight radial dependency. This effect is smaller for the larger XENON1T detector compared to XENON100 [109, 108].

Another potential background source in the ^{222}Rn decay chain is coming from the ^{214}Bi beta decay. However, its daughter ^{214}Po decays by emitting an alpha and exhibits only a very short half-life of $164\ \mu\text{s}$. Hence, both decays occur with high probability within the same event time window. This background can be suppressed to a negligible level by selecting events with single interactions as expected from WIMPs.

In XENON1T, detector materials and components in contact with liquid or gaseous xenon have been measured for their radon emanation prior to construction. Only materials with low emanation rates have been selected in order to reduce this background source [115, 116]. Furthermore, the separation of ^{222}Rn from xenon by cryogenic distillation has been successfully shown and provides a promising option for further suppression of the ^{222}Rn induced by background in XENON1T and its upgrade XENONnT [117, 64, 115].

2.5.3 Intrinsic ^{85}Kr

Given its production from air, xenon can contain krypton contaminations as explained in Section 2.2. Hereby, the radioactive isotope ^{85}Kr constitutes another background source by undergoing a beta decay with a half-life of 10.76 years and an end-point energy of 687 keV. Since this component cannot be reduced by selecting a fiducial volume, the only measure is given by the removal of krypton from the xenon. In XENON100, a $^{\text{nat}}\text{Kr}/\text{Xe}$ concentration

⁵See Section 2.6 for details on the XENON100 detector setup.

of (0.95 ± 0.16) ppt has been achieved by passing the gas through a cryogenic distillation column [118]. For XENON1T, the same technique is used by a new high through-put and high separation cryogenic distillation column that can be operated continuously during science data taking. Mass spectrometry measurements have been performed at the beginning of the first science run of XENON1T and one month after its end, yielding (2.60 ± 0.05) ppt and (0.36 ± 0.06) ppt, respectively [53]. This corresponds to a reduction of the background level from $\sim 10^{-3}$ events/(keV·kg·day) to $\sim 0.2 \cdot 10^{-3}$ events/(keV·kg·day).

2.5.4 ^{136}Xe Double-Beta Decay and Solar Neutrinos

Natural xenon contains the radioactive isotope ^{136}Xe with an abundance of 8.9%. It decays via double-beta decay with an end-point energy of 2458 keV and a half-life of $2.17 \cdot 10^{21}$ y [119]. As it is an intrinsic source, fiducialization is not effective in order to reduce this ER background. One option would be isotopic depletion. However, this background component is still of minor importance compared to the larger contribution from ^{222}Rn and will only become relevant in XENON1T as soon as efficient radon removal measures have been exploited (see Figure 2.5 right).

Solar neutrinos, scattering elastically off electrons, represent in principle an extrinsic background source. However, since the mean free path of neutrinos in matter is several light years those events are homogeneously distributed within the TPC. Hence, selecting a fiducial volume does not result in a reduction of the neutrino interaction rate. The only way to decrease this background component is an improvement in the ER rejection [120].

2.6 The XENON100 Experiment

The XENON100 experiment is equipped with a TPC of a height of 30.5 cm and a radius of 15.3 cm. It contains 62 kg of LXe and is surrounded by an active veto of 99 kg of LXe providing an efficient suppression of radioactivity from the outer detector components.

Additional shielding is provided by the operation of the detector in the underground laboratory LNGS and layers of 20 cm of lead, polyethylene, and 5 cm ultra-pure copper and water containers surrounding the cryostat. Figure 2.6 shows a schematic of the XENON100 shielding on the left and a photo of the cryostat when the shield was open, on the right. Due to the high hydrogen content, polyethylene and water are very efficient in thermalizing or even stopping fast neutrons produced by muon interactions in the surrounding rock of the cavern or in the shield materials. Exploiting the high atomic numbers of the materials, the lead and copper layers are supposed to stop natural gamma rays emitted by decays within the uranium and thorium decay chains. The copper was especially selected for low ^{210}Pb concentrations and its surface was electro-purified in order to minimize the radioactivity close to the cryostat.

Especially in underground locations, an increased ^{222}Rn concentration can be found due to emanation from the rock. To avoid background from ^{222}Rn decay daughters, the detector housing is constantly flushed with boil-off nitrogen.

Also visible in both pictures in Figure 2.6 is the calibration pipe. Being a copper tube twined around the cryostat, it is vertically adjusted to the TPC center. Radioactive sources emitting

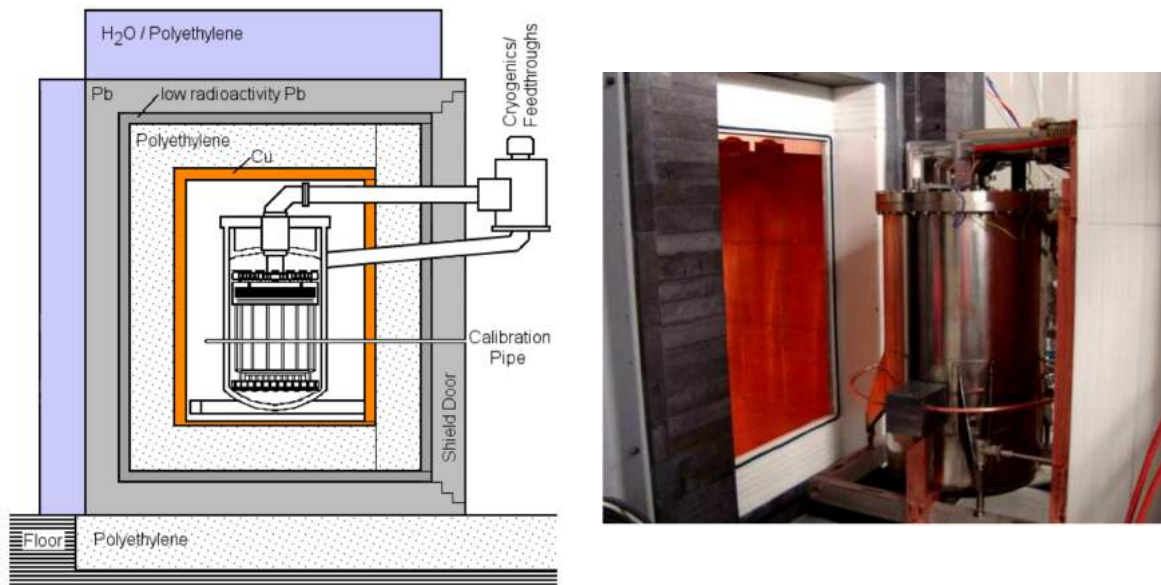


Figure 2.6: Left: Visualization of the shielding layers enclosing the XENON100 cryostat. The calibration pipe penetrates the shielding in order to bring calibration sources close to the cryostat. **Right:** Photo of the XENON100 cryostat when the shield was open. The calibration pipe, attached to the lower half of the cryostat, is visible. Pictures from [75].

gamma radiation can be placed inside at all azimuthal angles.

Figure 2.7 shows a drawing of the cylindrical XENON100 double wall stainless steel cryostat together with the contained TPC that is confined by the two PMT arrays at the top and at the bottom and by PTFE panels assembled to form a cylindrical shape. PTFE was chosen for its high reflection of VUV scintillation light [121]. Mesh electrodes optimized for optical transparency realize the required electric field strength. The drift field is applied between the cathode and the gate grid while the amplification field performs between the gate grid and the anode where the liquid-gas interface is enclosed. Grounded screening meshes close to the PMT arrays protect the light sensors from strong leaking fields. The gate grid, anode and the top screening mesh form the top mesh stack (indicated in Figure 2.7) with a spacing of 2.5 mm. In order to achieve a homogeneous drift field, 40 equidistant field shaping electrodes are installed. They are made out of thin copper wires that are running horizontally on the inside and on the outside of the PTFE panels. Only small deviations from a homogeneous field are observed and can be corrected in the data (see Section 2.3.4).

The two-phase TPC technology requires a stable liquid level in order to ensure a constant detector response. This is realized by a diving bell structure indicated in red in Figure 2.7. A constant stream of gas returning from the gas purification system pressurizes the bell. The pressure is released through a small pipe (bleeding tube) that leads to the LXe volume outside of the TPC. The height of the LXe level inside the bell is regulated by vertically moving the bleeding tube that is connected to a motion feedthrough. Additionally, the diving bell allows to increase the xenon level outside about 4 cm above the bell structure, which is advantageous for shielding.

The xenon is constantly evaporated from the liquid in the veto region and pumped through a zirconium getter to purify it from electronegative contaminations before leading it back

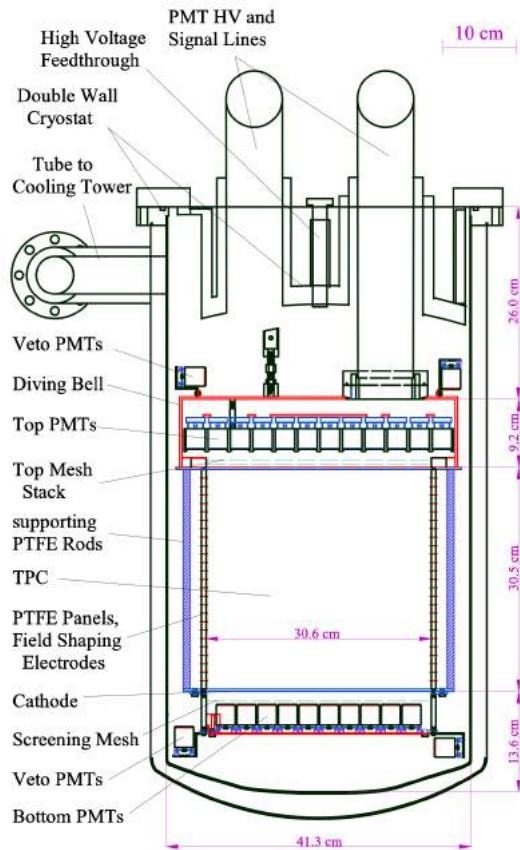


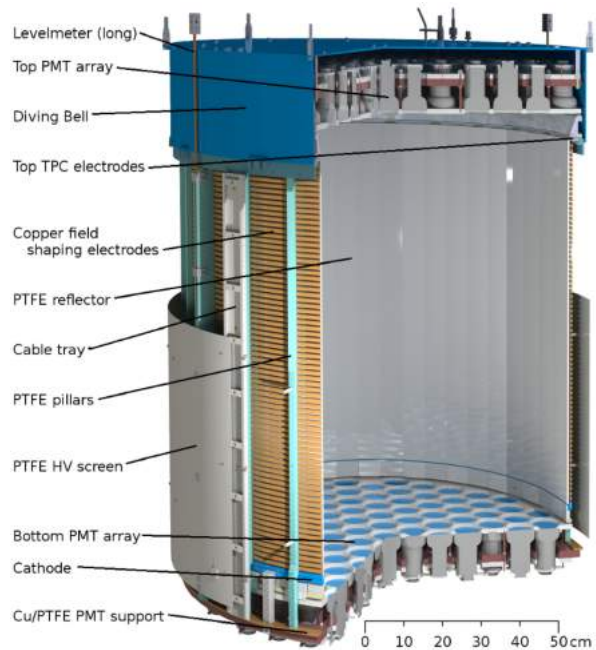
Figure 2.7: Drawing of the XENON100 cryostat with TPC. The total LXe mass of 161 kg is divided into the active region inside the TPC containing 62 kg and the veto region that comprises 99 kg. The TPC is confined by the two PMT arrays at the top and at the bottom and PTFE panels at the sides that form a cylindrical shape. See text for more explanations. Figure from [75]

into the cryostat. In addition, the gas system offers various ports to connect sources of radioactive nuclei that are dissolved in the xenon gas stream. Compared to the external gamma sources deployed in the calibration pipe, internal sources offer advantages in calibrating the central target of large LXe detectors. The deployment of internal sources for the background calibration in XENON100 was not necessary since the dominating background component results from radiation from the detector materials that can be well modeled with external sources. However, internal calibration sources are relevant for XENON1T since external gamma sources cannot penetrate the LXe up to the innermost volume anymore and therefore the dominating background is induced by ^{222}Rn . XENON100 was used to study the performance of internal calibration sources at the end of its operation period in preparation for calibrations in XENON1T. Some of these studies are described in Chapter 4.

The two PMT arrays are equipped with a total of 178 Hamamatsu R8520-06-A1 sensors with square windows of the size of one square inch. 98 of them are located in the top array arranged in a concentric circular pattern for an optimal X - Y position resolution and 80 PMTs are arranged in the bottom aiming for a maximum light collection efficiency. Due to the large refractive index of LXe, the S1 scintillation light is reflected at the liquid-gas interface resulting in a fraction of about 80% that is detected by the bottom array. Consequently, the energy threshold is dependent on the PMT coverage in this array. The active veto is watched by another 64 light sensors of the same kind.

The power to cool and keep the xenon below its evaporation temperature at 91°C and 2.2 atm is provided by a pulse tube refrigerator (PTR).

Figure 2.8: Three dimensional drawing of the XENON1T TPC. It features a target mass of 2.0t of liquid xenon and is confined by PTFE reflector panels and the top and bottom PMT arrays, instrumented with 248 light sensors. The 74 massive copper field shaping rings enclose the PTFE reflectors and ensure a close to homogeneous drift field between the cathode and the gate (one of the top TPC electrodes). See text for more explanations. Picture from [105]



More technical details on the XENON100 experiment can be found in [75].

2.7 The XENON1T Experiment

The more advanced XENON1T detector features a cylindrical TPC of 96 cm length and diameter, containing 2.0t of LXe. Figure 2.8 shows a three dimensional CAD drawing. The chamber is delimited horizontally by 24 interlocking PTFE panels forming a cylindrical shape which is surrounded by 74 massive field shaping electrodes in ring structure. The electrodes are made from OFHC copper selected for low radioactivity. The mesh electrodes generating the drift and amplification fields were constructed from stainless steel by etching and were spot-welded to stainless steel frames. Like in XENON100, screening meshes are placed in front of the PMT arrays for protection. A voltage of -1.55 kV has been applied during the first science run in order to establish a field-free region in front of the PMT photocathodes. Before construction, the field configuration was optimized for a high transparency of the meshes by electrostatic field simulations. The cathode was designed for bias voltage up to -100 kV providing a drift field of about 1 kV/cm between the cathode and the grounded gate grid. In the first science run of XENON1T a lower field of 0.12 kV/cm was applied. The anode was biased with 4.0 kV in the same run, resulting in an extraction field of about 10 kV/cm between the anode and the gate grid across the liquid-gas interface.

Since it has been proven itself in XENON100, a diving bell structure made of stainless-steel is used in XENON1T as well. The stable level of the liquid-gas surface is maintained by a continuous gas stream from the recirculation gas system and is adjusted via a vertically movable bleeding tube.

The planes of the TPC are equipped with a total of 248 Hamamatsu R1410-21 PMTs. The top array accommodates 127 tubes arranged for a good radial position reconstruction while the bottom array consists of 121 PMTs that are packed as tightly as possible to gain a maximum

light collection efficiency. The average quantum efficiency (QE) of all sensors is 34.5% at 178nm [94]. Those with the highest QEs were placed in the bottom array to further optimize the response to small scintillation signals from the liquid. The area between the individual tubes is covered by a PTFE reflector plate. Additionally, six Hamamatsu R8520 PMTs with quadratic windows of one square inch, the same kind that was used in XENON100, are installed next to the topmost field shaping copper ring in the LXe region outside of the TPC. Those PMTs are grouped into two groups of three and face downwards. They are intended to be used in detector calibration studies. All sensors were tested prior to the TPC construction under nitrogen atmosphere at room temperature, at -100°C and a fraction of about 18% in LXe. Details on these tests and their outcome can be found in [94].

While the active volume contains 2.0t of LXe as a target, the detector is operated with a total of 3.2t. These additional 1.2t add up from the 5 cm space between the field shaping rings and the cryostat wall, 5.7 cm space between the cathode and the bottom PMTs, between and below the bottom PMTs, the gas phase, and the gas purification system. Additional xenon can be filled in order to increase the liquid level outside of the TPC above the diving bell for a more effective shielding.

In contrast to several layers of passive shielding in XENON100, the XENON1T cryostat is immersed into a water tank of 10.2m height and 9.6m diameter that serves as an active veto against a residual muon flux of $(3.31 \pm 0.03)10^{-8} \text{ cm}^{-2}\text{s}^{-1}$ at an energy of $\sim 270\text{GeV}$ at the detector site [122]. Equipped by 84 Hamamatsu R5912ASSY PMTs with 8" windows, the emitted Cerenkov radiation can be detected in the water tank and correlated to events within the TPC. With this technique the background from muon-induced neutrons can be reduced to a negligible level. Additionally, the water itself moderates ambient neutrons induced by muons or (α, n) reactions in the surrounding rock cavern.

Since successfully used in XENON100, XENON1T employs the technique of pulse tube refrigerators (PTRs) as well. Two redundant devices are installed to keep the xenon at an operating temperature of -96°C and to allow for maintenance works while the detector is cold.

Figure 2.9 shows a 3D computer view on the auxiliary systems necessary for the operation of the XENON1T experiment and their relative placement to each other as well as their connections. The auxiliary systems comprise the cryogenic system providing the cooling power, the purification system for the online removal of electronegative impurities, the cryogenic distillation column for krypton removal, ReStoX for xenon storage and recovery, the bottle rack as an interface to xenon gas cylinders, and a gas analytics station for measuring the purity before injecting the xenon from the gas cylinders into the system. The following paragraphs will highlight the systems that are of relevance in the following chapters of this thesis. For more detailed descriptions and supplementary information on the other sub-systems the reader is referred to [105].

The bottle rack and the gas analytics were developed within this work and are explained in detail in Chapter 3.

Purification System As explained in Section 2.1, electronegative impurities, i.e., impurities that have a high tendency to attach free electrons such as O_2 and water vapor, are constantly removed from the detector by circulating gaseous xenon through a purification

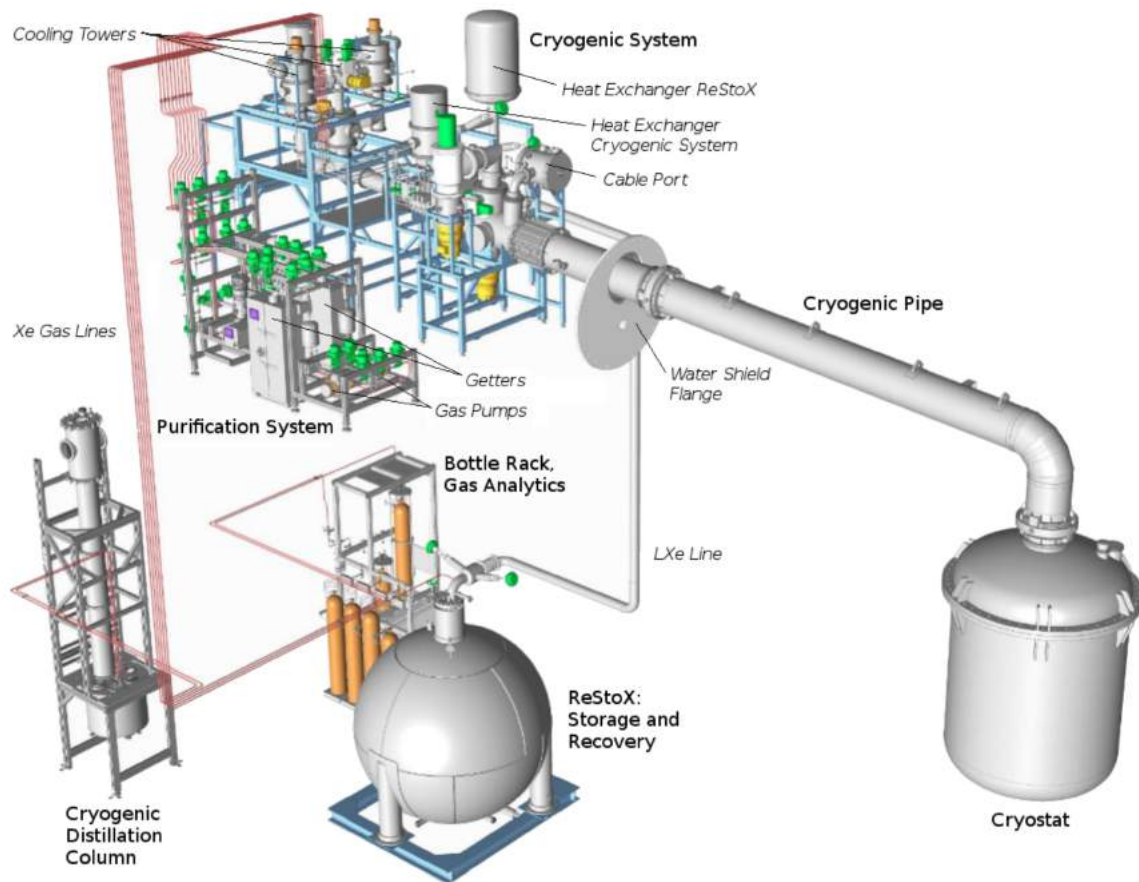


Figure 2.9: Three dimensional view on the auxiliary systems of the XENON1T experiment. It consists of the cryogenic system, the purification system, the cryogenic distillation column, the storage vessel ReStoX, the bottle rack, and the gas analytics station. See text for more information. Picture from [105]

system in order to increase the electron lifetime. Xenon is extracted from the liquid phase at the bottom of the cryostat and evaporated in a heat exchanger. Two redundant loops are available in the purification system allowing for maintenance work on one of them without interrupting the other. Each loop hosts one or two gas transfer pumps (QDrive) that drive the purification flow, a mass-flow controller and a high temperature rare-gas purifier from the company SAES Pure Gas of the type PS4-MT50-R, also referred to as *getter*. The getter contains a zirconium cartridge and removes oxides, carbides and nitrides from the xenon gas by forming irreversible chemical bonds with the material. According to its specifications, the purifier ensures impurity concentrations below 1 ppb if the inlet gas has a purity of 5 ppm or higher [123]. This number provides the guideline for the gas purity analytics described in Chapter 3.

The purified gas passes again through the heat exchanger where it is liquefied. The liquid is collected by a funnel leading it directly into the TPC at two opposite positions below the cathode mesh.

The purification gas loop is monitored by various pressure and temperature sensors for the verification of stable conditions. Additionally, a HALO+H₂O monitor from the company

Tiger Optics measures the water concentration, a good indicator for leaks.

Furthermore, the purification system is used to connect sources of radioactive nuclei that can be dissolved in the xenon gas stream. This way, the activity is transported into the detector and can be used for calibrating the central target. The calibration of the detector response to electronic recoils using such sources will be subject to Chapter 4.

The purification system also takes the task of distributing the xenon gas onto other systems. Beside the cryostat, it is connected to the storage system ReStoX, the cryogenic distillation column and the bottle rack.

Xenon Storage In the XENON100 experiment, the detector was filled by a total of 161 kg of LXe by drawing the gas from commercial gas cylinders at ambient temperature and liquefying it by using the cooling power of the PTR. However, for a multi-ton scale experiment like XENON1T this procedure would require about two months. Furthermore, it would not allow for a fast recovery of the LXe from the detector in case of emergency. The solution is provided by a newly developed xenon storage system called ReStoX (Recovery and Storage of Xenon) [124]. It is a vacuum insulated stainless steel vessel shaped like a sphere of a diameter of 2.1 m. Being able to withstand pressures of up to 73 bar, a maximum of 7.6 t of xenon can be stored safely at low temperatures as well as at ambient temperatures as a super-critical fluid. The cooling power is provided by liquid nitrogen (LN₂) that is extracted from an external tank and led through 16 LN₂ pipes welded to the outer surface of the inner vessel. Additionally, 16 thin stainless steel fins are installed inside the sphere in order to increase the heat exchange. The vessel was electro-polished to remove surface contaminations and hosts only metal sealed cryogenic valves in order to maintain the xenon purity. For the filling of the detector, gaseous xenon is extracted from ReStoX and led through an independent heat exchanger into the purification system. After the removal of impurities, it is re-condensed in the heat exchanger and transferred to the cryostat. The recovery from the detector into ReStoX is realized in a liquid phase via direct vacuum insulated lines.

Cryogenic Distillation Column As explained in Section 2.5.3, the radioactive isotope ⁸⁵Kr is a background source for LXe detectors due to its presence in air from which xenon is extracted. Exploiting the difference in vapor pressures of krypton and xenon (see Figure 2.2), krypton can be removed efficiently by cryogenic distillation. It will accumulate in the gas phase at the top within the distillation column while the krypton-depleted xenon can be withdrawn from the bottom. The column has a height of 5.5 m with a total length of 2.8 m of package material. Operated at a temperature of 178 K at 2.0 bar, it features a reduction factor for krypton in xenon of $(6.4_{-1.4}^{+1.9}) \cdot 10^5$ [125]. For a purification at maximum efficiency, the entire 3.3 t of xenon gas needed for detector operation, would have to be transferred from ReStoX through the distillation column into the cryostat. This would take about three weeks.

As an alternative, the operation of the column in parallel to science data acquisition with a fully operational TPC was successfully tried. 7% of the purification gas flow was directed through the column. The krypton concentration was reduced from about 60 ppb to 0.36 ± 0.06 ppt within approximately 70 days.

Apart from the possibility to reduce the krypton content in xenon, it has been shown that the

same can be done for radon contaminations by operating the column in reverse mode [64]. This option is currently under investigation within the XENON1T experiment.

Chapter 3

Xenon Gas Purity Analytics

The sensitivity of the XENON1T detector to dark matter particles is determined by the purity of the xenon gas therein. Electronegative¹ impurities such as O₂, CO₂, and N₂O attenuate the observed ionization signal (S2) of an interaction through electron attachment. The dependence of this attenuation on the drift time is described by an exponential function that takes the electron lifetime as a parameter (see Equation 2.12). With increasing electron lifetime, smaller energies can be measured at the bottom of the detector, and hence, the overall sensitivity of the detector to WIMP interactions increases.

Krypton impurities are present in commercial xenon because it is produced from air by distillation (see Chapter 2). Beta decays of the radioactive isotope ⁸⁵Kr contribute to the background in the XENON1T experiment.

This chapter describes the procedures and methods developed to monitor the purity of the xenon gas inventory in the XENON1T detector during its initial filling into the XENON1T gas system. First, the aims of this study are outlined in terms of gas purity levels and put in context with their implications on the experiment in Section 3.1. The chosen technique of measuring impurities, i.e., gas chromatography, is briefly introduced in Section 3.2. The experimental setup used during the xenon transfer campaign as well as the gas purity measurement device are described in Section 3.3. The measurement procedure is outlined in Section 3.4. The calibration method and procedure to evaluate impurity concentrations are explained in Section 3.5. Section 3.6 presents the outcome of the measurement campaign and the overall impurity content of the xenon inventory. The chapter is concluded with a summary of the results and their interpretation in terms of their impact on the XENON1T experiment in Section 3.7.

3.1 Motivation

The xenon inventory of approximately 150 gas cylinders was purchased commercially. Since no automatic procedure can be utilized to connect these cylinders to the XENON1T system and empty them, ensuring gas purity during gas handling is a challenge.

As mentioned in Chapter 2, gas purity plays an important role in the success of the XENON

¹Electronegativity is a chemical property that describes the potential of atoms and molecules to attract electrons.

experiments.

Electronegative impurities, such as O₂, CO₂, and N₂O, decrease the electron lifetime (see Section 2.3.4 for definition). Therefore, the number of charges from an interaction reaching the liquid–gas interface is reduced in correlation with the drift time. This leads to weaker S2 signals of events occurring at the bottom of the TPC compared to those occurring at the top. The S2 threshold as well as the energy resolution of the S2 signal due to the statistical uncertainty in the number of detected electrons, are influenced.

The general impurity level of electronegative components in commercial ultra-pure xenon is 1 – 10 ppm². These impurities usually do not originate from the production method of xenon itself³ but are introduced after the production by, for example, out-gassing⁴ of gas cylinders and small leaks at gas pipe connections. In general, measures are taken to prevent these routes for the introduction of impurities, for example, baking of cylinders and leak checks. However, the efficiency of such measures depends on how carefully they are implemented.

The XENON1T gas system is equipped with two getters within the purification system (see Section 2.7), which can reduce the amounts of electronegative impurities to below the ppb⁵ level if the inlet gas has a purity of 5 ppm or better. This value is the aim for the control of this impurity type during the transfer process.

A second important impurity category that must be controlled is ⁸⁵Kr. Its provenance in xenon gas and influence on the background level of XENON experiments have been discussed in Section 2.5.3. With its vapor pressure curve closest to that of xenon compared to the other gas components in air, it has potentially the highest impurity concentration given that the xenon is produced by air liquefaction. Depending on the number of distillation cycles executed during production, commercial xenon comes with typical krypton contents of 2 ppb to a few ppm. The XENON1T setup houses a distillation column designed to reduce the krypton concentration with a reduction factor of $F_{\text{red}} = (6.4^{+1.9}_{-1.4}) \cdot 10^5$ [125]. It purifies xenon at the maximum xenon flow rate of 6.5 kg/h, resulting in a time requirement of 23.5 d to process the entire xenon inventory of 3.67 tons. The fraction of gas that is enriched with krypton after the distillation is about 1%. Hence, for the entire xenon inventory, ~ 37 kg of off-gas is expected. The aim of controlling krypton impurities in xenon during the transfer is to ensure that the design value for XENON1T of 0.2 ppt of krypton in xenon can be reached within a minimal amount of xenon off-gas and time.

To achieve these two aims, the impurity concentration in the xenon inventory is monitored through gas chromatography. This measurement technique provides the possibility to quantify multiple impurity gases within one measurement cycle, and has a sensitivity that is adequate for our purpose. Furthermore, the setup is compact enough so that it can be installed at the detector site *Laboratori Nazionali del Gran Sasso* (LNGS) in Italy.

While optimizing the measurement procedure, the focus was on krypton impurities because they contribute directly to the background of the XENON1T experiment. Other measured impurities include hydrogen, oxygen, methane, and carbon monoxide. Hydrogen could be released into the xenon from steel surfaces that are electropolished [126]. A very high hydro-

²parts per million

³As explained in Section 2.5.3, these components have high separation efficiency from xenon by distillation owing to their low boiling temperatures

⁴The term out-gassing denotes the release of gas molecules attached to gas vessel surfaces.

⁵parts per billion

gen content can result in the accumulation of hydrogen in the gas phase of the TPC, which can induce a potential bias in the secondary scintillation signal. This hydrogen accumulation has been observed in multiple measurements of the gas phase from the xenon stored in the storage vessel ReStoX [127]. Nitrogen is a good tracer for air because it is the most abundant component. Air also contains krypton and oxygen, which are dangerous for detector operation. Methane and carbon monoxide are not expected to be present in the xenon gas from production, but the ability to quantify their concentrations provides another handle on monitoring impurities in the xenon inventory.

3.2 Basics of Gas Chromatography

The term *gas chromatography* refers to the separation and analysis of gas compounds. The separation is realized by distributing gas components between a mobile phase and a stationary phase. The stationary phase can be solid or liquid, whereas the mobile phase is a chemically inert carrier gas. This study will focus on gas–solid chromatography.

The material of the stationary phase is selected in terms of its gas adsorption properties. Filled into glass or metal tubing, it is called an *adsorption column*.

Adsorption, in general, refers to the attachment of a gas or liquid to the surface of a material. This can be realized either by van der Waals forces or by chemical reactions. For gas chromatography, the van der Waals forces are relevant. The inverse process of adsorption is called *desorption*. In an equilibrium state, the number of adsorbed molecules equals the number of desorbed molecules per unit time. More details on the theory of surface interactions can be found in [128].

The general concept of separation of gas components by gas chromatography is based on the transport of the sample through an adsorption column by using carrier gases such as helium, hydrogen, nitrogen, or argon. For short measurement times and for the operation of the adsorption column at low temperatures, gases with high flow rates and low molecular weight are advantageous because they can diffuse faster through the column without influencing the quality of separation [129]. These properties are provided by helium, which is used in this study.

Gas impurities in the carrier develop an adsorption/desorption equilibrium in the column and are pushed through the adsorption material by the carrier gas. The velocity at which the gases of interest, the analytes, are transported depends on the carrier gas flow and on their surface interactions with the adsorption materials.

The quantitative measurement of the gas components is performed using a detector connected to the column exit. In principle, any gas property of the components to be measured that is different from the carrier gas can be used for detection. Examples are different ionization potentials (flame ionization, photo-ionization, pulsed discharge ionization detectors (FID/PID/PDD)), mass (mass spectrometer (MS)), and thermal conductivity (thermal conductivity detectors (TCDs)). In this study, a pulsed discharge detector (PDD) is used, and will be described in the next section.

The detector current measured over time is denoted as *chromatogram*. It shows a peak for each gas component eluted from the column. Gas chromatography measurements are well reproducible because the peaks always occur at the same time with negligible variations. The

peak positions within a chromatogram can be changed by altering the column temperature or the gas flow and pressure of the carrier. Depending on the gases that shall be separated and the adsorption materials used, a wide range of temperatures from cryogenic levels up to several hundreds of °C can be used.

Further details about the gas chromatography technique can be found in [130][129].

3.3 Experimental Setup

The experimental setup for monitoring the gas purity of the XENON1T xenon inventory during its initial transfer to the storage vessel ReStoX consists of two parts: a gas handling system, called XENON1T *bottle rack*, and a gas chromatograph (GC). The bottle rack provides an interface between the purchased xenon gas cylinders and the XENON1T gas system, and the GC provides the means to determine the purity of the gas inside the cylinders.

Figure 3.1 shows pictures of the two systems at the XENON1T detector site LNGS. The bottle rack can be seen on the left. The four gas cylinders that are standing in a row in the front contain the xenon that needs to be filled into ReStoX. They are placed on platform scales, which monitor the weight of the cylinders while they are emptied in order to deduce the amount of xenon extracted. The spiral structures above those gas vessels are sampling volumes, also-called *pipettes*, which are used to extract small samples from each cylinder. The two blue gas cylinders in the back are placed in structures that can be pulled toward the ceiling to move the liquid nitrogen bath beneath, where the vessels can be immersed. This feature facilitates the collection of gas residuals from the gas cylinders through cryogenic pumping. The GC is shown in Figure 3.1 on the right, together with the computer to control the device. The setup is placed right next to the ReStoX sphere, which is visible in the back.



Figure 3.1: Pictures of the XENON1T bottle rack (left) and GC (right) as they are operated in the Gran Sasso Underground Laboratory.

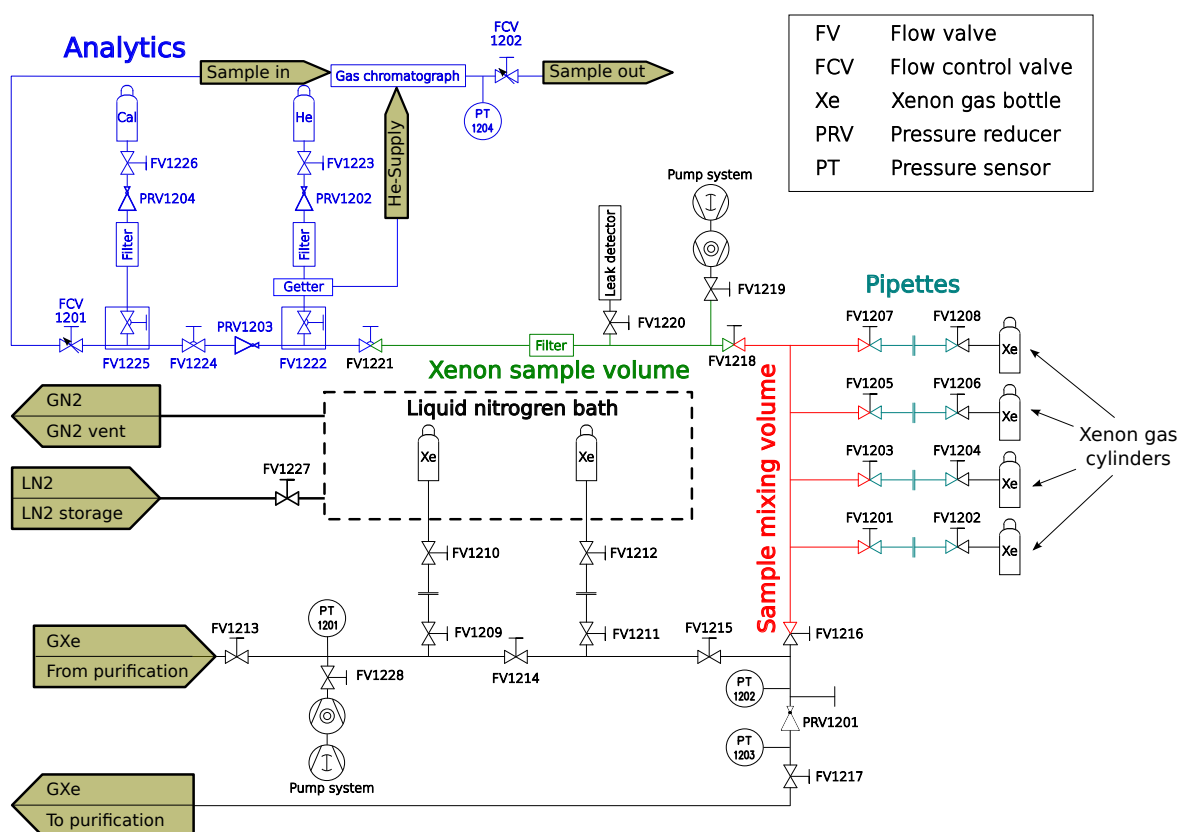


Figure 3.2: Schematic of the XENON1T bottle rack. The xenon gas cylinders are connected to the rack at their own valves FV 1202, FV 1204, FV 1206, and FV 1208. The pipettes (turquoise) are used to draw samples from the cylinders, and the samples are mixed in the sample mixing volume (red). The sample mixture is stored in the xenon sample volume (green), where it is decoupled from any operation on the xenon gas cylinders by FV1218. For a measurement, the sample is expanded further into the analytics section (blue), where its impurities are measured by the GC. The two xenon gas cylinders in the liquid nitrogen bath allow for the extraction of residual xenon gas from the cylinders through cryogenic pumping.

3.3.1 XENON1T Bottle Rack

The XENON1T bottle rack was designed during this work to extract xenon gas from the cylinders in which they are delivered by the suppliers. At the same time, the purity of the xenon gas should be measured. The overall structure of the bottle rack is shown schematically in Figure 3.2.

Four gas cylinders can be connected at the same time. Special provisions are taken to allow gas cylinders with different standards because they are purchased from suppliers all over the world (German, French, American, Italian, and Chinese).

To draw a sample, the evacuated pipette volumes marked in turquoise are filled with xenon from the cylinders. The gas is then expanded into the sample mixing volume (red). Care is taken to ensure good mixing of the four gas volumes by alternating valve operations. Instead of measuring the purity of each cylinder individually, the samples are mixed to save time. If

the mixture shows high contamination, its source is investigated by additionally determining the impurities in each of the four samples.

The sample mixture is then expanded into the xenon sample volume (green), which is decoupled from any action taken on the xenon gas cylinders. Finally, the gas is led into the analytics section (blue). This section comprises all components necessary for impurity measurements. The helium cylinder is marked with *He* and supplies the GC with its carrier gas. To ensure high sensitivity of all measurements, helium 6.0⁶ is used. The same gas is also used for helium background measurements (see Section 3.5.1). The cylinder marked with *Cal* is used to supply the calibration gas.

The sample pressure and flow are regulated by the flow control valves placed in front of the sample inlet and behind the sample outlet of the GC.

If the impurities measured in the sample drawn from the four gas cylinders meet the requirements, the xenon is led into the xenon storage vessel, ReStoX, by passing it through the XENONIT purification system.

Considering the time needed for pumping and baking the gas lines at the bottle rack every time new cylinders are connected, for measuring the gas impurities and for transferring the gas into ReStoX, this procedure allows for a maximum of eight cylinders to be emptied per day.

A special feature of the bottle rack is the possibility to recuperate residual xenon from the gas cylinders after the ReStoX filling process. The term *recuperation* refers to the transfer of xenon to a gas vessel through cryogenic pumping. This can be done by immersing a gas cylinder into a liquid nitrogen bath (see Figure 3.2). Owing to the lower boiling point of nitrogen, xenon gas is liquefied, which creates a pressure gradient toward the cylinder.

3.3.2 The Gas Chromatograph

A Trace GC Ultra Thermo Scientific⁷ purchased from S+H Analytic GmbH is used for the following measurements. It is a commercial device that was set up by the company to adapt to a wide range of analytical problems. Using high-purity pneumatic 6-port diaphragm valves⁸, it can be operated fully automatically. This way, a precise timing within the measurements is ensured, which is crucial to make sure they are reproducible.

Together with a packed column, referred to as *pre-separation column*, the valves are installed in an oven called *valve oven*. The column is filled with *HayeSep*[®] polymers, which are macroporous (pore size > 500 Å), spherical, ultra-pure resins. The material was developed by VICI[®], and promises a good separation performance in gas chromatography. The pre-separation column can be operated between ambient temperature and 160°C, and helps separate impurities from the xenon bulk of the sample.

In addition to the valve oven, a so-called *cryo oven* is implemented in the chromatography device, which can generate a wide range of temperatures between -99°C and 250°C, and hosts a second column packed with a molecular sieve with a pore size of 0.5 nm. The molecular sieve column, denoted as *main column*, is used to separate the analytes eluting simultaneously from the pre-separation column. At the end of the main column, a pulsed

⁶The number 6.0 states that the sum of all impurity concentrations is smaller than 10⁻⁶.

⁷<http://www.thermoscientific.com/>

⁸MDVG series from NORGREN

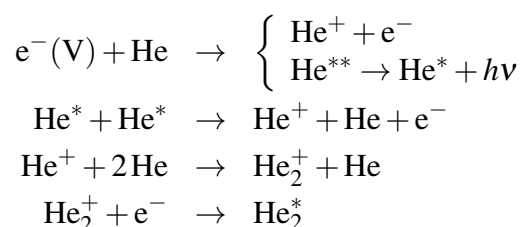
discharge detector is located, which is sensitive to all gases, except helium and neon; its operating principle will be described in the next subsection.

The internal GC setup is shown in Figure 3.4 in its configuration used in this study. In addition to the two mentioned columns denoted as PC1 and PC2 in the sketch, the overall setup further comprises two switching valves V1 and V2, a sampling volume of 20 cm³, and three pressure regulator valves PRV1–3.

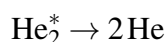
Pulsed Discharge Detector

A pulsed discharge detector (PDD) uses a high-voltage pulsed discharge between two platinum electrodes as the ionization source. It was first described in 1992 [131, 132].

In helium, the discharge triggers the following processes:



The formed excited diatomic helium dissociates to the ground state of two single helium atoms by emitting high energy photons with energies ranging between 13.5 and 17.5 eV [133]:



The photons are capable of ionizing every compound and element except for neon⁹. This process is the most relevant from the viewpoint of the functioning of a PDD, and is called *Hopfield emission*. The detector configuration that employs this effect to ionize analytes is called *helium discharge photo-ionization mode* [131, 132].

Figure 3.3 shows a schematic of the PDD used in this study. The discharge and ionization regions are spatially separated to avoid contamination of the discharge electrodes. Eluents from the column flow in the direction opposite to the helium flow in the discharge region. After ionization of the analytes by Hopfield photons, the resulting electrons are focused toward the collector electrode by two bias electrodes. The measured current I depends on the impurity concentration and the gas-specific ionization efficiency. A linear relationship between the detector signal and the concentration has been shown to exist over five orders of magnitude [135]. This allows for the measurement of traces with concentrations at the ppb level while calibrating the ionization efficiency at the ppm level. Assuming that one atom or molecule produces one electron after ionization, the efficiency ε is given by [135]:

$$\varepsilon = \frac{\int I \cdot dt}{F \cdot Q} = \frac{A}{F \cdot Q}, \quad (3.1)$$

⁹Neon has an ionization potential of 21.56 eV. The metastable helium He*, also created by the discharge, emits photons with an energy of 19.8 eV. This is close enough to the ionization potential of neon such that a very small but non-zero ionization efficiency is achieved, and a detector response for neon is present.

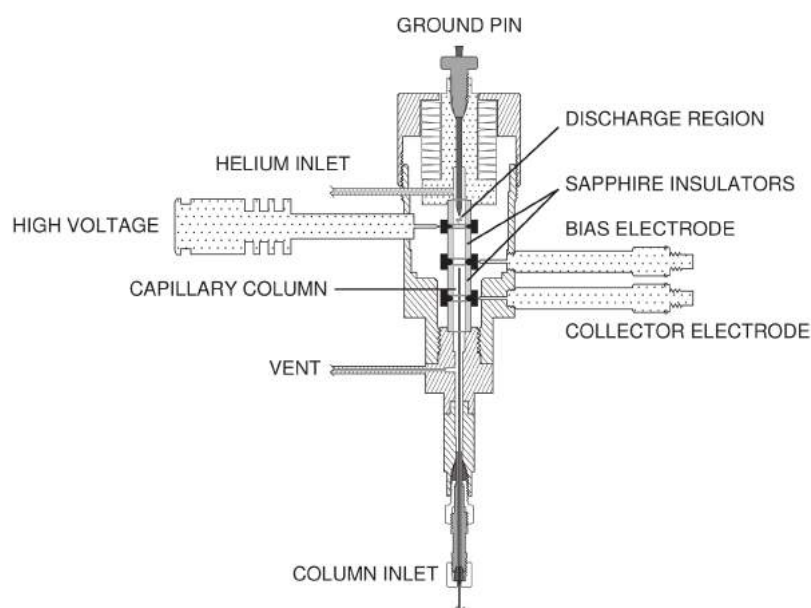


Figure 3.3: Schematic of a PDD in the so-called helium discharge photo-ionization mode, which uses Hopfield emission to ionize the analytes. See text for more explanation. Reprinted from [134]

where I denotes the electron current, t denotes the time, F denotes the Faraday constant and Q denotes the analyte's quantity in mol. The current integrated over time corresponds to the area A under the peak in the chromatogram.

ε depends not only on the type of gas passing through the detector but also on the flow of the carrier gas. The longer the residence time of the analytes in the detector, the higher is the ionization efficiency. Hence, the detector responds not only to impurity concentrations but also to changes in the gas flow.

The minimum quantities that can be detected with the employed PDD model are in the low ppb range [134].

3.4 Measurement Procedure

The measurement procedure implies the actuation of the two pneumatic valves within the internal GC setup (see Figure 3.4) as well as a temperature change in the cryo-oven. These processes are programmed to always take place at the same time after the start of the procedure in order to ensure reproducible measurements. The slowest analyte carbon monoxide elutes from the main column PC2 35 min after the start of the measurement. The detector signal is therefore recorded for a time of 40 min for all xenon sample measurements. The procedure is optimized to achieve good sensitivity for krypton, because this impurity directly affects the background level of the XENON1T experiment.

The solid lines between the valve ports of V1 and V2 in Figure 3.4 indicate that a gas flow is allowed, while the dashed lines mark disconnected ports. When actuating the valves, the

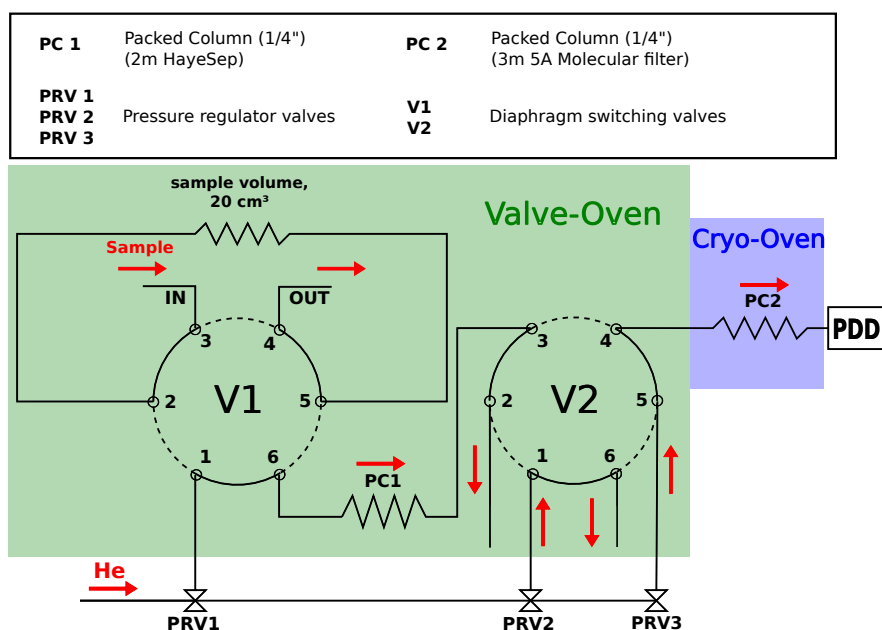


Figure 3.4: Internal GC configuration. The two valves V1 and V2, as well as the pre-separation column PC1 and the sample volume, are placed inside a valve oven (green) that is set to a constant temperature of 60°C. The main column PC2 is installed in the cryo-oven (blue) that runs at 60 and 120°C.

ports connected by dashed lines are linked, while the gas stream along the solid lines is interrupted.

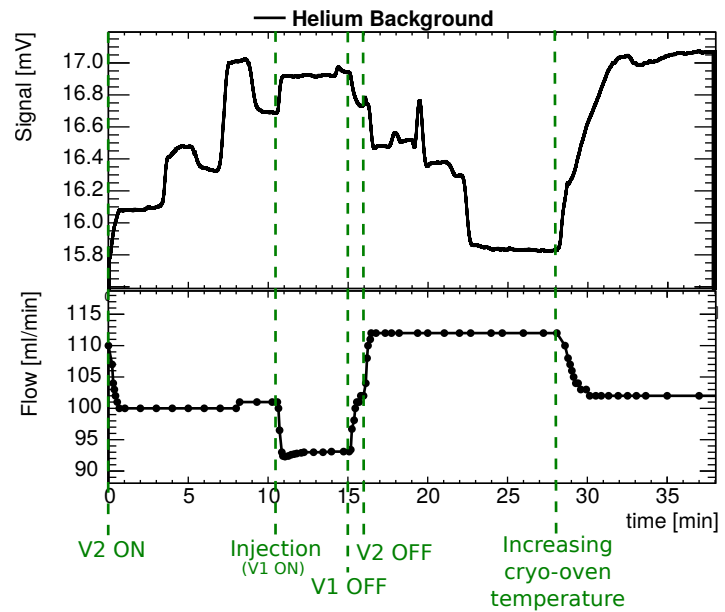
The temperature of the valve oven is maintained at 60°C, whereas the cryo-oven is operated at different temperatures during a measurement. The pressures in PRV1, PRV2, and PRV3 are maintained at values higher than one atmosphere. In what follows, the measurement procedure applied during the measurement time t is presented and its direct implications on the chromatogram are discussed by referring to the measurement of a pure helium sample, as shown in the upper panel of Figure 3.5. The lower panel in the same figure shows the gas flow behind the PDD as a function of t . As explained in Section 3.3.2, the detector responds not only to impurity concentrations in the carrier gas but also to changes in its flow. Hence, by comparing the detector signal to the gas flow, the two different causes can be disentangled.

Various steps are observed in the signal baseline as a result of the measurement procedure and the system features. They do not impact the sensitivity significantly because they are much reproducible and can therefore be subtracted (see Section 3.5.3).

$t < 0$: Before the start of the measurement, the sample volume is prepared by flushing it continuously with the sample gas at a flow rate of around 20 – 30 ml/min. The pre-separation column PC1 is separated from the sample as well as from the main column PC2. Both columns are flushed with clean helium.

$t = 0$ min: At the start of the measurement, V2 is actuated such that PC1 and PC2 are linked. As can be deduced from Figure 3.5, a change in the gas flow through the PDD is

Figure 3.5: Upper panel: Chromatogram of a pure helium sample. Since no impurities are present in the sample, all observed features in the detector signal as a function of time are results of the measurement procedure. They do not represent a problem in the quantification of impurity concentrations because they are highly reproducible, and can therefore, be subtracted. **Lower panel:** Gas flow behind the PDD during the measurement as a function of time. The flow is anti-correlated to the current measured by the detector.



coupled to this action, because of which the measured current increases. Two further upward steps of the baseline are observed at about 3.5 min and 7.5 min, while the flow stays constant. The fact that the two steps in the baseline are separated by about 4 min suggests that they are induced by oxygen and nitrogen impurities, that is, air, that passed through PC2. It will be shown later that the oxygen and nitrogen peaks are separated by roughly the same time in a chromatogram.

Downward steps occur about 2 min after the two upward steps, pointing to an injection of air into the system for two minutes, evoked by actuating V2. This might be explained by small volumes within the valve that have a connection to air and are emptied by valve actuation. A deeper understanding of this feature is beyond the scope of this study. After 9 min, the detector baseline stabilizes at a level higher than that at the beginning of the measurement, indicating a higher background level in PC1.

t = 10.5 min: The injection of the sample into the pre-separation column takes place 10.5 min after the start of the measurement procedure by actuating V1. This point of time is chosen to avoid the signals from impurities sitting on top of the mentioned steps in the baseline. Owing to valve operation, the gas flow through the detector decreases again, leading to an increase in the measured current.

Hereafter, the investigated gas sample is disconnected from its source and is pushed into PC1 by helium flowing from PRV1. For every measurement, the same sample gas flow and pressure are adjusted for the time of injection to ensure a constant sample size within the sample volume of 20cm^3 . It was found to be advantageous to have slight over-pressure at about 1020 mbar absolute in the sample volume to decrease the potential impact of small diffusive leaks.

t = 15 min: After 4.5 min of injection, V1 is switched back into its initial state. The sample volume is again separated from the columns and can be prepared for the next sample. This ensures that no contaminants from the previous sample are left in the volume when the

next sample is loaded. By this measure, the flow through the detector is increased, and consequently, the signal baseline shows an immediate downward step.

t = 16 min: As mentioned before, the purpose of the pre-separation column is to isolate the analytes from the xenon bulk of the sample; 5.5 min after the start of the sample injection, the analytes reach PC2, while the xenon is still in PC1. V2 is brought back into its initial state to separate the two columns and avoid contamination of the fine pored main column (PC2) with xenon. Furthermore, a large quantity of xenon would lead to detector saturation. Again, the valve operation evokes an immediate change in the signal baseline due to the decreasing gas flow in the PDD. Additional downward steps and small peaks are observed between 16 and 22 min, and are uncorrelated to the gas flow. Hence, they must have been induced by small changes in the internal impurity level induced by the present and preceding valve operations.

t = 28 min: After 28 min of the start of the measurement, the cryo-oven temperature increases to 100°C at a rate of 60 K per minute. The intention is to accelerate the elution of CO from the main column. This gas travels through the molecular sieve at considerably lower velocities than do the other analytes. By increasing the kinetic energy of the molecules, the elution of CO can be accelerated. This effect dominates the increase in the flow resistance of the column, which leads to a decrease in the gas flow through the PDD, and therefore, to an increase in the measured signal.

t > 40 min: After 40 min, all impurities have been eluted from the main column and the measurement ends. The temperature of the cryo-oven is left at 120°C to bake the main column¹⁰. This way, the packing material is cleaned from any residual contaminant, which is flushed out by the continuous stream of pure helium gas.

The measurement procedure does not allow for the separation of argon and oxygen, which makes it difficult to quantify them individually. This is owed to the optimization of the procedure for a short measurements time. For the separation of oxygen and nitrogen, the main column would have needed cooling to temperatures below 0°C which would have lengthened the time needed for the procedure. As a consequence, a reduced amount of measurements could have been performed per day resulting in an increased time for the transfer campaign of the xenon gas to ReStoX. However, Section 3.5.2 presents a method with which the oxygen concentration can be evaluated under the assumption that no argon is present in the sample.

3.5 Evaluation of Impurity Concentrations

The outcome of the measurement procedure described in the previous section is a chromatogram from which the impurity concentrations can be inferred. As introduced in Equation 3.1, the area under a peak A is proportional to the quantity of

¹⁰Higher baking temperatures are not applied because they affect the oxygen concentration measurement.

the analyte that passed through the PDD. Furthermore, the ionization efficiency ε is constant over five orders of magnitude [135] corresponding to concentrations between ppb and ppm for the given sample size of about 20cm^3 . This justifies a calibration with ppm concentrations while aiming to measure ppb levels, and provides the advantage that statistical fluctuations in the calibration gas peak areas are negligible.

The calibration is performed by comparing the peak area A_{xe}^k resulting from a gas component k in a xenon sample to the peak area A_{cal}^k measured in a calibration sample with known impurity concentration c_{cal}^k . The impurity concentration in the sample c_{xe}^k can then be evaluated as follows:

$$c_{\text{xe}}^k = A_{\text{xe}}^k \cdot \frac{c_{\text{cal}}^k}{A_{\text{cal}}^k} \quad (3.2)$$

In what follows, the evaluation of the peak areas within a chromatogram, as well as the procedure for calculating the minimal measurable gas concentration (decision threshold), will be explained. Furthermore, the calibration method will be validated at the end of this section.

3.5.1 Calibration Method and Background Subtraction

As mentioned in Section 3.4, the measurement procedure affects the shape of the chromatogram owing to gas flow changes and different background levels in the subsystems of the internal GC configuration. Hence, improved sensitivity is achieved by subtracting the detector baseline, i.e., the background. For this setup, two types of background measurements are considered: one with a sample of the same helium used as carrier gas and one with a clean xenon sample.

The helium background is required because the calibration gas is a mixture of helium and impurities. It is bought commercially and contains impurity concentrations of 5 to 15 ppm for individual gases with uncertainties between 2 and 10%¹¹. However, since this study focuses on the quantification of impurities in xenon samples, a xenon calibration gas mixture would have been more suitable from the viewpoint of excluding any bias from the bulk gas. Nevertheless, it was decided for a helium mixture for cost reasons.

Figure 3.6 left shows a chromatogram of the calibration gas mixture (red) together with the corresponding helium background chromatogram (black) in the upper panel. In the lower panel, the difference between the two chromatograms is plotted. The order of the individual peaks in a calibration measurement is identified by performing tests where only one of the gases contained in the mixture is injected. The time periods where the corresponding impurity peaks are expected are marked in blue. The blue lines in the difference chromatogram in the lower panel in Figure 3.6 left indicate the references to which the peak areas are calculated. The lines are determined by fitting a linear function to the difference chromatogram right and left of the peak, but excluding the peak region itself. In this specific case, the background measurement is aborted after 38 min owing to time constraints. This has no influence on the measurement results because the last analyte CO has passed the detector after 35 min. The figure clarifies that the features of the measurement procedure are very small compared

¹¹See Appendix B for the exact composition of the calibration gas mixture.

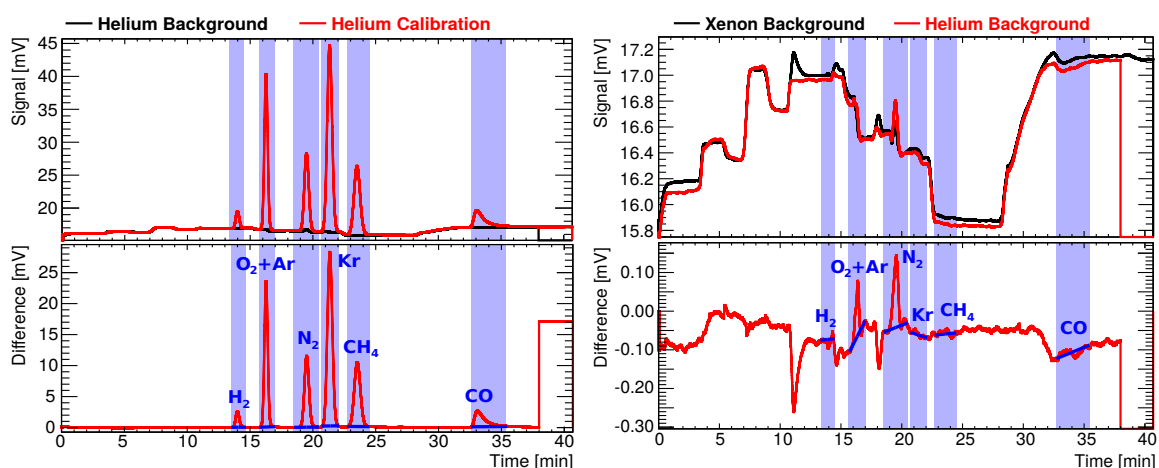


Figure 3.6: **Left:** Example of calibration (red) and corresponding helium background (black) chromatograms (upper panel) and their difference (lower panel). **Right:** Comparison of helium (red) and xenon (black) background chromatograms (upper panel). Their difference is shown in the lower panel. The time regions where gas peaks from impurities are expected are shaded in blue. The blue lines in the difference chromatograms represent the reference used for the evaluation of the peak region. They are constructed by fitting a linear function left and right of the peak, but excluding the peak region itself.

to those of the calibration gas peaks. Consequently, the uncertainty in the calibration is dominated by the uncertainty in the impurity concentrations in the calibration gas mixture. As mentioned before, O_2 and Ar cannot be separated using the configuration employed here. Therefore, their peaks coincide.

A xenon background measurement is required because the features originating from the measurement procedure are slightly different in xenon and helium samples. This can be deduced from Figure 3.6 right, which shows a helium (black) and a xenon background (red) measurement in the upper panel and the difference between the two chromatograms in the lower panel. As for the left plot, the individual peak regions are marked in blue together with the reference lines used for the evaluation of the peak integrals. The regions are adjusted to much smaller expected concentrations than those given by a calibration sample; note the very different scale on the y-axis in both panels compared to the left figure.

The difference shows clear peaks in the O_2+Ar and N_2 regions, indicating the presence of these impurities in the two background samples at different concentrations. Presumably, this is caused by a small diffusive air leak in the sample circuit. Only a diffusive air leak can be present because the sample is always held at over-pressure in the sample circuit. Owing to the density of xenon, which is more than one order of magnitude higher than that of helium, diffusion processes are suppressed in xenon. Hence, the effect of the leak is stronger in helium samples than in xenon samples.

Additionally, xenon differs from helium in terms of a higher resistance when being accelerated. At the time of injection ($t = 10.5$ min), the carrier gas becomes connected to the sample volume and starts flushing the sample out. A pressure gradient between the ~ 1 bar in the sample circuit and the 1.8 bar provided by PRV1 in the carrier gas is present, which

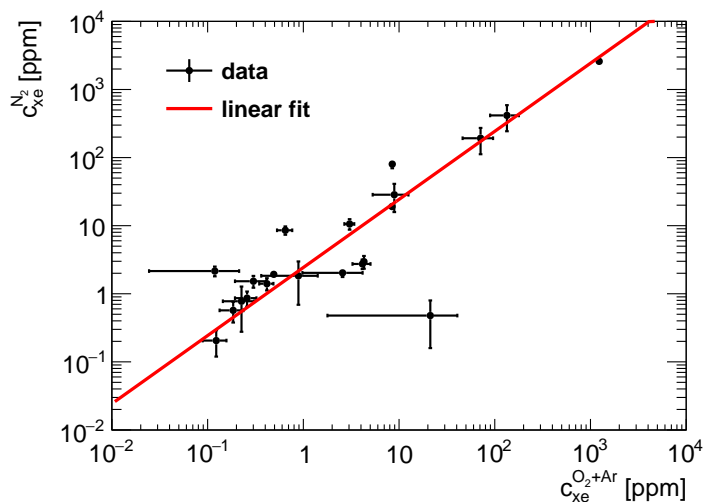


Figure 3.7: Correlation between measured N_2 and O_2+Ar concentrations denoted as $c_{Xe}^{N_2}$ and $c_{Xe}^{O_2+Ar}$. The red line shows the linear fit through the point of origin. Data points that differ from this line contain either oxygen and nitrogen concentrations that do not reflect the ratio in air or are contaminated additionally by argon.

equilibrates on different time scales depending on the sample gas. While the helium background measurement shows an increase in the baseline that levels off on a plateau (between 11 and 14 min), the xenon background shows a higher rise in the detector signal at the time of injection, followed by a decrease toward the same plateau as in the helium measurement (see Figure 3.6 right). This is because of a reduced gas flow through the detector owing to the resistance of the xenon sample, leading to an increase in the detector signal. The same explanation holds for other non-flat features in the difference chromatogram of helium and the background measurements outside of the peak regions.

No dedicated xenon gas is used for the background measurements for cost reasons. Therefore, xenon sample measurements are defined as background if they are purer in O_2+Ar and N_2 than the helium background and if no impurities from H_2 , Kr , CH_4 , and CO are visible.

3.5.2 Re-Calibration of O_2

Because the oxygen and argon gas peaks coincide in the chromatogram, their individual quantification is difficult. Equation (3.2) applies only if the ionization efficiency of the PDD is the same for both gases. However, the following study shows that this is not true. Nevertheless, a quantification of oxygen in the measured xenon is desirable owing to its high impact on the functioning of the XENON1T detector because of its electronegativity, which attenuates the charge signal through electron attachment. Argon, by contrast, is of minor importance because it is chemically inert and the abundance of the radio isotope ^{39}Ar in the atmosphere is about one order of magnitude lower than that of ^{85}Kr [136, 137], which contributes to the background level of XENON1T.

During the measurement campaign, it was found that the amount of N_2 measured in the

xenon samples is correlated to that of the O₂+Ar peak. This can be deduced from Figure 3.7, where the N₂ concentration $c_{\text{xe}}^{\text{N}_2}$ is plotted against the concentration of O₂+Ar $c_{\text{xe}}^{\text{O}_2+\text{Ar}}$. For the evaluation of the concentrations, Equation (3.2) is applied and the O₂+Ar peak is treated as if it was induced by only one impurity, and therefore, the sum of the two gas concentrations in the calibration mixture is used for c_{cal} . This procedure is performed under the assumption that oxygen and argon have the same ionization efficiency in the PDD.

The correlation factor of the data points in Figure 3.7 yields 0.998, which is close to 100% correlation. The most reasonable explanation for this relationship is the common origin of N₂ and O₂+Ar from air leaks. Their respective concentrations in the atmosphere are well known [79] and the ratios $R_{\text{air}}^{\text{O}_2}$ and $R_{\text{air}}^{\text{O}_2+\text{Ar}}$ can be defined as follows:

$$R_{\text{air}}^{\text{O}_2} = \frac{c_{\text{air}}^{\text{N}_2}}{c_{\text{air}}^{\text{O}_2}} = 3.727, \quad (3.3)$$

$$R_{\text{air}}^{\text{O}_2+\text{Ar}} = \frac{c_{\text{air}}^{\text{N}_2}}{(c_{\text{air}}^{\text{O}_2} + c_{\text{air}}^{\text{Ar}})} = 3.569 \quad (3.4)$$

where $c_{\text{air}}^{\text{N}_2}$, $c_{\text{air}}^{\text{O}_2}$, and $c_{\text{air}}^{\text{Ar}}$ are the concentrations of nitrogen, oxygen, and argon in air, respectively.

A linear function through the point of origin (red line in Figure 3.7) is fitted to the data from which the slope K of 2.4 ± 0.2 is retrieved. This value is significantly smaller than that of $R_{\text{air}}^{\text{O}_2+\text{Ar}}$ (3.569). Hence, it can be concluded that oxygen and argon do not have the same detector response, and therefore, $c_{\text{xe}}^{\text{O}_2+\text{Ar}}$ does not reflect the true impurity concentration $c_{\text{xe}}^{\text{O}_2}$ for oxygen due to its calibration under incorrect assumptions.

Assuming that the measured nitrogen concentration $c_{\text{xe}}^{\text{N}_2}$ is equal to $c_{\text{air}}^{\text{N}_2}$, the true oxygen concentration $c_{\text{xe}}^{\text{O}_2}$ present in any sample can be calculated as follows:

$$c_{\text{xe}}^{\text{O}_2} = \frac{K}{R_{\text{air}}^{\text{O}_2}} c_{\text{xe}}^{\text{O}_2+\text{Ar}} \quad (3.5)$$

This relation neglects the $\sim 1\%$ of argon in air and attributes the whole area of the O₂+Ar peak to only oxygen. To account for this negligence the difference between $R_{\text{O}_2}^{\text{air}}$ and $R_{\text{air}}^{\text{O}_2+\text{Ar}}$ is attributed to a systematic uncertainty on $R_{\text{air}}^{\text{O}_2}$, which propagates into an uncertainty related to $c_{\text{xe}}^{\text{O}_2}$.

The same assumption of the presence of only O₂ and no Ar holds when calculating $c_{\text{xe}}^{\text{O}_2}$ in the following. For argon, there is no measure to properly determine its quantity with the current setup and calibration mixture.

3.5.3 Uncertainties

All considered areas of gas peaks are determined from the difference chromatogram obtained by subtracting the background from the sample measurement, as explained above. Each sample is measured two to four times, such that the final impurity concentrations are calculated

as the averages of the individual measurements i . Hence, Equation 3.2 transforms to

$$c_{\text{xe}}^k = \sum_i^n \frac{1}{n} \frac{c_{\text{cal}}^k}{A_{\text{cal}}^k} \cdot A_{\text{xe}}^{k,i}. \quad (3.6)$$

The uncertainty on the evaluated impurity concentration originates from the individual uncertainties on the impurity concentrations in the calibration gas mixture and in the peak areas. In general, statistical fluctuations in c_{xe}^k are at least one order of magnitude smaller than the systematic ones, and are therefore, neglected. However, in some cases, the peak sizes of nitrogen and oxygen varied significantly among individual measurements of the same xenon sample, especially for large O₂ and N₂ contamination of the order of a few ppm. To account for the ignorance about which of the measured values is closest to the true impurity concentration, the uncertainty interval has been conservatively set to range between the smallest and the highest measured concentration.

The phenomenon of inconsistent measurements of the same sample has only been experienced for xenon samples, but never for helium samples. The cause is still under investigation.

Variations in pressure (within 1%) and flow (within 10%) of the sample have no effect on the evaluated impurity quantities.

Further systematic uncertainties pertaining to the peak areas arise from the uninterrupted flushing of the GC setup, leading to continuous improvement in the background level, and therefore, the detection sensitivity. This results in background and calibration measurements taken at slightly different detection sensitivities than the chromatogram of the xenon sample. These systematic errors are fixed values of the peak area, and therefore, dominate at small impurity concentrations close to the decision threshold

Within some periods of constant measurement conditions, a xenon background chromatogram cannot be found among the xenon sample measurements. In this case, a helium background is subtracted instead of the xenon background. The discrepancy in the background measurements of xenon and helium samples is then considered by incorporating an extra systematic uncertainty on A_{xe}^k .

3.5.4 Decision Threshold

The decision threshold for each gas impurity k is defined as the minimal concentration that should be present to exclude a detector baseline fluctuation at a 95% confidence level. The area A_L^k above which a potential peak is recognized as such is determined from the fluctuations in the peak areas in the xenon and helium background chromatograms. Assuming a Gaussian distribution with a mean of zero for the peak area A_i^k of one gas impurity k in a background measurement, A_L^k is given by the value at which the corresponding cumulative distribution function reaches 95%.

Using Equation (3.2), A_L^k is converted into the corresponding gas concentration c_L^k :

$$c_L^k = A_L^k \cdot \frac{c_{\text{cal}}^k}{A_{\text{cal}}^k} \quad (3.7)$$

This evaluation is performed separately for each measurement period because all periods have differences in terms of background stability, detector efficiency, and systematic uncertainties.

3.5.5 Verification of Calibration Method

An important aspect of this study is the verification of the applied calibration method to ensure the quality of the outcome of the measurement campaign.

The usage of a helium mixture to calibrate impurities in xenon samples can influence the results if the separation efficiency between the analytes and the bulk gas is different for helium and xenon samples. This difference can lead to variations in the time taken by the analytes to elute from the pre-separation column and might cause fractions of the impurities to be flushed out of the GC device together with the xenon bulk gas without reaching the detector. This is investigated by mixing xenon samples with known impurity concentrations, referred to as *xenon calibration gases* hereinafter, and measuring them.

The absolute scale of impurity concentrations is verified through a comparison with a mass spectrometry measurement.

Xenon Calibration Gases

For mixing the xenon calibration gas sample, the helium calibration gas is diluted with pure xenon and stored in a stainless-steel sampling cylinder. Two methods are applied to exclude systematic effects on the outcome of the measurements from the mixing itself.

The xenon is led through a hot zirconium getter to remove CH₄, CO, O₂, N₂, and water impurities. The krypton and argon concentrations are stated to be below 50 ppb in the gas certificate, and hence, they are negligible compared to the ppm level present in the helium calibration gas.

The gas denoted as *XeCal1* is produced by filling two connected sampling cylinders with helium calibration gas and adding xenon. Thereafter, one of the cylinders is immersed into a liquid nitrogen bath to store the entire gas mixture in the cylinder through cryogenic pumping. From the gases present in the helium calibration mixture, only helium and hydrogen have lower boiling points than nitrogen. Hence, all impurities but hydrogen are expected to be trapped in the cylinder in the nitrogen bath. From the measured pressures, we determine that the helium calibration gas is diluted by a factor of 5.46 ± 0.03 .

The second xenon calibration gas *XeCal2* is prepared by filling only one sampling cylinder with helium calibration gas and then xenon. Care is taken to prevent the helium gas mixture from leaving the cylinder by always maintaining a xenon pressure higher than that in the sampling vessel. A dilution factor of 4.02 ± 0.02 is achieved.

The uncertainties propagate from the uncertainty in the gas concentrations of the helium calibration gas and a 10% systematic uncertainty in the pressures measured during the mixing procedure.

From the dilution factors, the expected impurities in the two xenon calibration gas mixtures can be determined under the assumption that the gases are mixed homogeneously. We at-

Impurity	expected c_{Xe}^k [ppm]	measured c_{Xe}^k [ppm]	Impurity	expected c_{Xe}^k [ppm]	measured c_{Xe}^k [ppm]
H ₂	0.92 ± 0.04	0.77 ± 0.12	H ₂	1.25 ± 0.05	1.10 ± 0.06
O ₂ +Ar	2.73 ± 0.10	2.57 ± 1.59	O ₂ +Ar	3.72 ± 0.12	4.15 ± 0.89
N ₂	2.09 ± 0.22	2.03 ± 0.27	N ₂	2.84 ± 0.29	2.74 ± 0.44
Kr	2.13 ± 0.06	1.96 ± 0.19	Kr	2.89 ± 0.07	2.91 ± 0.11
CH ₄	0.98 ± 0.03	0.88 ± 0.09	CH ₄	1.32 ± 0.04	1.30 ± 0.04
CO	0.90 ± 0.03	0.78 ± 0.10	CO	1.22 ± 0.03	1.04 ± 0.24

(a) XeCal1

(b) XeCal2

Table 3.1: List of impurity concentrations in the two mixed xenon calibration gases XeCal1 (left) and XeCal2 (right), as expected from the mixing procedure and as measured by the GC setup described in this chapter. See text for more explanation.

tempted to achieve this by moving the sampling cylinders mechanically. The expected gas concentrations are given in Table 3.1 in the second column, and the values measured using the GC setup are given in the third column.

Most of the measured concentrations agree with the expected values within the uncertainties. Exceptions are the values of hydrogen in both gas mixtures, where 0.92 ± 0.04 ppm and 1.25 ± 0.05 ppm are the expected values, while 0.77 ± 0.12 ppm and 1.10 ± 0.06 ppm are the measured ones, respectively. The deviations in the measurements are -1.25σ and -2.5σ . Two explanations are possible. The separation efficiency of xenon and hydrogen may not be 100%, and fractions of the impurities do not reach the main column before its separation from the pre-separation column by actuating V2 at $t = 16$ min (see Section 3.4). Another explanation could be the loss of hydrogen during the mixing procedure owing to its high volatility. Which of the two hypotheses is true cannot be deduced from the data. We should consider that the evaluated hydrogen concentrations are about 15% lower than their true values. However, this is not a major drawback for the XENON1T experiment since a 15% uncertainty does not play a role for the detector operation. Hydrogen is efficiently removed by the two getters in the purification system.

Furthermore, the measurement results are systematically between 2% and 15% lower than the expectation. This holds for all impurities, except for O₂+Ar and Kr in XeCal2. The two explanations from above hold here as well: either a reduced separation efficiency or a bias from the mixing procedure could be present.

The data given in Table 3.1 allow us to conclude that the separation efficiencies of the helium and xenon samples differ by no more than about 15%. This is within the overall uncertainty of the measured impurity concentrations and justifies the use of the helium calibration gas.

Comparison with Mass Spectrometry Measurement

The absolute numbers of the measured impurity concentrations can be validated by comparing the results to the outcome of a mass spectrometry measurement. This is done for krypton impurities.

The deployed mass spectrometer is a rare gas mass spectrometer (RGMS) operated in combination with a custom-built gas chromatography setup. In this setup, gas chromatography is used to separate krypton from xenon. The extracted krypton is then led into the mass spectrometer, where the number of krypton atoms is determined. This combined setup can quantify krypton concentrations below 1 ppt with a precision of around 20%. Details about this setup and its performance can be found in [118].

A xenon sample was drawn from the gas cylinder *D337602* that contained 12 kg of xenon recuperated from the XENON1T cryostat. The GC measurement took place on April 15th, 2016, at LNGS. Another gas sample was filled into a pipette on July 18th, 2016, and was shipped to MPIK¹² in Heidelberg for the RGMS measurement.

The krypton concentrations evaluated using the two setups are as follows:

$$(0.019 \pm 0.001) \text{ ppm} \quad (\text{GC}) \quad \text{and} \\ (0.022 \pm 0.003) \text{ ppm} \quad (\text{RGMS}).$$

They are in very good agreement within the uncertainties, confirming that the absolute value of the krypton concentration determined by the GC is calibrated with sufficient precision by the applied method. This conclusion is expected to hold for the other gas impurities as well because they are evaluated using the same calibration method.

3.6 Results

The novel storage vessel ReStoX was commissioned and tested for the first time with xenon in 2015. The gas was transferred from the cylinders to the vessel in several intermediate steps to avoid risking losses or contamination. Hence, multiple measurement campaigns were performed using the GC with breaks, during which the device was shut down. This led to slight differences in the measurement conditions across individual campaigns.

All measurements of the XENON1T xenon inventory are listed in Table 3.2. The measurement periods indicated in the first column combine all results for which the same detector parameters apply. The analysis described in Section 3.5, is performed separately for each period.

The second column lists the gas cylinder IDs from which the xenon samples are extracted. If several IDs are given and separated by a “/”, the samples taken are mixed and the impurities in the mixture are quantified. The time required for the entire measurement and filling procedure, including sufficient time for pumping and baking of gas lines, allowed us to transfer the xenon from a maximum of eight cylinders to ReStoX per day. Each cylinder contains between 35 kg and 55 kg of xenon.

A few cylinders were refilled with gas from ReStoX when additional maintenance was necessary, gas processed by the distillation column, gas recuperated from the cryostat, or gas from another supplier (supplier 2). Which of the cases applies is stated in the third column of Table 3.2 as a remark. Hence, the combination of the cylinder IDs and the remark serves as a unique identifier of the measured samples.

The measurements of the samples *8673499 / 8984026 / 10092191 / APE856030H (original)*,

¹²Max-Planck-Institut für Kernphysik

ADPGXNH-1906661 / ADP65UF-859514 (original), and *ReStoX gas phase* were previously presented in [127]. The corresponding results are re-evaluated in this study by using the deeper understanding gained by analyzing the measurement data of the entire xenon inventory.

The results of the O₂ concentrations are evaluated by applying the re-calibration procedure described in Section 3.5.2. The values are determined under the assumption that only oxygen but no argon impurities are present in the sample. For reference, the values, calibrated by ignoring the different detector responses for O₂ and Ar, are listed in the last column of Table 3.2.

If the measured value is smaller than the decision threshold c_L^k , the threshold is taken as an upper limit. Typical decision thresholds are of the order of 0.01 ppm for Kr and 0.2–0.3 ppm for CO or N₂, and vary across impurity types and measurement periods. When no value is presented, the impurity in question could not be quantified in any of the measurements. This is primarily the case for CO, when several xenon measurements are taken in a short period with insufficient cleaning time for the main column in between two measurements. The result may be increased outgassing from the column when it is heated up during the measurement procedure. This effect coincides with the time in the chromatogram where the CO gas peak is expected, and hence, a quantification is not possible. Other reasons for not being able to determine the impurity concentrations in a xenon sample are anomalous peaks in the chromatogram that are clearly correlated to feedback effects of valve operations at the analytics section of the bottle rack (see Figure 3.2).

Red entries mark cases where the outcome of the individual measurements of the same sample was inconsistent. This means that a precise quantification of the corresponding impurities is not possible. Nevertheless, the mean concentration is given, but an asymmetric conservative uncertainty was defined, as stated in Section 3.5.3. The uncertainty interval ranges between the lowest and the highest measured concentration.

Rows marked in blue in Table 3.2 show the results where the determined impurity concentrations are not compatible with the purity requirements of the experiment for the initial xenon filling. An example is given by the sample *ADP660E-1935825 (original) (1039741 (original))*, where oxygen (nitrogen) concentrations above 70 ppm (130 ppm) and 190 ppm (400 ppm) are measured, respectively. Special attention was given to krypton impurities higher than 0.1 ppm, as in the case of the sample *D337586 / D337587 (original)*, where a concentration of (0.29 ± 0.04) ppm is determined. The xenon gas with low purity is not filled into ReStoX but processed by the distillation column and then fed directly into ReStoX.

The results in Table 3.2 will be discussed further in the following sections and will serve to predict the total impurity concentration in the xenon inventory, as well as to validate the cleanliness of the transfer procedure of xenon from the gas cylinders into ReStoX.

Period	Cylinder ID	Remark	Date	H ₂ [ppm]	O ₂ [ppm]	N ₂ [ppm]	Kr [ppm]	CH ₄ [ppm]	CO [ppm]	O ₂ +Ar [ppm]
A	215 / 214 / 8673103 / 8673115	original	2015-03-26	0.20 ± 0.06	14.4 ± 14.3	0.5 ± 0.3	< 0.06	< 0.2	< 0.1	21 ± 19
	208 / 209	original	2015-04-28	0.04 ± 0.01	0.13 ± 0.05	0.6 ± 0.2	< 0.02	< 0.02	< 0.06	0.19 ± 0.05
	8673492 / 8673498	original	2015-04-29	0.02 ± 0.01	0.15 ± 0.07	0.8 ± 0.5	< 0.02	< 0.02	< 0.06	0.23 ± 0.08
B	D337603 / D337604	from ReStoX	2015-07-20	< 0.25	< 0.33	2.1 ± 1.0	< 0.04	< 0.04	< 0.15	< 0.5
	D337602	from ReStoX	2015-07-22	0.12 ± 0.04	0.2 ± 0.1	1.5 ± 0.3	< 0.08	< 0.25	< 0.25	0.3 ± 0.1
D	215	from ReStoX	2015-07-22	0.09 ± 0.03	< 0.07	1.0 ± 0.2	< 0.08	< 0.02	—	0.10
	56	from ReStoX	2015-07-24	0.14 ± 0.03	0.08 ± 0.07	2.2 ± 0.4	< 0.15	< 0.75	< 0.75	0.12 ± 0.09
	214 / 229	from ReStoX	2015-07-25	< 0.075	< 0.07	1.7 ± 0.3	< 0.08	< 0.13	< 0.25	< 0.10
	122 / 123 / 120 / 115	original	2015-07-26	< 0.08	< 0.07	0.7 ± 0.4	< 0.01	< 0.25	< 0.70	< 0.10
	138	original	2015-07-27	< 0.05	0.03 ± 0.03	0.16 (+0.13) (-0.11)	< 0.045	< 0.13	< 0.25	0.025 ± 0.025
E	113 / 114 / 217 / 121	original	2015-07-28	< 0.075	0.44 ± 0.13	8.6 ± 1.2	< 0.01	< 0.25	< 0.70	0.65 ± 0.12
	T8467077 / T8459018 / T8467174 / T8466192	original	2015-08-26	< 0.12	< 0.02	< 0.25	< 0.025	< 0.45	< 0.45	< 0.1
	LK433536 / LK107988 / LK232483 / LK114132	original	2015-08-26	< 0.06	< 0.02	< 0.06	0.03 ± 0.02	< 0.04	< 0.4	0.10
	LK114132	original	2015-08-27	< 0.08	< 0.02	< 0.06	0.04 ± 0.01	< 0.03	< 0.36	< 0.09
	T421230 / T427548 / LK77062 / LK50936	original	2015-08-27	< 0.06	< 0.02	< 0.23	< 0.025	< 0.03	< 0.36	< 0.09
	T421230 / T427548	original	2015-08-27	< 0.06	< 0.02	< 0.23	< 0.025	< 0.03	< 0.36	< 0.09
	D198154	original	2015-08-28	< 0.06	< 0.02	< 0.17	< 0.02	< 0.35	< 0.36	< 0.09
	LK408021 / ND28905 / ND28922	original	2015-08-29	0.15 ± 0.12	< 0.02	< 0.05	< 0.02	< 0.03	< 0.31	< 0.09
	D817169 / D817170	original	2015-08-30	< 0.10	< 0.02	0.4 ± 0.3	< 0.025	< 0.35	< 0.27	< 0.09
	RG482124 / RG479017	original	2015-08-31	< 0.10	< 0.02	< 0.3 ± 0.2	< 0.025	< 0.35	< 0.27	< 0.09
	8673499 / 8984026 / 10092191 / APE856030H	original	2015-09-01	< 0.10	< 0.02	< 0.055	< 0.01	< 0.03	—	< 0.145
	8673499	original	2015-09-02	< 0.08	< 0.02	0.5 ± 0.2	0.34 ± 0.04	< 0.03	< 0.27	< 0.145
	502668 / 1219803	original	2015-09-02	< 0.10	< 0.02	0.9 ± 0.3	< 0.02	< 0.04	< 0.27	< 0.145
	2110426	original	2015-09-03	< 0.055	5.8 ± 0.8	19.1 ± 2.2	0.08 ± 0.01	< 0.03	< 0.27	8.5 ± 0.3
LK77062	original	2015-09-04	0.18 ± 0.07	1.0 (+1.0) (-0.7)	4.1 (+5.3) (-2.8)	< 0.15	< 0.04	< 0.27	1.4 (+1.5) (-1.0)	
1523717	original	2015-09-05	< 0.055	< 0.02	0.4 ± 0.2	< 0.02	< 0.03	< 0.26	< 0.145	
1219803 / 502668	original	2015-09-05	0.12 ± 0.06	6.1 (+1.5) (-1.7)	29 (+7) (-7)	< 0.01	< 0.03	< 0.26	8.9 (+2.4) (-2.4)	
ADPGXNH-1906661 / ADP65UF-859514	original	2015-09-06	< 0.065	0.6 ± 0.4	1.8 ± 1.1	0.08 ± 0.01	< 0.03	< 0.26	0.9 ± 0.5	
F	121 / 217	supplier 2	2015-11-17	< 0.05	7.2 (+8.5) (-5.5)	32 (+36) (-24)	0.04 ± 0.02	< 0.03	< 0.26	11 (+12) (-8)
	229	supplier 2	2015-11-17	< 0.05	0.07 ± 0.03	< 0.12	< 0.01	< 0.02	< 0.13	0.10 ± 0.03
	209	supplier 2	2015-11-18	< 0.05	1.2 ± 0.2	< 0.12	< 0.01	< 0.02	< 0.12	1.8 ± 0.1
	215	supplier 2	2015-11-18	< 0.045	< 0.03	< 0.12	< 0.01	< 0.02	< 0.045	< 0.045
	215 / 115 / 120 / D337604	supplier 2	2015-11-18	< 0.045	0.12 ± 0.02	< 0.12	< 0.01	< 0.02	< 0.12	0.17 ± 0.03
G	123 / 114 / 208 / D337603	supplier 2	2015-11-22	< 0.04	0.45 ± 0.15	< 0.25	< 0.015	< 0.02	< 0.12	0.66 ± 0.15
	D337602 / 138 / 122 / 113	supplier 2	2015-11-23	< 0.04	0.35 ± 0.11	< 0.24	< 0.015	< 0.02	< 0.15	0.52 ± 0.10
	10224033 / 10224061 / 10224019 / 10224049	original	2015-11-25	< 0.05	0.33 ± 0.05	2.0 ± 0.2	< 0.005	< 0.02	—	0.49 ± 0.02
	10224049	original	2015-11-25	< 0.05	0.08 ± 0.03	0.21 ± 0.09	0.005 ± 0.003	< 0.02	—	0.12 ± 0.03
	10223991 / 10224066	original	2015-11-25	< 0.05	< 0.01	< 0.19	0.005 ± 0.001	< 0.02	—	< 0.02
H	D337586 / D337587	original	2015-11-26	0.09 ± 0.04	0.18 ± 0.06	0.9 ± 0.2	0.29 ± 0.04	< 0.019	< 0.09	0.26 ± 0.07
	D300582 / D300583	original	2015-11-26	< 0.06	< 0.05	< 0.26	1.0 ± 0.2	< 0.02	< 0.09	< 0.07
	T7607154	original	2015-11-27	< 0.06	< 0.05	< 0.19	0.05 ± 0.03	< 0.02	< 0.09	< 0.07
	D300581 / D330699	original	2015-11-27	< 0.05	2.1 ± 0.5	10.6 ± 1.9	1.9 ± 0.2	0.04 ± 0.03	—	3.0 ± 0.4
	2444352	original	2015-11-28	< 0.075	0.28 ± 0.08	1.4 ± 0.3	< 0.03	< 0.02	—	0.42 ± 0.07
I	D198154	original	2015-11-28	< 0.045	0.09 (+0.16) (-0.08)	0.4 (+0.6) (-0.3)	< 0.03	< 0.02	< 0.09	0.13 (+0.23) (-0.11)
	1039741	original	2015-11-28	0.17 ± 0.06	91 ± 40	420 ± 170	—	< 0.025	—	130 ± 50
	ADP660E-1935825	original	2015-11-28	< 0.065	48 ± 22	190 ± 80	0.05 ± 0.04	< 0.02	—	71 ± 25
	ReStoX gas phase	original	2016-01-08	0.4 ± 0.2	3.0 ± 0.5	3.0 ± 0.6	0.05 ± 0.03	< 0.05	< 1.12	4.3 ± 0.3
J	D198154	air leak after distillation	2016-01-09	—	840 ± 120	2600 ± 300	—	—	—	1230 ± 40
	D337587	distilled xenon	2016-04-15	< 0.045	< 0.04	< 0.20	< 0.01	< 0.06	< 0.06	< 0.06
	D337602	recuperated from Cryostat	2016-04-15	< 0.045	5.8 ± 0.9	80 ± 10	0.022 ± 0.001	< 0.005	—	8.5 ± 0.5

Table 3.2: Results of all gas impurity measurements performed on the XENON1T xenon inventory prior to filling the gas into ReStoX. If the evaluated concentration did not exceed the 95% decision threshold c_L^k , the threshold is given as an upper limit. Blue rows mark samples where impurities were incompatible with the purity requirements of the experiment. Red entries show results where the results of individual measurements of the same sample were inconsistent. See text for more explanations.

3.6.1 Total Impurities in the Xenon Inventory

This measurement campaign aimed to control the impurity level in the xenon gas filled into the XENON1T gas system by identifying and rejecting the gas cylinders that contain impurity levels beyond the specifications. By discussing the total impurities in the entire xenon inventory, we will show that this goal was achieved and that the purification subsystems of XENON1T can further purify the gas to reach the purity levels required for the experiment.

Combination of Inventory Measurements

	H₂	O₂	N₂	Kr	CH₄	CO
lower limit [ppm]	0.009	0.15	0.8	0.003	0.00	0.00
upper limit [ppm]	0.07	0.9	3.9	0.04	0.02	0.2

Table 3.3: Expectation of impurity concentrations in the entire XENON1T xenon inventory. The values were determined from the combination of all gas bottle measurements listed in Table 3.2

Combining all of the measurements from Table 3.2 and taking into account the xenon mass in each cylinder, the impurity concentrations in the entire XENON1T xenon inventory can be inferred. Hereby, concentrations below the decision threshold had to be combined with measured values with corresponding uncertainties. Hence, the outcome are intervals that are expected to include the true impurity concentrations of the xenon inventory. The results are shown in Table 3.3.

H₂, O₂, N₂, CH₄, and CO are removed by the two hot getters in the XENON1T gas system. The getters ensures a purity level of < 1 ppb in terms of these gases, provided that the inlet gas has a total purity of 99.9995% or higher [123], that is, impurity concentrations lower than 5 ppm. According to the estimates in Table 3.3, the upper limit of the total concentration of the gases that can be removed by the getters from the entire xenon inventory is 5.1 ppm, and matches the purity specifications of the device. Hence, the experimental requirement of being able to reduce the concentrations of these gases to negligible levels is met.

Krypton impurities can be removed by cryogenic distillation. The distillation column used in the XENON1T experiment has a reduction factor of $F_{\text{red}} = (6.4^{+1.9}_{-1.4}) \cdot 10^5$ [125]. The experimental requirement in terms of the final krypton concentration in the detector is 0.2 ppt in order to achieve the target background level, and hence, the target sensitivity [108]. Given an upper limit of the krypton concentration in the xenon inventory of 47 ppb, it can be reduced to less than 1 ppt by processing the full inventory of 3.67 tons with the distillation column. This is close to the specification of the XENON1T experiment, such that the ER background is not dominated by ⁸⁵Kr but by ²²²Rn [108].

The reduction can be achieved within 3 weeks by operating the distillation column at the maximum gas flow rates. As an alternative, the distillation of xenon gas from the detector in parallel to a fully operational TPC was successfully tried. About 7% of the purification gas flow was directed through the column. This so-called online distillation mode provides the advantage that data acquisition does not have to be interrupted. Within 70 days, the krypton

concentration is reduced from about 60 ppb¹³ to (0.36 ± 0.06) ppt.

ReStoX Gas Phase Measurement

To cross check the impurity concentrations listed in Table 3.3, a sample was taken from the gas phase of the 3.67 tons of xenon stored in ReStoX. In contrast to the overcritical state of the xenon gas in the gas bottles, a separation between gas and liquid phases is possible in ReStoX owing to the low pressure of 1 bar and the low temperature of -108°C (xenon boiling temperature). The results yield the following concentrations: (0.4 ± 0.2) ppm for H_2 , (3.0 ± 0.5) ppm for O_2 , (3.0 ± 0.6) ppm for N_2 , (0.05 ± 0.03) ppm for Kr, < 0.05 ppm for CH_4 , and < 1.12 ppm for CO.

All values are on the upper edges of the concentration intervals given in Table 3.3 or above the upper edges. This can be explained by the lower boiling points of the impurity gases compared to that of xenon, which leads to their accumulation in the gas phase. A measure of the separation of components in a mixture owing to their different boiling points is the relative volatility α . It compares the saturation vapor pressures p^a and p^b of the components a and b at a given temperature T and is defined as follows:

$$\alpha(T) = \frac{p^a(T)}{p^b(T)} \quad (3.8)$$

Furthermore, for an ideal mixture, Raoult's law can be applied, which states that the partial vapor pressure p_{mixture}^k of each component k can be calculated by multiplying the vapor pressure of the pure component p_{pure}^k by its mole fraction c_{mixture}^k in the mixture:

$$p_{\text{mixture}}^k = p_{\text{pure}}^k \cdot c_{\text{mixture}}^k \quad (3.9)$$

Combining this with Dalton's law, which states that the total pressure p_{total} in a gas mixture is the sum of the partial pressures of all components, the following expression can be derived:

$$\frac{c_{\text{gas}}^k}{c_{\text{liquid}}^k} = \frac{p_{\text{pure}}^k}{p_{\text{total}}} = \alpha. \quad (3.10)$$

Hence, knowing the pressure of the ReStoX gas phase (~ 1 bar), the vapor pressure of krypton at the given boiling temperature of xenon (12.77 bar), and the measured krypton concentration in the gas phase, the krypton concentration in the liquid phase can be determined as follows:

$$c_{\text{liquid}}^{\text{Kr}} = (3.9 \pm 3.0) \text{ ppb}. \quad (3.11)$$

The uncertainty originates from the uncertainty in the measured krypton concentration in the ReStoX gas phase. The uncertainties in pressure and temperature are negligible.

This krypton concentration for the entire xenon inventory, derived from a measurement of

¹³This value should not be compared to the upper limit of krypton concentration of 47 ppb. The upper limit does not account for the outgassing of detector materials, which leads to an increase in the krypton content in xenon as soon as it is filled into the cryostat.

the gas phase, is compatible with the concentration estimated by combining all individual gas cylinder measurements, as given in Table 3.3. It is closer to the lower boundary of 0.003 ppm of the estimated interval. This emphasizes the success of controlling the impurities in xenon during the filling campaign.

A quantification of the concentrations of the other gases, namely H₂, O₂, and N₂, in the liquid is not possible from the gas phase measurement because they are overcritical at the vapor temperature of xenon. Therefore, only qualitative statements can be derived from the gas phase measurement for these impurities. The concentrations of N₂, CH₄, and CO measured in the ReStoX gas phase are in agreement with the expectations listed in Table 3.3. However, about six and three times higher concentrations than the corresponding upper limits are evaluated for H₂ and O₂, respectively. This can partly be attributed to the accumulation of these gases in the gas phase, as mentioned above. Another reason could be outgassing from the metal surfaces of ReStoX, where the electro-polishing procedure¹⁴ results, especially, in an increase in the hydrogen contamination.

3.6.2 Validation of Gas Handling Procedures

At the beginning of the filling campaign, about 280 kg of xenon gas was filled into ReStoX and then recuperated into the gas cylinders owing to additional maintenance work on ReStoX. Therefore, the gas has been measured another time before its second transfer to the storage vessel. This provides the means to validate the cleanliness of the filling and the recuperation procedure. The measurements from period A and from the sample 8673492 / 8673498 (*original*) in period B are compared to the results obtained using the cylinders marked “*from ReStoX*” in periods C and D (see Table 3.2). As for the evaluation of the overall impurities in the entire xenon inventory, the corresponding impurity concentrations are combined into one result, which is given in Table 3.4. As in the previous section, the limits of the intervals are thought of as conservative estimates considering the dominating systematic uncertainties.

	H ₂	O ₂	N ₂	Kr	CH ₄	CO
Original						
lower limit [ppm]	0.09	0.03	0.20	0.00	0.00	0.00
upper limit [ppm]	0.17	18.0	1.0	0.04	0.12	0.09
Recuperation						
lower limit [ppm]	0.04	0.02	1.3	0.0	0.00	0.00
upper limit [ppm]	0.15	0.14	2.2	0.06	0.13	0.30

Table 3.4: Comparison of impurity concentration intervals measured in original gas cylinders and after recuperation of the same gas from ReStoX

A good agreement is observed for all gases, except for N₂ where a higher concentration is observed in the recuperated gas. The most plausible explanation is that some air was introduced during the transfer and recuperation process by outgassing or by small diffusive leaks.

¹⁴During electro-polishing, the metal is immersed into an electrolyte containing concentrated acid solutions. A strong voltage is applied between the metal and an additional cathode, resulting in a current. The metal surface is oxidized, and at the cathode, hydrogen is produced via a reduction reaction.

However, the values remain within the same order of magnitude. The non-observation of this increase in the oxygen concentration may be due to the relatively large interval of the O₂ concentration in the original gas, which is driven by the measurement of the sample 215 / 214 / 8673103 / 8673115 (*original*), where the calibration measurement for this impurity failed. Furthermore, a relatively high decision threshold for the determination of the concentration in the recuperated gas is in play, resulting in small lower limits because a value of zero is added in cases of the samples for which the decision threshold is not exceeded.

As mentioned above, the getters in the XENON1T gas system can provide a purity level of < 1 ppb given that the inlet gas has a total purity of 5 ppm. Hence, this increase in nitrogen concentration is not worrisome from the experimental viewpoint.

An increased H₂ concentration is not observed after recuperation, as is expected based on the result of the ReStoX gas phase measurement discussed in the previous section. This is attributed to the fact that in this case, the concentration is determined for the entire xenon content of the cylinders (xenon is overcritical at room temperature) and not only for the gas phase where hydrogen could have accumulated. Furthermore, the gas is retrieved from ReStoX by cryogenic pumping using a liquid nitrogen bath. However, the boiling temperature of hydrogen is lower than that of nitrogen, making the recuperation process inefficient for hydrogen.

This study shows that the applied filling and recuperation procedures do not have a significant impact on the purity of xenon gas and that ReStoX was properly baked and pumped before it was filled. The results provide further evidence that the impurity concentrations of the xenon inventory evaluated from the individual measurements of the cylinders do apply after the transfer processes as well.

3.7 Summary and Outlook

This chapter introduced a procedure to ensure the gas purity of the xenon inventory in the XENON1T experiment before the initial filling into the storage vessel ReStoX.

An interface, the XENON1T bottle rack, was designed to connect the gas cylinders from the suppliers to draw samples for purity measurements and to transfer the gas from the XENON1T purification system to ReStoX. Care was taken during the design to facilitate the handling of four cylinders in parallel to save time. The cleanliness of the gas handling procedures performed with the bottle rack was verified by finding no significant decrease in the purity of xenon filled to ReStoX, and subsequently, retrieved into the gas cylinders.

The gas chromatography technique was selected for determining the contaminants. The measurement procedure was optimized to be fast and to have good sensitivity for krypton, a direct internal background component in the dark matter search. Very good sensitivities of 20 ppb for krypton and 0.1 ppm for nitrogen were achieved.

An important part of the quantification of impurity concentrations in a sample is the calibration of the measurement procedure. A helium gas mixture was used and the impurity concentrations were specified by the supplier. It was shown in Section 3.5.5 that for krypton impurities, the calibration performed using this mixture yielded results compatible with the measurements made using a mass spectrometer. Furthermore, we validated that the anticipated impurity concentrations can be retrieved in a self-mixed xenon sample within the

uncertainties and that no significant bias is expected due to the calibration with a helium mixture while measuring xenon samples.

The measurement procedure only allows us to measure oxygen and argon impurities as a combination, and therefore, an accurate quantification is difficult. A method was developed to calibrate the detector response to oxygen by correlating the results of O₂+Ar with the measured N₂ concentrations in Section 3.5.2.

During the measurement campaign, contaminated xenon gas was identified and purified by distillation before mixing it with the rest inventory. All measurements performed on the gas cylinders can be combined to infer the overall impurities in the XENON1T xenon inventory (see Section 3.6.1). Of special interest for the functioning of the experiment is the concentration of krypton, which is expected to range between 3 ppb and 40 ppb, and that of oxygen, which is expected to range between 150 ppb and 900 ppb.

The result for krypton, a background source in the experiment, was cross-checked with a measurement of the gas phase of the entire inventory, from which the krypton concentration in the liquid can be inferred. It yielded (0.05 ± 0.03) ppm, which is in good agreement with the estimation from the individual sample measurements.

Below ppt krypton concentrations could be achieved for the entire xenon inventory by redirecting about 7% of the XENON1T gas purification stream to the distillation column while continuously acquiring scientific data using a fully operational TPC. This online distillation allowed us to reduce the ⁸⁵Kr-induced background to a level negligible with respect to the ²²²Rn background [53].

Oxygen impurities in xenon directly impact the electron lifetime, and hence, the threshold and resolution of the charge signal (S2). Figure 3.8 shows the evolution of the electron lifetime from the initial detector filling until the time of writing. An overall rising trend is visible, while changes in the purification flow and cooling power of the pulse tube refrigerator lead to a decrease in purity in the short term.

A model has been developed that considers the outgassing rate from the detector materials and the purification efficiency. The best fit of the model to the data is shown by the red solid line. It yields an initial O₂ concentration of 48^{+34}_{-31} ppb [65]. This quantity is slightly lower than the lower limit of 150 ppb evaluated by combining the measurements performed using the gas cylinders. However, a direct comparison of the absolute values is difficult because purification measures such as the distillation of the ReStoX gas phase and the gas transfer via the two getters during detector filling compete with the outgassing from all materials in the XENON1T cryostat as well as in the gas system. Instead, a confirmation of this work of impurity control in the xenon inventory is given by the fact that the expected O₂ concentration and the value determined by the fit of the electron lifetime evolution are of the same order of magnitude.

The regimes of almost linear increases of the electron lifetime are dominated by the competing processes of purification and outgassing from detector materials. The regions of exponential growth show the efficient removal of intrinsic oxygen that is not continuously reproduced by outgassing. The linear regime is reached about two months after the detector filling, and hence, the initial oxygen contamination was successfully ensured to be sufficiently low by the presented purity measurements, such that the oxygen could be removed within that time. Nevertheless, the commissioning phase was set to about six months owing

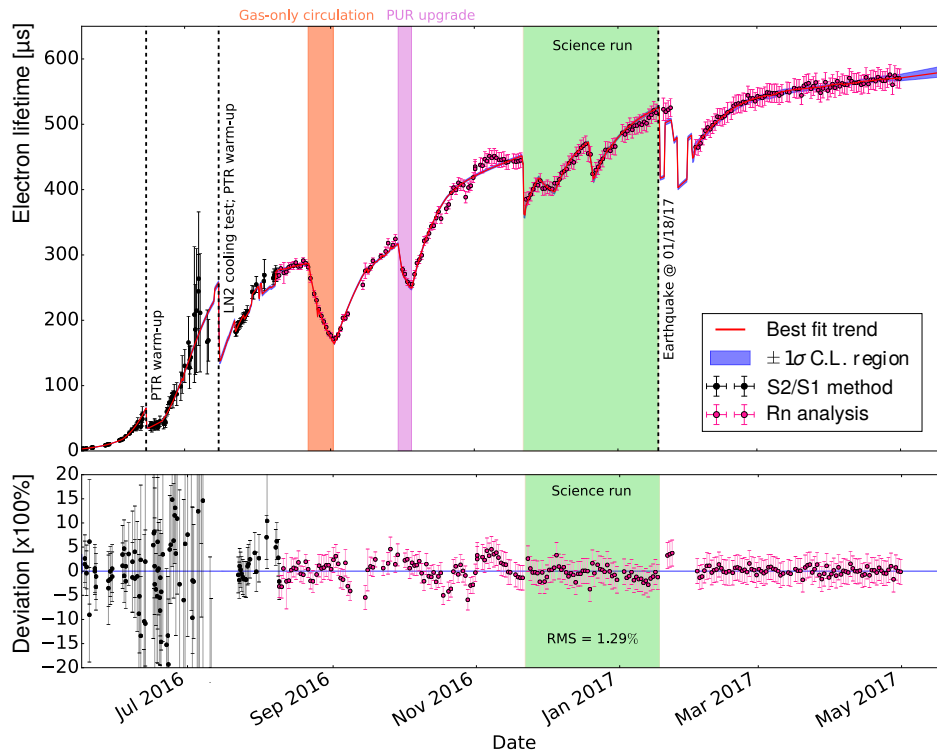


Figure 3.8: Electron-lifetime evolution in the XENON1T detector from initial filling of the detector beyond the first scientific run (green region). The electron lifetime provides a measure of the oxygen concentration in the detector, and from its evolution over time, the purification efficiency can be inferred. An overall increasing trend is visible, while changes in the purification flow and cooling power of the pulse tube refrigerators lead to purity decreases in the short term. The linear regimes mark time periods where the purification process competes with the outgassing of detector materials. During the times of exponential increases, the intrinsic oxygen impurities that are not continuously reproduced by outgassing are efficiently removed. The data is well described by the model shown by the red solid line. The deviations (see lower panel) are below 20% at the beginning and below 5% under more stable detector conditions. Figure from [65]

to the outgassing and the time needed for understanding and testing the detector features.

The commissioning phase was followed by the first scientific run of the XENON1T experiment, where the most constraining upper limit on the spin-independent WIMP-nucleon interactions for masses above 10 GeV could be set. The corresponding analysis is presented in Chapter 5.

Chapter 4

Calibration of the Background Region

Even though various measures are taken to suppress the background in dark matter search experiments, it is crucial to model the remaining signals induced by natural and cosmic radioactivity. By comparing the background prediction to the measured data, either a dark matter signal can be identified by an excess in the data or a constraint on the number of potential WIMP interactions among the background events can be set.

In the XENON experiments, the dominating background comes from natural gamma and beta radiation that induces electronic recoils (ER). As explained in Chapter 2, the charge-to-light signal ratio in liquid xenon (LXe) is higher for ER than for nuclear recoils (NR) due to their different track geometry. This difference provides a measure to discriminate between the two interaction types. Nevertheless, the ER region, i.e. the background region, overlaps with the nuclear recoil region, i.e. the signal region. Hence, statistical leakage of ER into the signal region can mimic WIMP interactions and has to be predicted in order to prevent a false discovery.

While in the XENON100 experiment external radioactive sources could be employed for the calibration of ER, the significantly larger size of the XENON1T detector does not allow an efficient ER calibration of the innermost target volume with external sources. A solution is provided by radioactive isotopes that can be dissolved in the xenon. This chapter is devoted to the study of two of these so-called internal sources, namely ^{220}Rn and tritium.

After an introduction to the source characteristics in Section 4.1 and the outline of the applied event selection criteria in Section 4.2, the ^{220}Rn and tritium sources are compared in Section 4.3 with respect to the injection efficiency of their activity into the sensitive volume. The spectral and spatial distributions of the respective ER calibration datasets are presented in Section 4.4. In Section 4.5, the shape of the calibrated ER background region (ER band) is investigated for the two sources and potential causes for shape variations are studied. In Section 4.6, the impact of the choice of the ER calibration source on the discrimination between ER and NR and therefore on the outcome of a dark matter search, is studied. Finally, the discrimination power is compared between the detectors XENON100 and XENON1T in Section 4.7. The chapter concludes with a summary and discussion of the results, in Section 4.8.

4.1 Calibration Source Characteristics

The XENON100 detector was small enough such that the radiation from external sources could penetrate the whole detector and induce low energetic single scatter events, as expected from WIMPs, with sufficient rate in all regions of the detector. However, the high stopping power of liquid xenon (LXe) which is beneficial for background reduction, is obstructive for the calibration of the fiducial volume (FV) within a multi-ton scale detector like XENON1T. Hence, internal calibration sources were investigated.

The challenge when employing internal sources, is to ensure a good mixture inside the FV but also the decrease of the ER event rate to background level within a reasonable time period after the deployment. In this context, calibration tests have been performed with the XENON100 detector in its last run in 2016.

For all dark matter results published by the XENON100 experiment, the gamma emitters ^{60}Co and ^{232}Th were used to calibrate the ER background. The sources were brought close to the cryostat by positioning them in a copper tube that is twine around the cryostat and is accessible from outside the passive shield (see Section 2.6). This calibration pipe is depicted in Figure 4.4 and is vertically adjusted to the TPC center allowing the sources to be placed at all azimuthal angles.

^{232}Th is the mother nuclide of a long decay chain that emits gammas with a variety of energies up to 2.6 MeV. In contrast, ^{60}Co undergoes a beta decay to ^{60}Ni which is left in an excited state and de-excites by emitting two photons with the energies 1.17 MeV and 1.33 MeV. For the calibration of the detector response to low energetic ER, only the low energy Compton interactions are of importance.

Three internal sources were deployed in XENON100 during the calibration test run: $^{83\text{m}}\text{Kr}$, ^{220}Rn , and tritium (^3H). $^{83\text{m}}\text{Kr}$ provides two energy lines at 9.4 keV and 32.1 keV that are primarily used for monitoring parameters like the S1 and S2 yields over time for detector stability. Furthermore, the distinct energy depositions serve for the determination of spatial dependencies of the signals (see Chapter 2) and the evaluation of the corresponding correction maps. For studies of the separation of the ER from the NR region (discrimination) in the WIMP energy range, however, a lower energetic and continuous spectrum is more suited. It is provided by the ^{220}Rn and tritium (^3H) sources.

^{220}Rn is emanated with an efficiency of $(40 \pm 10)\%$ from a ^{228}Th source with an activity of 33.4 kBq [138]. The noble gas was deployed in the TPC by directing the gas circulation stream of the XENON experiments through the source vessel. The ^{228}Th isotope was electro-deposited onto a stainless steel disc which is contained in a vacuum vessel. With a half-life of 1.9 y, ^{228}Th decays to ^{224}Ra which again decays with a half life of 3.6 d to ^{220}Rn . The part of the ^{220}Rn decay chain which is relevant for the calibrations, together with the corresponding half-lives and Q -values, is shown in Figure 4.1. The source provides the means to calibrate the detector response to low energy electronic recoils using ^{212}Pb beta decays. It can also be used to reconstruct fluid dynamics within the detector by delayed coincidence studies of ^{220}Rn and ^{216}Po decays as shown in [139].

With a Q -value of 569.8 keV and a branching ratio of 11.9%, the ground-state ^{212}Pb beta decay results in low energy ER that populate the energy region of interest. It has been shown,

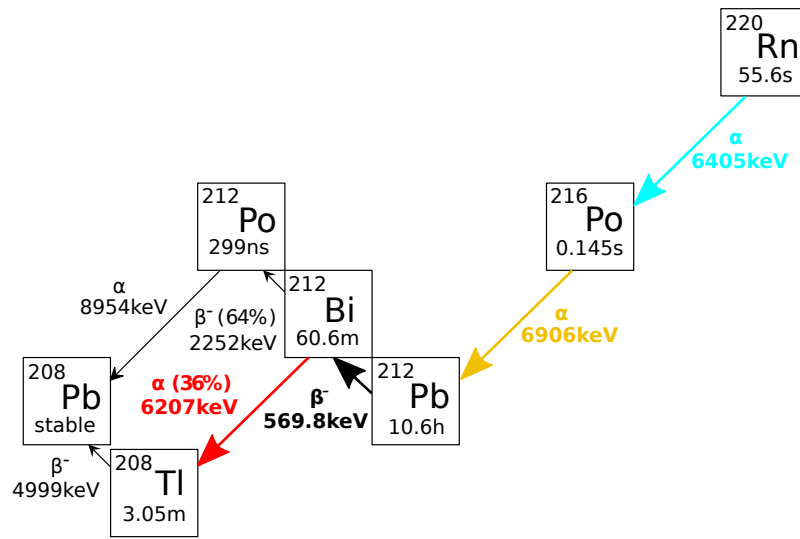


Figure 4.1: Scheme of ^{220}Rn decay chain. The Q -values and half-lives and branching ratios were taken from [76].

that 3 out of 10^4 decays fall within the interval of (2 – 30) keV [139]. This ratio is two orders of magnitude higher than that of the external thorium source. A further important feature of this internal source type is the rather short half-life of ^{212}Pb of 10.6h, that is long enough in order to allow a mixing within the detector volume, but sufficiently short to reduce the ER rate by a factor of 10^{-5} within one week.

Tritium (^3H) is also a good candidate for a source of low energetic ER by providing a beta spectrum with an end-point energy of 18.59keV [76]. It decays into ^3He with a half-life of 12.32y [76]. Due to this relatively long decay time, a removal mechanism has to be found. Pure tritium features a high diffusion rate into plastics and other detector materials [140], and has therefore potential to increase the overall detector background level. Tritiated methane CH_3T provides a potential solution: By featuring a larger molecule size, the diffusion into materials is reduced by one order of magnitude [140]. The dissolved methane can be adsorbed by the hot metal getters in the gas purification system of the experiment in order to remove the activity from the detector. This source type was successfully deployed and removed by the LXe dark matter experiment LUX [141, 54, 142] and was also used in PandaX [55].

Two tritiated methane sources were prepared for XENON100 with activities in the order of 5Bq to 10Bq. The methane was introduced into the recirculation gas stream in November 2015 and May 2016. The activity of the first injection could be removed, recovering the background level from before the source deployment. However, the same result could not be achieved after the injection of the second source where the low energy ER rate stayed approximately 3.5 times higher than the background rate. The reason for this different behavior is subject to investigations.

For the calibration of the NR response, a $^{241}\text{AmBe}$ source was placed next to the cryostat. By (α, n)-reactions, neutrons are generated with energies up to about 10MeV. As an alternative, a neutron generator has been constructed for XENON1T that can be immersed

into the water tank [143]. The neutrons are produced by Deuterium-Deuterium (DD) fusion with energies between 2.2 MeV and 2.7 MeV. An advantage of the generator compared to the $^{241}\text{AmBe}$ source is the adjustable neutron flux and the option to turn off the radiation when not needed.

4.2 Event Selection

Beside the low energetic ER events that serve for the calibration, interactions induced by alpha decays have been considered in this study. The time evolution of the activity of the ^{220}Rn source can be monitored by the primary radio-isotope that is introduced into the detector rather than the ^{212}Pb beta decays that are used for the ER calibration. Therefore, a short introduction to alpha spectroscopy is given before the event selection criteria of low energetic ER are presented.

4.2.1 Alpha Spectroscopy

Due to their high energies of several MeV and large stopping power, alpha particles have a very characteristic signature and only few event selection criteria have to be applied in order to identify them. The herein listed requirements are similar to those reported in [139].

Interactions taking place in the gas phase were deselected by comparing the fraction of S2 seen in the top PMT array to the fraction seen in the bottom array. Furthermore, only events that contain a single interaction are selected. This criterion removes the successive decays of ^{212}Bi (alpha) and ^{212}Po (beta) from the dataset. Due to PMT saturation at high energies, a dedicated position dependent correction has to be applied to the S1. This light correction was applied instead of the standard corrections described in Chapter 2, and has been previously described here [95]. The three-dimensional map was re-evaluated for the new data using the same procedure as in the reference. The new corrected S1 variable is called cS1_α . If not stated otherwise, a FV of ~ 47 kg target mass has been selected by requiring for the depth $Z \in [-175; -25]$ cm and for the squared radius $R^2 < 2 \cdot 10^4$ cm².

Figure 4.2 shows the cS1_α spectra for three different stages during the ^{220}Rn calibration data taking. The three datasets were collected within 24h. In the upper left, the source is open and the spectrum is dominated by three peaks, namely the ones from ^{212}Bi , ^{220}Rn , and ^{216}Po . In the upper right, the spectrum is shown after the source was disconnected from the purification gas stream. Due to their short half-lives ^{220}Rn and ^{216}Po decay within a few minutes after disconnection. Consequently, only the alpha decay of ^{212}Bi is left owing to the longer half life of ^{212}Pb with $T_{1/2} = 10.6$ h (see Figure 4.1). In the lower middle panel of Figure 4.2, the cS1_α spectrum is shown more than one week after the source was closed. The introduced activity was decayed and consequently, the background in this high energy region is dominated by the alpha peaks of ^{222}Rn and its daughter ^{218}Po . These two isotopes are introduced into the LXe by the emanation of ^{222}Rn from the detector materials and contribute to the ER background rate by the decay daughter ^{210}Pb that emits a beta. Additionally, small contributions from ^{220}Rn and ^{216}Po are visible which are, however, negligible for the ER background level of the detector compared to the larger observed rates of ^{222}Rn and ^{218}Po [144].

The spectra in Figure 4.2 are fitted by the sum of five Gaussians shown by the gray line. The

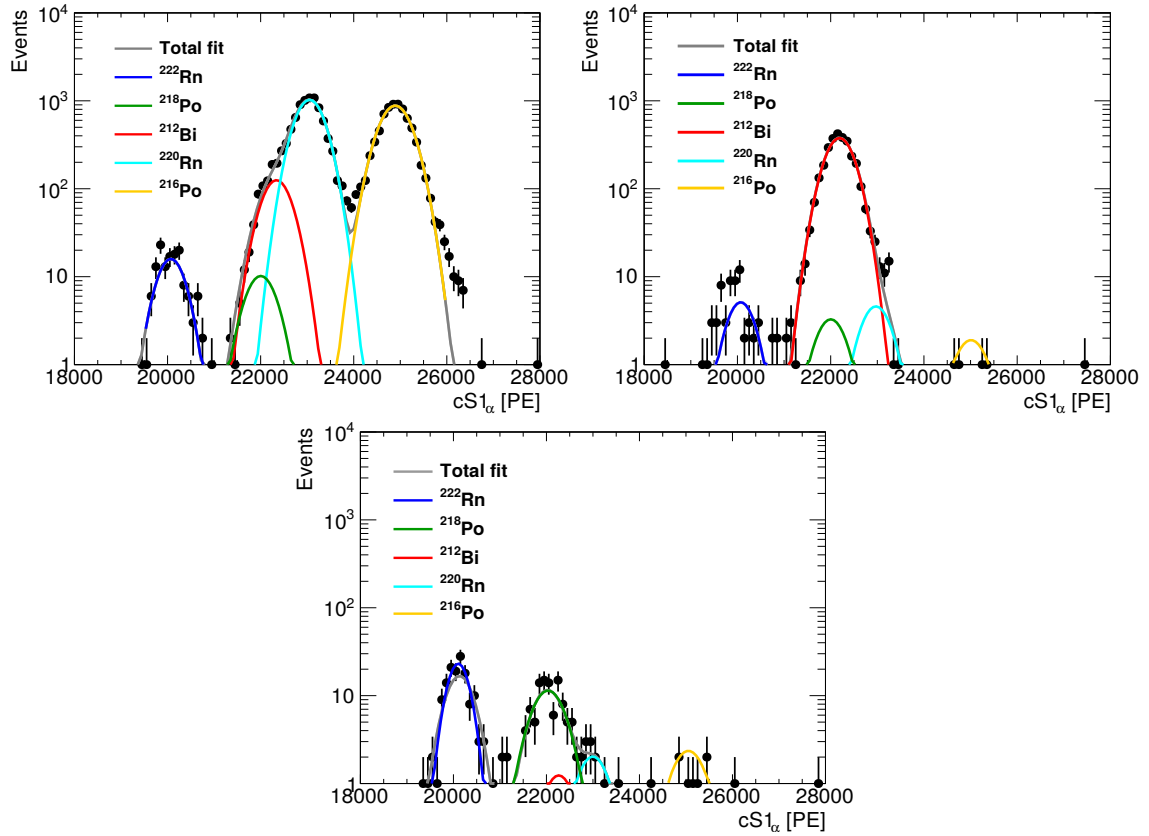


Figure 4.2: Alpha spectra at different stages of data taking with the ^{220}Rn source. **Upper left:** The source is open to the purification gas stream. **Upper right:** Shortly after the source was closed. **Lower middle:** 6 days after the source was closed. All spectra contain data from time intervals of 24 hours.

five means μ and widths σ have been initially determined from control samples where the spectrum is dominated by a maximum of two alpha lines, i.e., when no calibration source was connected to the detector (^{222}Rn and ^{218}Po), in the first few minutes after connecting the ^{220}Rn source (^{220}Rn and ^{216}Po), and hours after its disconnection (^{212}Bi). These reference values were used to fix the fit parameter of the Gaussian width and to limit the fit parameter of the mean to variations within $\mu \pm 0.5\sigma$. The scale of the Gaussians was left free during the fit, holding the information on the number of events induced by the respective alpha decay. This way, overlapping peak areas can be disentangled and their evolution can be monitored independently. The fitted Gaussian components of the individual isotopes are marked by colored lines as indicated in the legend in Figure 4.2.

For all identified isotopes, the mean $cS1_\alpha$ values and their ratio to their alpha energy Q_α are listed in Table 4.1. The ratio is referred to as S1 yield. For completeness, the values for ^{210}Po are given, even though their signature is not appearing in the shown spectra due to the selection of a fiducial volume. ^{210}Po events take place in close proximity to the PTFE TPC walls and feature a significantly reduced S2 signal compared to alpha decays within the fiducial volume. This specific event population is discussed in more detail in Section 5.4.2. The fact that the S1 yields are in agreement within the uncertainties points to a correct identification

Isotope	Q_α [keV]	$cS1_\alpha$ [PE]	S1 yield [PE/keV]
^{210}Po	5407	19560 ± 110	3.62 ± 0.02
^{222}Rn	5590	20110 ± 30	3.60 ± 0.01
^{218}Po	6115	22080 ± 100	3.61 ± 0.02
^{212}Bi	6207	22280 ± 80	3.59 ± 0.01
^{220}Rn	6405	23120 ± 100	3.61 ± 0.02
^{216}Po	6906	24960 ± 60	3.61 ± 0.01

Table 4.1: Properties of alpha decays identified in XENON100. The S1 yield is defined as the ratio between the measured $cS1_\alpha$ signal and the alpha energy Q_α . Values of Q_α from [76]

of the isotopic decays.

The identification of alpha events in XENON1T is very similar, with the major difference that the effect from the PMT saturation is not as strong as in XENON100. Therefore, no dedicated spatial alpha correction map was used in this work. The selection criteria for alpha events in XENON1T are described in Section 5.4.2. A fiducial volume of 1042kg xenon mass has been used.

4.2.2 Low Energetic Electronic Recoils

The ER events induced by the calibration sources in XENON100 in the low energy region ($< 30\text{keV}$) were selected using a very similar set of criteria as for the dark matter search data (see for example [56]). Two types of selection criteria are distinguished. Zeroth order criteria are supposed to remove waveforms that do not show the general properties of a physical energy deposition as well as those containing a high noise level. First order criteria select single scatter events and ensure that the reconstructed position is in agreement with the signal properties. The following zeroth order criteria have been applied:

- Per default, a two-fold PMT coincidence is required for a valid signal peak (S1 or S2). However, some PMTs have been identified to show a higher level of noise. If such a PMT contributed to the signal, the coincidence level is raised by one.
- Events made up of noise were rejected by requiring the ratio of the summed area of all other peaks beside the primary S1 and S2 and the sum of the primary S1 and S2 areas to exceed a threshold.
- The width of the S1 pulse was required to exceed a certain threshold in order to favor an origin from a physical interaction and not from electronic noise.
- A cut on the S2 pulse width was applied in order to remove interactions happening in the gas phase. They commonly show wider S2 signals than events from the liquid phase.

- The S1 signal was required to take place within the first half of the recorded waveform¹ in order to allow a potential secondary S2 of the event to be recorded.
- The time interval between the beginning of the waveform recording and the S2 signal was requested to be long enough to allow the maximum drift-time between the S1 and the S2.
- A criterion on the inhomogeneity of the waveform was applied, that favors peak-like signals within the event and removes noise events.
- Events that showed a low asymmetry between the fraction of the S2 signal, recorded by the top and bottom PMT array, were removed since they are likely to be not real S2 signals.

The first order selection criteria are the following:

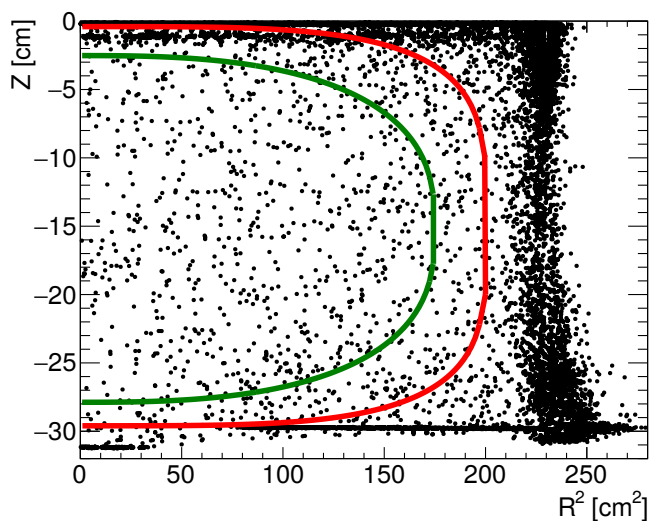
- The event position, reconstructed by three different algorithms was required to be consistent within an uncertainty margin. This criterion removes multiple scatter events.
- Every other than the main S1 had to be consistent with PMT noise.
- Every other than the main S2 had to be consistent with a signal from up to two electrons induced by photo-ionization at the cathode and of impurities in the xenon, after large primary S2 signals. Those single electron signals are typically below 70PE^2 .
- A low energetic neutron calibration source (^{88}YBe) was present inside the detector shielding during this study. It induced a small but measurable rate of NR that overlaps with the ER event population in the low S1 region. It was found that setting a higher threshold on $\text{cS2}_{\text{bottom}}$ than done in a dark matter search without the neutron source reduces this bias while the ER region stays unaffected. The new threshold was set to 300 PE.
- Two fiducial volume (FV) cuts were defined in order to avoid effects coming from incomplete light or charge collection at the TPC walls and the field meshes. Figure 4.3 shows the spatial distribution of background data together with the defined FV containing 48kg and 34kg xenon mass (red and green lines). If not stated otherwise, the 48kg is used for calibration data in the following, since the background radiation from the detector materials is negligible in those datasets. The 34kg cut is applied when background data or dark matter is studied in order to suppress the contribution from the detector components.

In XENON100 it was found, that the S2 signal detected by the PMTs located in the bottom array, features less spatial dependencies in the X - Y plane than the total recorded S2 signal. This is explained by the large solid angle that the bottom PMT array takes with respect to the gas phase, where the secondary scintillation occurs. Therefore, the variable $\text{cS2}_{\text{bottom}}$ is used in the following study.

¹See Section 2.4 for more explanations on event waveforms.

²The unit PE comprises the number of collected photoelectrons by the PMTs.

Figure 4.3: Distribution of low energy ($cS1 < 60\text{PE}$, i.e., $E_{\text{recoil}} < 30\text{keV}$) background data within XENON100. The 48 kg (32 kg) FV border is visualized by the red (green) line.



The smaller but similar set of selection criteria for ^{220}Rn ER data acquired with XENON1T is described in Section 5.1. The same requirements as applied during the dark matter search of the first science run of the experiment, are also used for the studies of the ER data recorded with XENON1T in this chapter.

4.3 Injection of Radio-Isotopes into the TPC

An important aspect of internal calibration sources is the verification that the radio-isotopes reach the fiducial volume. Furthermore, the fraction of activity that can be introduced into the detector is a parameter of interest for the performance of a source and can influence the preparation of future sources. And finally, the knowledge of the single scatter ER rate in the energy region of interest is crucial for scheduling the duration of calibration runs and judging, if a source is suited for ER calibrations at all.

4.3.1 Injection Mechanism

The internal sources, tritium and ^{220}Rn , are introduced into the TPC via the gas purification circuit in XENON100 and XENON1T. Depending on the detector size, the convection of the LXe in the cryostat, the purification gas flux, and the position of the gas in- and outlets, different times are required to obtain an equilibrium of the activity.

Figure 4.4 shows a schematic of the XENON100 cryostat. The active volume is indicated by the black dashed box. For purification, gas is evaporated from the liquid phase in the veto region outside of the TPC (green tube). It re-enters by pressurizing the bell and releasing the pressure into the veto region via the bleeding tube. This mechanism is supposed to ensure a constant liquid xenon level inside the TPC. The bell itself is acting like a dead end to the gas. Dissolved radio-isotopes therefore enter the veto region via the bleeding tube and are distributed within the detector by convection and diffusion. Only a small fraction of the activity reaches the gas phase of the TPC by diffusion and turbulences in the bell volume.

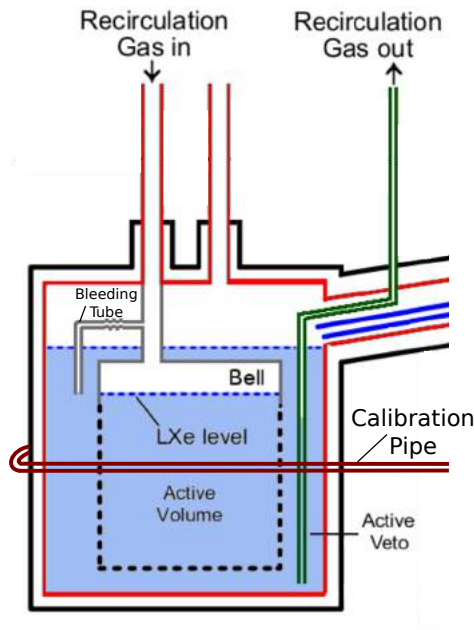


Figure 4.4: Schematic of the XENON100 detector with its gas in- and outlets. Xenon is evaporated in the veto region and directed to the purification system (outlet marked in green). After purification, the gas stream is used to pressurize the bell while the pressure is released over the bleeding tube. Figure from [75].

The XENON1T cryostat with its xenon in- and outlets is depicted in Figure 4.5. The purification gas stream is fed by evaporating LXe from below the TPC in a heat exchanger. Part of the purified gas pressurizes the bell structure while the rest is condensed in the same heat exchanger, collected by a funnel and injected into the TPC at two opposite positions below the cathode mesh. As in XENON100, the opening to the bell is acting like a dead end for the gas. With the setup in XENON1T, the activity of radio-isotopes injected into the purification gas stream is expected to be introduced directly into the LXe in the sensitive volume and not into the region outside the TPC like in XENON100.

4.3.2 Activity Evolution and Electronic Recoil Calibration Rate

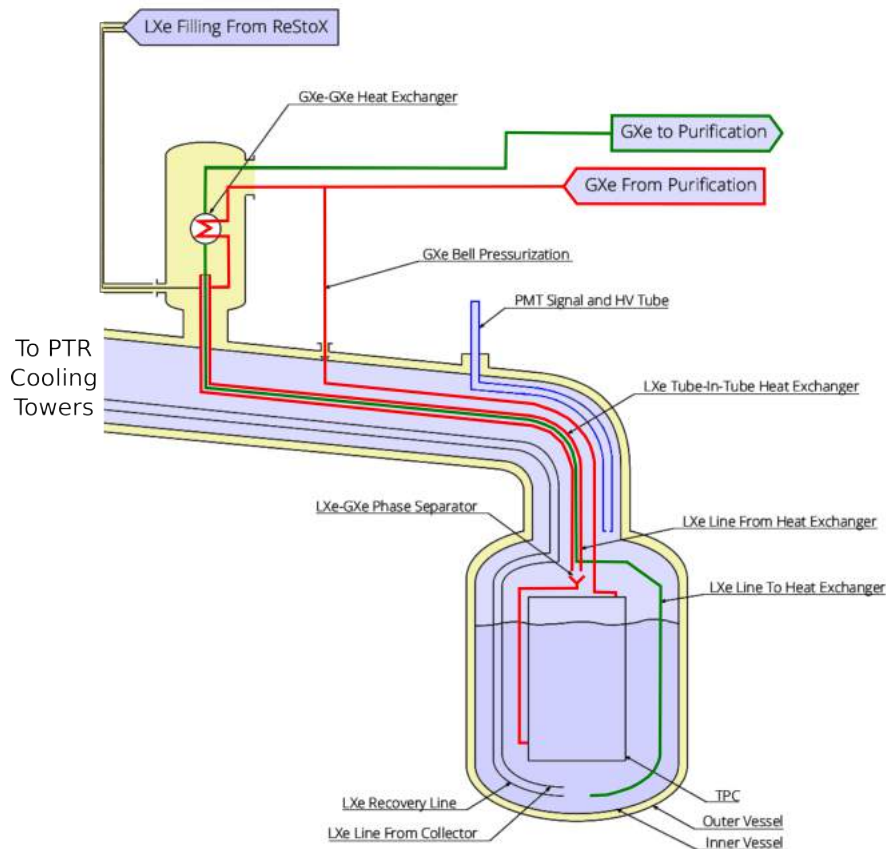
The ingrowth of the activity into the sensitive volume is an interplay between the extraction efficiency of the activity from the source, the gas re-circulation speed through the source and the convection in the LXe. Furthermore, the molecular size and vapor pressure of the radio-isotope itself with respect to xenon, might lead to a preference for the liquid or the gaseous xenon phase.

Figure 4.6 shows the evolution of the activity inside the detector after opening the internal sources to the purification gas stream as a function of time. While tritium was only used in XENON100, ^{220}Rn data is available in XENON100 and XENON1T. For the ^{220}Rn source, the overall α rate has been monitored in the region $cS1_{\alpha} \in [16000, 27000]$ in XENON100 and $cS1 \in [40000, 100000]$ in XENON1T, i.e., no distinction between isotopes was conducted. For tritium, ER events with $cS1 < 60\text{PE}$ were considered. The full tritium spectrum is contained in that energy region. All rates were evaluated inside the respective fiducial volumes defined for low energetic electronic recoils (48 kg super-ellipsoid) and alpha events (cylinders of 47 kg in XENON100 and 1042 kg in XENON1T) in Section 4.2.

It can be seen that an equilibrium rate can be achieved within about 15 min for ^{220}Rn in XENON100, about one hour for tritium in XENON100, and about 1.5 hours for ^{220}Rn in

Figure 4.5:

Schematic of the XENON1T detector. The xenon extraction pipe toward the purification system is marked in green. The liquid is evaporated in the heat exchanger. A fraction of the purified gas is used for the pressurization of the bell while the rest is condensed in the heat exchanger and the Tube-In-Tube heat exchanger. The liquid drops into a funnel and enters into the TPC at two opposite positions below the cathode mesh. The pipes for the back flowing xenon are marked in red. Figure from [105].



XENON1T. A deeper understanding of the different time scales that are the result of a complex interplay of xenon gas mixing processes and the radioactive decay of the isotopes, was beyond the scope of this thesis.

In order to determine the maximum activity of the source that reaches the TPC, the rate R over the time t was fitted by a logistic growth of the form:

$$R(t) = \frac{S}{1 + \omega e^{-k \cdot S \cdot t}}, \quad (4.1)$$

where S is the saturation value, k is the growth constant, and ω is a constant that comprises the ratio between saturation and initial rate. The parameter S is extracted from the fit result which is indicated by the red lines in Figure 4.6. The extracted saturation values for the four tested source-detector combinations are summarized in Table 4.2. The last column lists the ER rate in the WIMP energy region of interest (ROI), namely $[3, 30]$ PE in cS1 in XENON100 and $[3, 70]$ PE in XENON1T. These regions correspond to deposited ER energies of approximately $(1 - 12)$ keV in both detectors.

When deploying the ^{220}Rn source in XENON100 (Figure 4.6a), the saturation value yields (60.2 ± 3.0) mBq/kg, assuming a homogeneous distribution in the active volume. Since no isotopic distinction was performed, this rate includes both, ^{220}Rn and ^{216}Po decays in equal

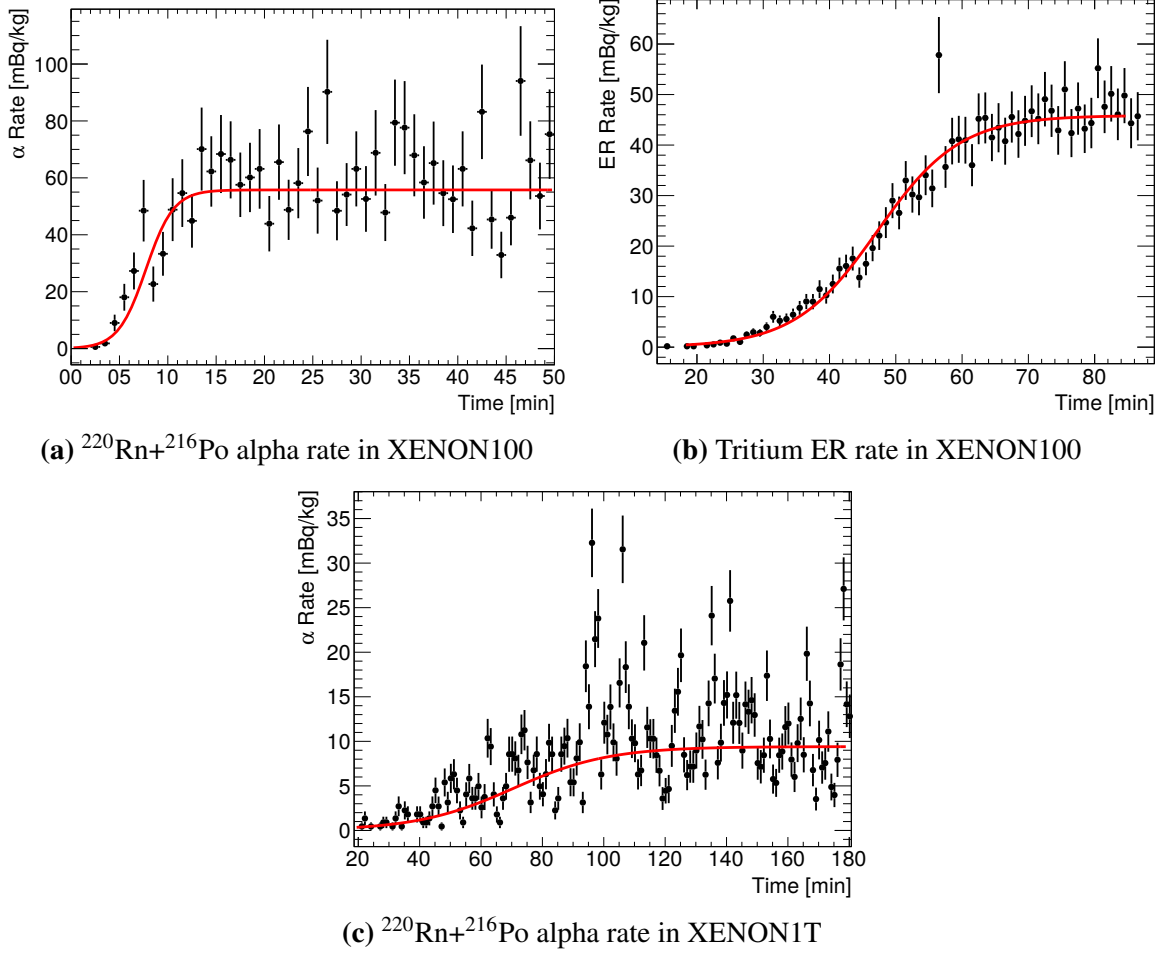


Figure 4.6: Activity evolution after connecting the internal sources ^{220}Rn and tritium to the xenon purification gas stream of XENON100 (upper row) and after connecting the ^{220}Rn source to XENON1T lower row. The fit results of a logistic function are shown by the red curves. See text for more explanations.

parts. The pure absolute ^{220}Rn rate amounts to (4.8 ± 0.2) Bq if the isotope was homogeneously distributed within the whole xenon inventory. Considering the source's activity of 33 kBq in ^{228}Th , assuming it to be in equilibrium with ^{220}Rn and taking into account the emanation efficiency of 40%, a maximum activity of about 2400 Bq in ^{220}Rn is possible if it dissolves homogeneously in the xenon. Comparing to the maximum observed ^{220}Rn rate, only a fraction of 0.2% reaches the active region of the TPC. This significantly decreased activity might be owed to the pipe length of 20m between the source and the detector inlet. Furthermore, the majority of the activity enters through the bleeding tube (see Figure 4.4) into the veto region. Due to the relatively short half-life of ^{220}Rn , most of the decays take place in the veto region, before the inner detector volume can be reached.

In XENON1T, the deployment of the same ^{220}Rn source resulted in a saturation value of the alpha rate of (10.8 ± 1.3) mBq/kg, corresponding to a pure ^{220}Rn rate of (9.7 ± 0.5) Bq in the whole xenon content of the detector. This is two times higher than the maximum ^{220}Rn

Source type	Detector	S [mBq/kg]	ER rate in ROI and FV [mBq]
^{220}Rn	XENON100	60.2 ± 3.0	19 ± 1
^{220}Rn	XENON1T	10.8 ± 1.3	40 ± 4
Tritium	XENON100	45.4 ± 1.7	772 ± 31

Table 4.2: Summary of saturation values S extracted from the fit of a logistic growth function to the activity evolution after the injection of an internal source. The maximal ER rate measured in the WIMP search energy region (ROI) and in the FV used for the dark matter search is given in the last column. The rate has been evaluated by applying the ER selection criteria described in Section 4.2. For XENON100, the ROI implies the cS1 range of $[3, 30]$ PE and for XENON1T $\text{cS1} \in [3, 70]$ PE due to different light yields. This corresponds to about $(1 - 12)$ keV in both detectors.

activity measured inside XENON100. Presumably, this increased activity concentration is a result of the improved XENON1T setup where the xenon coming from the purification system (and therefore from the source) is injected directly into the TPC and not in the veto region as done in XENON100. Hence, a higher fraction of the introduced activity decays within the active region and can therefore be detected. The length of the piping between the source and the XENON1T detector is of the same order as in XENON100 and therefore, does not play a dominant role for the comparison.

The measured equilibrium rate for tritium in XENON100 yields (45.4 ± 1.7) mBq/kg which corresponds to an activity of about (7.4 ± 0.3) Bq in the whole xenon content of the detector. The activity of the tritium source was roughly estimated to ~ 5 Bq [145] and is therefore in agreement with the measurement. In contrast to the ^{220}Rn source, close to 100% of the tritium source activity reaches the active region. This is the result of the long half-life of tritium of about 12 years which allows for mixing of the radio-isotopes in the detector before their decay. Presumably, this aspect also contributes to the longer time, the activity needs to reach the equilibrium rate.

The maximum ER in the region of interest for the WIMP search and within the FV used for the dark matter search, is listed in the last column of Table 4.2. The highest rate is provided by the tritium source, as a result of the low end-point of the beta spectrum ($Q_\beta = 18.6$ keV) which ensures about half of the induced ER events to end up in the region of interest in XENON100. The ^{212}Pb beta decay in the ^{220}Rn decay chain, however, has a higher end-point ($Q_\beta = 570$ keV) which leads to a spread of the ER rate over a larger energy region. Comparing the ER rates induced by the ^{220}Rn source in XENON1T and XENON100, an about two times higher rate in XENON1T is measured in this energy region. Like for the higher alpha activity, the increased number of events usable for calibration can be attributed to the improved injection mechanism in XENON1T. Furthermore, the maximum ER rate induced by the ^{220}Rn calibration source in XENON1T is four orders of magnitude larger than the background rate of the experiment and hence allows to gather high statistics in ER events within days.

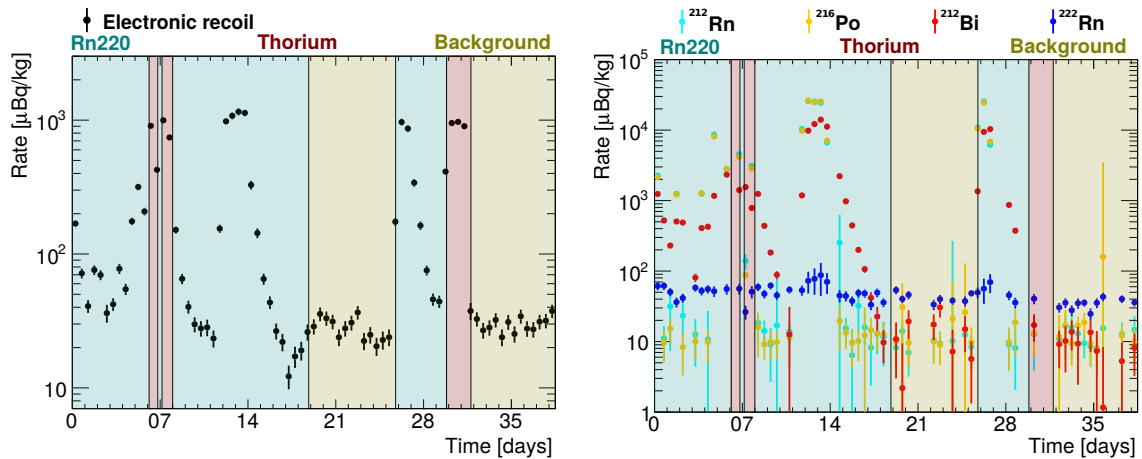


Figure 4.7: **Left:** ER rate below 60PE in cS1 versus time in intervals of 12h during the deployment of the different sources in XENON100 or background data taking. The colors of the time periods indicate to which dataset the taken data is attributed. **Right:** Evolution of the alpha decay rates of different isotopes in XENON100 during the same time periods as shown on the left.

4.3.3 Distinction of Datasets

The datasets used in this work to study the ER calibration data induced by the internal sources ^{220}Rn and tritium, were acquired with XENON100 during the detector's last run period. For comparison, background data and calibration data from the external thorium source was taken in the same run. Since ^{220}Rn , thorium and background data has been taken in alternation, a correct assignment of the acquired data to the sources had to be ensured. Special care needed to be taken when ^{220}Rn was deployed, since the introduced activity takes a few days to decay. During this time, no new calibration or background run should be started.

Figure 4.7 left shows the rate of selected ER events with $\text{cS1} < 60\text{PE}$ inside the 48 kg fiducial volume (FV) as a function of time³. Time periods are marked by colors, indicating to which source the taken data has been attributed. In the right panel of Figure 4.7, the same time periods are shown, together with the alpha decay rates of the individual isotopes that have been identified and quantified as described in Section 4.2.1. Each data point extends over a time of 12h. When no data point is visible in the alpha rate plot, the automatic fit did not converge due to low event statistics.

Clearly, the ER rate is correlated with the ^{212}Bi alpha rate. Within the first six days, the ^{220}Rn source was still in testing mode where only pulsed injections have been performed. Directly afterwards, the thorium source was deployed while the activity from ^{212}Bi was still visible and therefore events from its mother nuclide ^{212}Pb were still expected. However, the rate from ^{212}Bi is about one order of magnitude lower than for periods where the ^{220}Rn source was kept open on a longer term (i.e. between day 12 and 15). The fact that the ER rate is nevertheless equally high as during the ^{220}Rn source deployment leads to the conclusion that the majority of the ER events are originating from the thorium source and the attribution of

³To visualize if the deployed ^{220}Rn source activity has been decayed to background level, a 48kg FV has been used for background data as well. This results in an about one order of magnitude higher rate compared to the 34kg FV.

the data to this source is correct. For all other datasets, it could be verified that the ^{220}Rn source activity was decayed to background level before a new run was started.

Even though the calibration of the ER background with the ^{220}Rn source was intended to be accomplished by ground-state ^{212}Pb beta decays, it has been shown that only a very small fraction of the ER rate of 4% originates directly from this process [139].

This is related to the fact that the gas circuit exit in XENON100, i.e., the bleeding tube, is situated in the veto region. The injection mechanism of the internal sources will be explained in Section 4.3. Most of the ^{220}Rn source activity remains in the veto, whereas only a small amount reaches the active volume by xenon convection. Gamma rays from ^{212}Pb , ^{212}Bi , and ^{208}Tl decays occurring in the veto region, can therefore induce single scatter interactions in the active region. These events make up about 96% of the total low energy ER event rate. This result was gained from simulation studies and investigations of delayed coincidences of ^{212}Bi and ^{212}Po decays [139]. In XENON1T, the situation is expected to be different, since the activity of internal sources is pumped directly into the active region.

The tritium source has been deployed about one month after the last background run presented in Figure 4.7, was completed. In the meantime, no activities were introduced into the detector that could have caused an ER rate above the background level at the time of the injection of the tritiated methane.

4.4 Spatial and Spectral Distribution of Electronic Recoils

After having shown that the internal calibration sources ^{220}Rn and tritium induce measurable ER rates inside the FV that provide calibration data in the low energy range, the properties of the acquired ER data are compared among the datasets. For this study, the focus lies on the data acquired with the XENON100 detector, with which the internal sources were tested in preparation for the XENON1T experiment.

The deployment of internal ER calibration sources aims at the acquisition of data that is homogeneously distributed within the FV, as expected from the dominating ER background component ^{222}Rn in XENON1T (see Section 2.5). This way, spatial signal corrections are taken into account in the calibration similarly as in the science data.

The homogeneity of the ER calibration data acquired with XENON100 is studied in Figure 4.8 where the distributions in Z (right) and R^2 (left) are compared among the ^{220}Rn (red), thorium (black), tritium (blue), and background (green) datasets. For this purpose, events within the same cylindrical FV have been selected in all datasets. The cylindrical shape is more adapted to the detector geometry than the super-ellipsoids introduced in Figure 4.3. The FV ignores the cathode and gate mesh regions by removing events from 2 cm of the drift-length at the top and at the bottom as well as the outermost 1.7 cm in R . The histograms have been normalized to their integral to allow a direct comparison. For reference, the maximum borders in R^2 and Z of the 34 kg FV in which the dark matter search was conducted in XENON100, are marked by the black vertical lines.

The internal sources, tritium and ^{220}Rn , show a more homogeneous distribution in contrast to the thorium source. The external source calibrates predominantly the outer detector re-

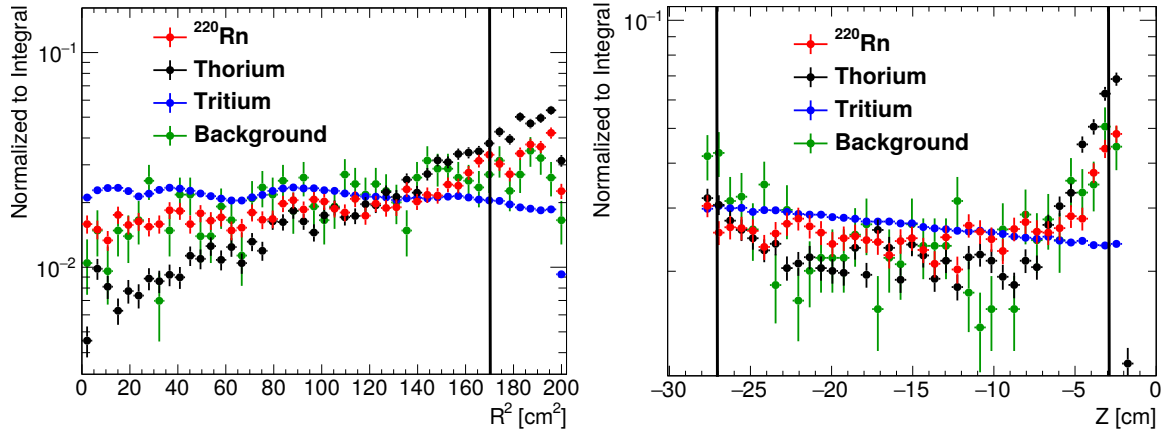


Figure 4.8: Spatial distribution of ER events in XENON100 with $cS1 < 70$ PE originating from the three sources and from background. A 47kg cylindrical FV has been selected to neglect events from the cathode and gate meshes as well as from close to the TPC wall. All histograms have been normalized to their integral. For reference, the approximate maximum borders of the 34kg FV that was used in the dark matter searches (in reality a super-ellipsoid) are shown by the black vertical lines.

gions as can be seen by the exponential decrease toward smaller R^2 . However, since also in XENON100 internal ER backgrounds from ^{85}Kr and ^{220}Rn are present, the fall-off is less strong in background data. Tritium shows almost a perfectly homogeneous distribution in R^2 with only slight wiggles owing to PMT saturation due to the high introduced rate, and a small decrease at high radii which could be due to event selection efficiencies.

The ER data from the ^{220}Rn source is distributed homogeneously in R^2 up to 140cm^2 and shows a rate increase beyond this value as a result of an additional contribution from decays that are accompanied by a gamma emission. Those events are suppressed in the inner detector volume due to the selection of single scatter events. However, at the TPC border, the gamma has a higher probability to escape from the detector without inducing a measurable second interaction. This effect is stronger close to the gas phase owing to the longer mean free path of gamma rays in the xenon gas with respect to the liquid, resulting in a higher escape probability. The Z distributions of ^{220}Rn , thorium, and background data show increases toward the detector edges for the same reason, while being flat in the middle. Since tritium is never accompanied by a gamma emission, no rate dependence on Z is expected. However, the data shows an exponential decrease toward the top of the TPC. This could be caused by the difference in the vapor pressures between the methane, to which the tritium is bound, and xenon (see Figure 2.2). Methane is more volatile than xenon and favors the gas phase rather than the liquid. Consequently, an increased depletion of tritium ER events is seen toward shallower TPC depths.

In summary, the ^{220}Rn source induces ER events distributed similarly as background data within the detector. The same is observed when the source is deployed in XENON1T. The corresponding figures can be found in the Appendix C.1. Tritium and thorium ER data show slight deviations from the background data that might introduce systematic uncertainties into the calibration of the ER background owing to the different spatial signal corrections.

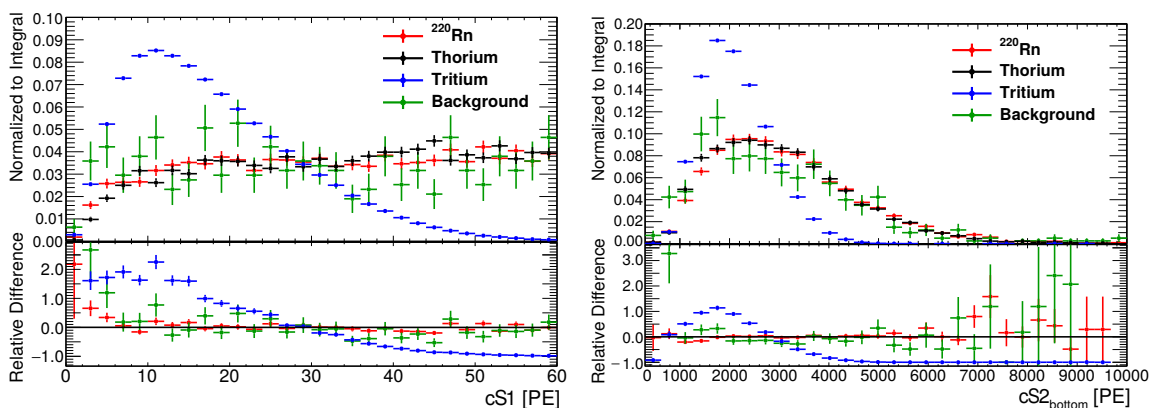


Figure 4.9: ER spectra in cS1 (left) and cS2_{bottom} (right) for the three calibration sources and background data. The data has been acquired in XENON100 within the 48kg super-ellipsoid FV. All histograms have been normalized to their integrals. The lower panel shows the relative difference to the thorium data. For the cS2_{bottom} spectrum $5 \text{ PE} < \text{cS1} < 60 \text{ PE}$ has been required in order to neglect the first two bins in the cS1 spectrum where the detection efficiency and cut acceptances are small.

Another important property of the ER data from calibration sources is its recoil spectrum. Since the data is supposed to serve for the calibration of the ER background, a similar distribution of deposited energy should be present. It will be shown in Section 4.6 that differences in the spectra can influence the outcome of the dark matter search.

Figure 4.9 compares the cS1 (left) and cS2_{bottom} (right) ER spectra of the three calibration sources to background data at low energy ($\text{cS1} < 60 \text{ PE}$). All datasets have been acquired with XENON100 within the 48kg super-ellipsoid FV. The upper panels contain the spectra themselves, normalized to their integrals whereas the lower panels show the relative difference to the well established thorium source data. For background and ^{220}Rn data, no overall systematic offset in comparison to thorium is observed. Only statistical fluctuations around a relative difference of zero are visible for $\text{cS1} > 5 \text{ PE}$ and $\text{cS2}_{\text{bottom}} > 2000 \text{ PE}$. Below these values, 2 to 3 times higher rates are observed in the background with respect to thorium calibration data. This effect can be explained by the high PMT noise level that was present during this study. Corresponding noise events could not entirely be removed for small signals by the event selection criteria. Since the data acquisition time was shortest for the thorium dataset (7 days), the corresponding spectrum is least affected. In ^{220}Rn data (18 days of acquisition time) the fraction of noise events is still smaller than in background (14 days of acquisition time) due to the introduced source activity. By requiring $\text{cS1} > 5 \text{ PE}$ in the cS2_{bottom} spectra presented in Figure 4.9 right, the discrepancy at low energies between thorium and radon data can be resolved. However, a slightly higher rate compared to thorium is still present in the background dataset due to the noise population. In the following, comparisons between ^{220}Rn and thorium data will concentrate on the energy region $5 < \text{cS1} < 60 \text{ PE}$. ER data taken with the ^{220}Rn source in XENON1T shows very similar spectra to the ones in XENON100 (see Figure 5.6 in the following chapter).

The similarity of the background and ^{220}Rn data with respect to thorium above 5 PE in cS1, is not shared by the tritium data. This is caused by the low end-point of the beta spectrum of 18.6 keV. The distribution features a much steeper falloff toward small values in cS1 and

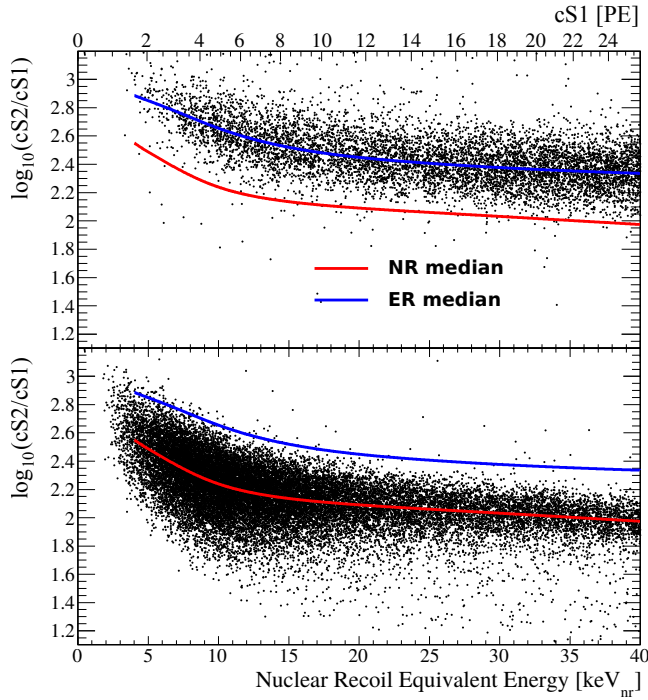


Figure 4.10: Demonstration of discrimination between ER (upper panel) and NR (lower panel) events. The data was acquired during the first science run of XENON100 using external gamma sources for ER and the $^{241}\text{AmBe}$ source for NR. The lines represent the NR (red) and ER (blue) medians. Figure from [146].

$cS2_{\text{bottom}}$. Toward larger values, both spectra show an exponential fall-off that starts earlier and is steeper than for the other sources in the case of $cS2_{\text{bottom}}$ and is not present in the other sources in the case of $cS1$. In the following, the influence of this spectral shape on the calibration of the ER background region will be discussed.

4.5 The Electronic Recoil Band

The aim of collecting ER data using radioactive sources is to calibrate the region of the dominating background from natural gamma and beta radiation inducing ER in liquid xenon dark matter detectors. As explained in Chapter 2, the ratio between the charge and the light signal is different for ER and NR and therefore provides the means to discriminate between the two processes. The variable $\log_{10}(cS2/cS1)^4$, also referred to as *discrimination parameter*, is commonly plotted versus $cS1$ to visualize the separation between ER and NR interactions. This parameter space is denoted as *discrimination space* and is shown in Figure 4.10 for ER calibration data (external thorium and ^{60}Co sources) in the upper panel and for NR calibration data ($^{241}\text{AmBe}$ source) in the lower panel. The data was acquired with XENON100 during its first science run [146]. The $cS1$ scale is marked at the top and the nuclear recoil energy scale at the bottom. The NR median defined by using the shown data is represented by the red line and the ER median by the blue line. With the calibration data, the acceptance to NR, i.e. signal-like events, can be evaluated while rejecting a certain fraction of ER background events. Due to the overlap of the two so-called *bands*, especially at low energies, statistical downwards leakage of ER events into the NR band can mimic WIMP interactions.

⁴This variable can be also formed with $cS2_{\text{bottom}}$ as will be done in all following studies. The separation between NR and ER events is not significantly influenced when using the total S2 signal or only the one detected by the bottom PMT array.

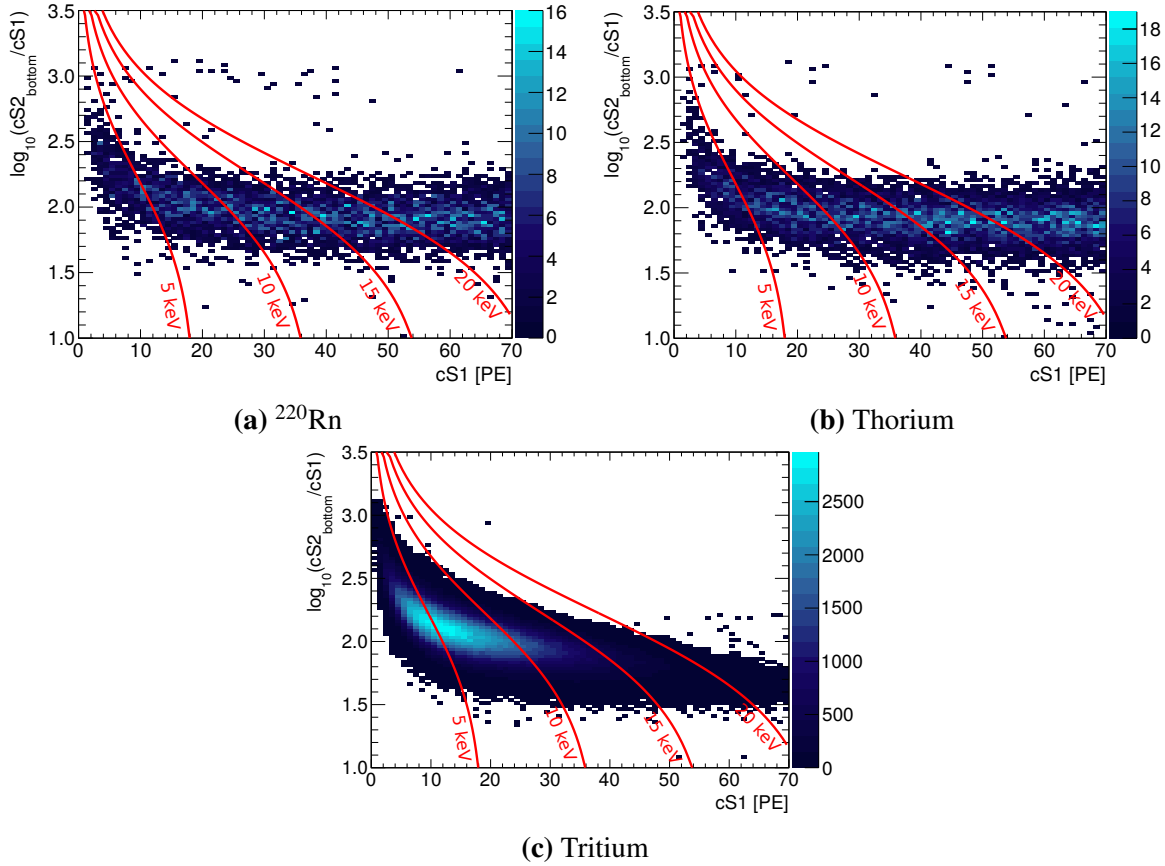


Figure 4.11: ER data in XENON100 shown in discrimination space ($\log_{10}(cS2_{\text{bottom}}/cS1)$ vs. $cS1$) for the different calibration sources. Mono-energetic lines are shown in red for 5, 10, 15 and 20 keV. They have been evaluated using Equation 2.8.

Hence, also after discrimination of the two processes, ER events still present the dominating background component. Furthermore, the shape of the calibrated ER band has an influence on the NR acceptance and consequently on the dark matter result.

The ER band shape determined with the different calibration sources introduced in this chapter, will be discussed in the following.

4.5.1 The Band Shape

The data of the three calibration sources ^{220}Rn (upper left), thorium (upper right), and tritium (bottom) acquired with XENON100 is presented in discrimination space in Figure 4.11. The number of events is indicated by the color scale. The red lines show four lines of constant ER energy evaluated using Equation 2.8. In order to compare the shape of the ER bands among the three sources, the projections in intervals of $cS1$ onto the discrimination parameter were modeled by Gaussians. The result is shown in Figure 4.12 for the thorium data with $cS1$ intervals of 2.5 PE, as indicated above each panel. The Gaussian fit is shown by the gray lines. The reduced χ^2 values are displayed in each canvas and are close to one, which indicates a good description of the data.

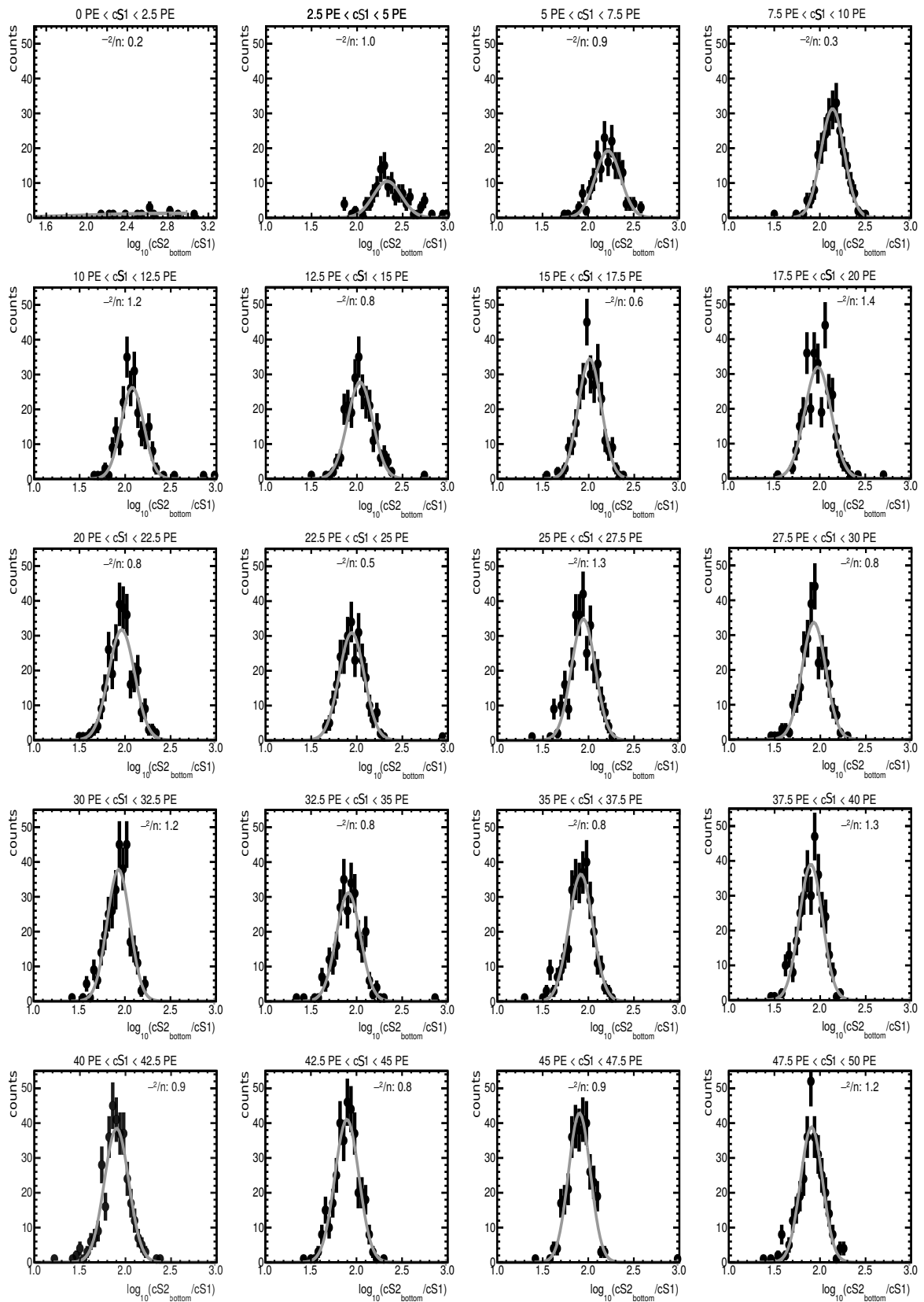


Figure 4.12: Comparison of projected thorium ER data in XENON100 on the discrimination parameter for intervals of 2.5 PE in cS1. Each distribution is fitted by a Gaussian from which the mean and 1σ width are extracted to model the band shape as a function of cS1.

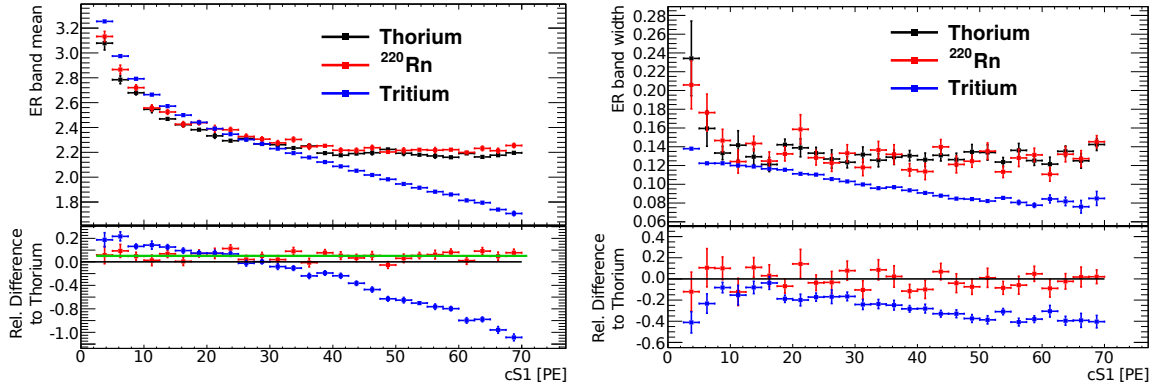


Figure 4.13: Comparison ER band means (left) and widths (right) as functions of cS1 extracted from Gaussian fits of the projections onto the discrimination parameter. Data acquired by XENON100 employing the three calibration sources thorium (black), ^{220}Rn (red) and tritium (blue) was used. The lower panels show the relative difference of ^{220}Rn and tritium to thorium data.

From the fit results, the means and the 1σ widths are extracted and displayed as functions of cS1 in Figure 4.13. The ER band means for thorium (black), ^{220}Rn (red) and tritium (blue) are shown on the left and the ER band width of the same datasets on the right. The uncertainties on the data points were gained from the error matrix of the fit result. The lower panels in Figure 4.13 present the relative difference to the thorium data, that has been extensively studied in XENON100 in the context of the dark matter searches. Large deviations of the band shapes are observed for the ER band from the internal tritium source. The band mean shows an almost linear decreasing trend above 10 PE while the means of the other two sources stay constant in that energy region. The deviation yields up to -100% . A similar trend is observed in the ER band widths where a deviation of the tritium graph with a minimum of -40% is visible. Below 10 PE, tritium data shows an up to 20% higher band mean than ^{220}Rn or thorium and an up to 40% lower band width. This very different behavior of the tritium ER band shape arises from its non-flat spectrum and is discussed in Section 4.5.2. While the ER band widths of thorium and ^{220}Rn data are well in agreement within the uncertainties, the ^{220}Rn band mean shows a systematic shift to higher values in the discrimination parameter with an average of $(1.0 \pm 0.1)\%$. This indicates an offset in $\text{cS2}_{\text{bottom}}$. Its origin can be found in the fluctuation of the S2 yield toward lower values during one of the thorium data acquisition periods. Further details can be found in the Appendix C.2. Consequently, it can be concluded that the ER band shapes of ^{220}Rn and thorium are in agreement.

4.5.2 Variations of the Band Shape

In order to investigate the influence of the recoil spectrum and detector parameters on the ER band shape, a toy Monte Carlo simulation has been written. It samples energies from a flat input spectrum and converts it into a number of photons N_p using a constant photon yield of 40 photons/keV. The energy dependence of the yield has been neglected since it is similar for ER induced by gamma or beta radiation [147] and was excluded to be responsible for the observed discrepancy between the tritium ER band and the bands from ^{220}Rn and thorium

data. N_p is smeared by a Poisson function to account for the fluctuations in the electron-ion recombination after the energy deposition. The recombination decreases the charge signal S2 but increases the light signal S1 (see Section 2.3 for more information). After the smearing, the number of produced electrons N_e is evaluated by transforming Equation 2.8 to:

$$N_e = 73 \cdot E(\text{keV}) - N_p. \quad (4.2)$$

The light collection efficiency is taken into account by a binomial distribution that takes the efficiency averaged over the whole detector (5.99%) as a parameter. The number of photoelectrons N_{PE} generated by the photons is then given by:

$$N_{\text{PE}} = \text{Binomial}(N_p, 5.99\%) \quad (4.3)$$

The conversion from the raw number of quanta N_{PE} and N_e to the signals S1 and S2 can be well described by Gaussian distributions. In the case of the S1, the Gaussian function models the multiplication step of single photoelectrons that create avalanche electrons inside the PMTs. Hence, as described in Section 2.3, the S1 resolution is influenced by the PMT resolution Δ_{PMT} to a single photoelectron. Δ_{PMT} has been determined to about 0.5 by LED calibrations in XENON100 [96]. In the case of an S2 signal, the Gaussian describes the amplification step of single electrons that are extracted from the liquid xenon into the gas phase by secondary scintillation. Due to the large number of secondary photons, the PMT resolution does not play a role. However, the fluctuations in the proportional scintillation process dominate the resolution of the S2 signal. The photoelectron gain of a single electron has been evaluated from data following the procedure from [97]. The gain yields $(9.096 \pm 0.069) \text{ PE/e}^-$ and features a width of $\sigma = 4.94 \text{ PE/e}^-$ [145].

The S1 and S2 signals are then given by

$$S1 = \text{Gauss}(N_{\text{PE}}, 0.5 \cdot \sqrt{N_{\text{PE}}}) \quad (4.4)$$

$$S2 = \text{Gauss}(8.78 \cdot N_e, 4.94 \cdot \sqrt{N_e}) \quad (4.5)$$

The simulated event is rejected if the S2 does not exceed a threshold of 150 PE.

This simplified simulation does not allow a direct comparison to the data recorded with XENON100. For this, a full detector simulation would be needed, where all signal fluctuations and detector resolutions are properly taken into account. Specifically, the following simplifications have been made: The electron-lifetime has not been considered which attenuates the S2 signal owing to the attachment of electrons to impurities along the drift-path. Hence, the resolution of the S2 is more decreased for interactions located at the bottom of the TPC, compared to events from the top. Furthermore, an average light collection efficiency within the detector has been applied, while its value varies depending on the event position. The photon yield was set to a constant value while it is known to vary between 17 and 45 photons/keV for ER between 1 and 20 keV [147]. The spatial dependence of the light collection efficiency of the S2 has been neglected.

Despite these simplifications, the simulation still allows to study qualitatively the influence of general parameters on the ER band shape.

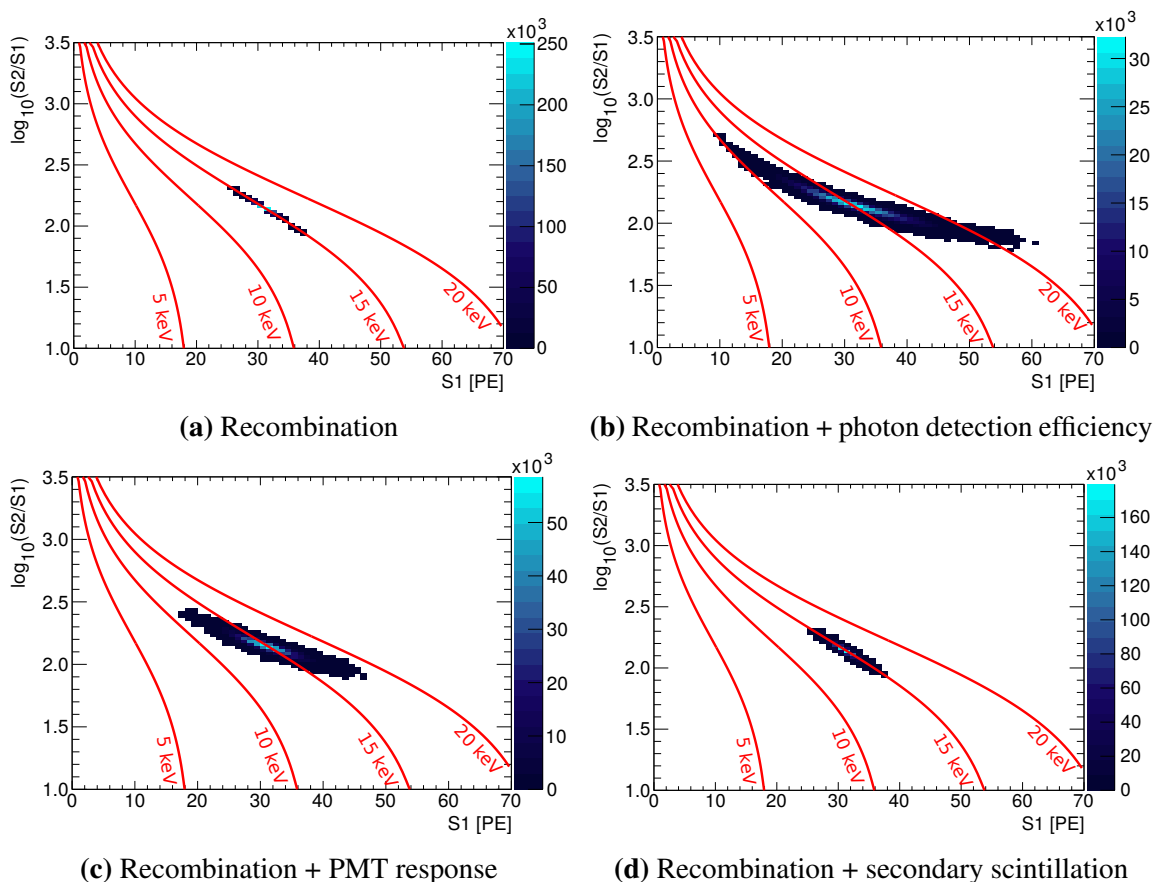


Figure 4.14: Distribution of simulated events in discrimination space from a mono-energetic line of 15 keV. Only signal fluctuations from the sources indicated below each panel are applied whereas all others are switched off. See text for more explanations.

Variations of the Signal Fluctuations

The ER band shape is primarily driven by the fluctuations in the S1 and S2 signals. The signal fluctuations implemented in the simulation are the electron-ion recombination, photon detection efficiency, resolution of the PMT response to S1 signals and the resolution of the proportional scintillation. A further limitation of the S2 resolution is given by the electron attachment due to impurities in the xenon. This has not been taken into account in the simulation. It primarily influences signals from small energy depositions, where only a small number of electrons is generated and therefore, the variations in the number of amplified electrons has a bigger impact.

In order to visualize the influence of the signal fluctuations on the ER band shape, simulated events of a mono-energetic line of 15 keV are plotted in discrimination space in Figure 4.14. Constant lines of energy are marked in red for 5, 10, 15, and 20 keV. In Figure 4.14a only recombination fluctuations are allowed, whereas all other signal fluctuations were turned off in the simulation. If always the same number of electron-ion pairs would recombine after their creation, all events could be found in one bin. However, due to the variations in the number of recombinations, the events can be found along the 15 keV energy line marked in red.

This fluctuation influences the width of the ER band. The recombination fluctuations only have to be taken into account when looking at S1 and S2 individually, as done in discrimination space. When combining the two signals to infer the deposited energy (Equation 2.8), the mono-energetic 15 keV line could be recovered with a 100% resolution in the simulated data. This is different for all following fluctuations, that are detector related and therefore influence the energy resolution.

Figure 4.14b shows the case, where additionally to the recombination fluctuations, the binomial smearing of the number of detected photons due to the photon detection efficiency was applied. Clearly, this fluctuation has the largest impact on the ER band width compared to the other signal variations. The events are not distributed along the 15 keV line any more but extend over a wide range in S1. This shows that a deposition of a single energy does also influence the ER band shape at smaller and higher S1 than its mean S1. The mono-energetic line contributes to the band width due to tails toward small discrimination parameters at high S1 and vice versa.

In Figure 4.14c, the recombination fluctuations and the smearing of the number of collected photo-electrons N_{PE} due to the PMT resolution are turned on in the simulation. Again, the events extend over a wider S1 region even though the impact is not as big as for the signal fluctuations induced by the photon detection efficiency.

Finally, Figure 4.14d visualizes the influence of the resolution of the secondary scintillation in addition to the recombination fluctuations. Since it only has an impact on the S2, the 15 keV line becomes broader compared to the case where only the recombination fluctuations are applied.

Variations of the Spectrum

After having shown how a mono-energy line is translated into the discrimination space, the influence of a whole spectrum on the ER band shape is studied.

Figure 4.15a shows the simulated ER band of a flat energy spectrum in discrimination space, together with lines of constant energies yielding 5, 10, 15, and 20 keV. All signal fluctuations and a S2 threshold of 150 PE have been applied. The other panels in Figure 4.15 visualize the influence of variations from the default parameters of the simulation. A truncated spectrum (Figure 4.15b) results in a diagonal cutoff since the band is not any more populated at high values of the discrimination parameter. As seen in the study of the mono-energetic line, this region consists of higher energetic events that are downwards fluctuated in S1. The diagonal cutoff of the simulated ER band is very similar to what is observed in tritium data (see Figure 4.9). When no S2 threshold is applied as in Figure 4.15c, the band looks approximately symmetric in the discrimination parameter at low S1, whereas the asymmetry is increased when applying a higher threshold of 450 PE, as done in Figure 4.15d. Note that it was zoomed into the low S1 region in both figures. The low energetic events that fluctuate to higher S1 are suppressed by the S2 threshold and the band at low S1 consists primarily of events fluctuating downwards in S1 from higher energies.

Following the procedure explained in Section 4.5.1, the Gaussian ER band means and the 1σ widths can be plotted as functions of S1 in order to compare the influences of the parameter variations on the band shape. This is done in the Figures 4.16 and 4.17.

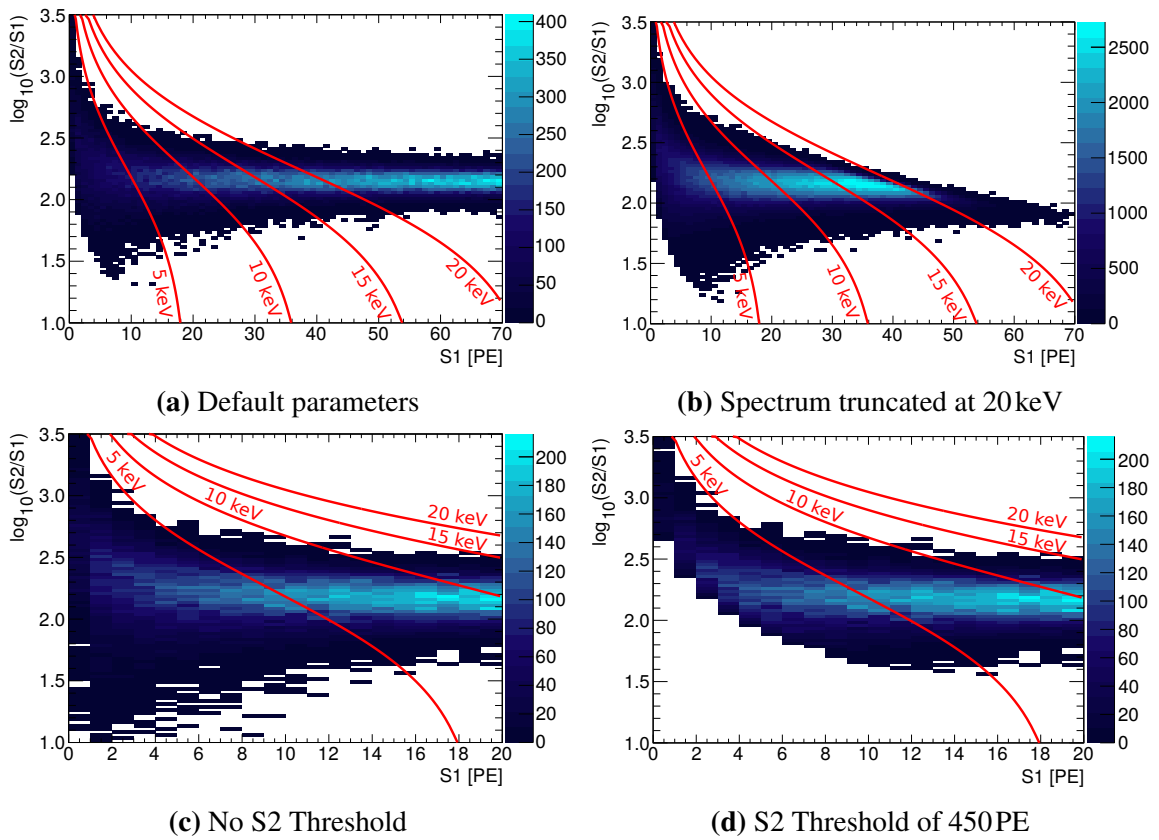


Figure 4.15: Visualization of influences of different parameters on simulated ER bands using a flat energy spectrum as input. (a) shows the ER band for the default values listed in the text. Deviations from those are indicated below each figure.

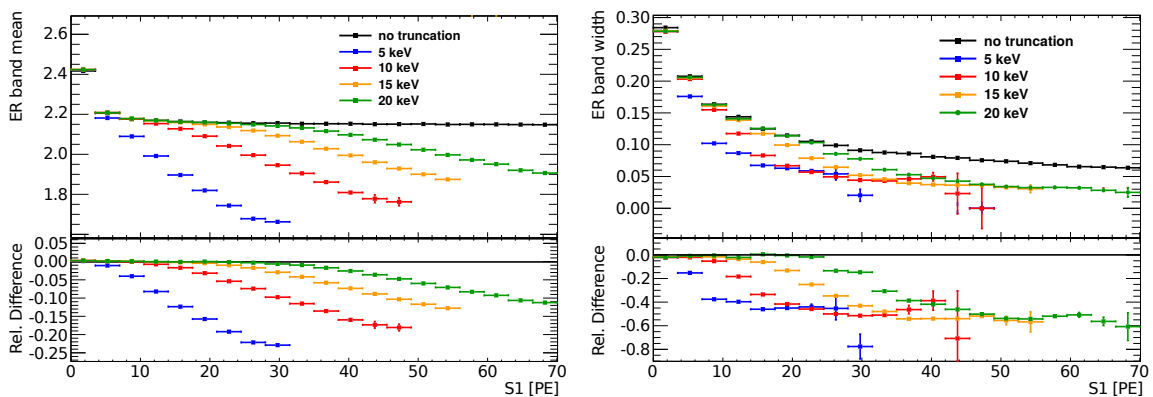


Figure 4.16: Influence of the cut-off energy (indicated in the legend) of a flat spectrum on the ER band mean (left) and the ER band 1σ width (right). The lower panels show the relative difference to the shape parameters of a spectrum without truncation.

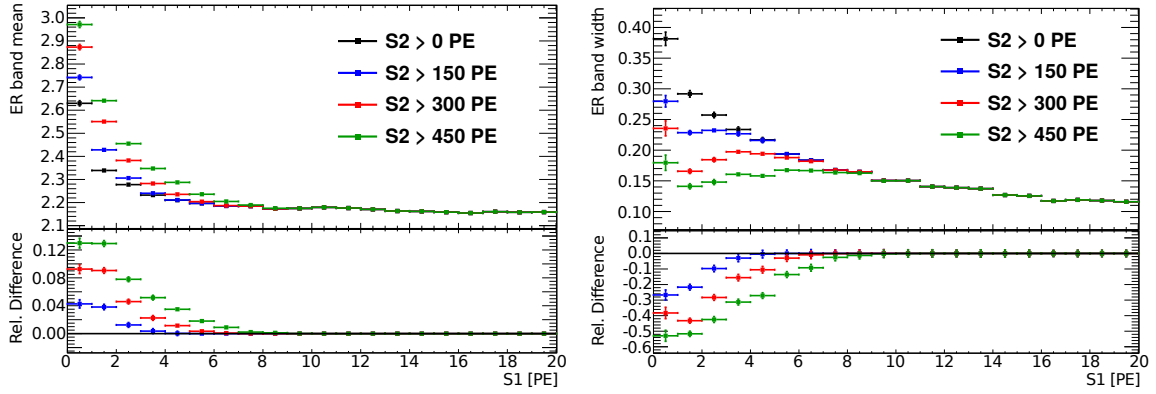


Figure 4.17: Influence of the S2 threshold on the ER band mean (left) and the ER band 1σ width (right). Note that it was zoomed into the low S1 region. The applied values for the respective graph are indicated in the legend. The lower canvas contains the relative difference to the case where no threshold has been used.

Figure 4.16 compares the ER band mean (left) and width (right) of simulated data, featuring a flat energy spectrum that is cut-off at different energies as indicated in the legend. The lower panels show the relative difference to the case of no truncation (black). The mean is falling off for high S1 due to the diagonal cutoff of the band. Consequently, the width becomes smaller for high S1. The picture is similar to the tritium calibration data which leads to the conclusion that the decreasing mean and width of the tritium ER band can be attributed to the fall-off of the tritium beta spectrum (see Figure 4.9).

Figure 4.17 shows the influence of the S2 threshold on the band shape parameters. Note that it was zoomed into the low S1 region. The applied threshold values are indicated in the legend. The lower panels reflect the relative difference to the case where no S2 threshold has been used (black). With an increasing S2 threshold the mean increases, while the width becomes smaller owing to the cut-off of the lower part of the band at small S1. An increased mean at low S1 is also seen in the tritium data with respect to thorium and ^{220}Rn (see Figure 4.13). This effect can be traced back to the spectral shape of the tritium data. The very steep fall-off of the tritium energy spectrum toward lower energies (see Figure 4.9) results in a larger fraction of events that fluctuate downward in S1 from higher energies, than those that fluctuate upward from lower energies. Hence, the ER band at low S1 and high values for the discrimination parameter is more populated than the ER band region for the vice versa case. Hence, the steep fall-off of the S2 spectrum of tritium creates the same effect as an S2 threshold and shifts the ER band mean upwards.

It can be concluded that the observed differences of the tritium ER band shape compared to the bands from the ^{220}Rn or thorium sources result from the different spectral shape of tritium. In the following section we will investigate the impact of this ER band shape deviation on the WIMP search, when calibrating the ER background of the detector with tritium.

4.6 Impact of the Calibration on the Dark Matter Results

In the previous section, the finding was that the shape of the ER band in tritium calibration data is significantly different than for data from the thorium and ^{220}Rn sources. In this section, the influence of this discrepancy on the dark matter search result, when using the calibration data to model the ER background, is investigated.

The overall background model in a XENON100 dark matter search was composed of a NR, a Gaussian ER, and an accidental coincidence component. The NR background component was predicted in the three science runs of XENON100 [56] to account only for about 3% to 10% of the total background rate in the WIMP search region. The spectral shape of accidental coincidences was assumed to be flat in previous XENON100 publications and was re-evaluated in the latest result [56]. Increasing rates for small signal values were found by selecting isolated S1 and S2 peaks from data and pairing them randomly. Accidental coincidences present the second largest background and yield fractions between 20% and 35% [56].

The Gaussian ER model in XENON100 was derived from thorium and ^{60}Co calibration data by a Gaussian parametrization of the ER band similarly to the procedure described in the previous section. It has been normalized to the events in the dark matter data above the WIMP search region. The Gaussian ER model represented the largest background component in the region of interest in all XENON100 WIMP searches and its rate was ranging between fractions of 55% and 72% of the total background rate [56]. For the evaluation of an upper limit on the WIMP nucleon-cross section, the outcome of all three background models was statistically treated in the parameter space of $cS1$ vs. $cS2_{\text{bottom}}$ by a likelihood function, following the procedure described in [148].

In this work, a simplified analysis was performed, with the aim to compare the differences in the search for a signal when modeling the Gaussian ER background with the three different sources ^{220}Rn , tritium and thorium. Hence, only the Gaussian ER background component has been taken into account while neglecting the contributions from accidental coincidences and NR. Furthermore, the observed data was interpreted following the procedure of Feldman and Cousins [149]. Confidence intervals on the number of signal events compatible with the observation, given the background prediction, were derived without interpreting the limits in the context of WIMP candidates.

Unfortunately, no dark matter data has been taken under the same conditions as the calibration data studied in this work. Therefore, the dark matter data from the published 225 live days of XENON100 [150] is analyzed.

The region of interest in this study will be defined by $cS1 \in [5, 30]$ PE. The upper bound has been adapted from previous XENON100 publications. The lower bound is motivated by two considerations: Firstly, the energy spectra of background, thorium and ^{220}Rn data show discrepancies below 5 PE (see Section 4.4) and secondly, less thorium calibration data is available in this run than in the science run. Hence, the ER band shape especially at low $cS1$ is less defined.

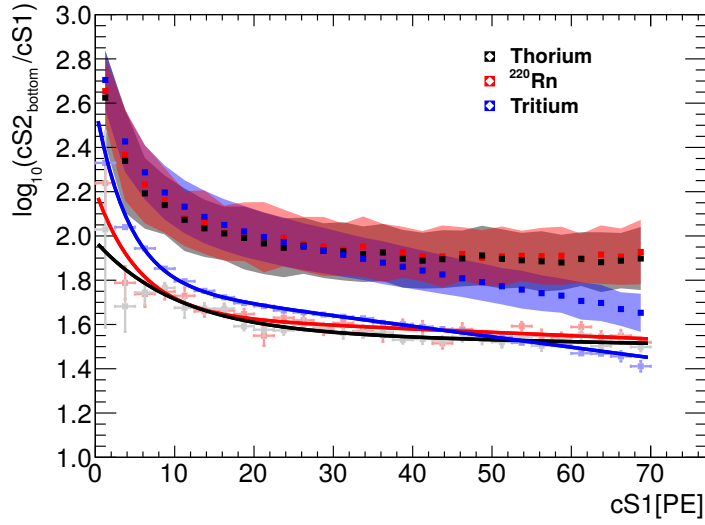


Figure 4.18: Comparison of ER band models evaluated from the thorium (black), ^{222}Rn (red), and tritium (blue) sources in the 34kg FV. The squares mark the Gaussian mean in each cS1 interval of 2.5 PE and the filled regions the 1σ width. The opaque data points below the band show the Gaussian quantiles from which the 99.75% discrimination lines have been constructed by fitting the empirical function $f(\text{cS1}) = e^{\alpha\text{cS1}} + \beta\text{cS1} + \gamma$.

4.6.1 Electronic Recoil Background Model

In the latest XENON100 WIMP searches, the electronic recoil background model was constructed as a probability density function (PDF) in the discrimination space or in cS1 versus cS2_{bottom} [150, 56]. However, analog to the optimum interval analysis employed for the first results of XENON100 [146], for this study the number of events below the ER band will be counted without considering the individual probability of each observed event.

In this work, the region below the ER band is confined in discrimination space by the energy region of interest $\text{cS1} \in [5, 30]$ PE and a so-called *discrimination line* that defines the degree of rejection of ER events.

The discrimination line is constructed from the ER band in calibration data by evaluating the corresponding Gaussian quantiles in each cS1 interval. The dependence of the quantiles on cS1 can be described phenomenologically by a function of the form

$$f(\text{cS1}) = e^{\alpha\text{cS1}} + \beta\text{cS1} + \gamma, \quad (4.6)$$

where α , β , and γ are empirical parameters that are determined by a fit in the region $\text{cS1} \in [5, 60]$ PE. Consequently, a 99.75% discrimination line, for example, is constructed such that 99.75% of the ER events lie above the line in discrimination space. The fit region has been extended to higher cS1 with respect to the region of interest in order to make use of the additional information on the ER band shape.

Figure 4.18 shows the ER band model of the three calibration sources thorium (black), ^{220}Rn (red), and tritium (blue). The squares mark the ER band means in each cS1 interval of 2.5 PE and the filled areas indicate the 1σ width. As an example, the 99.75% discrimination lines are displayed below the bands together with the data points that were used to construct them. The uncertainties on the quantiles reflect the combined uncertainties of the ER mean and width.

The number of ER events below any discrimination line was evaluated by scaling the three different models to the number of events observed in the dark matter search data above the source dependent 90% discrimination line. In this case, the 90% line has been chosen to decrease the statistical uncertainties on the scaling factor.

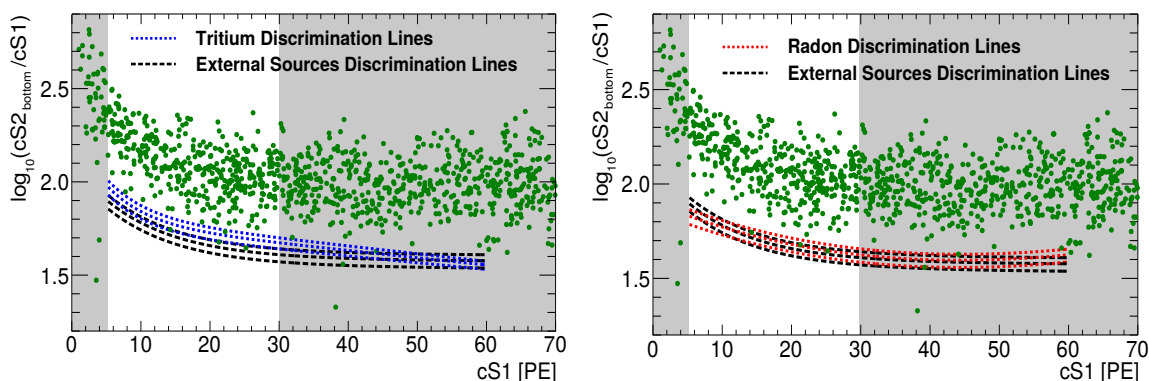


Figure 4.19: Left: Dark matter search data of XENON100 science run (green) with 99.5%, 99.75%, and 99.9% discrimination lines evaluated on tritium data (blue) and on external calibration data (black). The region of interest is left un-shaded to guide the eye. **Right:** Same data as on the left but the tritium discrimination lines were replaced by the ones evaluated from ^{220}Rn data.

The dark matter data from the published 225 live days of XENON100 [150] was acquired under different detector conditions than the data of this work. The observed higher S2 yield in the calibration data of this study is corrected in order to match the S2 yield present in the dark matter search data. Hereby, the mean and width of the ER band from thorium data acquired within this work, are scaled to the values of the ER band of calibration data acquired in the science run. The derived scaling factors are applied to the ER band parameters in tritium and ^{220}Rn data.

4.6.2 Results

Knowing the number of expected ER background events below the 99.5%, 99.75%, and 99.9% discrimination lines, an upper limit on the number of signal events can be evaluated by comparing the prediction to the observation. Figure 4.19 left shows the three mentioned ER discrimination lines evaluated from tritium data (blue) and from the external calibration data taken during the dark matter run (black). The discrimination lines, inferred from the calibrations performed during the science run, were found to be compatible with the lines gained from the thorium data of this study after correcting for the different detector conditions. The green data points in Figure 4.19 present the dark matter search data, while all selection criteria used in [150] have been applied. To guide the eye, the space outside of the region of interest has been shaded. All three discrimination lines evaluated on tritium data are systematically shifted upward as a result of the smaller ER band width with respect to the bands from the ^{220}Rn or external calibration sources. Only above 50 PE in cS1, the tritium discrimination lines start falling below the lines of the external sources due to the decreasing tritium ER band mean induced by the low end-point of the beta spectrum. In Figure 4.19 right, the same data as in the left panel is presented, together with the discrimination lines from ^{220}Rn data in red and the lines from the external calibration sources in black. The ^{220}Rn discrimination lines are compatible with the lines evaluated on the external sources, as expected from the compatible ER band shapes in those two calibration datasets.

Calibration source	N_{obs}	N_{exp}	90% CI	90% Sensitivity
99.5% Discrimination				
External Sources	3	2.0 ± 0.03	[0, 5.4]	
Tritium	4	1.88 ± 0.03	[0, 6.7]	3.9
^{220}Rn	3	1.97 ± 0.03	[0, 5.5]	
99.75% Discrimination				
External Sources	0	1.00 ± 0.02	[0, 1.6]	
Tritium	3	0.94 ± 0.02	[0.2, 6.5]	3.3
^{220}Rn	1	0.99 ± 0.02	[0, 3.4]	
99.9% Discrimination				
External Sources	0	0.40 ± 0.01	[0, 2.0]	
Tritium	2	0.38 ± 0.01	[0.2, 5.5]	2.9
^{220}Rn	0	0.39 ± 0.01	[0, 2.0]	

Table 4.3: Summary of number of observed (N_{obs}) and expected events (N_{exp}) below the respective discrimination line that was calibrated with one of the three sources thorium/ ^{60}Co , tritium or ^{220}Rn . The uncertainties on N_{exp} account for the statistical uncertainty of the scaling to the number of events above the source dependent 90% discrimination line. The resulting Feldman-Cousins 90% confidence interval (CI) is given for each configuration as well as the 90% sensitivity. In contrast to the CI, the sensitivity value was not calculated but taken from Table XII in [149].

Using the procedure of Feldman and Cousins [149], an upper limit at a 90% confidence level on the number of signal events, compatible with the observed number of events below the respective discrimination line, can be calculated. The results are summarized in Table 4.3 for the ER background expectations N_{exp} , the number of observed events N_{obs} and the corresponding 90% confidence interval (CI) on the number of signal events. Additionally, the 90% CL sensitivity is given for reference. It has not been explicitly calculated for the respective values of N_{exp} and N_{obs} but was extracted from Table XII in [149]. The table has a granularity of 0.5 for N_{exp} and therefore, is yielding the same value for all three sources at the same discrimination level. The sensitivity states the average upper limit that would be obtained, when performing a multiplicity of measurements under the assumption that no signal is present. The uncertainties on N_{exp} arise from the statistical uncertainty on the factor that scales the background model to the exposure of the dark matter.

For a 99.5% discrimination, N_{obs} , N_{exp} , and the CIs of the external calibration sources and ^{220}Rn data are compatible. Tritium shows a lower value for N_{exp} due to the higher discrimination lines that result in a smaller value for the scaling factor. For the same reason, a higher number of events is observed below the discrimination line. The combination of a lower background expectation and a higher number of events observed in the signal region results in a larger upper limit on the number of signal events. Interpreting this in the context of a specific dark matter candidate, a weaker upper limit could be set on its cross section.

Increasing the discrimination level to 99.75%, the discrepancy between tritium and the other two sources becomes more evident. While the lower bound of the CI of ^{220}Rn and external

	g_1 [PE/photon]	g_2 (cS2 _{bottom}) [PE/electron]
XENON100	0.052 ± 0.001	8.8 ± 0.4
XENON1T	0.144 ± 0.007	11.5 ± 0.8

Table 4.4: Comparison of photon (g_1) and electron (g_2) gains between the XENON100 and XENON1T detectors. See text for more explanations.

calibration data is compatible with zero, the increased number of observed events for tritium and the decreased number of expected events results in a non-zero lower bound of the CI. This suggests the presence of a signal at 90% confidence level. A similar situation is present when applying a 99.9% discrimination. Furthermore, the CIs of tritium data always show a higher upper limit than expected from the sensitivity. This is an indication for the under-estimation of the ER background. In contrast, the values of N_{exp} for ^{220}Rn and external calibration data are compatible with each other within the uncertainties and are also in good agreement with the observation.

It can be concluded that modeling the ER background in the presented way with tritium ER data, under-estimates the background and may even result in the interpretation of having observed a signal. The reason for this different behavior for tritium data lies in its spectrum that is not similar to the ER background of the experiment. It influences the ER band shape as shown in Section 4.5.2.

It should be stressed that this analysis does not present a thorough dark matter analysis that takes into account all background components and uncertainties, but used a simplified approach that concentrates on the relative comparison of the results when using the three investigated calibration sources.

To avoid a bias from the fact that tritium data is not compatible with the background of the experiment, the spectrum has to be taken into account in the background model by either correcting for the spectral shape or using Monte Carlo simulations. A more detailed discussion on the prospects of a tritium ER calibration for a dark matter search will follow in Section 4.8.

4.7 Discrimination Power in XENON100 and XENON1T

Comparing the separation of the ER band from the NR region holds information about the discrimination power of background within a WIMP search and therefore, about the discovery potential of a dark matter signal. As discussed in Section 4.5.2, fluctuations in the S1 and S2 signals determine the band width. The higher the detection efficiency for the generated quanta, the smaller the fluctuations in relation to the measured signal. Consequently, the photon and electron gains g_1 and g_2 , i.e., the number of detected photoelectrons per quantum that is generated at the interaction site (see Equation (2.8)), plays an important role.

Table 4.4 lists the g_1 and g_2 values evaluated by fitting the anti-correlation of cS2_{bottom} and cS1 for mono-energetic ER lines measured by XENON100 and XENON1T [145, 65]. Due to better performing PMTs in XENON1T, the g_1 of this experiment is almost three times as high as for XENON100 while only a small improvement of a factor of 1.3 with respect to XENON100 is present for g_2 . Consequently, a smaller ER band mean and 1σ width is

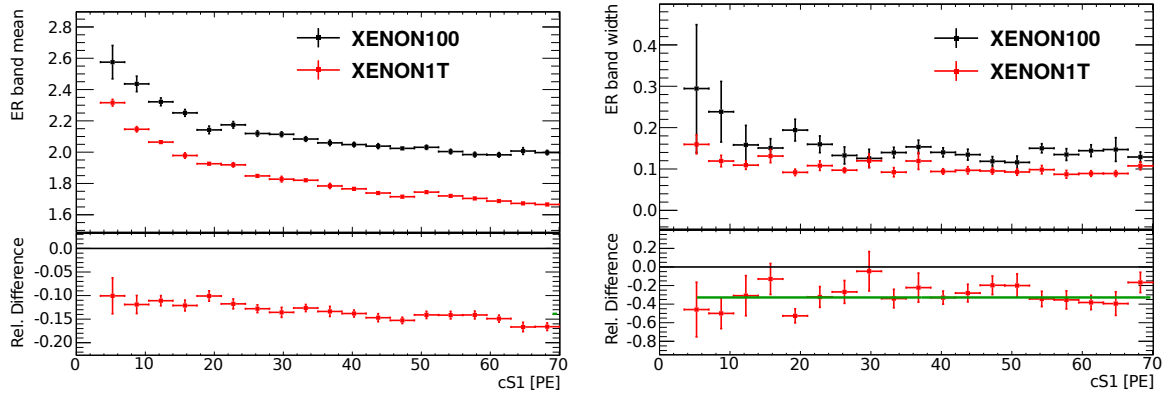


Figure 4.20: Comparison of ER band mean (left) and width (right) between XENON100 and XENON1T. The parameters have been extracted from ^{220}Rn calibration data. The x-axis of XENON100 has been scaled by a factor of 2.77 in order to match the cS1 energy scale of XENON1T.

expected in XENON1T data. This is visible in Figure 4.20 where the ER band means (left) and 1σ widths (right) are compared between XENON100 (black) and XENON1T (red) as functions of cS1. The band parameters have been extracted from ^{220}Rn calibrations in both detectors. For a better comparison, the x-axis of the XENON100 data is scaled by a factor of 2.77, the ratio of the g_1 values of the two xenon detectors. The lower panels in both plots show the relative difference of the XENON1T graphs with respect to XENON100.

The ER band mean of XENON1T data is shifted by 14% and the width by 33% to lower values. The slope visible in the ER band mean of XENON1T for large cS1 is typical for the smaller S2 yield but larger S1 yield. For higher energetic ER, the cS1 becomes non-negligible compared to the measured $\text{cS2}_{\text{bottom}}$ and hence, the logarithm of the ratio of the two signals is decreasing with cS1.

The ER band width in XENON1T is constantly reduced over cS1 with an average of $-(33 \pm 3)\%$, as determined by the fit of a constant (solid green line in Figure 4.20 right).

The observed decrease in the ER band width in XENON1T with respect to XENON100, is expected to improve the discrimination of ER events to NR. This is investigated in Figure 4.21. On the left, the 99.75% discrimination line as well as the NR and ER medians for XENON100 (green colors) and XENON1T (blue colors) are shown in discrimination space in the WIMP search regions of the two experiments while the XENON100 x-axis has been scaled in order to match the one of XENON1T. The lines for ER have been determined from ^{220}Rn data and the NR median was extracted from data of the external $^{241}\text{AmBe}$ neutron source [75]. While for XENON100 the discrimination line (dark green dashed) is situated beneath the NR median (light green), the XENON1T discrimination line (dark blue dashed) is almost identical with the NR median in XENON1T (light blue). The higher ER discrimination line with respect to the NR median in XENON1T compared to XENON100 is a result of the decreased ER band width in XENON1T. The lower panel in Figure 4.21 left shows the absolute difference between the ER and NR means for XENON100 (green) and XENON1T (blue). Even though the difference is smaller in XENON100 than in XENON1T below 25 PE, the discrimination line in XENON100 is still located below the NR median in

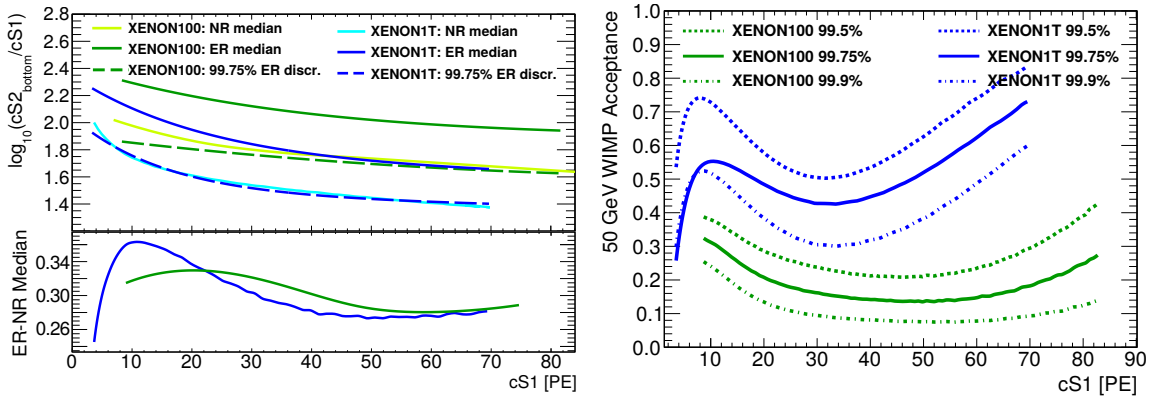


Figure 4.21: Left: Comparison of the 99.75% discrimination line to the NR and ER medians for XENON100 (green colors) and XENON1T (blue colors) in the WIMP search regions of the two experiments. The XENON100 x-axis has been scaled to the XENON1T cS1 energy scale by multiplying with a factor of 2.77. The lower panel compares the differences between the ER and NR medians in XENON100 (green) and XENON1T (blue). **Right:** Acceptances to a simulated 50GeV WIMP signal in the XENON100 (green) and XENON1T (blue) detector at 99.5% (dot-dashed), 99.75% (solid), and 99.9% (dashed) ER discrimination.

that region. It can be concluded that the ER width is dominating over the separation of the ER and NR regions and is therefore decisive for the discrimination power in XENON100. Consequently, a smaller acceptance to WIMP signals at a certain discrimination level is expected for XENON100. Above 25 PE, the separation between the ER and NR medians is better in XENON1T with respect to XENON100. Combined with the smaller ER band width, a better discrimination can be observed in XENON1T in that energy region.

The improved discrimination power in XENON1T becomes more clear when comparing the acceptances to a 50GeV WIMP signal in XENON100 and XENON1T as done in Figure 4.21 right. The acceptance is plotted for 99.5% (dot-dashed), 99.75% (solid), and 99.9% (dashed) ER discriminations as a function of cS1. As for the left graphic in the same figure, the x-axis of the XENON100 lines has been scaled to the XENON1T cS1 energy scale. The acceptances in XENON1T are 20 to 40 % higher than in XENON100 depending on the deposited WIMP energy. The total acceptance in the dark matter search energy region for a 99.75% discrimination yields 49% in XENON1T and only 20% in XENON100. Hence, the significant improvement of the sensitivity of the XENON1T detector to dark matter by two orders of magnitude with respect to XENON100 [108], is not only owing to the 28 times reduced background level and the 30 times larger fiducial mass of XENON1T, but is also due to the higher photon gain.

The increased gain is attributed to a higher light collection efficiency within the detector, as well as to the higher quantum efficiencies of the XENON1T PMTs. The PMT quantum efficiency multiplied by their electron collection efficiency makes up a ratio of about 1.6 between XENON1T and XENON100 [75, 94]. Hence, the missing factor of 1.8 to equal the ratio of 2.8 between the photon gains of the two detectors has to come from the higher number of PMTs, the improved geometry of the arrays, the usage of high reflectivity materials, high opacity meshes, and the installation of the field shaping rings outside of the TPC such

that large flat reflector surfaces are present in XENON1T [105].

4.8 Summary and Discussion

In this chapter, the two novel ER calibration sources of the radio-active isotopes ^{220}Rn and tritiated methane (tritium) were investigated in terms of their potential to calibrate the ER background region for a dark matter search.

Due to the liquid xenon's high stopping power, external sources of gamma emitters as used at XENON100, cannot induce low energetic events in the FV of a multi-ton LXe detector as XENON1T with high statistics. The problem is addressed with sources of radio-isotopes that are directly dissolved in the LXe. It has been shown with tests in XENON100 and in XENON1T, that the activity can be spread within the detector and that the ER events are close to homogeneously distributed in the FV (see Section 4.3). Furthermore, ER rates of about 20 mBq for ^{220}Rn in XENON100, 40 mBq for ^{220}Rn in XENON1T and 772 mBq for tritium in XENON100 have been found in the respective FV and WIMP search energy region. Those rates are several orders of magnitude higher than the background levels of the two detectors and therefore allow for the collection of calibration data within days.

In terms of the source performance, tritium seems to be the most promising due to its high ER rate and the high efficiency with which the source is brought into the detector. However, while the removal of the activity introduced by the ^{220}Rn source decays within one week, the injected tritiated methane has to be removed actively owing to the relatively long half-life of tritium. This turned out to be non-trivial in the tests conducted with XENON100 [145]. Furthermore, the two internal sources differ in the emitted ER spectra (see Section 4.4). ^{220}Rn induces ER, homogeneously distributed in the low cS1 region while the tritium beta spectrum has only a low end-point of 18.6 keV and hence, is not flat in the WIMP search energy region of 1 – 12 keV in ER energies. However, a flat spectrum is observed in background data.

96% of the ER events in the ^{220}Rn data are induced by gammas from decays in the veto region [139]. The small discrepancy seen in the ER bands of thorium and ^{220}Rn data could be attributed to detector related fluctuations in the S2 yield. A potential difference in the energy deposition of gamma and beta interactions could not be investigated by comparisons between ^{220}Rn and thorium data. Such studies are also not possible with tritium data due to the overwhelming influence of the spectral shape of tritium decays. Maybe future studies in XENON1T are able show the differences between ER induced by gamma and beta radiation.

It has been shown in Section 4.5 that the ER band shape is significantly different for the data taken with the tritium source with respect to ^{220}Rn or the well established gamma sources in XENON100. This can have a significant impact on the dark matter result as discussed in Section 4.6. When using the tritium calibration as it is, to model the ER background for a dark matter search, the background is underestimated and signal claims are possible whereas the background prediction inferred from ^{220}Rn data is compatible with the observation.

In order to use tritium data for the calibration of the ER background, two options are conceivable: The data can be corrected for the spectral shape similarly to [142] or a Monte Carlo could be fit to tritium data. The first option implies that the detector resolution and the

recombination fluctuations are well known at the given detector conditions in order to take into account the signal variations. The second option implies that the detector response to ER events is fitted by a Monte Carlo Markov Chain algorithm, where the calibration source specific recoil spectrum is implemented. This was done for the first dark matter search in XENON1T (see Chapter 5). Parameters like the photon yield and recombination fluctuations can be extracted from the fit result and could be fed into the MC together with the ER spectrum expected from background. The result would be simulated data that takes into account the detector response to ER without potential biases from the energy spectrum of the calibration source.

A further disadvantage of the tritium source is, that its removal from the detector is not ensured by waiting for its radioactive decay due to the relatively long half-life of 12 years. Capturing the tritiated methane in a hot zirconium getter in the gas purification loop did not result in the ER rate, present before the deployment of the source in XENON100 [145]. A possible explanation of the remaining activity could be exchange reactions of hydrogen between the methane and the PTFE walls that confine the active detector volume. This is the reason why this source has not been used in XENON1T so far. Problems with the removal of tritiated methane from a LXe detector have also been encountered by PandaX [151].

The advantage of the ^{220}Rn source is its flat spectrum that is close to what is expected from the ER background in XENON100 as well as in XENON1T. Hence, the calibration data could be used directly for background modeling without any Monte Carlo fitting or corrections. No additional information on the detector resolution or recombination fluctuations would be needed. Furthermore, as an internal source, ^{220}Rn is expected to generate events very similar to the dominating background from ^{222}Rn in XENON1T.

This novel source was successfully used for the first time in a dark matter direct detection experiment and its data served for the ER calibration in the first science run of XENON1T. As a result of the shown good performance, other LXe dark matter experiments like LZ are also considering to use ^{220}Rn for detector calibrations [152].

Using the data gained from ^{220}Rn deployed in XENON1T and XENON100, the power to discriminate between ER and NR in the two LXe detectors has been compared. XENON1T shows a better discrimination power yielding in a factor of 2.5 higher acceptance to a 50 GeV WIMP with respect to XENON100. As a result of the higher light collection efficiency within the detector and better performing PMTs, fluctuations in the S1 signal are reduced, which leads to a smaller ER band width.

The increased sensitivity of XENON1T to dark matter was exploited in the first dark matter search of this new detector. The corresponding WIMP search analysis is presented in the following chapter.

Chapter 5

First Dark Matter Result of XENON1T

The first dark matter result of XENON1T reports on 34.2 live days of dark matter search data acquired between November 22, 2016 and January 18, 2017. At the time of writing, this analysis results in the most stringent exclusion limit on spin-independent WIMP-nucleon cross sections above WIMP masses of 10 GeV. This chapter summarizes the analysis of the first science run of the XENON1T detector. The data properties and the event selection criteria are briefly outlined in Section 5.1 and a short introduction to the nuclear recoil (NR) calibration data is given in Section 5.2. Special focus lies on the study of the electronic recoil (ER) data taken with the novel ^{220}Rn source introduced in Chapter 4. This source was used for the first time within a dark matter search for the calibration of ER background events induced natural gamma and beta radiation. This component presents the dominating background in XENON1T. The quality of the taken ^{220}Rn calibration data is monitored and its compatibility with the ER background present in the detector is verified in Section 5.3. It was shown in Chapter 4 that differences between calibration and background data can lead to a bias in the dark matter result. The ^{220}Rn data was further used to define a selection criterion to remove events from the the signal region in the dark matter search data. This so-called *blinding* avoids tuning the analysis on potential signal events (blind analysis). At the same time, the ER background region in the dark matter data was ensured to be accessible for studies of selection criteria and background predictions. Furthermore, so-called *wall events* are studied in Section 5.4. Those are interactions that take place in close proximity to the detector wall and restrict the choice of the fiducial volume (FV) due to mis-reconstruction toward smaller radii. The total background model, as well as the prediction for the background contribution of wall events, are described in Section 5.5. Section 5.6 presents the exclusion limit on spin-independent WIMP-nucleon cross sections. The chapter is concluded with Section 5.7 where the findings are summarized in the context of other dark matter search experiments.

5.1 Data Quality and Event Selection

The data quality of the first XENON1T science run was ensured by sufficient detector stability, such that fluctuations of parameters like temperature, pressure and liquid level did not impact the analysis. While the xenon was continuously purified, deviations were within 0.1% for the temperature and pressure and within 8% for the liquid level. The electron lifetime

was monitored regularly and was taken into account in the correction of the charge signal S2. The photo-multiplier tube (PMT) high voltage was constant for all sensors while 35 of them were off or not considered in the analysis due to a low single photoelectron (PE) detection efficiency or performance issues. The response of the PMTs was monitored by periodic calibrations with LED pulses.

The data acquisition (DAQ) efficiency for single photoelectron pulses was, on average, 92% during the science run with deviations smaller than 2%. An average DAQ live time of 92% could be achieved during the run.

The event selection criteria are similar to the ones used in XENON100 [56] and were optimized to extract signals from physical interactions and to reduce non-WIMP like backgrounds. All criteria have been developed either on calibration data or on simulated waveforms and were tested on the ER events that were accessible within the blinded WIMP search data (see Section 5.3 for the definition of the blinding criterion).

The event selection requirements can be divided into criteria that select physical interactions (noise and data quality criteria) and those that enhance the signal over background ratio (WIMP search criteria). The noise and data quality requirements comprise the following:

- In order to reduced the probability of a signal being made of PMT dark counts, a threefold PMT coincidence within a time window of 50 ns is requested for any S1 or S2 candidate.
- Each event is required to contain a S2 above a threshold of 200 PE.
- The integral of all signals in the region before the S2 is not allowed to be larger than 300 PE. This excludes events that are made up of signals from uncorrelated single electrons or PMT dark counts.
- Any event closely following a high energy event within a few nanoseconds is vetoed in order to neglect signals coming from the single electrons induced by photo-ionization of impurities in the LXe. This effect is primarily seen after large S2 signals.
- Since diffusion causes a broadening of the electron cloud, the width of the S2 pulse has to be correlated to the event's depth in the TPC.
- The S1 and S2 PMT hit patterns are compared to the reconstructed event position using a likelihood function to measure the consistency. This and the previous requirement favor S1 and S2 signals that come from the same interaction.

The requirements on potential WIMP signals are the following:

- Having very low interaction cross sections with nucleons, WIMPs are expected to scatter only once in the TPC. Hence, only events that contain a single interaction are selected. Any additional S2 signal has to be consistent with the characteristics of a single electron signal originating from photo-ionization of impurities or delayed extraction of electrons from the liquid phase.
- The active muon veto is used to reduce the background from muon-induced neutrons to a negligible level by requiring each event not to take place within 10 ms after a muon veto trigger.

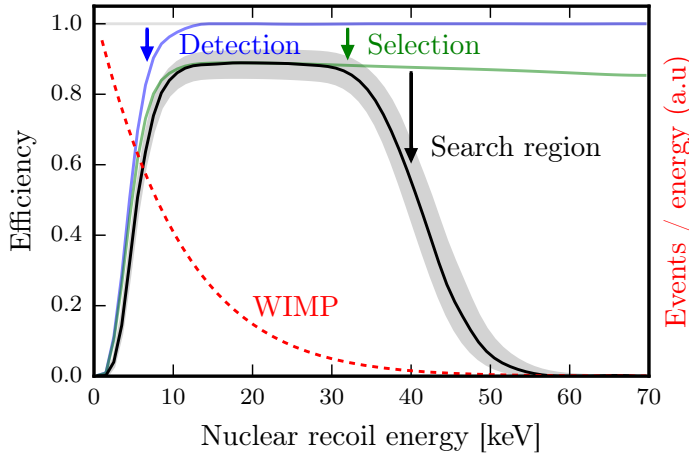


Figure 5.1: Comparison of NR detection efficiencies at three analysis stages as functions of recoil energy. All curves have been evaluated in the fiducial volume. For reference, the energy spectrum of a 50 GeV WIMP is shown in red. See text for more explanations. Figure from [53].

- A cylindrical fiducial volume (FV) containing a xenon mass of (1042 ± 12) kg is used. The FV was defined before unblinding the WIMP signal region by studying the spatial distribution of the accessible ERs in the blinded dark matter search data (see Section 5.3.2).

The impact of the selection criteria on the NR detection efficiency (blue) is shown in Figure 5.1 as a function of NR energy. The detection efficiency comprises the efficiency for recording S1 and S2 signals from physical interactions and was evaluated using a Monte Carlo code that simulates the complete chain of event generation, including shapes of S1s and S2s, light propagation, and the detector-electronics chain. The threefold PMT coincidence requirement causes the fall-off of the detection efficiency below 10 keV.

The impact of the above listed event selection criteria on the NR detection efficiency was evaluated on control samples in calibration data and on simulated events. The event selection reduces the efficiency (green curve in Figure 5.1) from 1.0 to 0.82 above 10 keV due to an overlap of the noise and background population with the signal region.

The WIMP search is restricted by requesting $cS1 \in [3, 70]$ PE and $cS2_{\text{bottom}} \in [50, 8000]$ PE where $cS2_{\text{bottom}}$ is the corrected S2 signal recorded by PMTs located in the bottom array. The impact of this energy requirement on the combined detection and selection efficiency is demonstrated by the black curve. For reference, the spectrum of a 50 GeV WIMP is represented by the red line in Figure 5.1. The signal is unaffected by the energy restriction but is predominantly reduced by the decrease of the detection efficiency toward low recoil energies.

5.2 Nuclear Recoil Calibration

In order to gain knowledge about the detector response to NR, the same external $^{241}\text{AmBe}$ neutron source was used as employed in XENON100 [75]. It was placed next to the cryostat by means of a calibration belt system shown in Figure 5.2 left.

The source generates neutrons by an (α, n) -reaction. The α -particle is emitted by ^{241}Am decays that have a half-life of 433 years and an end-point energy of 5.6 MeV. When interacting

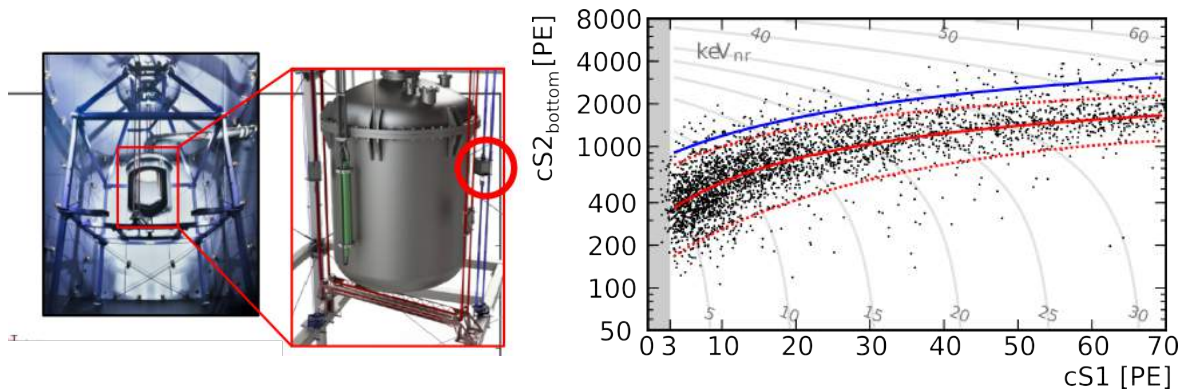


Figure 5.2: **Left:** View on the calibration belt system. A purely vertical belt (I-belt) can be used to insert calibration sources into the water tank and place them at different heights next to the cryostat. A so-called U-belt allows to also bring sources beneath the cryostat. Figure from [105], **Right:** Calibration data taken with the external $^{241}\text{AmBe}$ source. The XENON1T response to NRs was evaluated by fitting the data with L_y and Q_y from [83] as priors. Figure from [53].

with ^9Be the following reaction can be induced:



Depending on the α energy, the generated neutrons have energies of up to 10 MeV [153]. The data taken with the $^{241}\text{AmBe}$ source is shown in Figure 5.2 right. The XENON1T response to those NR was evaluated by using a Markov Chain Monte Carlo fit where the priors of the effective scintillation yield L_{eff} and the charge yield Q_y (see Section 2.3.3) are set to the values reported in [83]. Hence, the fit is constrained by this external data.

5.3 Studies on Electronic Recoil Calibration Data

The calibration of the detector response to ER aims at modeling the dominating background in the dark matter search constituted from ER events. In XENON1T, the highest background rate is expected to come from ^{222}Rn ($T_{1/2} = 3.8\text{d}$) that emanates from the detector materials into the liquid xenon (LXe) and whose daughter isotope ^{210}Pb ($T_{1/2} = 22.3\text{y}$) induces ER events by beta decays. Due to the long half-life of the two isotopes, they have the chance to distribute in the LXe within the TPC. Hence, the resulting background cannot be suppressed by the selection of a FV. In the XENON100 detector, the ER background was dominated by radiation from the detector materials. Therefore, the experiment could calibrate this background by using external gamma sources that are brought close to the cryostat. In XENON1T, the usage of radio-isotopes that can be dissolved in the LXe is more adapted. For the calibration of the ER background region in XENON1T, the same ^{220}Rn source was used as introduced in Chapter 4. In contrast to the decay chain of the background initiator ^{222}Rn , all isotopes in the ^{220}Rn chain have half-lives below 11 hours. Hence, when introducing the ^{220}Rn source into the detector, its activity decays below background level on the time scale of one week. The single scatter ER events used for the calibration are induced by beta

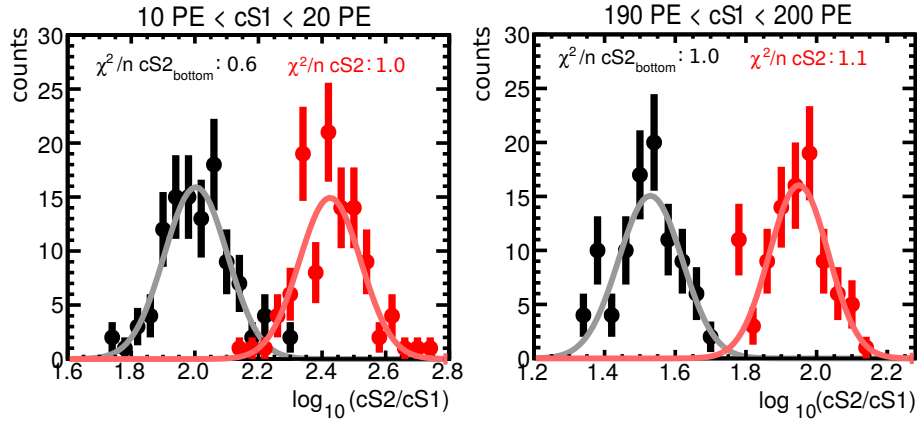


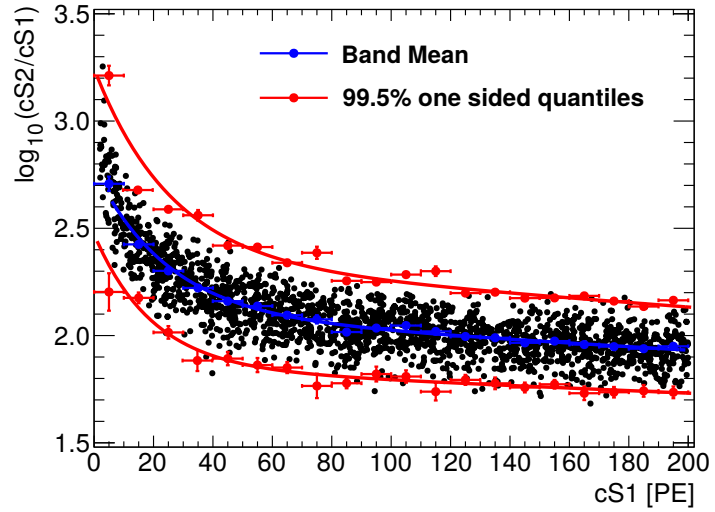
Figure 5.3: Demonstration of Gaussian fit to ^{220}Rn calibration data acquired with XENON1T, projected onto $\log_{10}(cS2_{\text{bottom}}/cS1)$ (black) and $\log_{10}(cS2/cS1)$ (red) in the $cS1$ intervals $[10, 20]$ PE (left) and $[190, 200]$ PE (right). The intervals represent examples for the low and high energy region of the ER band. The solid lines represent the best-fit result. Respective reduced χ^2 values are listed inside each panel.

decays of ^{212}Pb ($T_{1/2} = 10.6\text{h}$). A source activity could be brought into the TPC that induces a maximum ER rate of (40 ± 4) mBq in the FV and within the WIMP search energy region. This rate is large enough to allow for the acquisition of enough statistics within a few days. In this section, a selection criterion will be introduced that removes events from the WIMP signal region (blinding cut) in order to ensure a blind analysis. Furthermore, the ER calibration data is studied in detail to ensure its compatibility with background data and exclude a potential bias in the ER background model that can influence the dark matter result. As a foundation for these two studies, the ER band shape is modeled in the following.

5.3.1 The Electronic Recoil Band

NR and ER interactions can be distinguished by exploiting the difference in energy loss per unit track length between the two processes. The parameter $\log_{10}(cS2/cS1)$, also referred to as *discrimination parameter*, is commonly used to discriminate the two event populations. The discrimination parameter plotted versus $cS1$ is denoted as *discrimination space*. Analog to the procedure introduced in Chapter 4, the shape of the ER band can be modeled by projecting the data onto the discrimination parameter in intervals of $cS1$ and fitting Gaussian functions from which the mean and the width are extracted. Figure 5.3 shows two examples of the $\log_{10}(cS2/cS1)$ distributions of ^{220}Rn ER calibration data, in the low energy region $cS1 \in [10, 20]$ PE (left) and the high energy region $cS1 \in [190, 200]$ PE (right). The red population represents the data using the total measured and corrected S2 signal in the discrimination parameter and the black population shows the outcome when using only the S2 signal recorded by the bottom PMT array ($cS2_{\text{bottom}}$). The fit-results of the Gaussians are demonstrated by the solid lines and the respective reduced χ^2 values are given within each panel at the top. The χ^2 values are close to 1.0 which indicates that the data is well described by the Gaussians. Similarly good agreement has been observed for all other intermediate $cS1$ intervals of the size of 10PE. Furthermore, no difference could be found

Figure 5.4: ER calibration data from the ^{220}Rn source presented in discrimination space (black points). The Gaussian mean is shown by the blue point in each cS1 interval of 10 PE and the corresponding 99.5% one-sided boundaries are marked by the red points. The uncertainties are derived from the error matrix of the Gaussian fit result. Solid lines are empirical parameterizations of the corresponding data.



between the 1σ widths when comparing the employment of cS2 or cS2_{bottom}.

Figure 5.4 shows the calibration data acquired with the ^{220}Rn source in the discrimination space. The Gaussian means are presented in blue in each cS1 interval. As an example, the 99.5% one-sided Gaussian quantiles have been evaluated and are shown by the red points. The associated uncertainties on the means and Gaussian quantiles in each cS1 interval have been evaluated from the error matrix of the Gaussian fit. The dependence of the mean and the quantiles on cS1 can be described by a phenomenological function of the form:

$$f(\text{cS1}) = e^{\alpha \cdot \text{cS1}} + \beta \cdot \text{cS1} + \gamma \quad (5.2)$$

where α , β , and γ are empirical parameters. The fit-result is represented by the blue and red lines for the ER band mean and the 99.5% one-sided quantiles, respectively.

In the following, lower Gaussian quantiles constructed on ^{220}Rn data will serve to define a blinding cut and to compare the leakage of ER events into the signal region below the ER band in background and ^{220}Rn data.

5.3.2 Blinding Criterion

Blinding the dark matter search data has the aim to avoid optimizing data selection criteria and the background model on potential signal events. At the same time, the ER background has to be studied in the science data to identify detector anomalies, to test event selection criteria and to evaluate the compatibility of the background with calibration data to exclude biases in the ER background model. Hence, a blinding selection criterion intends to reject events in the region most sensitive to WIMPs, while allowing a large as possible fraction of ER events.

For the definition of the blinding criterion, the 1% Gaussian quantile of the ER band was used. The corresponding functional form in discrimination space is denoted as *99% discrimination line* and is derived from Gaussian quantiles as described in Section 5.3.1.

In addition, all events with an uncorrected S2 smaller than 150 PE were excluded from the blinding. This population is mostly made out of randomly paired S1 and S2 signals, called *accidental coincidences* [56]. The ratio between accidental coincidences and events from

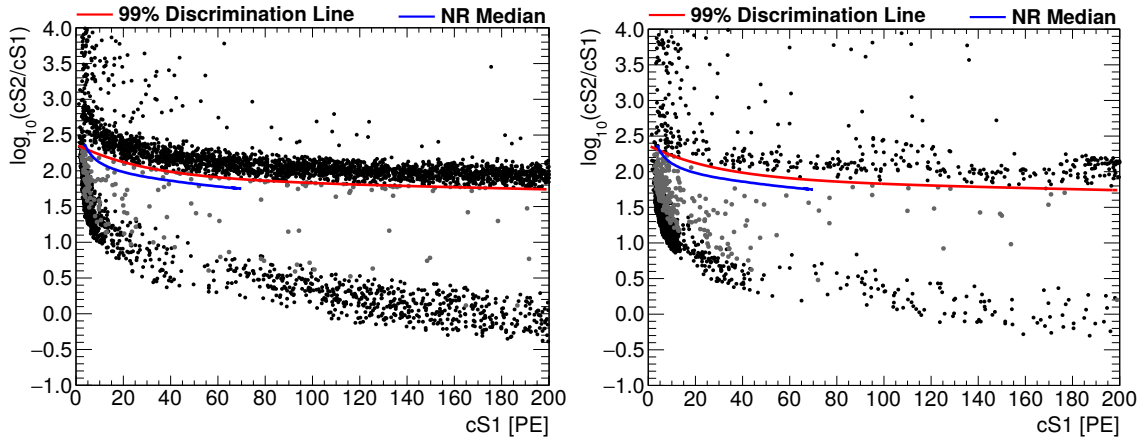


Figure 5.5: Effect of blinding criterion on ^{220}Rn (left) and background (right) data in discrimination space. Only basic data quality requirements have been applied for the generation of these figures. Events that are affected by the blinding are marked in gray. For reference, the NR median is shown as a blue line and the 99% discrimination line that marks the upper boundary of the blinded region in $\log_{10}(cS2/cS1)$ is shown in red.

physical ER interactions is different in ^{220}Rn and dark matter search data. Hence, the accidental coincidence population has to be accessible in the dark matter search data in order to derive a background model (see Section 5.5).

The WIMP search is restricted to the cS1 region between 3 and 70 PE (see Section 5.1). Nevertheless, the blinding criterion was applied to events with cS1 up to 200 PE in order to have a region, also referred to as *sideband region*, where the background prediction could be tested before unblinding the signal region between 3 and 70 PE.

Figure 5.5 shows the effect of the defined blinding criterion on ^{220}Rn (left) and dark matter search (right) data in discrimination space. Only basic data quality requirements have been applied in the two plots, ensuring the quality and correct classification of S1 and S2 peaks. The population at low values in the discrimination parameter is the accidental coincidence population that can be significantly reduced by further requirements on the correlation between S1 and S2. Furthermore, events characteristic for interactions taking place in the gas phase are visible above the ER band at high values of the discrimination parameter. They are deselected by the requirement on the S2 pulse width. Blinded events are marked in gray in Figure 5.5 and unblinded ones in black. It should be noted that the application of the blinding criterion to ^{220}Rn data is only for demonstration. The full dataset was available for analysis while the criterion was only used in the dark matter search data.

For reference, the 99% ER discrimination line is presented in red and the NR median in blue. The NR median was extracted from the Markov Chain Monte Carlo fit of $^{241}\text{AmBe}$ data and was modeled only in the WIMP search energy region.

The defined blinding criterion was successfully applied to the dark matter search data during the definition of event selection criteria and the construction of the background model. No event in the signal region was revealed before these two important parts of the analysis were fixed. After the successful test of the background prediction in the sideband region,

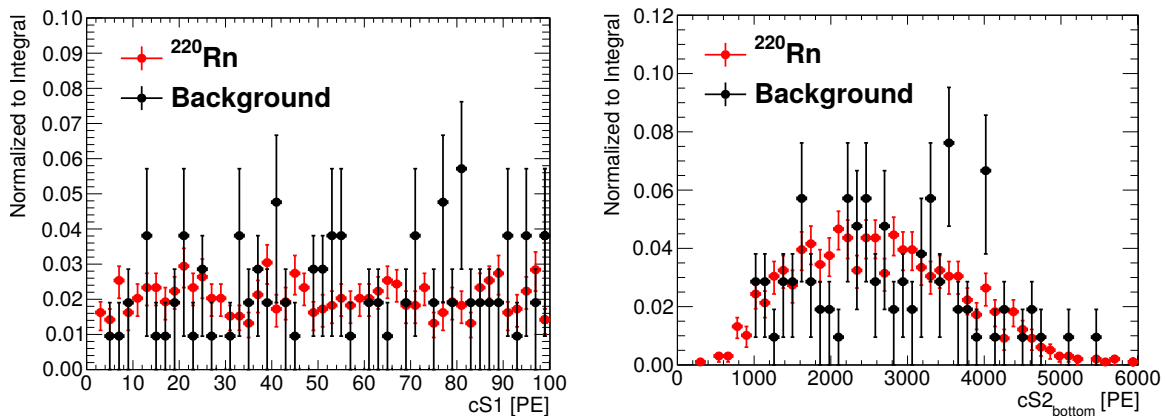


Figure 5.6: Comparison of ^{220}Rn (red) and background (black) spectral shapes in $cS1$ (left) and $cS2_{\text{bottom}}$ (right) for $cS1 \in [0, 100]$ PE. The distributions have been normalized to their integral.

a staged unblinding of the signal region was performed starting with an exposure of 4 live days that were evenly distributed within the science run period. The fact that this partial unblinding did not induce any changes, neither in the event selection nor in the background prediction, indicates that all necessary information for the analysis was provided despite the not accessible signal region.

5.3.3 Compatibility of Calibration and Background Data

It has been shown in Chapter 4 that a difference in the shapes of the ER band in calibration data compared to the ER background in dark matter search data can have an impact on the outcome of the WIMP search. Hence, a comparison of the spectra shall validate that the bulk of the ER background is properly calibrated with the ^{220}Rn source. Furthermore, the calibration data serves for the prediction of the rate of the non-Gaussian leakage component of ER. In XENON100, a population of events that leak below the ER band in discrimination space and do not follow the Gaussian shape of the bulk ER distribution, was observed during all dark matter runs [56]. It will be investigated if this feature is also seen in XENON1T.

The studies on the bulk distribution were performed before unblinding the dark matter signal region and were repeated after the unblinding with the full dataset. In both cases no discrepancy was observed between ^{220}Rn and background data. Here, the status after unblinding is presented as a validation of the background model used for the dark matter search.

The comparison of the non-Gaussian component in both datasets could be only performed with the access to the signal region, hence in the unblinded state of the data.

The Spectra of the Electronic Recoil Bulk Distribution

Comparing the Gaussian parameters of the ER bands in discrimination space is rather challenging due to the very low ER background rate. However, it was found in Chapter 4 that the spectra in $cS1$ and $cS2$ play a crucial role for the band shape. Hence, this study will focus on the comparison of the spectra of ^{220}Rn and background data.

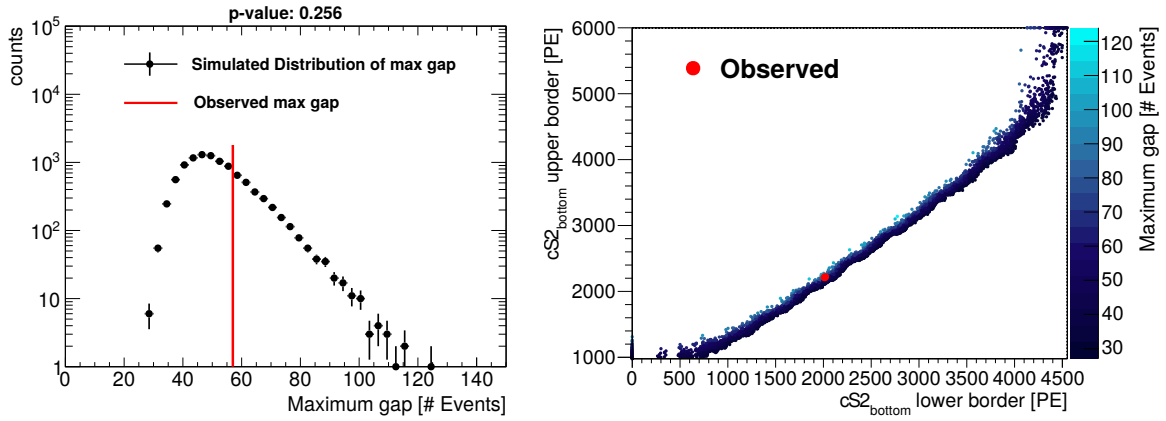


Figure 5.7: Left: Distribution of maximum gap for simulated $cS2_{\text{bottom}}$ spectra. Events have been randomly sampled from the ^{220}Rn $cS2_{\text{bottom}}$ distribution which has also been used as probability density function for the evaluation of the maximum gap. The observed maximum gap is marked by the red line. **Right:** Distribution of maximum gap boundaries in $cS2_{\text{bottom}}$. The observation is indicated by a red dot. The color scale shows the maximum gap value. See text for more explanations on both plots.

Figure 5.6 overlays the spectral shapes of ^{220}Rn data and the ER background in $cS1$ (left) and $cS2_{\text{bottom}}$ (right) for $cS1 \in [0, 100]$ PE. The distributions have been normalized to their integral and the uncertainties follow the Poisson statistics of the number of events in the respective bin. The $cS1$ spectrum of background agrees within the uncertainties with the spectrum of ^{220}Rn data. No systematic offset in several consecutive bins can be observed. However, the $cS2_{\text{bottom}}$ spectrum of the background only starts above 995 PE whereas ER events from the ^{220}Rn source can be observed below these values. Given the low statistics in background data it could be a statistical effect. Potential systematic effects from the data processor, the cuts and the spatial distribution within the FV have been excluded.

In the case of a different shape between the ^{220}Rn and background spectrum, the density of background events would differ at a certain position in the spectrum. Hence, the gap in $cS1$ or $cS2_{\text{bottom}}$ between two neighboring events in the spectrum would be larger in that region, while being smaller in other regions. The statistical significance of such under-densities can be determined using the same test statistic as in the Maximum Gap Method [154]. Hereby, it is assumed that the ^{220}Rn distribution is the true underlying distribution which should be respected by the background data. To test the background data for gaps in the spectra, the following procedure is applied: The same number of events as contained in the background spectrum is randomly drawn from the ^{220}Rn $cS2_{\text{bottom}}$ ($cS1$) distribution. Each two consecutive $cS2_{\text{bottom}}$ ($cS1$) data points of that random distribution serve as boundaries between which the integral of the ^{220}Rn $cS2_{\text{bottom}}$ ($cS1$) spectrum is calculated. The maximum integral is denoted as *maximum gap*. This procedure has been repeated 10000 times in order to generate the maximum gap distribution. The outcome is shown for the $cS2_{\text{bottom}}$ spectrum in Figure 5.7 left. In the same way, the observed maximum gap is evaluated from background data. It's value is indicated by the red line in the same figure. By integrating the maximum gap distribution, evaluated on the $cS2_{\text{bottom}}$ spectrum, above the observation, a p-value of 0.26 is obtained. This relatively large p-value points to a good agreement between the

cS2_{bottom} distributions of ^{220}Rn and background data. Figure 5.7 right shows the simulated maximum gap boundaries for the cS2_{bottom} spectrum with the respective maximum gap value on the color scale. The observation is marked by a red dot. In contrast to what one could naively expect from the spectrum, the observed maximum gap is not between 0 and 995 PE but has higher boundaries of 2042 PE and 2188 PE. The same procedure has been applied to the cS1 spectrum, resulting in a p-value of 0.86 and an observed maximum gap between 44 PE and 48 PE.

It can be concluded that the non-observation of background events below 995 PE in the cS2_{bottom} is likely to be a statistical effect and that no significant under-densities are present in neither the cS1 nor the cS2_{bottom} spectrum. Hence, a calibration of the ER background region with the data from the ^{220}Rn source is not expected to result in a bias in the background model.

The non-Gaussian Leakage Component

A second comparison between background and ^{220}Rn ER data is not related to the bulk distribution but focuses on its tail.

Due to the observation of leakage events below the ER band in calibration as well as in background data in all three dark matter runs of XENON100, a prediction for this component has been incorporated into the corresponding background models [56]. This so-called *non-Gaussian leakage* features uncommonly low S2 signals with respect to the reconstructed S1 and was first reported by [146, 155]. Possible explanations are multiple gamma interactions within the TPC where at least once the energy is deposited in a region from which the ionization electrons cannot be extracted. An example for such a region insensitive to the charge signal is located between the cathode and the bottom PMT array. This non-Gaussian leakage event population was modeled in XENON100 by evaluating the *leakage fraction* in calibration data, i.e., the fraction of events below a specific discrimination line, and subtracting the Gaussian contribution expected from the band [150]. In the final results of the XENON100 experiment this model was expanded by the prediction of accidental coincidences of uncorrelated lone S1 and S2 signals [56].

In order to see if this non-Gaussian ER component is also present in XENON1T, the leakage fractions for different discrimination lines (DL) in ^{220}Rn data are listed in the second column of Table 5.1 for the energy region $\text{cS1} \in [0, 200]$ PE. The uncertainties of the listed values in the table account for the systematics of the discrimination lines as well as for the 1σ Poisson uncertainty. A good agreement within the uncertainties is present between the observed fractions and the expectation from the Gaussian distribution for the 50% and 1σ DL. In contrast, the leakage fraction of $(1.1 \pm 0.4)\%$ evaluated for the 99.5% discrimination line deviates by about 1.5σ from the expectation of 0.5%. Hence, it can be concluded that this non-Gaussian background component is also present in XENON1T. It has about the same strength as in XENON100 since similar leakage fractions were found for the same discrimination level in that experiment [145]. Comparing the leakage fractions found in ^{220}Rn data to the ones in dark matter search data listed in the third column in Table 5.1, good agreement can be found within the uncertainties. Furthermore, a good agreement with the Gaussian expectation is found for dark matter data for the 50% and 1σ discrimination lines. This indicates that the lines that were constructed on ^{220}Rn data, apply to the ER background as well.

	^{220}Rn	DM	Gaussian Expectation
Total Number of Events	1930	180	
Fraction below 50% DL	$(49.6 \pm 1.3)\%$	$(55 \pm 4)\%$	50%
Fraction below 1σ DL	$(17.6 \pm 1.3)\%$	$(15 \pm 3)\%$	16%
Fraction below 99.5% DL	$(1.1 \pm 0.4)\%$	$(2.2^{+1.2}_{-1.7})\%$	0.5%
Events below 99.5% DL	22 ± 8	$4^{+2.2}_{-3.1}$	Rn: 9.7 Bkg: 1.8

Table 5.1: Comparison of ^{220}Rn and background ER leakage fractions for different discrimination lines (DL) evaluated in the region $cS1 \in [0, 200]$ PE. The discrimination lines have been defined on ^{220}Rn data. As a reference, the last row lists the observed number of events below the 99.5% discrimination line together with the expectation assuming the ER band to be entirely Gaussian distributed in the rightmost column.

In contrast to the ^{220}Rn data, the leakage fraction below the 99.5% in which the non-Gaussian component should become prominent, is also in agreement with the Gaussian model in dark matter data. However, the measured value of $(2.2^{+1.2}_{-1.7})\%$ lies 1σ above the expectation of 0.5%. The asymmetric uncertainties result from the Poisson distribution that becomes asymmetric for low count rates. The statistical uncertainties are relatively large for the small number of observed events below the 99.5% discrimination line of $4^{+2.2}_{-3.1}$ (see last row of Table 5.1).

Since the non-Gaussian leakage is observed in the ^{220}Rn calibration data and its presence cannot be excluded in background data, it has been taken into account in the background model of the dark matter analysis. Following the procedure in [56], the background contribution was predicted by modeling accidental coincidences and accounting the remaining non-Gaussian fraction to a so-called *anomalous leakage* component with a flat energy spectrum.

It should be noted that the leakage does not scale with the time of data taking since this parameter differs by about one order of magnitude between the ^{220}Rn and the dark matter search data. Hence, the leakage effect is not related to exposure but seems to be truly correlated to the total number of recorded ER events in the dataset.

5.4 Investigation of Wall Events

For the suppression of background, induced by radiation from the detector materials, the selection of an inner fiducial volume (FV) is a powerful tool. At the same time, the FV should be as large as possible since the number of expected WIMP interactions scales directly with the target mass (see Equation 1.12). Those two competing considerations drive the optimization of the FV choice.

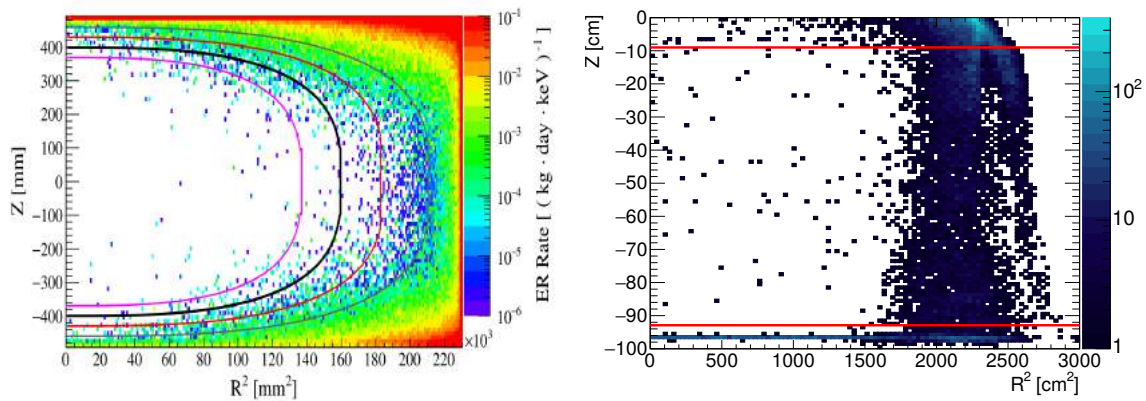


Figure 5.8: **Left:** Spatial distribution of simulated ER event rate from the detector materials in the energy region (1-12) keV in XENON1T. The lines mark fiducial volumes with xenon masses of 800kg (purple), 1000kg (thick black), 1250kg (red), and 1530kg (brown). The rate in the white regions is smaller than $1 \cdot 10^{-6}(\text{kg}\cdot\text{day}\cdot\text{keV})^{-1}$. Figure from [108]. **Right:** Spatial distribution of low energy ($cS1 < 70$ PE) background events within the XENON1T TPC. The number of events is indicated by the color scale. The trunk-like feature at high radii is an artifact from the position reconstruction algorithm. It is straight in the vertical direction in raw data but is bent by the field distortion correction. The red lines indicate the upper and lower boundaries of the cylindrical FV.

5.4.1 Considerations on the Fiducial Volume Choice

The simplest geometry for the FV is a cylinder since this shape is well adapted to the detector geometry. However, in XENON100 super-ellipsoids have been used which are more adapted to the spatial distribution of the background induced by radioactive contaminations in the surrounding materials. The same shape was expected to be suited for XENON1T as well.

Figure 5.8 left shows the simulated spatial ER event rate in the active volume of XENON1T induced by radiation from the detector materials. The lines represent possible choices of FV with xenon masses of 800kg (purple), 1000kg (thick black), 1250kg (red), and 1530kg (brown). The super-ellipsoid shape follows the spatial distribution of the background and allows to make optimal use of the target. Up to masses of about 1200kg, the contribution of the materials to the total background rate was expected to be one order of magnitude smaller than the rate expected from ^{222}Rn , hence negligible [108]. However, a different spatial distribution of the background in XENON1T was observed due to an imperfect position reconstruction. Figure 5.8 right shows the low energetic background events with $S1 < 70$ PE recorded during the first science run of 34.2 live days. The number of events is indicated by the color scale. When comparing to the left plot in the same figure, it can be noted that the spread in R^2 is different in the observed background. While the simulated event rate decreases by four orders of magnitude within about 5 cm, the background data is spread more evenly over a region of about 11 cm in R .

The very peculiar trunk-like shape that is present at high R^2 is an artifact from the position reconstruction algorithm. The algorithm tends to place events occurring close to the TPC wall at the maximum radius ($R_{\text{max}}^2 = 2209\text{cm}^2$). However, due to slight inhomogeneities of

the drift field, the electron cloud, especially from events with high depth, does not reach the liquid-gas interface at the maximum radius. Hence, the separation in R between the artifact and the main population becomes larger for decreasing Z . By correcting for the distortion of the drift field, events can be shifted toward higher radii than the maximum TPC radius and the shape of the artifact is changed from a straight vertical line to the trunk-like shape. It should be noted that the “trunk” is not a problem for the background of a WIMP search since for this matter only inwards reconstructed events are of importance.

It can be observed in Figure 5.8 right that the events predicted by the simulation at the bottom (see Figure 5.8 left), are reconstructed at the cathode. Furthermore, an event population is expected to show at the top of the TPC as well. However, no events are observed in that region that could be compatible with the expectation. This can be explained by a limited efficiency of the peak finding algorithm to separate S1 and S2 peaks for short drift times and is under investigation [65]. For this reason, the upper border of the FV in Z region has been defined at -9 cm as indicated by the upper horizontal red line in Figure 5.8 right. The value of the lower Z boundary is driven by the aim to exclude the events reconstructed at the cathode and is set to -93 cm (lower horizontal red line in Figure 5.8 right).

The size of the FV can now only be tuned in the direction of R . The background events from the detector wall seem to suggest a fiducial volume of the shape of a truncated cone. However, it was found that this shape does not provide a significant advantage over a simple cylinder in the trade-off between background suppression and high fiducial mass [65]. This is due to the fact that the events from the TPC wall do not populate the ER band but leak below the band into the signal region.

While trying to exploit the xenon mass in the active region of XENON1T, an increased number of events was observed when scaling up the cylindrical FV beyond ~ 1042 kg, corresponding to $R^2 > 1370$ cm². This is demonstrated in Figure 5.9, where the dark matter search data is shown in a cylindrical FV of 1.5 t xenon mass in discrimination space by the green data points. The red points indicate events below the NR median (purple line) for the smaller FV indicated above each panel. When increasing the FV, i.e. when extending its radius, more events appear below the NR median and leak into the signal region. This study was conducted in the sideband region of energies above 100 PE in cS1. The gained results led to the restriction of the FV to a mass of ~ 1042 kg in order to suppress these leakage events from the wall. After the definition of the FV, the signal region was unblinded for events located outside of the FV for further studies of this population.

The background from events that suffer from charge losses at the detector wall and are reconstructed into the FV, was first observed by the LXe detectors ZEPLIN-II [157] and Xed-I [158] and is also existent in the LUX [159] and PandaX [55] instruments.

These findings led to the investigation of events taking place at the detector wall in XENON1T, referred to as *wall events* in the following, with the aim to understand their origin and features and incorporate them into the background prediction of the dark matter search.

5.4.2 ²¹⁰Po Alpha Decays at the Wall

When investigating the high energy region of the background data it was found that ²¹⁰Po alpha decays provide a good test population to study the origin of wall events. ²¹⁰Po de-

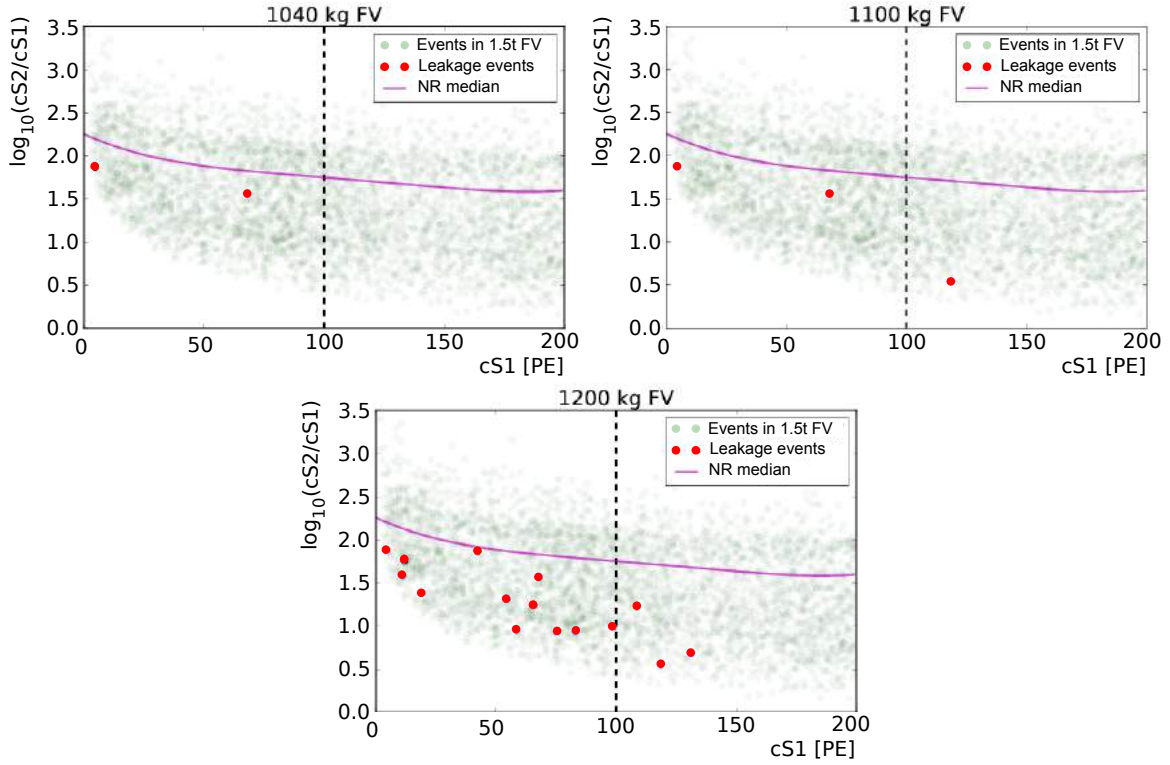


Figure 5.9: Distribution of ER events in the dark matter search data in discrimination space. The green data points mark events within a cylindrical FV of 1.5t xenon mass. The red points show events that leak below the NR median (purple line) in a smaller FV as indicated above each panel. Figure from [156].

cays with a half-life of 138.4d by emitting an alpha particle with an end-point energy of $Q_\alpha = 16.0\text{MeV}$ [76]. It is a daughter nuclide in the ^{222}Rn decay chain coming after the long-lived ^{210}Pb which has a half-life of 22.2y and is an internal background source for LXe detectors (see Chapter 2). Figure 5.10 shows the decay scheme of ^{222}Rn together with the respective half-lives and the end-point energies of the alpha decays.

The isotope ^{210}Po is expected to be present at the surfaces of the detector components due to the accumulation of ^{222}Rn daughter nuclides during the construction and storage of the components in a non-radon free environment. This surface contamination, induced by ^{222}Rn , has been observed and studied also by other low background experiments such as CUORE [160], BOREXINO [161], and LUX [162].

Identification of ^{210}Po decays

To identify alpha decays in XENON1T, only few quality selection criteria are necessary, since alpha particles feature high energies and stopping powers and therefore induce a clear and almost background free signature in LXe detectors.

Only signals with $cS1 > 30 \cdot 10^3 \text{PE}$ are considered and the pulse width of the S2 is required to be below a certain value in order to reject gas events. The drift time has to be larger than $4\mu\text{s}$ to reject interactions from the gas phase as well as those that are induced by single electrons

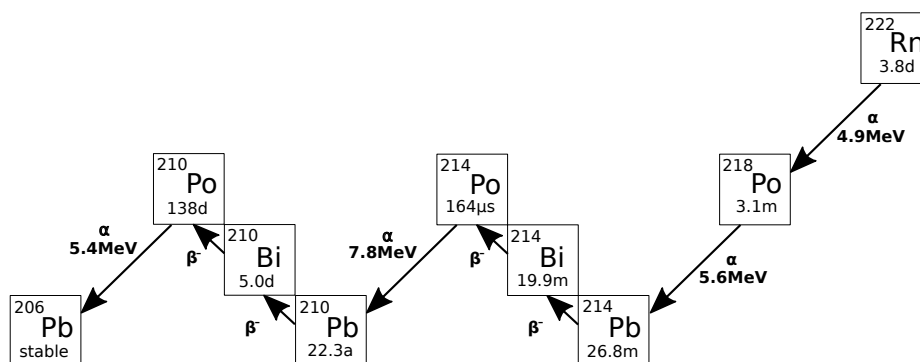


Figure 5.10: Decay scheme of ^{222}Rn , a daughter isotope of the uranium decay chain. Half-lives and end-point energies from [76].

after big S2s. A loose criterion on the correlation between the fraction of the total S1 area detected by the top PMT array ($S1_{\text{aft}}$: S1 area fraction top) and the reconstructed Z-position is applied. It removes a number of outliers having small $S1_{\text{aft}}$ and small TPC depths¹. The Z coordinate is required to be larger than -96cm in order to avoid events from the cathode that cannot be attributed to a distinct alpha decay due to a poor light collection efficiency in that region that smears out the alpha peaks in the cS1 spectrum. This cathode population has a rate of $\sim 3\text{mBq}$ which is approximately five times smaller than the rate of ^{210}Po and is therefore neglected in this analysis.

Figure 5.11 left shows the selected events recorded during the first dark matter science run of XENON1T in cS1 vs. cS2 space. The color scale indicates the number of events per bin. The distribution shows a population with two peaks at high cS2 values of approximately $120 \cdot 10^3\text{PE}$ and one population at a significantly lower cS2. The red line marks the cS2 value of $80 \cdot 10^3\text{PE}$ that defines the border between the two populations. Their cS1 spectra are shown in Figure 5.11. The population with $cS2 > 80000\text{PE}$ is shown in black and the one with $cS2 < 80 \cdot 10^3\text{PE}$ is presented in red.

A similar picture is revealed by XENON100. Figure 5.12 shows for comparison events selected with the same criteria as presented in Section 4.2.1 in the $cS2_{\text{bottom}}^2$ vs. $cS1_{\alpha}$ space. $cS1_{\alpha}$ denotes the S1 signal corrected for the PMT saturation that is dependent on the event position (see Section 4.2.1). Again, the red line separates the high and the low $cS2_{\text{bottom}}$ populations.

Using the cS1 spectrum, the individual alpha decays can be identified in both detectors. Table 5.2 lists the S1 yields, i.e., the mean cS1 signal divided by the respective Q_{α} of the three isotopes ^{210}Po , ^{222}Rn , and ^{218}Po detected with XENON100 and XENON1T. The mean cS1 was determined by Gaussian fits to the spectra. The uncertainties represent the systematic from the fit while the statistical uncertainties are negligible. The S1 yields in XENON100 are compatible amongst the isotopes within the uncertainties which points to a correct identifica-

¹The cut is shown as a red line in Figure D.1 in the Appendix D

²In XENON100 the variable $cS2_{\text{bottom}}$, i.e. the S2 signal detected by only the bottom PMT array, is preferred against the total detected S2 signal. This is related to the more homogeneous signal correction of $cS2_{\text{bottom}}$ in the horizontal plane. The same has been found in XENON1T which led to the usage of $cS2_{\text{bottom}}$ in the final dark matter analysis. However, at the time when this analysis was performed the $cS2_{\text{bottom}}$ variable was not yet available.

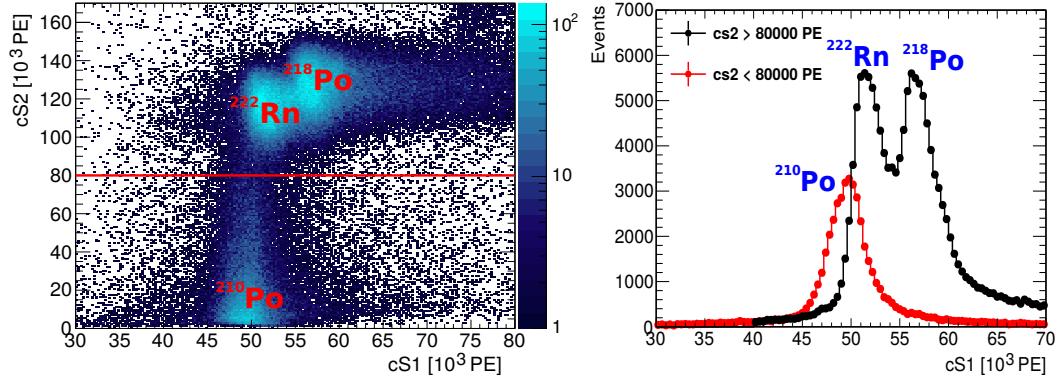
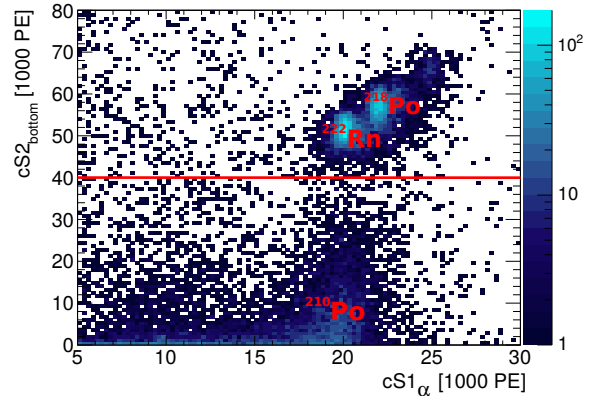


Figure 5.11: **Left:** Event distribution of high energetic background data recorded during the first science run on XENON1T in $cS1$ vs. $cS2$ space. The color scale shows the number of events per bin. The red line separates the homogeneously distributed events from ^{222}Rn plus ^{218}Po and the ^{210}Po decays that can be found only at the TPC edge. **Right:** Projection of the same data onto $cS1$ when requiring $cS2 > 80 \cdot 10^3$ PE (black) and $cS2 < 80 \cdot 10^3$ PE (red).

Figure 5.12: Alpha Events in XENON100 in the $cS2_{\text{bottom}}$ vs. $cS1_{\alpha}$ space. The populations of the distinct isotopes have been marked in red. The red horizontal line at $cS2_{\text{bottom}} = 40 \cdot 10^3$ PE separates the region of ^{218}Po and ^{220}Rn alpha decays from the region of ^{210}Po decays.



		^{210}Po	^{222}Rn	^{218}Po
	Q_{α} [keV]	5407	5590	6115
XENON100	S1 yield [PE/keV]	3.62 ± 0.02	3.60 ± 0.01	3.61 ± 0.02
XENON1T	S1 yield [PE/keV]	9.17 ± 0.01	9.25 ± 0.02	9.25 ± 0.01

Table 5.2: Comparison of S1 yields for alpha decays measured in XENON100 and XENON1T.

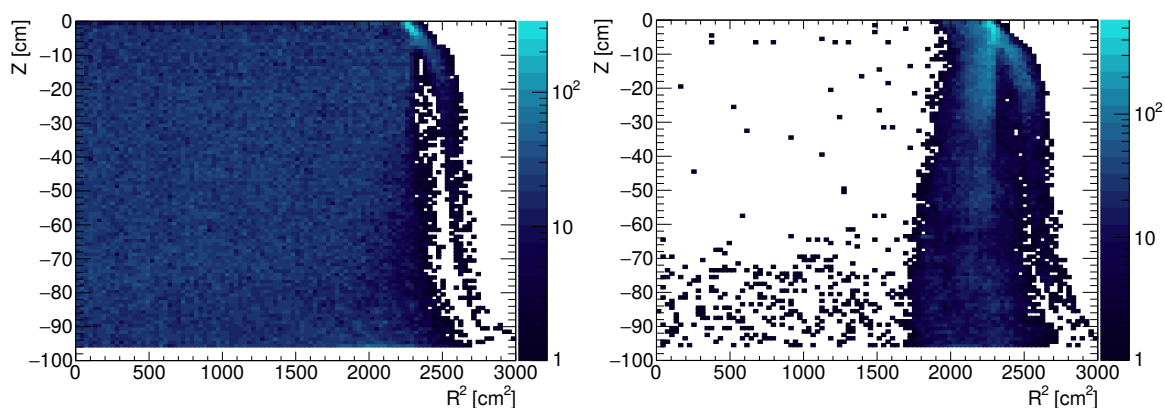


Figure 5.13: Spatial distribution of ^{222}Rn and ^{218}Po alpha decays (left) and ^{210}Po decays (right) in XENON1T. The trunk-like feature at high radii is an artifact from the position reconstruction algorithm. It is straight in the vertical direction in raw data but is bent by the field distortion correction.

tion and a linear energy scale of alpha decays in that energy region. However, in XENON1T the light yield of ^{210}Po is significantly reduced compared to the other two isotopes. This could be caused by a bias in the spatial correction of the S1 signal close to the detector border: As a result of surface contaminations, ^{210}Po decays take place at the PTFE walls. However, its reconstructed position is spread over about 9 cm in R . Since the light collection efficiency decreases toward the outer edge of the detector [105], a smaller correction factor is applied to events that are reconstructed inwards. This leads to the decreased light yield of ^{210}Po in XENON1T.

The larger light yields for all alpha decays in XENON1T with respect to XENON100 is a result of the higher light collection efficiency and the smaller drift field³ that allows a larger fraction of electron-ion pairs to recombine and form excited xenon atoms that emit scintillation light.

Spatial Distribution

The reason for the reduced charge collection of ^{210}Po interactions is the spatial distribution within the detector. While ^{222}Rn and ^{218}Po are mostly homogeneously distributed within the TPC, ^{210}Po decays occur only at the edge of the TPC. This can be deduced from Figure 5.13 where ^{222}Rn and ^{218}Po (^{210}Po) events are shown on the left (right) in the Z vs R^2 space in XENON1T. The number of events is indicated by the color scale.

The fact that ^{222}Rn and ^{218}Po is present within the whole LXe while ^{210}Po decays occur only at the detector edge points to ^{210}Po contaminations on the PTFE surfaces. Alpha decays in the bulk material could not be seen due to their high energy loss per unit track resulting in short ($\sim\mu\text{m}$) mean free paths in materials. Since only a peak from ^{210}Po is visible in the cS1 spectrum when requiring small $\text{cS2} < 80 \cdot 10^3$ PE it can be concluded that ^{222}Rn and ^{218}Po are not trapped on the PTFE surfaces in contrast to ^{210}Po . Otherwise, a similar rate of all isotopic decays would be expected in the low cS2 regime.

³In XENON100 a drift field of 400 V/cm was present during this work while in XENON1T the drift field yielded 120 V/cm.

The origin of the event population with $Z < -60$ cm and $R^2 < 1600$ cm² in Figure 5.13 right is under investigation. Given the small number of selection criteria that comprise only spatial and energy requirements, and a very loose requirement on the correlation between the $S1_{\text{aft}}$ and the Z coordinate, the population could vanish when applying more data quality criteria. The rate of this low Z population is negligible in comparison to the rate induced by radiation from the detector wall and therefore not of importance for this study. In the following, $R^2 > 1600$ cm is additionally required to study further properties of ^{210}Po events at the wall.

The Rate

With the observed ^{210}Po decay rate, the hypothesis of the plate-out of ^{222}Rn decay daughters on the detector materials during their production and storage can be validated. This study serves to exclude that the accumulation of ^{210}Po on the PTFE surfaces is related to the presence of ^{222}Rn contaminated LXe around the material.

In the first science run of XENON1T a total of 157846 events from ^{222}Rn and ^{218}Po were recorded in the whole active target. From the cS1 spectrum the ratio between the number of ^{222}Rn and ^{218}Po decays is evaluated to 1.02 ± 0.01 . The slight deviation from 1.0 might be explained by the accumulation of ^{218}Po at the cathode since it is positively charged after the decay.⁴

Having 34.2 days of background data, the ^{222}Rn rate can be inferred to be (27.0 ± 0.1) mBq in the whole sensitive volume, corresponding to (13.7 ± 0.2) $\mu\text{Bq/kg}$ if a homogeneous distribution is assumed in the LXe.

The total number of detected ^{210}Po alpha decays during the science run amounts to 43378, corresponding to a rate of (14.7 ± 0.1) mBq. This value is expected to be a lower limit for the true ^{210}Po activity in the detector since a reduced detection efficiency is expected for this isotope owing to the charge loss at the wall. The presence of a charge signal has been required for ^{210}Po interactions. Events with a radius smaller than 40 cm were neglected, as well as the cathode region. A rough estimate can show if the observed ^{210}Po rate is compatible with an origin from ^{222}Rn decays that take place in the LXe. All radio-isotopes in the ^{222}Rn decay chain before ^{212}Pb have half-lives of the order of days or less. They can be assumed to be in equilibrium with each other considering the long half-life of ^{212}Pb . The activity A_{Po} of ^{210}Po in dependence of time can then be inferred from the activity A_{Rn} of ^{222}Rn by:

$$A_{\text{Po}}(t) = \frac{A_{\text{Rn}} \lambda_{\text{Pb}}}{\lambda_{\text{Po}}} \left(1 - e^{-\lambda_{\text{Po}} t} \right), \quad (5.3)$$

with the corresponding decay constants λ_{Po} and λ_{Rn} . In the nine months between the initial filling of the detector with LXe and the start of data taking, a ^{210}Po activity of about 0.6 mBq could have grown in from the ^{222}Rn present in the 3.3 t of xenon in the detector. This is by no means in agreement with the observation of (14.7 ± 0.1) mBq. Hence, the activity from ^{210}Po on the PTFE surfaces was already present before the initial detector filling. Consequently,

⁴For comparison, the same ratio was determined to 1.4 ± 0.2 in XENON100. The cause for this increase in detection efficiency of ^{218}Po in XENON1T might be the larger detector volume and therefore longer drift path until the cathode can be reached. The ^{218}Po ion has more time to either decay ($T_{1/2} = 3$ min) or attract an electron and become neutral. Furthermore, the convection pattern that played the dominant role for ion-drift in XENON100 [139] might look differently in XENON1T.

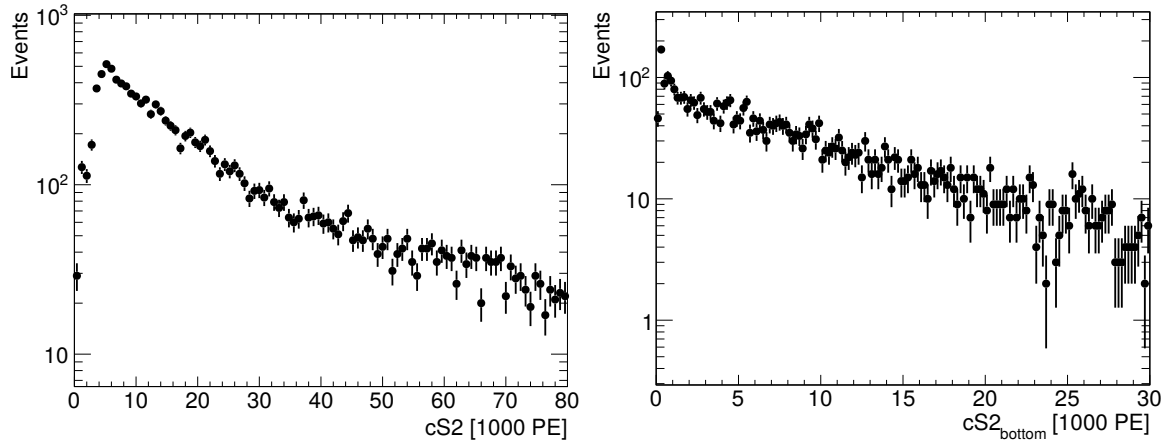


Figure 5.14: $cS2$ ($cS2_{\text{bottom}}$) spectrum of ^{210}Po decays in XENON1T (left) and XENON100 (right). The charge signal of these events is reduced by up to 95% due to their proximity to the detector wall where electrons get attached.

its accumulation already took place during construction and storage of the detector material.

5.4.3 Position Resolution and Charge Loss of Wall Events

In Section 5.4.2, the presence of ^{210}Po in the detector was inferred from its alpha spectrum and was predominantly observed at the detector border. The alpha particles with an energy of 5.4 MeV have a mean free path of about $40\ \mu\text{m}$ in LXe [163]. This close proximity to the TPC wall was observed to have an impact on the resolution of the reconstructed position of these events, as well as on the charge signal. It will be shown in Section 5.4.4 that these properties are shared by low energy ER events induced by radiation from the detector materials.

S2 Distribution

Figure 5.14 shows the $cS2$ ($cS2_{\text{bottom}}$) spectrum of ^{210}Po events recorded with XENON1T on the left and XENON100 on the right. In both detectors it falls off exponentially with slopes of the same order of $10^{-6}\ \text{PE}^{-1}$. Furthermore, both spectra share the feature of a rate decrease toward small $cS2$ that starts at much higher values than the applied S2 threshold. This points to an efficiency loss at small $cS2$ which could be induced by a physical or a detector related effect and is subject to further investigations.

In XENON1T, a mean $cS2$ value of about $111 \cdot 10^3\ \text{PE}$ would be expected for ^{210}Po alpha decays if approximately the same S2 yield applies for those interactions as for ^{222}Rn decays. The maximum rate in the $cS2$ spectrum, however, is observed at about $6 \cdot 10^3\ \text{PE}$ corresponding to only 5% of the expected charge signal. For XENON100, this value is of the same order. One hypothesis for this charge loss is the attachment of electrons, generated at the interaction site, to the PTFE.

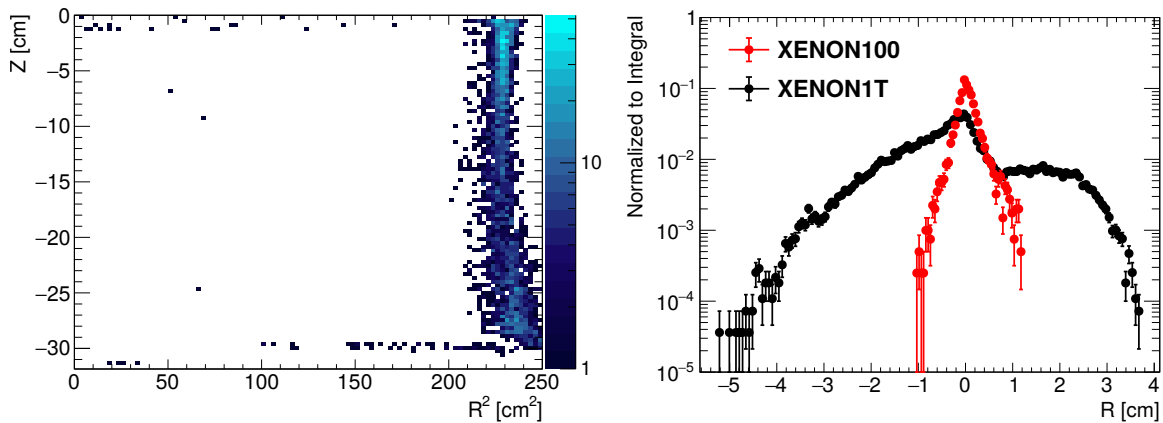


Figure 5.15: **Left:** Spatial distribution of ^{210}Po events in XENON100. The number of events are indicated by the color scale. **Right:** Shape comparison of R^2 distribution of ^{210}Po events in XENON100 and XENON1T. The drift length of XENON1T has been restricted to $Z > -30$ cm in order to match the length of the XENON100 TPC. The maximum of the two distributions has been shifted to zero under the assumption that this is a good approximation for the position of the detector wall.

Position Reconstruction Resolution

Ideally, the position of ^{210}Po decays would be reconstructed at the maximum TPC radius of 48 cm in XENON1T due to the μm range of alpha particles in LXe. However, in Figure 5.13 left, a spread in R over up to 9 cm is observed. Furthermore, the transverse spread is dependent on the TPC depth of the event. For comparison, the same ^{210}Po population observed in background data of XENON100 is shown in Figure 5.15 left. A more accurate position reconstruction than in XENON1T can be noticed since the events are only scattered over up to 2 cm with no strong dependence on Z . This becomes even more prominent when overlaying the ^{210}Po R distributions of the two detectors normalized to their respective integrals. The maximum has been shifted to zero assuming that this position is a good approximation for the PTFE wall. To take into account that the resolution of the position reconstruction in XENON1T is affected by the larger drift length due to which the lateral diffusion of the electron cloud is increased, only events with a depth of up to 30 cm, the maximum drift length of XENON100, have been considered. Interactions taking place close to the wall are reconstructed inwards by up to 5 cm in XENON1T and only about 1 cm in XENON100. It should be noted that the position reconstruction algorithm was adapted and tuned over several years in XENON100 and similar efforts are ongoing in XENON1T that already show improvements at the time of writing.

From simulations, the mean distance between the true and the reconstructed event position (mean error) in XENON1T was evaluated to about 3 cm at outer radii and uncorrected S2 signals at the threshold of 200 PE [65]. The resolution in the same detector region improves to a mean error of about 1 cm for S2s larger than about $6 \cdot 10^3$ PE which applies for the majority of the ^{210}Po decays observed in XENON1T (see above). Hence, the position reconstruction resolution in R in XENON1T is decreased by a factor of 9 compared to the expectation from the simulation. The cause is investigated in Figure 5.16.

In order to verify that the size of the detected uncorrected S2 signal does not have an influ-

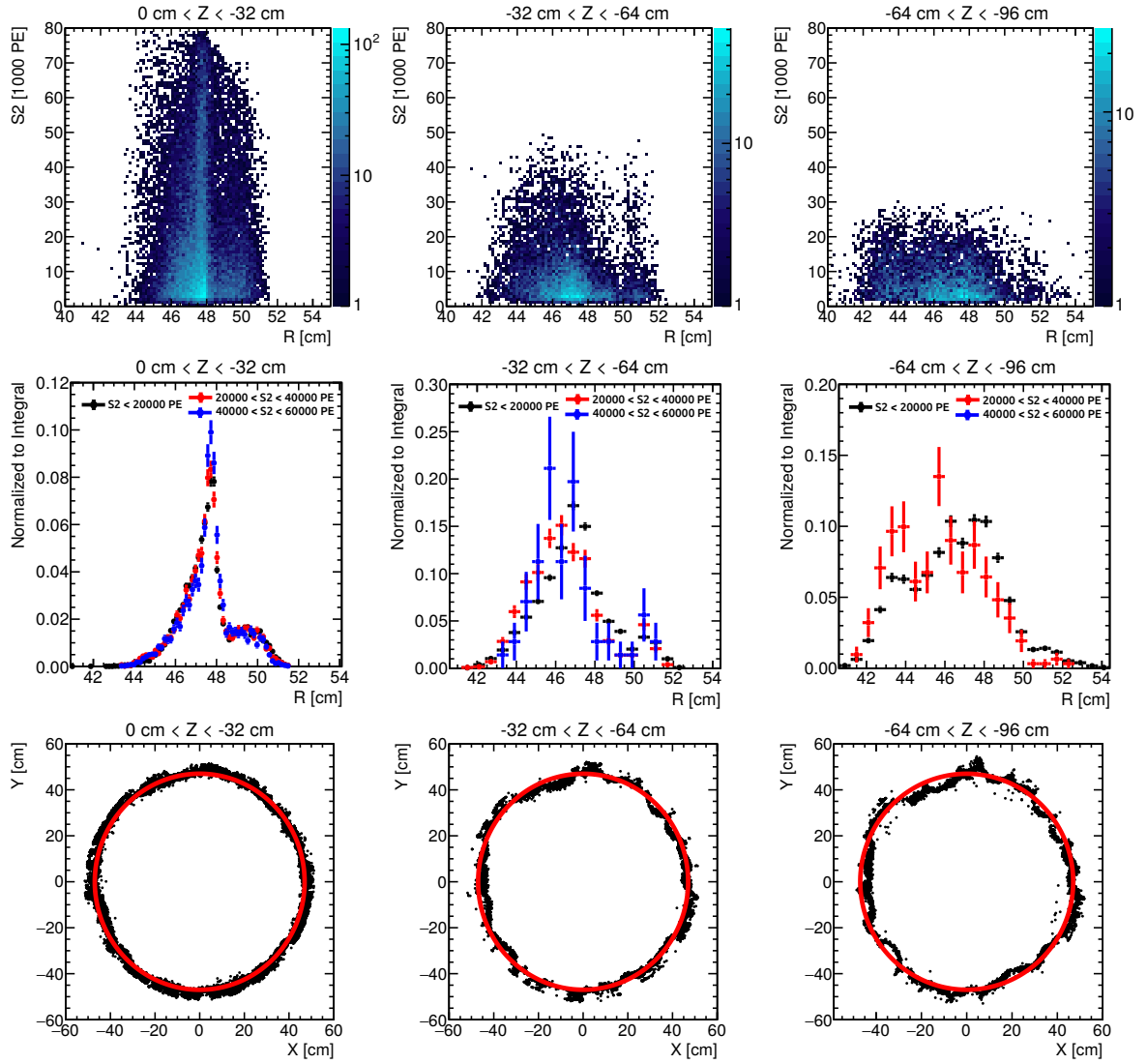


Figure 5.16: Top row: Uncorrected S2 vs R^2 distribution of ^{210}Po events for different Z ranges as indicated above each panel. The number of events is given by the color scale. **Middle row:** Comparison of projections of the data shown in the upper panels onto R for the S2 intervals $[0, 20000]$ PE (black), $[20000, 40000]$ PE (red), and $[40000, 60000]$ PE (blue). **Bottom row:** X-Y distribution of the same events for the same Z intervals. The red circle marks the true TPC radius. Events that are lying outside are over-corrected by the field distortion correction.

ence on the uncertainty of the reconstructed position of ^{210}Po events, S2 is plotted versus R in the top row of Figure 5.16. The number of events is indicated on the logarithmic color scale and the selected TPC depth increases from left to right as indicated above each panel. As expected, large S2 values up to $80 \cdot 10^3$ PE are only possible at the top since no correction for electron attachment to impurities has been applied. Large S2 signals seem to show the same spread in R as smaller S2 signals. As predicted by the simulation, no correlation between S2 and the spread in R is observed. This becomes more evident when projecting the data onto R for different S2 intervals as done in the middle row of Figure 5.16. The distributions of the S2 intervals $[0, 20000]$ PE, $[20000, 40000]$ PE, and $[40000, 60000]$ PE are presented in black, red, and blue, respectively. The histograms have been normalized to their integrals. The shapes of the projections onto R are in good agreement within the statistical uncertainties between the individual S2 intervals. However, they differ among different Z intervals. A larger spread for higher TPC depths is seen. It can be concluded that the transverse resolution of the position reconstruction algorithm is not dominated by the size of the raw S2 signal that is in general smaller for events from the bottom of the TPC due to electron attachment during their drift to the liquid-gas interface. Instead, the uncertainty of the event position is dominated by the Z position of the event itself.

This is supported by the X - Y distributions shown for the same three Z ranges in the bottom row of Figure 5.16. The red circle marks the true TPC radius known from the detector design. Some events are reconstructed outside of the TPC due to over-correction of the field distortion. A clear inwards trend of the event radii is seen from small to large Z values. The peculiar shape with its notches that becomes more prominent toward higher depths, is correlated with the arrangement of the vertical PTFE panels that confine the TPC [105]. Hence, it is suspected that the observed X - Y distribution of wall events can be attributed to a field distortion in the X - Y -plane that is not yet included in the field distortion correction. The hypothesis is supported by the observation that the feature represented by the notches becomes stronger for increasing TPC depths: Electrons from interactions taking place at the bottom follow the field lines for a longer time and therefore can be more distorted before they are extracted from the liquid. This issue is not observed in XENON100⁵. In contrast to XENON1T, the field shaping electrodes are located inside the TPC in XENON100 which might be the cause for the different X - Y distributions in the two detectors.

The behavior of ^{210}Po shown in Figure 5.16 is observed for low energetic background events as well that are taking place in close proximity to the wall. However, the distributions are more smeared due to less statistics and a further decrease in the position resolution at low energies. The corresponding Figure D.3 can be found in the Appendix D.

5.4.4 Comparison of Wall Events from ^{210}Po and Low Energy Background

The properties of wall events, described in the previous section, were derived from alpha interactions close to the TPC edge in XENON1T. However, for the dark matter search, only low energetic ER interactions are of interest. The low energy recoils, primarily induced by beta and gamma radiation from the detector wall, were observed to leak into the signal region

⁵The X - Y distribution of ^{210}Po events in XENON100 can be found in Figure D.2 in the Appendix D.

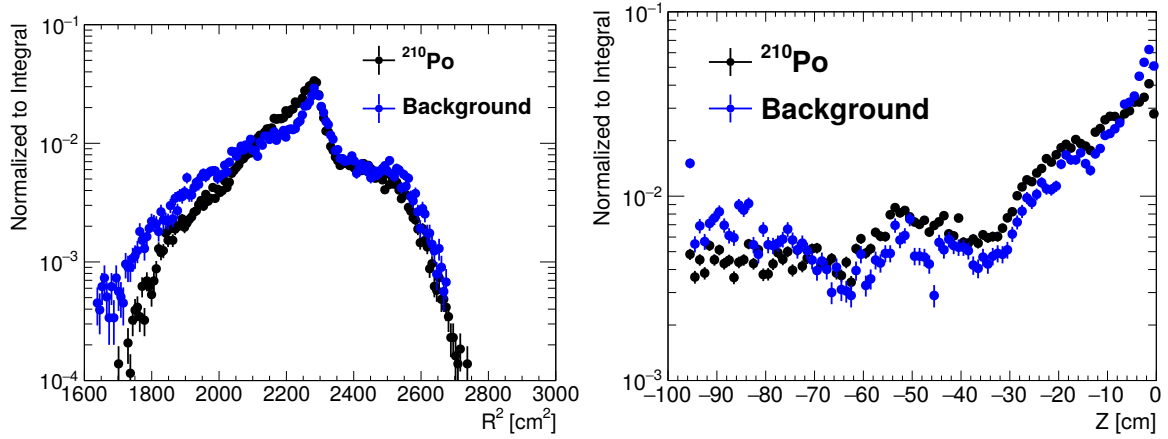


Figure 5.17: Comparison of R (left) and Z (right) distributions of ^{210}Po to low energy background events in XENON1T. Background events are required to have a $cS1$ smaller than 70 PE. The histograms are normalized to their integrals.

due to a reduced charge signal (see Section 5.4.1). By comparing to the properties found for ^{210}Po decays that are certain to take place on the detector wall, the origin of the low energy ER events that populate also the NR region can be concluded. This study has been performed before unblinding the WIMP signal region inside the FV of 1042 kg xenon mass. However, an unblinding of the signal region for events outside of the FV has been performed to allow the following investigations.

Figure 5.17 compares the shapes of the R^2 (left) and Z (right) distributions of ^{210}Po events (black) to the low energy ($cS1 < 70\text{PE}$) background in the dark matter search data (blue) recorded during the first science run of XENON1T. The histograms have been normalized to their respective integral.

The general shape of the ^{210}Po R^2 distribution is shared by the ER background population, though the distribution of the latter is a bit more smeared out. This is explained by the longer mean free path of gamma particles (up to several centimeters for the energies present in the uranium and thorium decay chain [163]) compared to alpha ($\sim\mu\text{m}$) and beta ($\sim\text{mm}$) particles. Furthermore, the position reconstruction algorithm features a lower precision for S2 signals from low energetic decays. While the ^{210}Po distribution can be well described by an exponential in the region $[1900, 2200]\text{cm}^2$ with a slope of $(7.07 \pm 0.02) \cdot 10^{-3}\text{cm}^{-2}$, the R^2 distribution of low energy background events below 2300cm^2 seems to be constituted out of two exponentials. The exponential increase in the region $[1900, 2200]\text{cm}^2$ yields $(3.8 \pm 0.2) \cdot 10^{-3}\text{cm}^{-2}$ and is a bit reduced compared to ^{210}Po .

The smeared R^2 distribution of low energy background events with respect to the ^{210}Po distribution is the reason why low energy interactions possess a finite probability to be reconstructed inside the fiducial volume restricted by $R^2 < 1365\text{cm}^2$.

The shape of the Z distributions of ^{210}Po and background events (see Figure 5.17 right) are in good agreement within the uncertainties except for a larger rate close to the cathode and the gate meshes (bottom and top) in background. This might be due to radioactive elements within the mesh material that emit gammas and betas but not high energetic alphas. Both event populations, background as well as ^{210}Po , show increasing rates toward the top which

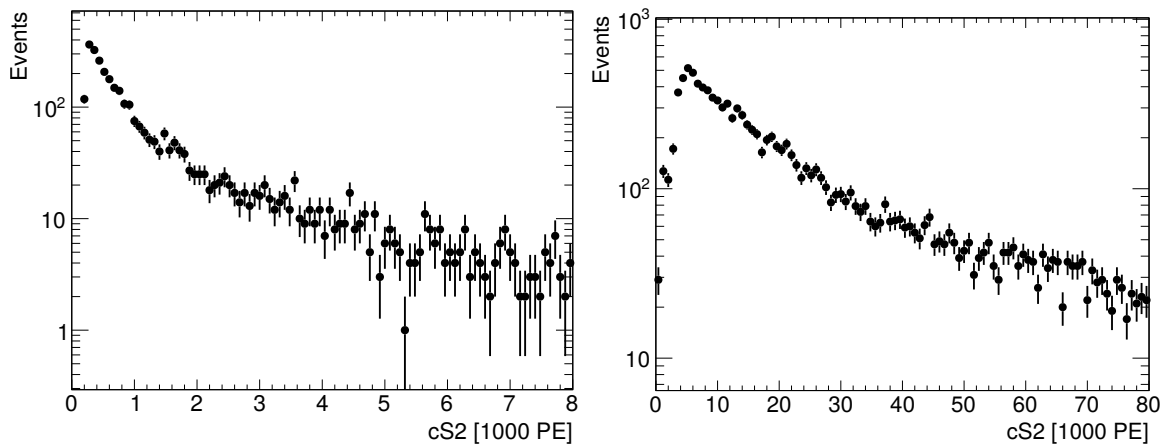


Figure 5.18: Left: cS2 spectrum of low energy events ($cS1 < 70$ PE) recorded during the first science run of XENON1T and passing all dark matter search criteria. **Right:** cS2 distribution of ^{210}Po interactions taking place in close proximity to the PTFE detector wall. Plot already shown in Figure 5.14 left.

is presumably correlated to a higher strength and inhomogeneity of the drift-field at the top part of the TPC [65]. Consequently, a higher efficiency of extracting the electrons from the interaction site is present since the attraction of charges to the PTFE can be overcome in more cases. The field deviations result from the detector geometry and might be additionally influenced by charges accumulating on the materials. They are under investigation using finite element simulations (COMSOL [164]) in order to adapt the field distortion correction.

Concerning the distribution of the charge signal of the low energy ER background, a feature of two exponentials is visible as in the R^2 distribution. Figure 5.18 left shows the cS2 distribution of the same background events whose R^2 and Z distributions were investigated in Figure 5.17. As for ^{210}Po alpha events (compare Figure 5.18 right), two exponential fall-offs with different slopes are observed. Background events feature a significantly steeper slope (about 3 orders of magnitude higher for $cS2 < 2000$ PE) compared to ^{210}Po data in the same region. Note the different scale on the x-axis in the two plots in Figure 5.18. The steeper exponential slope of the cS2 distribution of the low energetic ER background might be caused by the very different energy loss per unit track length of low energetic gamma and beta interactions compared to alpha particles. This difference results in varied charge yields. Additionally, the longer mean free path of gammas and betas might result in smaller charge losses than for alpha events since the interaction site can be located further away from the PTFE wall, leading to the faster fall-off of the cS2 spectrum of background events. A better understanding of the potential correlation between the R^2 and cS2 distributions of wall events are subject to future investigations.

As observed for ^{210}Po decays, an efficiency drop-off at low cS2 is present in the dark matter search background as well. However, in the case of the low energetic background events, this could be also explained by the detection efficiency. The events close to the efficiency threshold in cS2 are the most relevant ones for the background from wall events in the dark matter search. The resolution of the position reconstruction is additionally reduced for very small S2 signals and therefore, a correlation between the inwards reconstruction of

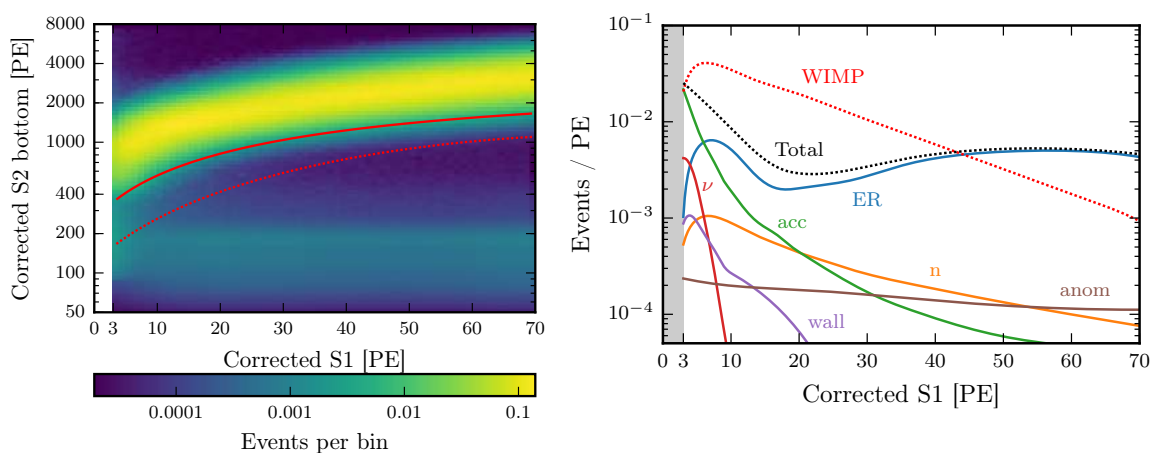


Figure 5.19: Left: Combination of all background models shown in the $cS2_{\text{bottom}}$ vs $cS1$ space inside the fiducial volume. The solid red line shows the NR median and the dashed red line the -2σ quantile. Figure from [65] **Right:** Projection of the individual components onto $cS1$ between the NR median and the -2σ quantile called reference region. The labels match the ones in Table 5.3. For comparison, the expected distribution of WIMPs having a mass of 50 GeV and a WIMP-nucleon cross section of $\sigma = 10^{-46} \text{ cm}^2$ is shown by the red dotted line. Figure from [53].

events from the wall and their measured S2 has to be taken into account in the background prediction from wall events.

5.5 The XENON1T Background Model

The background for the first dark matter search with XENON1T was modeled considering the following six background sources: The Gaussian part of the ER band within the fiducial volume, NR from neutrons and coherent scattering of solar neutrinos, accidental coincidences of uncorrelated lone S1 and S2 signals, a flat component of non-Gaussian leakage of ER events below the band that cannot be accounted for by accidental coincidences (see Section 5.3.3), and the wall events that were discussed in Section 5.4.

The six background components will be explained in the following and the method to construct the model of the wall event background is presented. For the final WIMP search analysis, the parameter space $cS2_{\text{bottom}}$, i.e., the corrected S2 signal detected by the bottom PMT array, versus $cS1$ has been used. Even though no major differences were found when performing the analysis with the total detected charge signal $cS2$ or with $cS2_{\text{bottom}}$, the latter was chosen before unblinding. The motivation is the more homogeneous collection of the secondary scintillation light on the bottom PMT array.

5.5.1 The Background Components

The combination of the probability density function (PDF) of the six background components in the parameter space $cS2_{\text{bottom}}$ versus $cS1$ is shown in Figure 5.19 left within the WIMP search region restricted by $cS1 \in [3, 70] \text{ PE}$ and $cS2_{\text{bottom}} \in [50, 8000] \text{ PE}$ and inside

the FV of 1042kg xenon mass. The NR median and the -2σ quantile are shown as a solid and dashed red line, respectively. The region between those lines is denoted as *reference region* and excludes 99.6% of the ER background while accepting about half of the WIMP candidate events. The WIMP search data is statistically interpreted by a profile likelihood [148], where the background model PDF is taken into account within the full search region. A projection of each background contribution to cS1 within the reference region is shown in Figure 5.19 right. In the following, we will refer to that figure when discussing the individual background components. For comparison, the expected PDF of a 50 GeV WIMP with an interaction cross section to nucleons of $\sigma = 10^{-46} \text{ cm}^2$ is shown as a red dotted line.

Downwards fluctuations of events from the ER band due to the overlap of the ER and NR regions, present the most dominant component above 10 PE in cS1 (blue in Figure 5.19 right). The ER band in background data within the fiducial volume is predominantly populated by β -decays of ^{85}Kr and ^{214}Pb , the daughter nuclide of ^{222}Rn . The ER background model was constructed by fitting a Markov Chain Monte Carlo simulation to ^{220}Rn calibration data. The best-fit photon yield and recombination fluctuations are extracted and found to be comparable to the ones found by the LUX collaboration [141]. The model incorporates uncertainties on the electron and photon yield parameters g_1 and g_2 , the spatial corrections of S1 and S2, the electron-extraction efficiency at the liquid-gas interface, and the event-selection efficiency.

The background from NR is composed of three sources: radiogenic and cosmogenic neutrons (orange in Figure 5.19), and coherent scattering of solar neutrinos (solid red in Figure 5.19). The recoil energy spectra of these processes were calculated in [108]. They were converted to cS1 and cS2_{bottom} by applying a nuclear recoil response model which has been derived from the Monte Carlo fitting of the nuclear recoil calibration data (see Section 5.2) using the same detector parameters and corresponding uncertainties as for the ER background model. The energy-conversion was constrained by the NEST model [147]. The expected rate of cosmogenic neutrons is one order of magnitude smaller than the other two considered components and is therefore neglected. Coherent neutrino scatters induce the second highest background rate below ~ 5 PE while radiogenic neutrons feature the second highest rate after the ER background, between 20 and 50 PE.

As mentioned in Section 5.3, uncorrelated S1 and S2 signals contribute to the background and are denoted as accidental coincidences (green in Figure 5.19 right). Isolated S1s (also lone S1s) can originate from interactions taking place in regions with a reduced charge collection efficiency, e.g. below the cathode. Isolated S2s (also-called lone S2s) can be induced by photo-ionization at the electrodes or by interactions in detector regions with poor light collection. The model is built using dark matter search data in which the WIMP sensitive region was blinded but events with a S2 signal smaller than the threshold of 200 PE were accessible. Adapting the procedure from [56], the rate and spectrum of lone S1s were estimated from S1s occurring before the main S1 in an event. The lone S2 rate and spectrum were evaluated by looking at events where no valid S1 could be found before the S2. By randomly pairing the isolated S1s and S2s and applying the event selection criteria on those created events, the accidental coincidence rate and its spectrum was modeled. Accidental

coincidences dominate the overall background rate below ~ 8 PE.

As a result of the studies of leakage below the ER band in ^{220}Rn calibration data (see Section 5.3.3) and due to its previous observation in XENON100 [56] a flat background component was added (brown in Figure 5.19 right). It accounts for non-Gaussian leakage of ER events below the band that are not already considered by the accidental coincidence model.

The wall leakage background component (violet in Figure 5.19 right) is made up of interactions taking place close to the PTFE walls of the TPC, i.e., predominantly ER from radioactivity in the detector materials. These wall events were studied in Section 5.4. They can be reconstructed inwards into the fiducial volume due the limited position reconstruction resolution in the order of several cm in the outer detector region. Additionally, these wall events suffer from a reduced S2 signal resulting in a downwards shift from the ER band into the NR region. This effect presents a dangerous background for the WIMP search. The spectral distribution of the corresponding background model was evaluated within the scope of this thesis and will be described in the following Section 5.5.2.

A summary of the expected number of events in the dark matter search data of 34.2 live days and in the reference region, is given for each background component in Table 5.3. Uncertainties smaller than 0.005 events are omitted but are properly taken into account in the profile likelihood analysis that is performed in the whole WIMP search region restricted by $cS1 \in [0, 70]$ and $cS2_{\text{bottom}} \in [50, 8000]$. The abbreviations in parentheses in Table 5.3 match the ones used in Figure 5.19 right. The largest background comes from the overlap between the ER band with the NR region with $0.26_{-0.07}^{+0.11}$ events in the reference region. Since the most stringent constraint is given by the data itself, this value is directly evaluated during the statistical treatment of the data in the likelihood analysis. This is why the value is given in parentheses in Table 5.3.

	Number of Events
Electronic recoils (<i>ER</i>)	$(0.26_{-0.07}^{+0.11})$
Radiogenic neutrons (<i>n</i>)	0.02
CNNS (<i>v</i>)	0.01
Accidental Coincidence (<i>acc</i>)	0.06
Wall leakage (<i>wall</i>)	0.01
Anomalous (<i>anom</i>)	0.01 ± 0.01
Total Background	$0.36_{-0.07}^{+0.11}$

Table 5.3: Expected number of background events for each individual component in the reference region between the NR median and the -2σ quantile within the WIMP search region and the fiducial volume. Uncertainties of less than 0.005 events are omitted. The ER rate is unconstrained in the likelihood. Here, the best-fit values are given in parentheses. Table from [53].

5.5.2 Wall Leakage Background

The properties of so-called wall events have been investigated in Section 5.4. It was found that a finite probability is present for this population to be reconstructed inside the FV. Due to charge loss at the PTFE wall they feature a reduced S2 signal and therefore can occur below the ER band. This is why this component is referred to as *wall leakage background*. The corresponding background prediction was constructed from low energy background data outside of the 1042kg FV in which the WIMP search region was unblinded, before the unblinding inside the FV. The same selection criteria have been applied as for the dark matter search (see Section 5.1). The rate and the spectral shape of the wall leakage background have been determined independently.

The Rate

The rate was inferred from the population below the NR median (see Figure 5.9) in order to only take into account events where charge loss occurred. Figure 5.20 shows the number of events over the xenon mass inside cylindrical FVs m_{Xenon} . The cylinders have the same height as the 1042 kg FV but different radii which are indicated at the top. The uncertainties on the data points were inferred from statistics. For the background rate estimate, the xenon mass range was restricted to values below 1300kg. At higher fiducial masses, internal background sources, i.e., radioactive isotopes dissolved in the LXe, start suffering from charge loss and become “wall-like” as well. Hence, there would be an overlay between the internal and external ER background sources whereas only the component coming from the detector wall is responsible for the wall leakage background.

The R^2 distribution of wall events was observed to be exponentially decreasing toward smaller radii in Section 5.4.4. Hence, the number of wall events expected in the 1042kg FV is extracted from an exponential fit (red line) to the data shown in Figure 5.20. The systematic uncertainty due to a potential deviation from the fit model is gained from the difference to the result of a power falloff fit of the form $1/m_{\text{Xenon}}^p$ (green dashed line). The result for the whole science run yields (0.5 ± 0.3) events for $cS1 < 70$ PE [156].

The Spectral Shape

The charge loss at the PTFE wall removes any strong correlation between $cS1$ and $cS2_{\text{bottom}}$ that is present for ER events for which the charge can be fully collected. Hence, the two variables $cS1$ and $cS2_{\text{bottom}}$ can be studied independently.

Figure 5.21 shows the distribution of $cS1$ vs. R on the left and $cS2_{\text{bottom}}$ vs. R on the right, with the number of events on the logarithmic color scale. The Z range was set to be the same as for the 1042kg FV. The radius of the FV is marked by the red solid lines. Only events that were identified to have suffered from charge loss with high probability by lying below the 99.5% ER band discrimination line, were considered. The step in the density distribution that can be observed at $R \sim 48$ cm is related to the artifact in the position reconstruction that has been previously described as the “trunk-like” feature.

The $cS1$ spectrum is entirely uncorrelated to R . Consequently, all shown events outside of the FV (38247 events) are used for the prediction of the $cS1$ spectrum. It is modeled using the kernel density estimation (KDE) method [165, 166]. A KDE allows to estimate the PDF

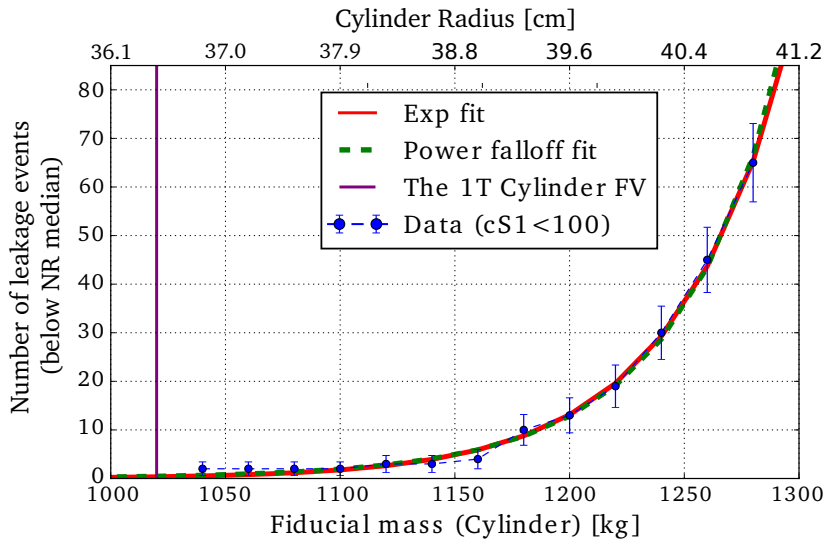


Figure 5.20: Number of events below NR median vs. xenon mass in cylinder volumes whereas the cylinders only differ by their radii as indicated by the scale at the top. Uncertainties are purely statistical (Poisson distributed). The red solid line shows the exponential fit result and the green dashed line the result from the power fall-off fit. Figure from [156].

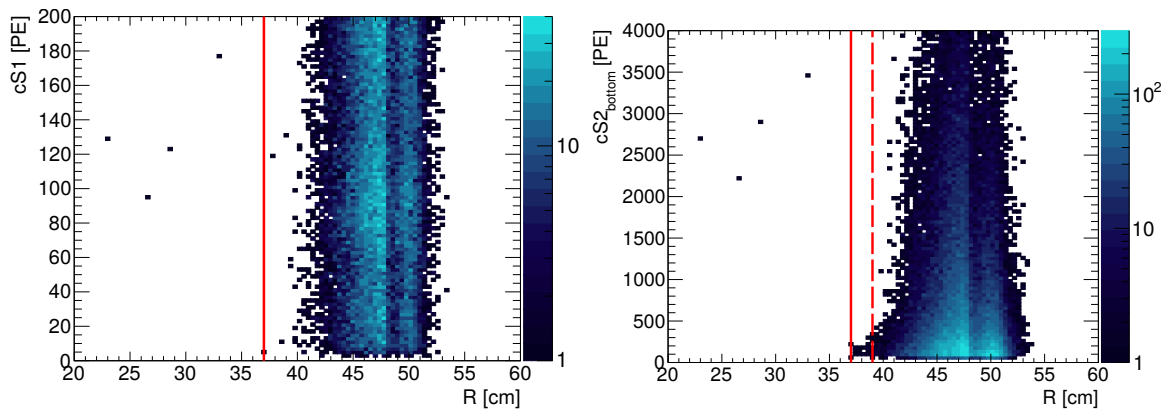


Figure 5.21: Left: Correlation of $cS1$ with the TPC radius R for events passing all selection criteria but fall below the 99% ER discrimination line. The number of events per bin is indicated by the color scale. The red line marks the radius of the 1042kg cylindrical FV. All events with higher radii have been used to model the $cS1$ spectrum. **Right:** $cS2_{\text{bottom}}$ vs. R for the same event selection except that the S2 threshold $S2 > 200$ PE was replaced by $cS2 > 200$ PE to avoid a Z-dependence. The red solid line indicates the radius of the 1042kg cylindrical FV. Events falling between the solid and dashed red lines have been used to model the $cS2_{\text{bottom}}$ spectrum.

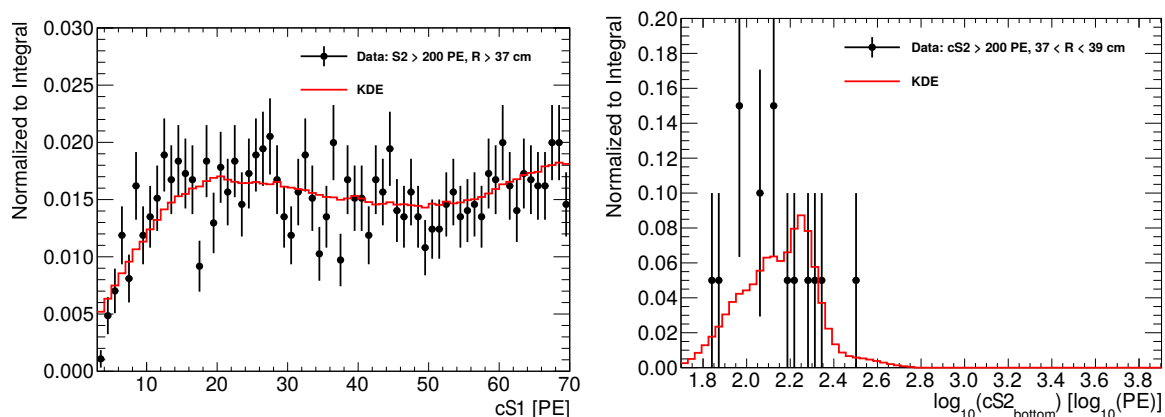
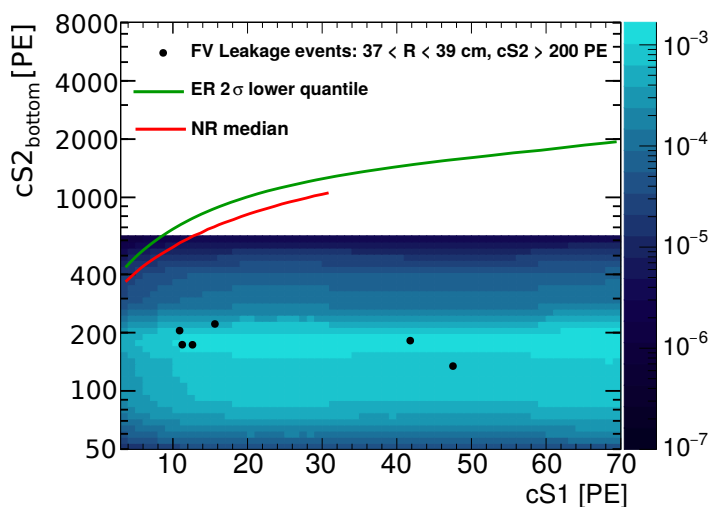


Figure 5.22: Control samples from which the $cS1$ (left) and $cS2_{\text{bottom}}$ (right) spectra have been modeled by kernel density estimation (KDE). See text for more explanations.

of a measured distribution in a non-parametric way. It is advantageous when only limited statistics is available since it allows to also extrapolate the PDF into regions where no events have been measured. This is primarily an issue for the $cS2_{\text{bottom}}$ spectrum but for consistency the same method has been applied for the $cS1$ spectrum. The result is shown in Figure 5.22 left in red, together with the original data in black. Good agreement between the data and the estimated PDF can be observed within the statistical uncertainties.

For $cS2_{\text{bottom}}$, a slightly larger spread over R for smaller charge signal values can be found in Figure 5.21 right. This points to a small correlation of $cS2_{\text{bottom}}$ to R , owing to the decreased position reconstruction resolution for small $S2$ signals. Especially the number of outliers is larger in the low energy regime. Those outliers present the population of interest for the background prediction. Hence, only events within with $R \in [37, 39]$ cm were considered for the prediction of the $cS2_{\text{bottom}}$ spectrum in the FV. The upper boundary is marked by the red dashed line in Figure 5.21 right. The event distribution within this R region is considered to be similar to the one inside the FV. The $S2$ threshold of 200 PE was transferred to a threshold on $cS2$ of the same value to generate the plot. This avoids a Z dependence of the threshold in order to not affect the non-uniform Z distribution of wall events (see Figure 5.17 right). If

Figure 5.23: Normalized PDF of the wall leakage background component in $cS2_{\text{bottom}}$ vs. $cS1$. The black points show the leakage events outside of the FV radius within $37 < R < 39$ cm from which the $cS2_{\text{bottom}}$ spectrum was modeled. For reference, the ER -2σ quantile and the NR median are given in green and red, respectively. White regions represent areas with probabilities below 10^{-7} which are considered to be negligible.



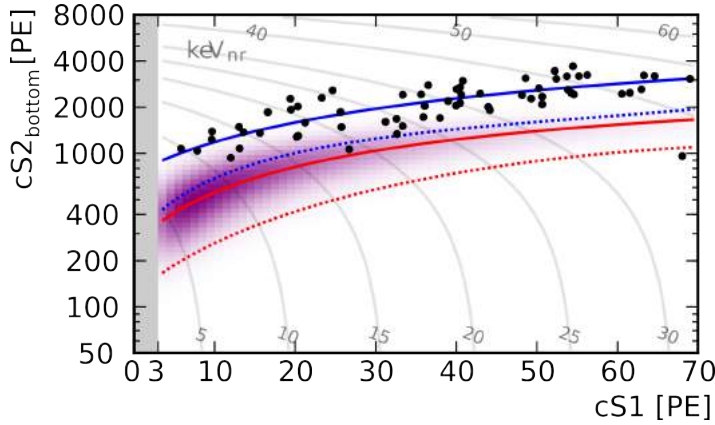


Figure 5.24: Dark Matter search data of the first science run of XENON1T acquired within 34.2 live days. The ER (blue) and NR (red) medians and -2σ quantiles are marked as solid and dashed lines, respectively. For reference, the PDF of a 50 GeV WIMP signal is indicated in purple. Figure from [53]

the stricter criterion of $S2 > 200$ PE had been applied, only wall events from the upper part of the TPC would have been used to model the $cS2_{\text{bottom}}$ spectrum, leading to a potential bias. The statistics in the region $R \in [37, 39]$ cm can be increased by considering events with $cS1$ up to 500 PE. This is justified by the non-correlation of $cS1$ and $cS2_{\text{bottom}}$. A total of 19 events was found in this described region. The $cS2_{\text{bottom}}$ spectrum was modeled by a KDE as well. Figure 5.22 right shows the result in red, together with the original data in black.

To gain the PDF in the $cS1$ vs. $cS2_{\text{bottom}}$ space, the normalized spectra are convoluted. The result is presented in Figure 5.23. For reference, the NR median (green line) and the 99.5% discrimination line (red) are marked, as well as the data points of the events in the interval $R \in [37, 39]$ cm (black). The probability is below 10^{-7} in the white region and is considered to be negligible.

This PDF is scaled by the event rate, derived from the exponential fit as explained above, and taken into account in the statistical interpretation of the measured data inside the FV.

The contribution of this wall leakage background component in the reference region (0.01 events) is as large as the background from anomalous leakage and coherent neutrino scattering.

5.6 Results on WIMP-Nucleon Interactions

The dark matter search dataset acquired over 34.2 live days contains a total of 63 events that pass the selection criteria and fall into the dark matter search region restricted by $cS1 \in [3, 70]$ PE and $cS2_{\text{bottom}} \in [50, 8000]$ PE. This corresponds to an ER rate of $(1.93 \pm 0.25) \cdot 10^{-4}$ events/(kg·day·keV_{ee}⁶). The observation is in good agreement with the expected rate of $(2.3 \pm 0.2) \cdot 10^{-4}$ events/(kg·day·keV_{ee}) predicted by simulations [108] and updated by the concentration of natural krypton measured by rare-gas mass spectrometry [118] in xenon samples from the detector.

The dark matter search data is presented in Figure 5.24 in the $cS2_{\text{bottom}}$ vs. $cS1$ space with the ER (blue) and NR (red) medians and -2σ quantiles given as solid and dashed lines, respectively. As an example, the PDF for a 50 GeV WIMP signal is indicated in purple. The

⁶The unit keV_{ee} means “keV electron equivalent” and indicates the energy scale derived from ER calibrations with mono-energetic lines.

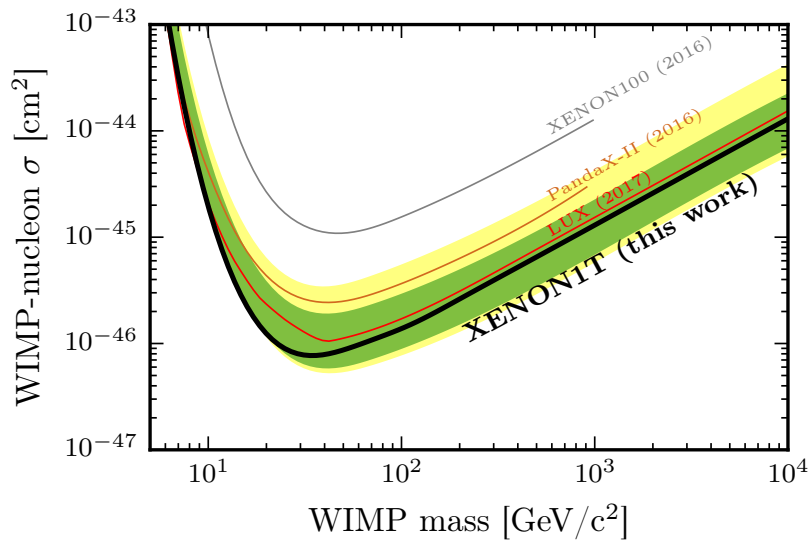


Figure 5.25: 90% confidence level limit of the spin-independent WIMP-nucleon scattering cross section as a function of the WIMP mass (black). The green and yellow bands indicate the 1- and 2- σ sensitivity regions, respectively. As a reference, the results of LUX [54] (red), PandaX-II [55] (brown), and XENON100 [56] (gray) are shown. Figure from [53].

event, which is well separated from the ER region with a $cS1$ of 68.0PE, was thoroughly investigated and was found to be a real event to the best of our knowledge. However, the combination of its charge and light signal does not have a high compatibility with either the background model or a WIMP signal. Therefore, its contribution to the likelihood is very small. In contrast, the event located 2.4σ below the ER mean with $cS1 = 26.7$ PE has the largest influence on the WIMP search result due to its closeness to the NR median.

The statistical interpretation of the data was performed by an extended unbinned profile likelihood in the $cS1$ - $cS2_{\text{bottom}}$ parameter space. The asymptotic formulae for likelihood-based tests described in [167] were applied. Shape uncertainties on the most important parameters were estimated from the posteriors of the NR and ER calibration fits and propagated to the likelihood. The uncertainty of the rate of each background component was included as well. In order to take into account mis-modeling of the ER background, a safeguard parameter was employed as described in [168].

The likelihood's best-fit value evaluated in the dark matter search data favors the background-only hypothesis. The corresponding upper limit at a 90% confidence level on the spin-independent WIMP-nucleon cross section is shown by the black line in Figure 5.25. The limit is power constrained to -1σ of the sensitivity band and is different by a maximum of 10% from the unconstrained limit for all WIMP masses. Light and charge emissions for WIMPs below 1 keV were omitted. None of the best-fit values of the nuisance parameters deviates significantly from its nominal value.

At the time of writing, this dark matter search result imposes the strongest upper limit on spin-independent WIMP-nucleon interactions for WIMP masses above 10 GeV with a minimum at $m = 35$ GeV yielding $\sigma_0^{\text{SI}} = 7.7 \cdot 10^{-47} \text{ cm}^2$.

5.7 Summary and Conclusions

This chapter outlined the analysis of the first dark matter result of the XENON1T detector. Special attention was given to the investigation of the acquired ER calibration data in Section 5.3 and to the understanding of so-called *wall events* in Section 5.4 that contribute to the background of the WIMP search. Furthermore, a model for the wall event population has been developed in Section 5.5.2.

The ER data from the novel internal ^{220}Rn calibration source, which was studied in Chapter 4, has been used for the first time during a science run. It was employed to define a blinding criterion in Section 5.3.2 that removes events from the signal region in the dark matter search data in order to avoid adjusting the event selection and background models to potential signal events. At the same time, the blinding criterion allows access to 99% of the ER background data in order to monitor detector anomalies, to study the performance of the event selection and to verify the compatibility of the ER calibration data with the background.

By applying the blinding criterion, no event in the signal region was revealed until the process of establishing the event selection and background model was finished. The background prediction was successfully tested in a control region featuring higher cS1 values than the WIMP search energy region. After unblinding the signal region, no disagreement between the background model and the observation was found, i.e., no unforeseen background component has been observed. The fact that neither the event selection nor the background prediction were changed post-unblinding indicates that all necessary information for the analysis was contained in the dark matter search data, despite the inaccessible signal region.

Additionally, the compatibility of the acquired ^{220}Rn calibration data with the ER background in XENON1T was verified in Section 5.3.3. As discussed in Chapter 4, deviations between the two datasets can lead to a different result in the dark matter search. In this chapter, the finding is that the ^{220}Rn and the dark matter search data show ER bands that feature a compatible component of non-Gaussian leakage of events toward smaller values in the discrimination parameter ($\log_{10}(\text{cS2}/\text{cS1})$). Hence, at the given statistical uncertainties, it can be concluded that the ER calibration data does not only properly model the bulk of the ER band but also the non-Gaussian ER leakage into the signal region. Therefore, no bias is expected for the dark matter result when modeling those two background components with the calibration data.

An additional background component from interactions taking place in close proximity to the detector wall was identified during the process of finding an optimal fiducial volume (FV) that allows as large as possible expected WIMP scattering rates but at the same time suppresses the background radiation from the detector materials. These wall events represent a dangerous background since they leak below the ER band into the signal region and can be reconstructed inside the FV, even though the interaction took place outside. For this reason, the radius of the FV had to be restricted to smaller values than necessary in the presence of only the ER background component from the detector materials. This led to the loss of about 200 kg of fiducial mass (see Section 5.4.1).

In Section 5.4, the wall event population was studied in order to understand their origin and properties. High-energetic ^{210}Po alpha decays ($Q_\alpha = 5.4\text{ MeV}$) provide a good test population for the wall event type. By comparing the rate of ^{210}Po to ^{222}Rn , it can be concluded that ^{210}Po is present on the surfaces as a contamination induced by the accumulation of decay daughters of ^{222}Rn during the construction of the detector components. The surface contamination induced by ^{222}Rn on different materials has been studied in other low-background experiments as well, such as CUORE [160], BOREXINO [161], and LUX [162]. Due to the short mean free path of alpha particles ($\sim\mu\text{m}$) in liquid xenon, it is ensured that the ^{210}Po alpha particle deposits its energy at the wall. With that knowledge, general properties for events occurring at the detector edges can be derived.

It was found that ^{210}Po events suffer from losses in the charge signal of up to 95% and that they feature a poor resolution of the position reconstruction in R resulting in a deviation of up to 5 cm from their actual position at the wall. Comparing the ^{210}Po population to low energetic ER interactions located in the outer detector region, similar distributions in the charge signal cS2 and in R are found. This indicates the same origin of the low energetic background as the ^{210}Po , namely the PTFE surfaces. A possible explanation are the beta decays of the isotopes ^{214}Pb , ^{214}Bi , ^{210}Pb , and ^{210}Bi that occur within the ^{220}Rn decay chain. Beta particles have an average range of a few millimeters in liquid xenon and therefore deposit their energy close enough to the PTFE surface to feature a similar charge loss and R distribution as ^{210}Po decays. A direct comparison of the rate in the low energy region to the ^{210}Po rate is difficult due to the reduced detection efficiency, related to the attenuated S2 signal.

The R distribution of ER in the WIMP search energy region is slightly more smeared than distribution of ^{210}Po events, presumably due to the further decrease of the position reconstruction resolution for low energetic events. This results in a finite probability that some events are reconstructed inside the FV. Hence, an additional background component from those wall events has to be considered.

The background of wall events (also wall leakage background) was first reported in liquid xenon detectors by the ZEPLIN-II [157] and Xed-I [158] experiments. Furthermore, the LUX experiment modeled this background not only in energy but also spatially [169]. In contrast, the PandaX experiment suppressed the wall leakage background component to a negligible contribution by selecting a conservative FV [55].

For the first dark matter search in XENON1T, the energy spectrum and rate of wall events inside the FV with $R = 37\text{ cm}$ and in the WIMP search energy region was inferred from the population beyond the FV radius. The procedure is described in Section 5.5.2, resulting in a prediction of 0.01 events in the reference region between the median of the NR band and its -2σ quantile within the WIMP search energy region of $\text{cS1} \in [3, 70]\text{ PE}$. This value is of the same size as the background expected from coherent scattering of solar neutrinos and from anomalous leakage of ER events below the band that are not accidental coincidences of lone S1s and S2s. Furthermore, the wall leakage background component is approximately one order of magnitude smaller than the dominating background from ER induced by ^{222}Rn , whose value yields $0.26^{+0.11}_{-0.07}$ events in the reference region.

Further studies are ongoing to improve the resolution of the position reconstruction algorithm in the outer detector regions. By comparing the resolution to that achieved in XENON100 (see Section 5.4.3), the collaboration is confident that an improvement by a factor of approximately 4 is possible.

The impact of the surface contaminations of ^{222}Rn progenies on the background level within the XENON1T dark matter search are subject to future investigations as well.

The presented analysis of the first science run data acquired with the XENON1T detector, has proven an excellent sensitivity to spin-independent WIMP-nucleon interactions, resulting in the most stringent limit of the corresponding cross section for WIMP masses above 10 GeV with a minimum at $m = 35 \text{ GeV}$ yielding $\sigma_0^{\text{SI}} = 7.7 \cdot 10^{-47} \text{ cm}^2$, at the time of writing.

Summary and Outlook

After the successful operation of the XENON100 experiment, its successor, XENON1T, has taken over by proving its own potential, to be the most sensitive experiment in the direct search for spin-independent WIMP-nucleon interactions, at the time of writing.

XENON1T is the first experiment that employs the technology of dual-phase liquid xenon time projection chambers with a target mass in the multi-ton scale. This brings new challenges.

In general, the large detector size of XENON1T is advantageous for the reduction of background from external radiation by self-shielding, and provides the prerequisite for the unprecedented sensitivity to dark matter interactions. However, the same feature is rather obstructive for the calibration of the innermost target volume. The external gamma sources used in XENON100 for calibrating the dominating background type, namely electronic recoils induced by beta and gamma radiation, do not provide a sufficiently high rate within the WIMP search region in XENON1T. Furthermore, the definition of a fiducial volume in a new detector requires the understanding of effects present at the detector borders in order to optimize the volume to its maximum reasonable size.

The 3.3 tons of xenon that are necessary to operate XENON1T need to be maintained at the high purity standards necessary for the detector's performance. Krypton contaminations contribute directly to the intrinsic background with its radioactive isotope ^{85}Kr , whereas oxygen attenuates the secondary signal (S2) by attracting the ionization-electrons due to its large electronegativity.

The mentioned challenges of gas purity, background calibration and the understanding of the data acquired with the newly constructed detector, were addressed in this thesis.

In Chapter 3, the monitoring of the xenon gas purity during the initial filling of the experiment's storage vessel ReStoX was described. Using the technique of gas chromatography, the concentrations of krypton and oxygen impurities were quantified in a variety of samples extracted from the gas cylinders delivered by the suppliers, prior to the storage of the contained xenon. A fraction of 12% of the gas was identified as being contaminated, and had to be purified separately.

These measures provided the foundation for the successful first science run of XENON1T. The krypton concentration was ensured to be below 40 ppb, enabling the collaboration to reduce the ^{85}Kr -induced background by cryogenic distillation in parallel with the science data acquisition to a level below the background from subsequent decays of ^{222}Rn . The result is the lowest background level ever achieved in a dark matter search experiment with $(1.93 \pm 0.25) \cdot 10^{-4} \text{ events}/(\text{kg} \cdot \text{day} \cdot \text{keV}_{\text{ee}})$. Furthermore, the oxygen concentration was guaranteed to be below 0.9 ppm. Consequently, the electron lifetime improvement efforts were

primarily hampered by the outgassing of detector materials.

Chapter 4 investigated novel sources of radio-isotopes that can be dissolved in the liquid xenon, such as tritium and ^{220}Rn . Their technical challenges and their calibration performance were outlined.

While the tritium source is advantageous in providing high event rates of the order of tens of mBq/kg in the region of interest, it has the drawback that its spectrum is not flat, as expected from background radiation in the XENON detectors. This introduces a discrepancy into the background model that might, in the worst case, even result in a false discovery. To resolve this issue, for example corrections of the spectral can be applied and Monte Carlo simulations can be used. Furthermore, the removal of the tritium activity from the detector is not ensured by its radioactive decay due to the isotope's relatively long half-life of about 12 years. Hence, active removal techniques are required that are subject to further investigations.

More promising as calibration source is the isotope ^{220}Rn , whose activity is decreased by five orders of magnitude within one week after its injection into the detector. Even though the source provides only a rate of the order of 10^{-2} to 10^{-1} mBq/kg, calibration data with sufficient statistics can be acquired within a few days. The compatibility between ^{220}Rn calibration data and the background of the experiment within the uncertainties was shown, leading to the usage of the ^{220}Rn data for background modeling in the first science run of XENON1T.

The analysis of the first science run of XENON1T was subject to Chapter 5. A background source originating from the surface of the TPC was identified. It influences the choice of the radius of the cylindrical fiducial volume since those events can be mis-reconstructed towards smaller radii due to the finite position reconstruction resolution in the outer detector regions. Because of charge losses owing to the attachment of electrons to the PTFE wall, the secondary signal (S2) is reduced by up to 95%, resulting in a shift of these events into the region of expected WIMP signals. The properties of this so-called *wall event* population were investigated by comparison to alpha events from ^{210}Po present at the PTFE surfaces that confine the TPC. The wall events are induced by decays of ^{210}Pb , by gamma radiation from the uranium and thorium decay chains of intrinsic contaminations in the PTFE, and by recoiling ^{206}Pb nuclei, the daughter of ^{210}Po .

The studies performed in this work provide a better understanding of wall events and enabled us to model its spectrum in order to account for it in the background prediction of the dark matter analysis.

Improvements of the position reconstruction algorithm are under investigation, with the aim of suppressing the wall event background component. This will allow us to enlarge the fiducial volume in the future to exploit a higher xenon mass while maintaining the low background level. Furthermore, the presence of ^{210}Po decays at the PTFE surfaces with relatively high rates may motivate R&D in the field of surface cleaning in order to avoid background from these contaminations in future detectors.

The newly constructed XENON1T detector has proven its functionality by reporting the most constraining limit on the spin-independent WIMP-nucleon cross-section for WIMP

masses above 10 GeV with a minimum of $7.7 \cdot 10^{-47} \text{ cm}^2$ at a mass of 35 GeV. The XENON collaboration is now eager to improve this result by almost a factor of five by exploiting the full projected sensitivity of the experiment with an exposure of 2 years [108].

In parallel, preparations and R&D are ongoing for a detector upgrade to XENONnT. Containing a total of approximately 7 t of xenon, the sensitivity will be improved by one order of magnitude with respect to XENON1T, provided that the background rate from natural radioactivity can be further reduced by one order of magnitude. Besides a potential discovery of dark matter, this unprecedented detector performance will also open the door to physics channels such as the detection of coherent neutrino-nucleon scattering or the neutrinoless double beta decay of ^{136}Xe [170].

Appendices

Appendix A

Virial Theorem

The virial theorem provides a general equation in classical mechanics. It states that the total kinetic energy $\langle T \rangle$ of a stable system of N particles interacting by a potential force, is proportional to the total potential energy $\langle V_{\text{tot}} \rangle$. The angle brackets indicate averaged quantities over time. Its explicit form is expressed by

$$\langle T \rangle = -\frac{1}{2} \sum_{k=1}^N (\mathbf{F}_k \cdot \mathbf{r}_k), \quad (\text{A.1})$$

with \mathbf{F}_k the force on the k -th particle at the position \mathbf{r}_k . For power law forces with the exponent n , this equation transforms to

$$\langle T \rangle = \frac{n}{2} \langle V_{\text{tot}} \rangle \stackrel{n=-1}{=} -\frac{1}{2} \langle V_{\text{tot}} \rangle. \quad (\text{A.2})$$

The last relation applies to gravitational forces with $n = -1$. The average kinetic energy then equals half of the average negative potential energy.

Appendix B

Gas Compositions

Main components	Mole percent	Trace Gases	Mole ppm
Nitrogen	78.08	Carbon dioxide	350
Oxygen	20.95	Neon	18.18
Argon	0.93	Helium	5.24
		Methane	1.8
		Krypton	1.14
		Hydrogen	0.53
		Nitrous oxide (N ₂ O)	0.31
		Carbon monoxide	0.25
		Xenon	0.087

Table B.1: Air composition [79]

Measured gas impurities	Mixture 1 [ppm]	Mixture 2
H ₂	4.97 ± 0.15	5.00 ± 0.15
O ₂ + Ar	17.06 ± 0.45	14.91 ± 0.39
O ₂	10.80 ± 0.32	9.77 ± 0.29
N ₂	12.60 ± 1.30	11.40 ± 1.10
Kr	11.10 ± 0.22	11.60 ± 0.23
CH ₄	5.17 ± 0.10	5.30 ± 0.11
CO	5.16 ± 0.10	4.88 ± 0.10

Table B.2: Composition of employed helium gas mixtures for the calibration of the Gas Chromatograph (see Chapter 3). Mixture 1 was used for the calibration of all gas chromatography measurements while Mixture 2 served for the production of xenon calibration gas samples.

Appendix C

Electronic Recoil Calibration Studies

C.1 Spatial Distribution of ER Data in XENON1T

Figure C.1 shows the R^2 (left) and Z (right) distributions of ER events acquired with XENON1T in the WIMP search energy region $cS1 \in [0, 70]$ PE, when no source (green) or the ^{220}Rn source (red) was deployed. Events from the cathode and gate region have been neglected by requiring the electron drift time to be smaller than $4\mu\text{s}$ and $Z > -95\text{ cm}$. Furthermore, the radius was required to be smaller than 40 cm in order to avoid effects from increased positions reconstruction uncertainties, field distortion, and charge losses at the PTFE wall (see Section 5.4). In Z , ^{220}Rn and background agree in a flat distribution below -20 cm . Above that value, ^{220}Rn remains flat while the additional component from detector materials becomes prominent in background data, beside the internal sources that are dominating in the inner detector region. Also in R^2 , ER events from the ^{220}Rn source are well homogeneously distributed while the background shows a rate increase at low depths because of the proximity to the radiation from the TPC wall.

C.2 On the Discrepancy between ^{220}Rn and Thorium Data

The systematic offset of $(1.0 \pm 0.1)\%$ in the ER band mean between ^{220}Rn and thorium data (see Section 4.5.1) was investigated in order to find out if it could be owing to a physical difference between gamma and beta interactions or if it is a detector systematic.

Effects from the data selection criteria, acting differently on the two datasets could be excluded. However, studying the S1 and S2 yields during the the data taking periods, fluctuations could be found that can explain the offset in the ER band means.

Alpha peaks are very well suited for monitoring the yield since they are not influenced by the ER rate introduced by the calibration sources. Figure C.2 shows the S1 and S2 yields as functions of time. The S1 yields have been evaluated by fitting the $S1_\alpha$ spectrum as described in Section 4.2.1 and extracting the Gaussian means. The S2 yields were determined by selecting events with $cS1_\alpha$ within the 3σ range of the Gaussian peaks and fitting a Gaussian to the corresponding $cS2_{\text{bottom}}$ spectrum. Due to overlaps in the $cS1_\alpha$ spectrum, only ^{222}Rn and ^{216}Po decays have been considered for the $cS2_{\text{bottom}}$ yield. The uncertainties are

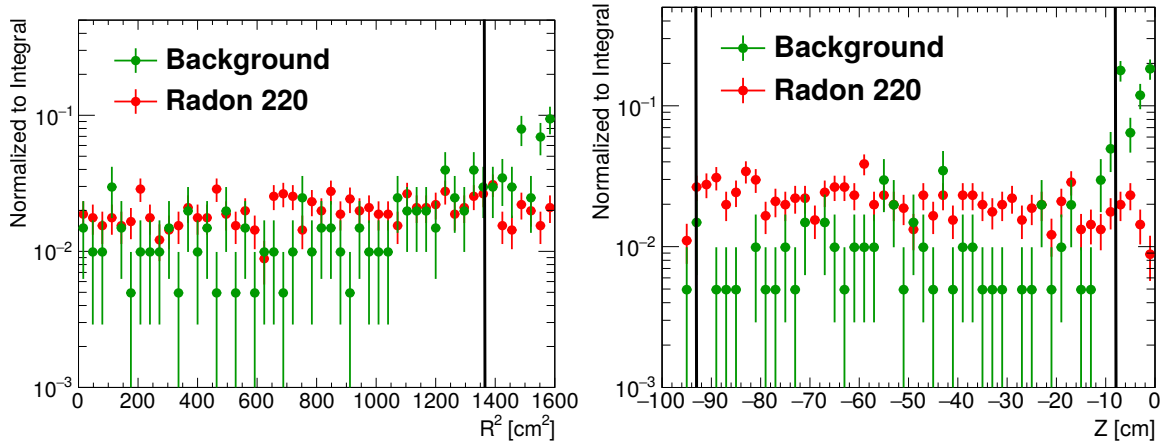


Figure C.1: Comparison of R^2 (left) and Z (right) distributions of ER interactions induced in XENON1T by the ^{220}Rn source (red) and background (green) in the WIMP search energy region $cS1 \in [0, 70]$ PE. Events in the cathode and gate region have been neglected as well as those with $R^2 > 1600 \text{ cm}^2$. The histograms have been normalized to their integral. For reference, the borders of the 1042 kg cylindrical FV utilized in the dark matter search are visualized by the vertical black lines.

extracted from the error matrix of the fit. The colors of the data points indicate the isotope from whose decay the yield is determined: blue ^{220}Rn , cyan ^{222}Rn , red ^{212}Bi , and yellow ^{216}Po . While ^{220}Rn , ^{212}Bi , and ^{216}Po are only present during the ^{220}Rn data taking period ^{222}Rn is constantly emanating from the detector materials. The absence of ^{222}Rn data points can be due to high detector dead times during source deployment or non converging fits, since the automatic fitting algorithm is sensitive to fluctuations in the data. The means of the yields and the corresponding 1 % intervals are marked by the horizontal solid and dashed lines, respectively. The vertical black lines separate time periods of deployment of different sources, as indicated above the canvases.

The fluctuations of the S1 yields over time are well within 1 %. Additionally all data points follow the same trend suggesting that variations in detector parameters could be responsible. The average S1 yields of ^{220}Rn and ^{216}Po are slightly higher than the ones of ^{212}Bi and ^{222}Rn since the ^{220}Rn source was used mostly in time periods where the S1 yield was higher. The S1 yields during the thorium data taking periods are in good agreement with the overall average. Hence, no systematic effect is expected from this.

In contrast to the S1 yields, the S2 yields show a dependence on the alpha energy. ^{216}Po has a ~ 3 % higher average value that is not in agreement with the overall variations in the ^{222}Rn graph, that are within $(1 - 2)$ %. The investigation of this unexpected non-linear energy scale in S2 was beyond the scope of this thesis. Averaging the S2 yields during the thorium data taking periods, a value of $(9.152 \pm 0.001) \text{ PE/keV}$ is gained. This deviates from the overall average of $(9.2579 \pm 0.0001) \text{ PE/keV}$ by about 1 % and translates to about 1 % discrepancy in the discrimination parameter as well.

Hence, the observed discrepancy in the ER band mean in the ^{220}Rn and thorium data can be explained by a deviation in the S2 yield and is most likely not the result of differences in the energy deposition of gamma and beta particles.

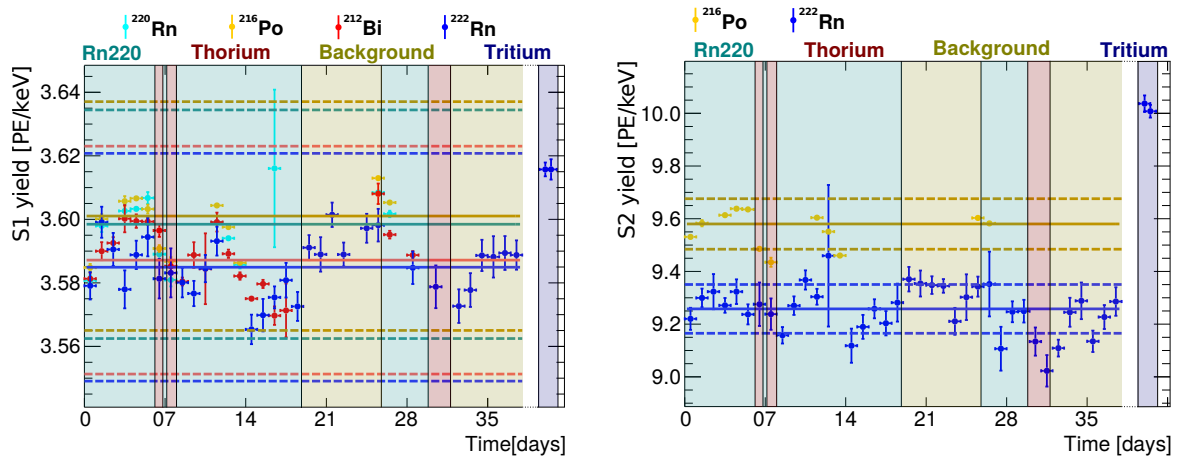


Figure C.2: **Left:** S1 yield extracted from the mean of a Gaussian fit to the alpha peaks of ^{220}Rn (cyan), ^{216}Po (yellow), ^{212}Bi (red), and ^{222}Rn (blue). The color of the shaded time periods indicates to which source the taken data has been attributed. Tritium data was taken about two months after the last background dataset. The horizontal lines mark the average yield (solid) and the corresponding $\pm 1\%$ interval (dashed). The period of tritium data was not used for the evaluation of the average due to its larger deviation. **Right:** Same constellation as in the left plot for the S2 yield. The yield was extracted from the mean of Gaussian fits to the S2 spectrum of the ^{216}Po and ^{222}Rn peaks which have been chosen for their good separation from other peaks in cS1_α .

Appendix D

Wall Event Studies

The following figures are referenced in Chapter 5 in the context of the studies, performed on wall events.

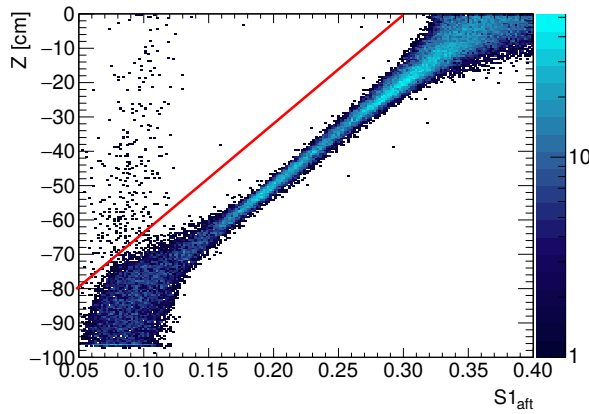


Figure D.1: Distribution of ^{210}Po decays ($cS2 < 80000\text{PE}$, $cS1 \in [40000, 60000]$) in Z vs. the fraction of the total S1 detected by the top PMT array (S1 area fraction top: S1_{aft}) recorded with XENON1T. The number of events is indicated by the color scale. All events placed above the red line are rejected since they do not show the same strong correlation between Z and S1_{aft} as observed in the majority of the population.

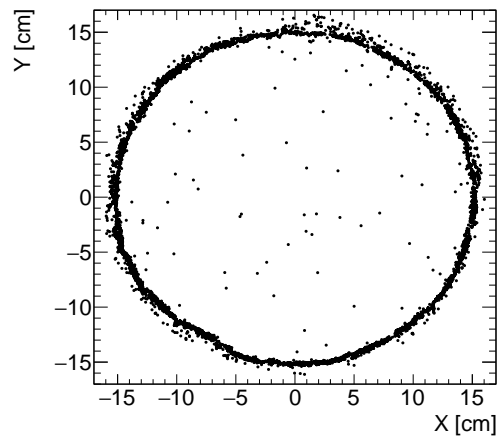


Figure D.2: X-Y distribution of ^{210}Po events in XENON100

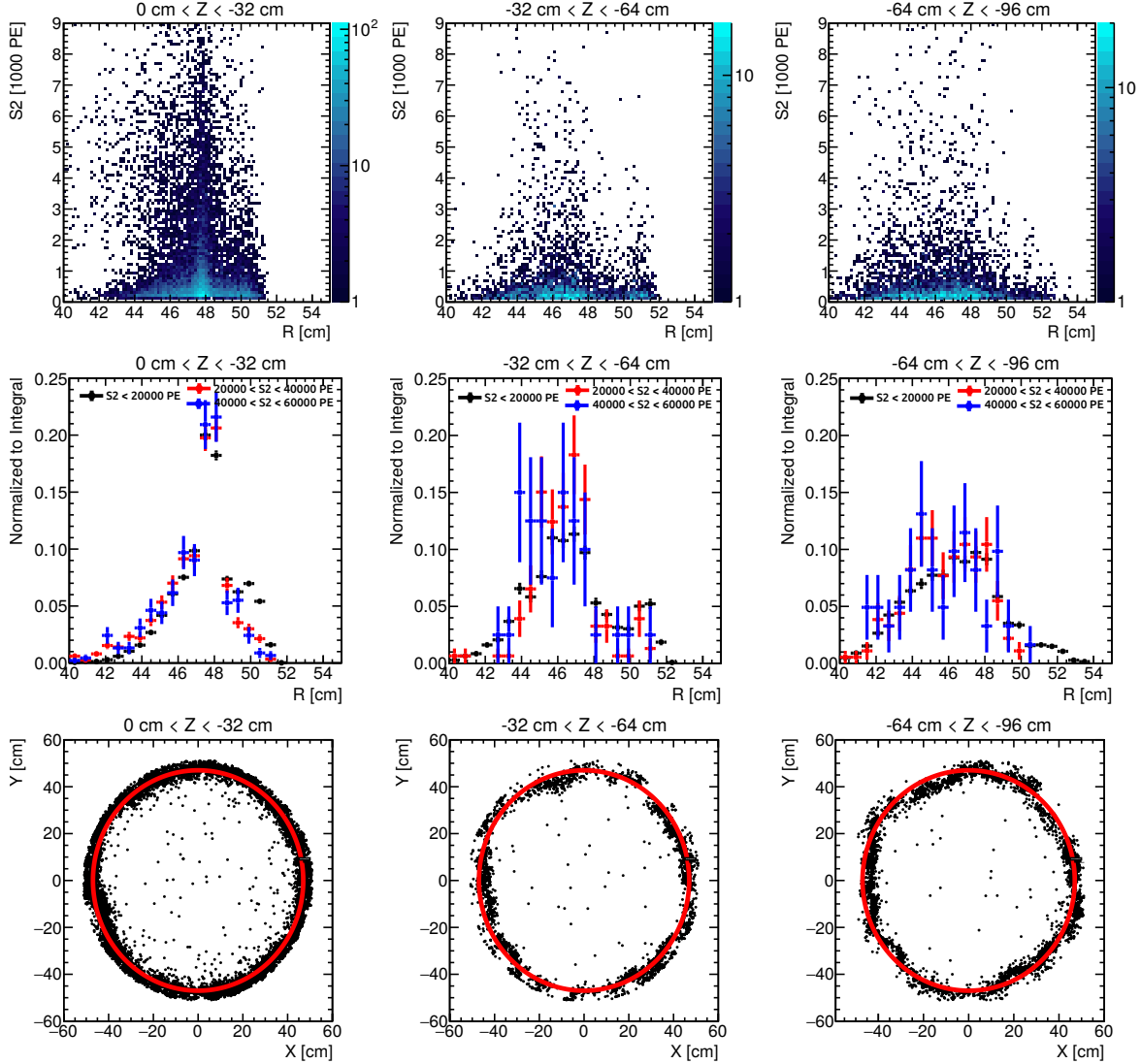


Figure D.3: Top row: Uncorrected S2 vs. R^2 distribution of low energy ($cS1 < 70$) background events within XENON1T passing the dark matter search criteria, for different Z ranges as indicated above each panel. The number of events is given by the color scale. **Middle row:** Comparison of projections of the data in the upper plots onto R for the S2 intervals [0, 20000] PE (black), [20000, 40000] PE (red), and [40000, 60000] PE (blue). **Bottom row:** X-Y distribution of the same events for the same Z intervals. The red circle marks the true TPC radius. Events that are lying outside are over-corrected by the field distortion correction.

List of Figures

1.1	Rotation curve of the galaxy NGC 6503	4
1.2	Bullet Cluster	5
1.3	Sky map of temperature fluctuations in the CMB	6
1.4	Power spectrum of the CMB temperature fluctuations	6
1.5	Dark matter freeze-out model	8
1.6	Illustration of the possible WIMP detection channels	10
1.7	Comparison of WIMP rates in different target materials	12
1.8	Scheme of common energy readout channels in direct detection experiments	14
1.9	Overview on current results of dark matter direct detection experiments . .	15
2.1	Sketch of the working principle of a two-phase time projection chamber . .	18
2.2	Vapor Pressures curves of gas components of air	20
2.3	Schematic of the transformation of deposited energy in xenon	21
2.4	Event waveform recorded by XENON1T	27
2.5	Prediction of electronic recoil background rates in XENON100 and XENON1T	29
2.6	Passive shielding of XENON100	32
2.7	Drawing of the XENON100 cryostat with TPC	33
2.8	Three dimensional drawing of the XENON1T TPC	34
2.9	The auxiliary systems of the XENON1T experiment	36
3.1	Pictures of the XENON1T bottle rack and gas chromatograph	42
3.2	Schematic of the XENON1T bottle rack	43
3.3	Schematic of a pulsed discharge detector	46
3.4	Internal configuration of the gas chromatograph	47
3.5	Influence of the measurement procedure on the chromatogram	48
3.6	Comparison of background and calibration chromatograms	51
3.7	Correlation between measured N ₂ and O ₂ +Ar concentrations	52
3.8	Electron-lifetime evolution in the XENON1T detector	65
4.1	Scheme of ²²⁰ Rn decay chain	69
4.2	Alpha spectra of data from the ²²⁰ Rn source in XENON100	71
4.3	Distribution of low energy background data within XENON100	74
4.4	Schematic of the XENON100 detector with gas in- and outlets	75
4.5	Schematic of the XENON1T cryostat with gas in- and outlets	76
4.6	Evolution of the ²²⁰ Rn and tritium source activities within the detector . . .	77
4.7	Time Evolution of alpha and low energy ER rate in XENON100	79

4.8	Spatial distribution of ER calibration events in XENON100	81
4.9	ER calibration spectra in XENON100	82
4.10	Demonstration of discrimination between ER and NR	83
4.11	ER calibration data in XENON100 in discrimination space	84
4.12	Projections onto the discrimination parameter	85
4.13	Comparison of ER band means and widths of calibration data in XENON100	86
4.14	Distribution of mono-energetic simulated events in discrimination space	88
4.15	Visualization of influences of different parameters on simulated ER bands	90
4.16	Influence of the spectral cut-off energy on the ER band shape	90
4.17	Influence of the S2 threshold on the ER band shape	91
4.18	Comparison of ER band models	93
4.19	Dark matter search data with calibrated discrimination lines	94
4.20	Comparison of ER band shape between XENON100 and XENON1T	97
4.21	Discrimination power and WIMP acceptances in XENON100 and XENON1T	98
5.1	Nuclear recoil detection efficiencies in XENON1T	103
5.2	Nuclear recoil calibration in XENON1T	104
5.3	Demonstration of Gaussian fit to ^{220}Rn calibration data in XENON1T	105
5.4	ER calibration data from ^{220}Rn in XENON1T in discrimination space	106
5.5	Effect of blinding criterion on ^{220}Rn and background data	107
5.6	Comparison of ^{220}Rn and Background spectral shapes	108
5.7	Maximum gap distribution	109
5.8	Spatial distribution of simulated and observed ER background in XENON1T	112
5.9	Wall leakage events in dark matter search data	114
5.10	Decay scheme of ^{222}Rn	115
5.11	cS1-cS2-spectrum of alpha decays in XENON1T	116
5.12	cS1-cS2-spectrum of alpha decays in XENON100	116
5.13	Spatial distribution of alpha decays in XENON1T	117
5.14	cS2 spectra of ^{210}Po in XENON100 and XENON1T	119
5.15	Comparison of spatial distribution of ^{210}Po in XENON100 and XENON1T	120
5.16	Correlation of S2 and Z for ^{210}Po decays in XENON1T	121
5.17	Spatial distribution of ^{210}Po and low energy background events in XENON1T	123
5.18	cS2 spectrum of wall background events in XENON1T	124
5.19	Background model of XENON1T	125
5.20	Wall leakage rate prediction	129
5.21	Correlation of wall event signals with the TPC radius	129
5.22	Model of wall leakage background spectra	130
5.23	Probability density function of wall events in cS1-cS2 _{bottom}	130
5.24	Dark Matter search data of the first science run of XENON1T	131
5.25	Exclusion limit of WIMP-nucleon scattering cross sections in XENON1T	132
C.1	R^2 and Z distributions of electronic recoils in XENON1T	148
C.2	Light and charge yield evolution in XENON100	149
D.1	^{210}Po decays in XENON1T in Z vs. S1 _{aft}	151
D.2	X-Y distribution of ^{210}Po events in XENON100	151

D.3 Correlation of Z and $cS2$ for low energy Wall events in XENON1T 152

List of Tables

3.1	List of impurity concentrations in the two self-made xenon calibration gases	56
3.2	Results of gas impurity measurements of the XENON1T xenon inventory .	59
3.3	Expectation of impurity concentrations in the XENON1T xenon inventory .	60
3.4	Validation of gas handling procedure	62
4.1	Light yields of alpha decays in XENON100	72
4.2	Summary of activities of internal calibration sources	78
4.3	Impact of calibration source on the dark matter result	95
4.4	Comparison of photon and electron gains in XENON100 and XENON1T .	96
5.1	Comparison of ^{220}Rn and background ER leakage fractions	111
5.2	S1 yields for alpha decays in XENON100 and XENON1T	116
5.3	Background expectation in XENON1T	127
B.1	Air composition	145
B.2	Composition of the helium gas mixture used for the GC calibration.	145

Bibliography

- [1] T. Marrodán Undagoitia and L. Rauch, *Dark matter direct-detection experiments*, J. Phys. **G43** (2016) no. 1, 013001, arXiv:1509.08767.
- [2] K. Freese, *Review of Observational Evidence for Dark Matter in the Universe and in upcoming searches for Dark Stars*, EAS Publ. Ser. **36** (2009) 113–126, arXiv:0812.4005.
- [3] F. Zwicky, *Spectral displacement of extra galactic nebulae*, Helv.Phys. Acta **6** (1933) 110–127.
- [4] V. C. Rubin and W. K. Ford, Jr., *Rotation of the Andromeda Nebula from a Spectroscopic Survey of Emission Regions*, Astrophysical Journal **159** (1970) 379.
- [5] Y. Sofue and V. Rubin, *Rotation curves of spiral galaxies*, Ann. Rev. Astron. Astrophys. **39** (2001) 137–174, arXiv:astro-ph/0010594.
- [6] R. Genzel *et al.*, *Strongly baryon-dominated disk galaxies at the peak of galaxy formation ten billion years ago*, Nature **543** (2017) 397–401, arXiv:1703.04310.
- [7] P. Repetto, E. E. Martínez-García, M. Rosado, and R. Gabbasov, *Mass content of UGC 6446 and UGC 7524 through HI rotation curves: deriving the stellar discs from stellar population synthesis models*, Mon. Not. Roy. Astron. Soc. **468** (2017) no. 1, 180.
- [8] F. Iocco, M. Pato, and G. Bertone, *Evidence for dark matter in the inner Milky Way*, Nat Phys **11** (2015) 245–248.
- [9] K. G. Begeman, A. H. Broeils, and R. H. Sanders, *Extended rotation curves of spiral galaxies - Dark haloes and modified dynamics*, MNRAS **249** (1991) 523–537.
- [10] Y. Mellier, *Probing the universe with weak lensing*, Ann. Rev. Astron. Astrophys. **37** (1999) 127–189, arXiv:astro-ph/9812172.
- [11] G. M. Bernstein and M. Jarvis, *Shapes and shears, stars and smears: optimal measurements for weak lensing*, Astron. J. **123** (2002) 583–618, arXiv:astro-ph/0107431.
- [12] S. D. Epps and M. J. Hudson, *The weak-lensing masses of filaments between luminous red galaxies*, Mon. Not. Roy. Astron. Soc. **468** (2017) no. 3, 2605.

- [13] A. Krolewski, K.-G. Lee, Z. Lukić, and M. White, *Measuring Alignments between Galaxies and the Cosmic Web at $z \sim 2-3$ Using IGM Tomography*, *The Astrophysical Journal* **837** (2017) no. 1, 31.
- [14] D. Harvey, R. Massey, T. Kitching, A. Taylor, and E. Tittley, *The non-gravitational interactions of dark matter in colliding galaxy clusters*, *Science* **347** (2015) 1462–1465, [arXiv:1503.07675](#).
- [15] P. A. R. Ade *et al.*, (Planck Collaboration), *Planck 2015 results. XIII. Cosmological parameters*, *Astron. Astrophys.* **594** (2016) A13, [arXiv:1502.01589](#).
- [16] P. D. Group), C. Patrignani, *et al.*, *Big-Bang nucleosynthesis*, *Chin. Phys. C* **40** (2016) 100001.
- [17] R. Adam *et al.*, (Planck Collaboration), *Planck 2015 results. I. Overview of products and scientific results*, *Astron. Astrophys.* **594** (2016) A1, [arXiv:1502.01582](#).
- [18] P. A. R. Ade *et al.*, (Planck Collaboration), *Planck 2013 results. I. Overview of products and scientific results*, *Astron. Astrophys.* **571** (2014) A1, [arXiv:1303.5062](#).
- [19] M. Milgrom, *A modification of the Newtonian dynamics as a possible alternative to the hidden mass hypothesis*, *Astrophysical Journal, Part 1* **270** (1983) 365–370.
- [20] J. D. Bekenstein, *Relativistic gravitation theory for the MOND paradigm*, *Phys. Rev.* **D70** (2004) 083509, [arXiv:astro-ph/0403694](#). [Erratum: *Phys. Rev.* **D71**, 069901(2005)].
- [21] J. E. Felten, *Milgrom’s revision of Newton’s laws - Dynamical and cosmological consequences*, *Astrophysical Journal* **286** (1984) 3–6.
- [22] N. E. Mavromatos, M. Sakellariadou, and M. F. Yusaf, *Can the relativistic field theory version of modified Newtonian dynamics avoid dark matter on galactic scales?*, *Phys. Rev.* **D79** (2009) 081301, [arXiv:0901.3932](#).
- [23] C. Alcock *et al.*, (MACHO Collaboration), *The MACHO project: Microlensing results from 5.7 years of LMC observations*, *Astrophys. J.* **542** (2000) 281–307, [arXiv:astro-ph/0001272](#).
- [24] S. D. M. White, C. S. Frenk, and M. Davis, *Clustering in a Neutrino Dominated Universe*, *Astrophys. J.* **274** (1983) L1–L5.
- [25] G. Gelmini and P. Gondolo, *DM Production Mechanisms*, In Bertone, G. (ed.): *Particle dark matter* 121–141.
- [26] T. Kaluza, *Zum Unitätsproblem in der Physik*, *Sitzungsber. Preuss. Akad. Wiss. Berlin. (Math. Phys.)* (1921) 966–972.
- [27] O. Klein, *Quantentheorie und fünfdimensionale Relativitätstheorie*, *Zeitschrift für Physik* **37** (1926) 895–906.

- [28] A. Boyarsky, O. Ruchayskiy, and M. Shaposhnikov, *The Role of sterile neutrinos in cosmology and astrophysics*, *Ann. Rev. Nucl. Part. Sci.* **59** (2009) 191–214, arXiv:0901.0011.
- [29] A. Kusenko, *Sterile neutrinos: The Dark side of the light fermions*, *Phys. Rept.* **481** (2009) 1–28, arXiv:0906.2968.
- [30] R. D. Peccei and H. R. Quinn, *CP Conservation in the Presence of Instantons*, *Phys. Rev. Lett.* **38** (1977) 1440–1443.
- [31] L. Visinelli and P. Gondolo, *Dark matter axions revisited*, *Physical Review D* **80** (2009) no. 3, 035024, arXiv:0903.4377.
- [32] V. Kuzmin and I. Tkachev, *Ultrahigh-energy cosmic rays, superheavy long living particles, and matter creation after inflation*, *JETP Lett.* **68** (1998) 271–275, arXiv:hep-ph/9802304. [*Pisma Zh. Eksp. Teor. Fiz.*68,255(1998)].
- [33] O. Buchmueller, C. Doglioni, and L.-T. Wang, *Search for dark matter at colliders*, *Nature Physics* (2017) 217–223. Progress Article.
- [34] A. de Cosa, (ATLAS and CMS Collaborations), *LHC results for dark matter from ATLAS and CMS*, in *Proceedings, 12th Conference on the Intersections of Particle and Nuclear Physics (CIPANP 2015): Vail, Colorado, USA, May 19-24, 2015*. 2015. arXiv:1510.01516.
- [35] A. M. Sirunyan *et al.*, (CMS Collaboration), *Dark Matter Summary Plots from CMS for LHCP and EPS 2017*, Wiki Open Access, 2017.
- [36] V. A. Mitsou, *Overview of searches for dark matter at the LHC*, *J. Phys. Conf. Ser.* **651** (2015) no. 1, 012023, arXiv:1402.3673.
- [37] L. E. Strigari, *Galactic Searches for Dark Matter*, *Phys. Rept.* **531** (2013) 1–88, arXiv:1211.7090.
- [38] J. Conrad, *Indirect Detection of WIMP Dark Matter: a compact review*, in *Interplay between Particle and Astroparticle physics (IPA2014) London, United Kingdom, August 18-22, 2014*. 2014. arXiv:1411.1925.
- [39] M. W. Goodman and E. Witten, *Detectability of certain dark-matter candidates*, *Phys. Rev. D* **31** (1985) 3095.
- [40] A. K. Drukier, K. Freese, and D. N. Spergel, *Detecting cold dark-matter candidates*, *Phys. Rev. D* **33** (1986) 3495–3508.
- [41] J. Silk *et al.*, *Particle Dark Matter: Observations, Models and Searches*. Cambridge Univ. Press, Cambridge, 2010.
- [42] F. J. Kerr and D. Lynden-Bell, *Review of galactic constants*, *Mon. Not. Roy. Astron. Soc.* **221** (1986) 1023.

- [43] M. C. Smith *et al.*, *The RAVE Survey: Constraining the Local Galactic Escape Speed*, *Mon. Not. Roy. Astron. Soc.* **379** (2007) 755–772, arXiv:astro-ph/0611671.
- [44] J. D. Lewin and P. F. Smith, *Review of mathematics, numerical factors, and corrections for dark matter experiments based on elastic nuclear recoil*, *Astropart. Phys.* **6** (1996) 87–112.
- [45] C. McCabe, *The Astrophysical Uncertainties Of Dark Matter Direct Detection Experiments*, *Phys. Rev.* **D82** (2010) 023530, arXiv:1005.0579.
- [46] R. H. Helm, *Inelastic and Elastic Scattering of 187-Mev Electrons from Selected Even-Even Nuclei*, *Phys. Rev.* **104** (1956) 1466–1475.
- [47] M. T. Ressell and D. J. Dean, *Spin dependent neutralino - nucleus scattering for A approximately 127 nuclei*, *Phys. Rev.* **C56** (1997) 535–546, arXiv:hep-ph/9702290.
- [48] P. Toivanen, M. Kortelainen, J. Suhonen, and J. Toivanen, *Large-scale shell-model calculations of elastic and inelastic scattering rates of lightest supersymmetric particles (LSP) on I-127, Xe-129, Xe-131, and Cs-133 nuclei*, *Phys. Rev.* **C79** (2009) 044302.
- [49] V. Chepel and H. Araujo, *Liquid noble gas detectors for low energy particle physics*, *JINST* **8** (2013) R04001, arXiv:1207.2292.
- [50] T. Saab, *An Introduction to Dark Matter Direct Detection Searches & Techniques*, in *The Dark Secrets of the Terascale: Proceedings, TASI 2011, Boulder, Colorado, USA, Jun 6 - Jul 11, 2011*, pp. 711–738. 2013. arXiv:1203.2566.
- [51] G. Angloher *et al.*, (CRESST Collaboration), *Results on light dark matter particles with a low-threshold CRESST-II detector*, *Eur. Phys. J.* **C76** (2016) no. 1, 25, arXiv:1509.01515.
- [52] R. Agnese *et al.*, (SuperCDMS Collaboration), *New Results from the Search for Low-Mass Weakly Interacting Massive Particles with the CDMS Low Ionization Threshold Experiment*, *Phys. Rev. Lett.* **116** (2016) no. 7, 071301, arXiv:1509.02448.
- [53] E. Aprile *et al.*, (XENON Collaboration), *First Dark Matter Search Results from the XENON1T Experiment*, arXiv:1705.06655.
- [54] D. S. Akerib *et al.*, (LUX Collaboration), *Results from a search for dark matter in the complete LUX exposure*, *Phys. Rev. Lett.* **118** (2017) no. 2, 021303, arXiv:1608.07648.
- [55] A. Tan *et al.*, (PandaX-II Collaboration), *Dark Matter Results from First 98.7 Days of Data from the PandaX-II Experiment*, *Phys. Rev. Lett.* **117** (2016) 121303.

- [56] E. Aprile *et al.*, (XENON Collaboration), *XENON100 Dark Matter Results from a Combination of 477 Live Days*, Phys. Rev. **D94** (2016) no. 12, 122001, arXiv:1609.06154.
- [57] R. Bernabei *et al.*, *Final model independent result of DAMA/LIBRA-phase1*, Eur. Phys. J. **C73** (2013) 2648, arXiv:1308.5109.
- [58] P. Agnes *et al.*, (DarkSide Collaboration), *First results from the DarkSide-50 dark matter experiment at Laboratori Nazionali del Gran Sasso*, Physics Letters B **743** (2015) 456 – 466.
- [59] E. Armengaud, , *et al.*, (EDELWEISS Collaboration), *Constraints on low-mass WIMPs from the EDELWEISS-III dark matter search*, Journal of Cosmology and Astroparticle Physics **2016** (2016) no. 05, 019, arXiv:1603.05120.
- [60] C. Amole *et al.*, (PICO Collaboration), *Dark Matter Search Results from the PICO–60 C₃F₈ Bubble Chamber*, Phys. Rev. Lett. **118** (2017) 251301.
- [61] E. Aprile *et al.*, (XENON Collaboration), *Search for Electronic Recoil Event Rate Modulation with 4 Years of XENON100 Data*, Phys. Rev. Lett. **118** (2017) no. 10, 101101, arXiv:1701.00769.
- [62] *Laboratori Nazionali del Gran Sasso*, www.lgns.infn.it.
- [63] G. Bellini *et al.*, (Borexino Collaboration), *Cosmic-muon flux and annual modulation in Borexino at 3800 m water-equivalent depth*, JCAP **1205** (2012) 015, arXiv:1202.6403.
- [64] E. Aprile *et al.*, (XENON Collaboration), *Online ²²²Rn removal by cryogenic distillation in the XENON100 experiment*, Eur. Phys. J. **C77** (2017) no. 6, 358, arXiv:1702.06942.
- [65] *Private Communication*, XENON1T Collaboration.
- [66] E. Aprile, C. E. Dahl, L. DeViveiros, R. Gaitskell, K. L. Giboni, J. Kwong, P. Majewski, K. Ni, T. Shutt, and M. Yamashita, *Simultaneous measurement of ionization and scintillation from nuclear recoils in liquid xenon as target for a dark matter experiment*, Phys. Rev. Lett. **97** (2006) 081302, arXiv:astro-ph/0601552.
- [67] B. Dolgoshein, V. Lebedenko, and B. Rodionov, *New Method of Registration of Ionizing-particle Tracks in Condensed Matter*, JETP Letters **11** (1970) 315.
- [68] A. Bolozdynya, V. Egorov, B. Rodionov, and V. Miroshnichenko, *Emission detectors*, IEEE Transactions on Nuclear Science **42** (1995) no. 4, 565–569.
- [69] A. Bolozdynya, *Two-phase emission detectors and their applications*, Nuclear Instruments and Methods in Physics Research Section A: Accelerators, Spectrometers, Detectors and Associated Equipment **422** (1999) no. 1–3, 314 – 320.

- [70] E. Aprile, K. L. Giboni, P. Majewski, K. Ni, and M. Yamashita, *Proportional light in a dual-phase xenon chamber*, IEEE Transactions on Nuclear Science **51** (2004) no. 5, 1986–1990.
- [71] E. M. Gushchin *et al.*, *Electron emission from condensed noble gases*, Sov. Phys. JETP **49** (1979) 5.
- [72] E. Aprile and T. Doke, *Liquid Xenon Detectors for Particle Physics and Astrophysics*, Rev. Mod. Phys. **82** (2010) 2053–2097, arXiv:0910.4956.
- [73] L. S. Miller, S. Howe, and W. E. Spear, *Charge Transport in Solid and Liquid Ar, Kr, and Xe*, Phys. Rev. **166** (1968) 871–878.
- [74] A. Zell *et al.*, *Stuttgart Neural Network Simulator*, <http://www.ra.cs.uni-tuebingen.de/SNNS/>.
- [75] E. Aprile *et al.*, (XENON Collaboration), *The XENON100 dark matter experiment*, Astroparticle Physics **35** (2012) no. 9, 573 – 590.
- [76] *Brookhaven National Laboratory, national nuclear data center*, 2015. <http://www.nndc.bnl.gov/>.
- [77] *Echte Werte: Technische Gase in Zahlen, Daten und Fakten.*, http://www.westfalen-austria.at/fileadmin/user_uploads/Westfalen_AG/Technische_Gase/Allgemein/Prospekte_Technische_Gase/Echte_Werte_Zahlen.pdf. Westfalen AG.
- [78] Dortmund Data Bank GmbH, *Vapor Pressure of Methane*. http://www.ddbst.com/en/EED/PCP/VAP_C1051.php.
- [79] M. u. N. B.-W. Landesanstalt für Umwelt, *Zusammensetzung der Luft*, <Http://www4.lubw.baden-wuerttemberg.de/servlet/is/18340/>, 2013.
- [80] X. Du, K. Bailey, Z.-T. Lu, P. Mueller, T. P. O’Connor, and L. Young, *An atom trap system for practical ⁸¹Kr dating*, Review of Scientific Instruments **75** (2004) 3224–3232.
- [81] I. T. Steinberger and U. Asaf, *Band-Structure Parameters of Solid and Liquid Xenon*, Physical Review B **8** (1973) 914–918.
- [82] R. Reininger, U. Asaf, I. T. Steinberger, P. Laporte, and V. Saile, “Free” electrons and excitons in fluid krypton, Physical Review B **26** (1982) 6294–6296.
- [83] B. Lenardo, K. Kazkaz, A. Manalaysay, J. Mock, M. Szydagis, and M. Tripathi, *A Global Analysis of Light and Charge Yields in Liquid Xenon*, IEEE Trans. Nucl. Sci. **62** (2015) no. 6, 3387–3396, arXiv:1412.4417.
- [84] R. Platzman, *Total ionization in gases by high-energy particles: An appraisal of our understanding*, The International Journal of Applied Radiation and Isotopes **10** (1961) no. 2, 116 – 127.

- [85] S. Kubota, M. Hishida, and J. Raun, *Evidence for a triplet state of the self-trapped exciton states in liquid argon, krypton and xenon*, Journal of Physics C: Solid State Physics **11** (1978) no. 12, 2645.
- [86] J. Jortner *et al.*, *Localized Excitations in Condensed Ne, Ar, Kr, and Xe*, The Journal of chemical physics **42** (1965) 4250.
- [87] A. Hitachi, T. Takahashi, N. Funayama, K. Masuda, J. Kikuchi, and T. Doke, *Effect of ionization density on the time dependence of luminescence from liquid argon and xenon*, Phys. Rev. **B27** (1983) 5279–5285.
- [88] A. Hitachi, T. Takahashi, N. Funayama, K. Masuda, J. Kikuchi, and T. Doke, *Effect of ionization density on the time dependence of luminescence from liquid argon and xenon*, Phys. Rev. B **27** (1983) 5279–5285.
- [89] T. Doke, A. Hitachi, J. Kikuchi, K. Masuda, H. Okada, and E. Shibamura, *Absolute Scintillation Yields in Liquid Argon and Xenon for Various Particles*, Japanese Journal of Applied Physics **41** (2002) no. 3R, 1538.
- [90] E. Aprile, C. E. Dahl, L. DeViveiros, R. Gaitskell, K. L. Giboni, J. Kwong, P. Majewski, K. Ni, T. Shutt, and M. Yamashita, *Simultaneous measurement of ionization and scintillation from nuclear recoils in liquid xenon as target for a dark matter experiment*, Phys. Rev. Lett. **97** (2006) 081302, arXiv:astro-ph/0601552.
- [91] T. Doke, A. Hitachi, S. Kubota, A. Nakamoto, and T. Takahashi, *Estimation of Fano factors in liquid argon, krypton, xenon and xenon-doped liquid argon*, Nucl. Instrum. Meth. **134** (1976) 353–357.
- [92] J. Angle *et al.*, (XENON Collaboration), *A search for light dark matter in XENON10 data*, Phys. Rev. Lett. **107** (2011) 051301, arXiv:1104.3088. [Erratum: Phys. Rev. Lett.110,249901(2013)].
- [93] C. Silva, J. P. da Cunha, A. Pereira, V. Chepel, M. I. Lopes, V. Solovov, and F. Neves, *Reflectance of polytetrafluoroethylene for xenon scintillation light*, Journal of Applied Physics **107** (2010) .
- [94] P. Barrow *et al.*, *Qualification Tests of the R11410-21 Photomultiplier Tubes for the XENONIT Detector*, JINST **12** (2017) no. 01, P01024, arXiv:1609.01654.
- [95] M. Weber, *Gentle Neutron Signals and Noble Background in the XENON100 Dark Matter Search Experiment*. PhD thesis, Ruprecht-Karls-Universität, Heidelberg, 2013.
- [96] E. Aprile *et al.*, (XENON Collaboration), *Analysis of the XENON100 dark matter search data*, Astroparticle Physics **54** (2014) 11 – 24.
- [97] E. Aprile *et al.*, (XENON Collaboration), *Observation and applications of single-electron charge signals in the XENON100 experiment*, J. Phys. **G41** (2014) 035201, arXiv:1311.1088.

- [98] T. Doke, A. Hitachi, J. Kikuchi, K. Masuda, H. Okada, and E. Shibamura, *Absolute Scintillation Yields in Liquid Argon and Xenon for Various Particles*, Japanese Journal of Applied Physics **41** (2002) no. 3R, 1538.
- [99] J. Lindhard, M. Scharff, and S. H. E., *Range concepts and heavy ion ranges, (Notes on atomic collisions, II.)*, Mat. Fys. Medd. Dan. Vid. Selsk. **33** (1963) 1–42.
- [100] A. Hitachi, T. Takahashi, N. Funayama, K. Masuda, J. Kikuchi, and T. Doke, *Effect of ionization density on the time dependence of luminescence from liquid argon and xenon*, Phys. Rev. B **27** (1983) 5279–5285.
- [101] A. Hitachi, T. Doke, and A. Mozumder, *Luminescence quenching in liquid argon under charged-particle impact: Relative scintillation yield at different linear energy transfers*, Phys. Rev. B **46** (1992) 11463–11470.
- [102] G. Plante *et al.*, *New Measurement of the Scintillation Efficiency of Low-Energy Nuclear Recoils in Liquid Xenon*, Phys. Rev. **C84** (2011) 045805, arXiv:1104.2587.
- [103] D. S. Akerib *et al.*, (LUX Collaboration), *Low-energy (0.7-74 keV) nuclear recoil calibration of the LUX dark matter experiment using D-D neutron scattering kinematics*, arXiv:1608.05381.
- [104] E. Aprile *et al.*, (XENON Collaboration), *Response of the XENON100 Dark Matter Detector to Nuclear Recoils*, Phys. Rev. **D88** (2013) 012006, arXiv:1304.1427.
- [105] E. Aprile *et al.*, (XENON Collaboration), *The XENON1T Dark Matter Experiment*, arXiv:1708.07051.
- [106] R. Brun and F. Rademakers, *ROOT - An Object Oriented Data Analysis Framework*, Nucl. Inst. Meth. in Phys. Res. **A 389** (1997) 81–86. <http://root.cern.ch/>.
- [107] E. Aprile *et al.*, (XENON Collaboration), *The neutron background of the XENON100 dark matter search experiment*, J. Phys. **G40** (2013) 115201, arXiv:1306.2303.
- [108] E. Aprile *et al.*, (XENON Collaboration), *Physics reach of the XENON1T dark matter experiment*, JCAP **1604** (2016) no. 04, 027, arXiv:1512.07501.
- [109] E. Aprile *et al.*, (XENON Collaboration), *Erratum: Study of the electromagnetic background in the XENON100 experiment [Phys. Rev. D 83, 082001 (2011)]*, Phys. Rev. D **85** (2012) 029904.
- [110] E. Aprile *et al.*, (XENON Collaboration), *Material screening and selection for XENON100*, Astroparticle Physics **35** (2011) no. 2, 43 – 49.
- [111] E. Aprile *et al.*, (XENON Collaboration), *Material radioassay and selection for the XENON1T dark matter experiment*, arXiv:1705.01828.

- [112] L. Baudis, A. D. Ferella, A. Askin, J. Angle, E. Aprile, T. Bruch, A. Kish, M. Laubenstein, A. Manalaysay, T. M. Undagoitia, and M. Schumann, *Gator: a low-background counting facility at the Gran Sasso Underground Laboratory*, Journal of Instrumentation **6** (2011) no. 08, P08010, arXiv:1103.2125.
- [113] G. Heusser, M. Laubenstein, and H. Neder, *Low-level germanium gamma-ray spectrometry at the $\mu\text{Bq/kg}$ level and future developments towards higher sensitivity.*, Proc. of Intern. Conf. Isotop. Environm. (2004) . Studies Aquatic Forum.
- [114] G. Heusser, M. Weber, J. Hakenmüller, M. Laubenstein, M. Lindner, W. Maneschg, H. Simgen, D. Stolzenburg, and H. Strecker, *GIOVE - A new detector setup for high sensitivity germanium spectroscopy at shallow depth*, Eur. Phys. J. **C75** (2015) no. 11, 531, arXiv:1507.03319.
- [115] S. Brünner, *Mitigation of ^{222}Rn induced background in the XENONIT dark matter experiment.* PhD thesis, Ruprecht-Karls-Universität, Heidelberg, 2017.
- [116] N. Rupp, *On the detection of ^{222}Rn with miniaturized proportional counters: background, sensitivity studies and results for XENONIT*, Master's thesis, Ruprecht-Karls-Universität, Heidelberg, 2015.
- [117] S. Brünner, D. Cichon, S. Lindemann, T. Marrodán Undagoitia, and H. Simgen, *Radon depletion in xenon boil-off gas*, Eur. Phys. J. **C77** (2017) no. 3, 143, arXiv:1611.03737.
- [118] S. Lindemann and H. Simgen, *Krypton assay in xenon at the ppq level using a gas chromatographic system and mass spectrometer*, Eur. Phys. J. **C74** (2014) 2746, arXiv:1308.4806.
- [119] J. B. Albert *et al.*, (EXO-200 Collaboration), *Improved measurement of the $2\nu\beta\beta$ half-life of ^{136}Xe with the EXO-200 detector*, Phys. Rev. **C89** (2014) no. 1, 015502, arXiv:1306.6106.
- [120] M. Schumann, L. Baudis, L. Bütikofer, A. Kish, and M. Selvi, *Dark matter sensitivity of multi-ton liquid xenon detectors*, JCAP **1510** (2015) no. 10, 016, arXiv:1506.08309.
- [121] M. Yamashita, T. Doke, K. Kawasaki, J. Kikuchi, and S. Suzuki, *Scintillation response of liquid Xe surrounded by PTFE reflector for gamma rays*, Nuclear Instruments and Methods in Physics Research Section A: Accelerators, Spectrometers, Detectors and Associated Equipment **535** (2004) no. 3, 692 – 698.
- [122] M. Aglietta *et al.*, (LVD Collaboration), *Muon “depth-intensity” relation measured by the LVD underground experiment and cosmic-ray muon spectrum at sea level*, Phys. Rev. D **58** (1998) 092005.
- [123] S. P. Gas, *PS4-MT50-R Getter Specifications*, http://www.saespuregas.com/Library/specifications-brochures/s110-233_a_521.pdf.

- [124] E. Aprile, W. CHEN, J. Stutzmann, D. Thers, P. Briend, and F. Durand, *Facility and method for supplying liquid xenon*, 2013. EP Patent App. EP20,130,151,810.
- [125] E. Aprile *et al.*, *Removing krypton from xenon by cryogenic distillation to the ppq level*, Eur. Phys. J. **C77** (2017) no. 5, 275, arXiv:1612.04284 [physics.ins-det].
- [126] N. Yoshimura, T. Sato, S. Adachi, and T. Kanazawa, *Outgassing characteristics and microstructure of an electropolished stainless steel surface*, Journal of Vacuum Science & Technology A: Vacuum, Surfaces, and Films **8** (1990) no. 2, 924–929, <http://dx.doi.org/10.1116/1.576897>.
- [127] V. Pizzella, *Purity control of the XENONIT gas inventory prior to initial filling and studies of mixing properties of impurities in gaseous xenon*, Master's thesis, Università di Roma, Rome, 2016.
- [128] M. C. Desjonqueres *et al.*, *Concepts in surface physics (2nd ed.)*. New York: Springer-Verlag, 1996. Corrected printing 1998.
- [129] G. Guiochon and C. L. Guillemin, *Gas chromatography*, Review of Scientific Instruments **61** (1990) no. 11, 3317–3339.
- [130] B. A. Rose, *Gas chromatography and its analytical applications. A review*, Analyst **84** (1959) 574b–595.
- [131] W. Wentworth, S. Vasin, S. Stearns, and C. Meyer, *Pulsed discharge helium ionization detector*, Chromatographia **34** (1992) 219.
- [132] W. Wentworth, S. Vasin, S. Stearns, and C. Meyer, *Pulsed discharge emission detector Application to analytical spectroscopy of permanent gases*, Chromatographia **34** (1992) 226.
- [133] D. Forsyth, *Pulsed discharge detector: theory and applications*, Journal of Chromatography A **1050** (2004) no. 1, 63 – 68. Current State of Element Selective Detection in Chromatography.
- [134] V. I. C. I. (VICI), *Pulsed Discharge Detector Models D-4-I-TQ-R and D-4-I-TQI-R Instruction Manual*, .
http://www.vici.com/support/manuals/d4_therm.pdf.
- [135] W. Wentworth, H. Cai, and S. Stearns, *Pulsed discharge helium ionization detector: Universal detector for inorganic and organic compounds at the low picogram level*, Journal of Chromatography A **688** (1994) no. 1, 135 – 152.
- [136] P. Benetti *et al.*, (WARP Collaboration), *Measurement of the specific activity of ar-39 in natural argon*, Nucl. Instrum. Meth. **A574** (2007) 83–88, arXiv:astro-ph/0603131.

- [137] X. Du, R. Purtschert, K. Bailey, B. E. Lehmann, R. Lorenzo, Z.-T. Lu, P. Mueller, T. P. O’Connor, N. C. Sturchio, and L. Young, *A new method of measuring ^{81}Kr and ^{85}Kr abundances in environmental samples*, *Geophysical Research Letters* **30** (2003) no. 20, n/a–n/a. 2068.
- [138] R. Lang, A. Brown, E. Brown, M. Cervantes, S. Macmullin, D. Masson, J. Schreiner, and H. Simgen, *A ^{220}Rn source for the calibration of low-background experiments*, *Journal of Instrumentation* **11** (2016) no. 04, P04004, arXiv:1602.01138.
- [139] E. Aprile *et al.*, (XENON Collaboration), *Results from a Calibration of XENON100 Using a Source of Dissolved Radon-220*, arXiv:1611.03585.
- [140] H. Miyake, M. Matsuyama, K. Ashida, and K. Watanabe, *Permeation, diffusion, and solution of hydrogen isotopes, methane, and inert gases in/through tetrafluoroethylene and polyethylene*, *Journal of Vacuum Science & Technology A: Vacuum, Surfaces, and Films* **1** (1983) no. 3, 1447–1451.
- [141] D. S. Akerib *et al.*, (LUX Collaboration), *Tritium calibration of the LUX dark matter experiment*, *Phys. Rev.* **D93** (2016) no. 7, 072009, arXiv:1512.03133.
- [142] A. Dobi, *Measurement of the Electron Recoil Band of the LUX Dark Matter Detector With a Tritium Calibration Source*. PhD thesis, University of Maryland, 2014.
- [143] R. F. Lang, J. Pienaar, E. Hogenbirk, D. Masson, R. Nolte, A. Zimbal, S. Röttger, M. L. Benabderrahmane, and G. Bruno, *Characterization of a Deuterium-Deuterium Plasma Fusion Neutron Generator*, arXiv:1705.04741.
- [144] E. Aprile *et al.*, (XENON Collaboration), *Intrinsic backgrounds from Rn and Kr in the XENON100 experiment*, . in preparation.
- [145] *Private Communication*, XENON100 Collaboration.
- [146] E. Aprile *et al.*, (XENON Collaboration), *First Dark Matter Results from the XENON100 Experiment*, *Phys. Rev. Lett.* **105** (2010) 131302.
- [147] B. Lenardo, K. Kazkaz, A. Manalaysay, J. Mock, M. Szydagis, and M. Tripathi, *A Global Analysis of Light and Charge Yields in Liquid Xenon*, *IEEE Trans. Nucl. Sci.* **62** (2015) no. 6, 3387–3396, arXiv:1412.4417.
- [148] E. Aprile *et al.*, (XENON Collaboration), *Likelihood Approach to the First Dark Matter Results from XENON100*, *Phys. Rev.* **D84** (2011) 052003, arXiv:1103.0303.
- [149] G. J. Feldman and R. D. Cousins, *A Unified approach to the classical statistical analysis of small signals*, *Phys. Rev.* **D57** (1998) 3873–3889, arXiv:physics/9711021.
- [150] E. Aprile *et al.*, (XENON Collaboration), *Dark Matter Results from 225 Live Days of XENON100 Data*, *Phys. Rev. Lett.* **109** (2012) 181301, arXiv:1207.5988.

- [151] X. Ji, (PandaX Collaboration), *Dark Matter Search*, TeV Particle Astrophysics (2017) . Conference talk.
- [152] D. S. Akerib *et al.*, (LZ Collaboration), *LUX-ZEPLIN (LZ) Conceptual Design Report*, arXiv:1509.02910.
- [153] J. Marsh, D. Thomas, and M. Burke, *High resolution measurements of neutron energy spectra from AmBe and AmB neutron sources*, Nuclear Instruments and Methods in Physics Research Section A: Accelerators, Spectrometers, Detectors and Associated Equipment **366** (1995) no. 2, 340 – 348.
- [154] S. Yellin, *Finding an upper limit in the presence of an unknown background*, Phys. Rev. D **66** (2002) 032005.
- [155] V. N. Lebedenko *et al.*, *Result from the First Science Run of the ZEPLIN-III Dark Matter Search Experiment*, Phys. Rev. **D80** (2009) 052010, arXiv:0812.1150.
- [156] P. A. Breur, *Backgrounds in XENONIT*, . PhD thesis in preparation.
- [157] G. Alner *et al.*, *First limits on WIMP nuclear recoil signals in ZEPLIN-II: A two-phase xenon detector for dark matter detection*, Astroparticle Physics **28** (2007) no. 3, 287 – 302.
- [158] J. Kwong, *The Development of Two-Phase Xenon Dark Matter Detectors*. PhD thesis, Princeton U., 2009.
- [159] D. S. Akerib *et al.*, (LUX Collaboration), *Results from a search for dark matter in the complete LUX exposure*, Phys. Rev. Lett. **118** (2017) no. 2, 021303, arXiv:1608.07648.
- [160] M. Clemenza, C. Maiano, L. Pattavina, and E. Previtali, *Radon-induced surface contaminations in low background experiments*, The European Physical Journal C **71** (2011) no. 11, 1805.
- [161] M. Leung, *The Borexino Solar Neutrino Experiment: Scintillator purification and surface contamination*. PhD thesis, Princeton University, 2006.
- [162] C. Lee, *Mitigation of Background for the Large Underground Xenon Dark Matter Experiment*. PhD thesis, Case Western Reserve University, 2015.
- [163] M. Berger, J. Coursey, M. Zucker, and J. Chang, *ESTAR, PSTAR, and ASTAR: Computer Programs for Calculating Stopping-Power and Range Tables for Electrons, Protons, and Helium Ions (version 1.2.3)*. National Institute of Standards and Technology, Gaithersburg, MD, 2005.
<http://physics.nist.gov/Star>. accessed July, 13 2017.
- [164] *COMSOL Multiphysics*, <https://www.comsol.com>. COMSOL Inc.
- [165] E. Parzen, *On Estimation of a Probability Density Function and Mode*, Ann. Math. Statist. **33** (09, 1962) 1065–1076.

- [166] M. Rosenblatt, *Remarks on Some Nonparametric Estimates of a Density Function*, Ann. Math. Statist. **27** (09, 1956) 832–837.
- [167] G. Cowan, K. Cranmer, E. Gross, and O. Vitells, *Asymptotic formulae for likelihood-based tests of new physics*, Eur. Phys. J. **C71** (2011) 1554, arXiv:1007.1727. [Erratum: Eur. Phys. J.C73,2501(2013)].
- [168] N. Priel, L. Rauch, H. Landsman, A. Manfredini, and R. Budnik, *A model independent safeguard against background mismodeling for statistical inference*, JCAP **1705** (2017) no. 05, 013, arXiv:1610.02643.
- [169] D. S. Akerib *et al.*, (LUX Collaboration), *Improved Limits on Scattering of Weakly Interacting Massive Particles from Reanalysis of 2013 LUX Data*, Phys. Rev. Lett. **116** (2016) no. 16, 161301, arXiv:1512.03506.
- [170] J. Aalbers *et al.*, (DARWIN Collaboration), *DARWIN: towards the ultimate dark matter detector*, JCAP **1611** (2016) 017, arXiv:1606.07001.

Danksagung

An dieser Stelle möchte ich allen meinen Dank aussprechen, die diese Arbeit ermöglicht und zu ihrem Gelingen beigetragen haben.

Ganz ohne Frage würde diese Doktorarbeit nicht vorliegen, wenn Prof. Dr. Manfred Lindner nicht meinen Wunsch, nach dunkler Materie zu suchen, erfüllt und mir eine Stelle in der XENON Gruppe des MPIK angeboten hätte. Ihm danke ich besonders für die Möglichkeit, an diesem hochaktuellen Forschungsthema und noch dazu bei einem der führenden Experimente mitwirken zu dürfen. Mein Dank geht gleichfalls an Prof. Dr. Loredana Gastaldo, die sich für die Zweitbegutachtung dieser Arbeit bereit erklärte.

Des weiteren möchte ich allen Korrekturlesern danken, die die Arbeit mit vielen wertvollen Verbesserungsvorschlägen aufwerteten. Hier seien gebührend erwähnt Dr. Teresa Marrodán Undagoitia, Dr. Hardy Simgen, Dr. Stefan Brünner, Dr. Guillaume Eurin, Natascha Rupp, Dr. Ludwig Rauch, Dr. Sebastian Lindemann, Dr. Bernhard Schwingenheuer, Christian Bittel und nicht zuletzt zwei ominöser kanadische "Proofreader".

Für ihre Betreuung in allen Gaschromatographiefragen, ihren Beistand beim Lösen von GC-Rätseln wie z.B. Haifischzähnen und ihre Mitwirkung beim Design des famosen Bottle Racks möchte ich Dr. Hardy Simgen und Dr. Sebastian Lindemann danken. Veronica Pizzella danke ich für ihre Unterstützung bei den GC-Messungen am Gran Sasso.

Dr. Teresa Marrodán Undagoitia gilt mein Dank für ihre gute Betreuung bei allen Analysefragen und ihre motivierende und aufmunternde Art, die wieder den Forschergeist in mir weckte, wenn ich mal wieder dachte, dass ich auf dem Holzweg sei.

Den Mitgliedern der XENON Gruppe des MPIK verdanke ich eine tolle Doktorandenzeit, in der ich gerne morgens den Berg zum Institut hoch radelte. Beistand im Auf- und Ab des Doktorandenlebens bekam ich besonders von Stefan Brünner, Natascha Rupp, Guillaume Eurin und Ludwig Rauch durch ständig offene Ohren und Türen, lebhafte und lehrreiche Diskussionen und so manches "Betthupferl". Des weiteren sei allen in der Lindner Abteilung des Instituts gedankt für eine schöne Zeit am Institut mit vielseitigem Austausch über den Teller- und hinaus.

Mein Dank gilt ebenfalls der XENON Kollaboration, diesem bunten Haufen an Wissenschaftlern, verstreut über die ganze Welt. Da eine Liste von über hundert Namen den Rahmen hier sprengen würde will ich stellvertretend nur die folgenden erwähnen. Ich danke Dr. Rino Persiani, Jean-Marie Disdier und Danilo Tatananni, ohne die die Füllkampagnen von ReStoX und damit die GC-Messungen nicht möglich gewesen wären. Des weiteren geht ein spezieller Dank an Sander Breur für inspirierende Gespräche über virtuelle und reale Detektorvolumina und Untergrundlecks von den Detektorwänden in Chicago und die gute Zusammenarbeit bei der Entwicklung des Wall Leakage Modells.

Meinem Mitbewohner Danny Rehl möchte ich für die vielen interessanten Gespräche beim Abendessen danken, aufmunternde Worte und für ein entspanntes und unkompliziertes Zusammenwohnen.

Spezieller Dank geht an meine Familie, für ihr Verständnis und die Faszination für meine Tätigkeiten und ihren moralischen Beistand. Im Besonderen möchte ich meinen Eltern danken, ohne deren bedingungslose Unterstützung ich es nicht bis zu einer Promotion gebracht hätte.

Zu guter Letzt sei noch Christian Bittel gebührend erwähnt, der mich zwar erst auf dem letzten Stück des Doktorandenweges begleitete, das aber mit vollster Unterstützung. Ihm danke ich von Herzen für sein Interesse für die physikalischen Mysterien der Welt, die auch in mir wieder die Faszination für Physik weckten, wenn sie mir mal verloren gegangen war, für sein Verständnis in so mancher Doktorandenkrise und für seine aufopferungsvolle Hilfe beim Endspurt des Schreibens.